Decadal-scale evolution of Elwha River downstream of Glines Canyon dam

Perspectives from numerical modeling

by

Kathryn Grace De Rego

MA, Geography and Mediaeval History, University of St. Andrews, 2010

MSc, Earth and Quaternary Sciences, Indiana State University, 2012

A THESIS SUBMITTED IN PARTIAL FULFILLMENT
OF THE REQUIREMENTS FOR THE DEGREE OF

Doctor of Philosophy

in

THE FACULTY OF GRADUATE AND POSTDOCTORAL STUDIES
(Geography)

The University of British Columbia
(Vancouver)

March 2018

Abstract

The goal of this study is to understand the legacy of dams on river channel evolution. Most major world rivers are dammed, and these features have pervasive impacts on downstream geomorphology. Dam removals have become a popular restoration technique. However, little is known about how rivers respond to dam removal on long timescales, especially with regards to sediment exchanges between the channel and floodplain. We examine how dam emplacement and removal have affected channel stability and migration along Elwha River, a cobble-bedded wandering stream. Two dams were built on the river in the early 20th century, blocking sediment supply to the reaches below them. The dams were removed between 2011 and 2014.

A numerical model, MAST-1D, is adapted to simulate channel evolution on the set of reaches between the two dams. New representations of bank erosion, vegetation encroachment, and avulsion are developed to make the model suitable for cobble-bedded streams. In the model, channel width and migration oscillate between a range of values, increasing after avulsions due to reorganization of channel geometry. The model is successful at simulating channel change during the sediment-starved period following dam emplacement. While it replicates the general pattern of channel change following dam removal, the simulations underestimate the competence of the system to export the initial pulse of sediment from the former reservoir deposit. Constraining the volume and caliber of sediment supply from the reservoir is crucial for predicting sediment deposition and storage downstream.

Model simulations indicate that dam emplacement results in channel armoring, which reduces the competence of the flow to undercut bank toes, reducing the migration rate and leading to net channel narrowing. Both field and model data show that activation of floodplain channels via avulsion and, to a lesser extent, bank erosion, were responsible for increased levels of channel-floodplain exchange during the post-removal period. We predict that in the future, Elwha River will be more laterally unstable than it was in the 20th century, both due to the legacy of the dam removal and because of climate change.

Lay Summary

This thesis is one of many studies that seek to understand the environmental impact of dams. The sand, gravels, and cobbles that are found on the banks and bottoms of rivers move over time, causing the river to migrate. Dams trap sediment behind them and drastically change the structure of the channel downstream. If the dams are removed, then that sediment is suddenly released, creating a risky environment for downstream communities and ecosystems.

We used a numerical model to characterize how construction and removal of a dam on Elwha River will affect the movement of sediment downstream. We found that the channel migrates a lot less when the dam is place because it is coarser and harder to erode. We expect the river to migrate more in the future both because sediment supply from upstream has returned and because of changes in flow due to climate change.

Preface

Much of the content of this thesis is based on an adaptation MAST-1D, a numerical model developed by J.W. Lauer, E. Viparelli, H. Piègay, and C. Li. I have made significant changes to the model, which include those described in Chapter 2 as well as algorithms to allow the model to simulate hydrographs and other bug fixing. I also customized model parameters and inputs to Elwha River. J. Walden, under the supervision of J.W. Lauer, performed the photosieving analysis in Chapter 3. The remainder of the thesis is my original intellectual work.

Table of Contents

List of Tables

List of Figures

Acknowledgments

The Renaissance scientist Sir Isaac Newton famously wrote that 'if [he has] seen further, it is by standing upon the shoulders of giants.' My own foray into science has conjured an image far less majestic. Doing a PhD sometimes felt like trying to balance on the tip of a pyramid in the middle of an earthquake. Despite two decades of schooling, I was not prepared for how hard it would be to do independent research. Even though I moved around a lot before Vancouver, I underestimated the difficulty of transitioning to life in a big city. But my pyramid is strong and sturdy, and I was able to stand in the end.

My advisors and committee formed the top of the pyramid, providing the core knowledge needed to complete this PhD and also creating a sound surface to stand on. Marwan Hassan was my primary source of guidance; he made sure that I was on the right track and steered me back when I went astray. If it weren't for his vision and encouragement at crucial stages, I don't think I would've ever finished. Brett Eaton was the 'voice of reason.' He has a talent for explaining concepts in terms that make sense, and the best advice I've received–both with regards to my project and for graduate school in general–came from Brett. Wes Lauer went above and beyond the call of committee member. I'm so grateful for his patience and the amount of effort he put into my programme: explaining MAST-1D and helping generate ideas, introducing me to other researchers, and imparting incredible foresight. In 2015, Wes joined me in the field and made me collect a bunch of samples I didn't think I had time for. Every single one of them proved crucial when I wrote up this thesis.

A pyramid isn't very tall without a ton of bricks, and the scope of my knowledge would be short indeed without the support and inspiration from my many labmates. Our conversations in lab meetings really helped shape my ideas. More importantly, the long PhD journey was enjoyable because I shared it with such kind-hearted and insightful 'travel companions.' I'll admit I won't entirely miss getting my beer served in mason jars, but I will fondly remember sharing stories and laughing over the absurdities of academia. Special shout-outs go to Carles Ferrer-Boix and Shawn Chartrand, who were especially generous with their expertise over the years, and to Leo King, who was an encouraging and empathetic office-mate and friend, particularly during the dreaded 'final stage.'

My field assistants quite literally dug up the stone for this metaphorical pyramid. It turns out that doing 1000 kg bulk samples on swift, cobble-bedded rivers isn't easy, but Rose Beagley, Aron Zahradka, and Lawrence Bird made it doable with their outdoor expertise, drive, and sheer muscle. Jane Walden was my right-hand woman during the 2015 field season and beyond. Her enthusiasm, outdoor prowess, dependability, and friendship made that five weeks on the river both successful and incredibly fun. And not all digging requires shovels and buckets. A huge part of research involves finding computer bugs and making technology work efficiently. Vincent Kujala responded to all my computer woes with patience and determination, and I would've never finished my model runs without his bottomless database of computer tips and tricks. He was never able to train me to do updates regularly, but every time I see the update pop-up on my personal computer, I feel the appropriate level of guilt.

As a 'professional student,' I spent the entirety of my 20s at university. In that decade, I made very little money but struck the jackpot on wonderful friends. They have been the mortar of my grad school life, holding it together and giving it shape and consistency as I grew. When I was running into walls with code, it was nice to be able to vent my frustrations as Badger the reckless gnome druid. Even in the most challenging times, catching up with friends–whether in person or by phone or Skype or letter–gave me an immense sense of joy and contentment. Seeing friendships grow stronger despite the obstacles of time and distance has been one of the most rewarding experiences of adulthood, and the support and encouragement I've received has made me a better scientist, and, more importantly, a better person.

I am also incredibly fortunate to have inherited a large, loving family. The older I get, the more I value the unconditional love I've received from both sides of the family. Grandma Ivy, Uncle David, and Auntie Danette were integral to the success of my time in Vancouver; they provided me with a legal address, car help, unlimited portions of delicious food, and a warm and loving place to escape when I was feeling homesick. It's not always easy living far from family, but Tara, Steve, Can Can, Cha Cha, and Ping Pong have given me a better home than I could have ever asked for.

I've also been blessed with a multitude of wonderful Christophers. Christopher Quick was my first friend in Vancouver and my closest; he has been loyal, understanding, and supportive through good times and bad. Christopher De Rego excelled in his role as the practical twin and gave me good doses of common sense during some pivotal moments. Christopher Semiao entered my life somewhat late into my PhD journey. He has become the skeleton of my pyramid–the steel rebar put in during renovations to make it earthquake-proof. When my model crashed for the 100^{th} time, Chris S. drove across the city at midnight to give me a shoulder to cry on. Then he did the same thing when it crashed for the 101^{st} time. And the 102^{nd}. I saw the light at the end of the tunnel because Chris was holding a lantern there. His contributions are endless, but he wants to be especially recognized for some chauffeur services that made the timely completion of this Acknowledgements section possible.

One time in middle school, I was driving home from the commissary with my dad in his old blue Ford Ranger. He told me I would be the more difficult teenager. He wasn't entirely wrong. My parents raised my brother and me to to think independently and to strive to con-

tribute to society in great ways. I repaid them by moving as far away as possible, developing a worldview completely different from theirs, and choosing a financially unstable lifestyle. Yet despite everything, Mom and Dad have been my greatest cheerleaders. Their 'I love you' is what formed the base of my pyramid, and the values they taught me have proven more important than anything else I've ever learned.

If you take the time to read this thesis, you'll notice that I use the word 'we,' even though I am the sole listed author. Science written in the third person is soulless, and using 'I' felt weird and inaccurate. They say it takes a village; thanks for being mine.

Dedication

To my family–past, present, and future.

Chapter 1

Introduction

1.1 Motivation and research questions

Earth's surface is a dynamic composite of erosional and depositional landforms. The great diversity of our landscapes are built on this canvas; sediments and sediment movement form the foundation for our ecosystems and the structure over which we have built our civilizations. Rivers and floodplains in particular have been instrumental to human development as they create fertile agricultural land and convenient means of transport, trade, and energy. Rivers provide us with aquatic resources such as fish, and hydropower supplies electricity to millions of people. However, they are also dangerous; flooding is frequent and destructive, and erosion puts structures at risk. Since we live so intimately with alluvial landscapes, an understanding of how sediment is routed through them is crucial to developing safe, lasting infrastructure while protecting our precious natural resources.

Church (2002) notes that the transfer of sediment through the landscape on geomorphically significant timescales is characterized by the dynamics of sediment storage. The 'sediment cascade,' or movement of material through storage reservoirs, is responsible for the spatial and temporal distribution of sediment transport through drainage basins. Sediment tends to travel in a diffusive nature, both because of stochastic variability in particle velocity (*Martin et al.*, 2012) and because of differences in transportability related to size (*Church*, 2002). Rivers act as the 'plumbers' of drainage basins in that they route material in source areas, filtering it on the way through selective transport (*Gomez et al.*, 2001; *Hoey and Ferguson*, 1994), deposition and re-entrainment in temporary reservoirs such as point bars and floodplains (*Church and Slaymaker*, 1989), and physical and chemical weathering (*Heller et al.*, 2001; *Sklar et al.*, 2006). The kinetic energy required to transport sediment is provided by the flow of water, which is fundamentally dependent on climate but also modulated by land cover, elevation, and local geology. Together, the hydrologic and sediment regimes determine the shape and size of rivers (*Lane*, 1955; *Leopold and Maddock*, 1953; *Eaton et al.*, 2004) and the rate at which they route sediment between reservoirs (*Constantine et al.*, 2014).

Humans have been modifying the sediment cascade for millennia and are now arguably the greatest geomorphic agents on Earth (*Hooke*, 1994, 2000). We have, for example, altered flow routing and channel geometry by building canals and drainage systems (*Hooke*, 2000; *Lauer et al.*, 2017), changed the frequency of flooding by modifying the permeability of land cover (e.g. *Bledsoe and Watson*, 2001), increased the supply of sediment to large floodplains via agricultural soil erosion (*Hassan et al.*, 2017), and reduced channel-floodplain connectivity through bank protection, levees, and channelization. But one of the greatest human impacts on the landscape has been the construction of dams. Streams have been dammed for hundreds of years to store water and generate power. During the early 20th century, dam building on large rivers became common. In his census of dams in the United States, *Graf* (1999) found that every major river contains at least one, and that they store about 5000 m^3 of water per American. These dams have left a pervasive imprint on the sediment cascade; they often alter the sediment transport regime by cutting off supply, reducing peak flows and increasing base flow (*Andrews*, 1986; *Graf*, 2006; *Magilligan and Nislow*, 2005). Reducing the sediment supply to a river causes channel stabilization, which lowers rates of flooding and migration and decreases biodiversity (*James and Singer*, 2008; *Gregory and Park*, 1974; *Kloehn et al.*, 2008; *Konrad et al.*, 2011; *Poff et al.*, 2007; *Williams and Wolman*, 1984). The rate and timing of dam building has varied on a global scale. Many developing countries are experiencing eras of large dam construction, with massive projects planned that will impact some of the world's largest rivers (*Nones et al.*, 2013; *Rubin et al.*, 2015). In the US, however, dam construction peaked between the 1950s to 1970s, and has been in decline since (*Graf*, 1999). In fact, many of the dams constructed during the first half of the 20th century have surpassed their design lives and pose risks to nearby communities. The need to manage aging structures, combined with increasing concern about endangered species and the desire to restore 'natural' conditions to basins, has made dam removal an increasingly popular river restoration technique (*Grant*, 2001). To date, over 1000 dams have been removed in the United States, most within the past decade, and the trend is expected to continue for the foreseeable future (*O'Connor et al.*, 2015).

Most dams disrupt the sediment cascade by trapping incoming sediment loads in the reservoirs behind them. When the dams are removed, that sediment is released to downstream reaches, often catastrophically. Few dam removals have been studied scientifically, so our knowledge of the evolution of rivers and floodplains after the sediment 'faucets' have been turned back on is based on a handful of recent studies (e.g. *Burroughs et al.*, 2009; *East et al.*, 2015; *Major et al.*, 2012; *Warrick et al.*, 2015; *Wilcox et al.*, 2014). It appears that channels are very efficient in transporting fine sediment, with most of it leaving the basin regardless of the flow regime during removal (*East et al.*, 2015; *Grant and Lewis*, 2015; *Major et al.*, 2012). Less is known about bed material, which is important for determining channel shape and morphology. So far, it seems as though most coarse material is deposited immediately downstream of the dam and has little morphologic impact farther downstream (*Grant and Lewis*, 2015; *Major et al.*, 2012), although it is not clear how generalizable this finding is, particularly with regards to larger rivers with active floodplains. Most available data is collected on rivers within the first few months to years after the removal. While we have gained valuable insights into how large pulses of sediment affect channel morphology, virtually nothing is known about how these streams will respond on decadal timescales as the formerly sediment-starved channels adjust to transport higher loads. Potential responses include greater flood risk and more frequent channel instability. The working hypothesis implicit in many dam removal projects is that the channel returns to its pre-dam state quickly. However, conceptual models of river response to dam removals include channel widening and an increase in migration rate, and very few studies have quantified these effects on real systems (*Burroughs et al.*, 2009; *Doyle et al.*, 2002; *Major et al.*, 2012).

The goal of this study is to assess the decadal-scale impact of dam emplacement and removal on the sediment cascade for Elwha River. The Elwha is a steep, cobble-bedded river on the north end of the Olympic Peninsula in Washington, USA. Like many rivers in the Pacific Northwest, it was dammed in the early 20th century to supply hydropower in the wake of growing industrial demand. *Mapes* (2013) has recounted a history of the power projects and their role in the success of the nearby town of Port Angeles. Construction of the 32 meter high Elwha Dam was initiated by Thomas Aldwell, who saw the steep and powerful river as a profitible resource for hydropower. The dam was completed in 1913, and, as expected, soon brought business to Port Angeles, elevating it from a sleepy pioneer town to a bustling industrial port. The Puget Sound Mills and Timber Company arrived in 1914, and was followed by the Washington Pulp and Paper Company. Demand from the paper industry led to the construction of the 64 m high Glines Canyon Dam 14 km upstream from Elwha Dam in 1927. Business waned in the mid-20th century, and by 1949, most remaining customers used the regional power grid and only the paper mill still extracted electricity from the two dams.

Because of a deal with the state fish commissioner, Thomas Aldwell was exempted from building a fish passage structure on Elwha Dam, which was (and still is) a legal requirement for any dam in the state of Washington. Prior to dam construction, the river provided habitat for all five species of Pacific salmon as well as trout, eulachon, and lamprey. The dam blocked 113 km of habitat, and the absence of anadromous fish led to nutrient deficiencies in the Elwha catchment (*Munn et al.*, 1999). By the late 20th century, the population of salmon downstream of Elwha Dam was only about 1% of that in the early 20th century (*Department of the Interior*, 1995; *Duda et al.*, 2011b). The history of dam decommissioning is recounted in detail by *Mapes* (2013) and is briefly summarized here. Efforts to remove the dams began in 1986, when the Lower Elwha Klallam Tribe and environmental organizations both petitioned the Federal Energy Regulatory Commission (FERC) for dam removal, noting that since Glines Canyon Dam lay within Olympic National Park, it could not legally be relicensed. The idea initially recieved little support from the federal government. However, following passage of the Electric Consumers Protection Act (also in 1986), environmental regulations became more stringent on hydropower projects. It became cheaper to remove Glines Canyon and Elwha

Dams than to update them to reflect the new standards. The bill calling for removal of the two dams was passed in 1992. After several years of political turmoil, funding for the removals was negotiated, and demolition began in September 2011.

The Elwha River project included funding for scientific research before and in the few years following dam removal in order to assess its impact on wildlife biology (e.g. *Pess et al.*, 2008; *Jenkins et al.*, 2015), riparian and coastal ecology (e.g. *Duda et al.*, 2011a; *Foley et al.*, 2015; *Morley et al.*, 2008), and geomorphology (e.g. *Draut et al.*, 2011; *Draut and Ritchie*, 2015; *East et al.*, 2015; *Magirl et al.*, 2015). Most of the latter has been focused on documenting the fate and impact of the initial sediment pulse that was released downstream of Elwha and Glines Canyon Dams in 2011 and 2012. At this early stage in Elwha River's recovery, there has only been brief speculative focus on the decadal-scale processes, including long-term migration rates, channel-floodplain connectivity, and the sensitivity of these processes to climatically-driven hydrologic variability.

This thesis is centered around the fundamental question:

How has dam emplacement and removal impacted Elwha River geomorphology between the former Glines Canyon and Elwha Dam sites on decadal timescales?

We are particularly interested in the impact of the sediment supply disturbances on processes of channel-floodplain coupling, which include migration, width change, avulsion, and the competence of the channel to evacuate sediment both from the former reservoir deposits and from its banks. This leads to a number of sub-questions:

1. How do steep, coarse, cobble-bedded rivers like the Elwha behave on decadal timescales under steady sediment and discharge regimes?

2. What processes lead to channel width change, and how are they impacted by channel impoundment?

3. What are the main processes that contributed to geomorphic change during periods of sediment starvation and sediment excess? Can the same processes explain channel evolution during both sediment supply scenarios?

4. What is the long-term legacy of the dams on Elwha River, and how long will the effects last?

5. What impact, if any, does decadal-scale climate variability have on channel evolution, and is the effect different before and after dam removal?

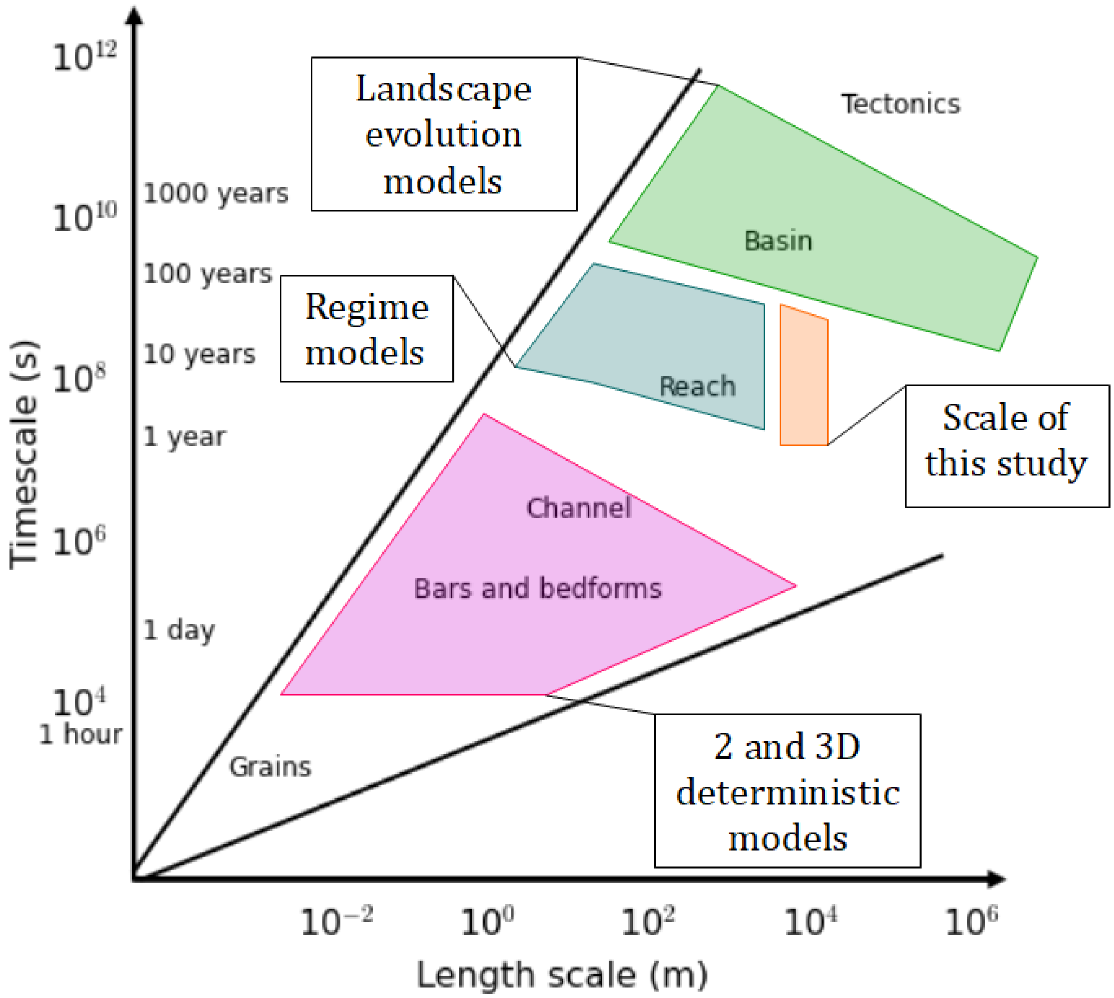

Figure 1.1: Conceptual diagram of geomorphic processes and appropriate numerical models. Based on a similar conceptualization by *Church* (2008).

1.2 Research approach and available tools

To answer the research questions listed above, we use a numerical modeling approach. Numerical modeling is useful for a number of reasons. When properly calibrated and verified, it is useful for projecting past and future periods for which there is little to no field data. By comparing calculated output to field data, we are able to test whether certain model assumptions appear to be valid, and this can provide information on which processes are most important to the system. Finally, numerical models are valuable tools for hypothesis testing and can be an efficient way of generating ideas and prioritizing field observation.

All models are approximations of reality. It is important to select numerical models that have suitable underlying assumptions for the system in question and which consider the appropriate spatial and temporal scales. A schematic showing the range of geomorphic features, and corresponding models, relevant on common spatial and temporal scales is presented in Figure 1.1. In this study, we are most concerned with processes on the multi-reach scale (multiple kms and through sections of river that may behave in unique ways) and timescales ranging from about 5 to 150 years. Two and three-dimensional deterministic models offer detailed representations of reach-scale landforms, and many incorporate channel-floodplain coupling (*Darby and Van de Wiel*, 2003; *Nelson et al.*, 2003). However, they are too computationally expensive to run for decadal timescales without making assumptions about the discharge regime that are overly simplistic for our research questions. Over long timescales, it is common to use either regime or landscape evolution models. The former attempt to predict channel dimensions using a single 'channel-forming' flow and steady state sediment flux and caliber (e.g. *Lane*, 1955; *Eaton et al.*, 2004). Since dam emplacement and removal involves changes to the governing sediment regime, these models are inappropriate for our purposes. Landscape evolution models have been used to interpret large-scale disturbances, but they usually rely on regime relations when predicting lateral change (*Tucker and Hancock*, 2010).

In practice, most numerical modeling projects on multi-reach, decadal timescales involve the use of 1-dimensional models (*Lauer et al.*, 2016). This presents us with a problem: most 1-dimensional models neglect either lateral or longitudinal fluxes (e.g. *Czuba et al.*, 2012; *Ferguson and Church*, 2009; *Konrad*, 2012), but, as noted above, both are important in the context of dam emplacement and removal. This issue has not gone unnoticed; *Doyle et al.* (2002) remarked upon how changes in channel width are incorporated into conceptual models of dam removal, but most analysts use models that assume fixed banks when assessing system response. While some 1-D models are attempting to incorporate both longitudinal and lateral processes (e.g. *Parker et al.*, 2011; *Eke et al.*, 2014), they are designed for fine-grained lowland systems with low gradients that function very differently to the high-energy systems in the Pacific Northwest. Therefore, an additional goal of this project is to develop a decadal-scale numerical model that is appropriate for steep, cobble-bedded rivers and their lateral and longitudinal complexity.

1.3 Thesis organization

The thesis is organized into four parts. In Chapter 2, we explain in more detail why appropriate decadal-scale numerical models are lacking for coarse-bedded, steep rivers like the Elwha. A 1-dimensional model is proposed that incorporates both longitudinal and lateral change. There are two novel components. The first is that we include algorithms for bank erosion and vegetation growth that together allow the channel to exchange sediment with the floodplain while adjusting its width and capacity. The bank function is based on theories of bank stability for systems with floodplains composed of primarily gravel and cobble-sized material. A simple function representing avulsion, based on the accumulation of excess sediment in the channel, is also added to the model to simulate channel-floodplain coupling resulting from the abandonment and activation of channels. These additions represent what we hypothesize are integral processes operating on the coarse, steep, and active rivers of the Pacific Northwest. We use the model to qualify how these systems behave under very simple governing hydrologic and sediment supply regimes.

Chapter 3 is devoted to confirmation of the model. We simulate evolution of Elwha River between 1918 and 2016, which includes both emplacement and removal of Glines Canyon Dam. Results from the model are compared with a suite of field and remotely sensed data. By noting where the it was successful and where it failed, we are able to test the whether the model assumptions are valid for periods of sediment starvation and excess. Comparing and contrasting simulations with and without representation of the dams sheds light on the impact of sediment supply disturbances on channel stability.

The long-term evolution of Elwha River is explored in Chapter 4. The goal of this section is to characterize how rates of sediment transport and channel-floodplain coupling may affect the long-term recovery to pre-dam levels. We consider two sources of disturbance: the decadal-scale legacy of the dams and climate variability. In order to quantify the range of variability in model response, a Monte-Carlo approach is used, with discharge treated stochastically. We examine metrics of sediment transport and channel stability for a variety of sediment supply scenarios, including one representing Elwha's history of damming. Our analysis shows the importance of hydrology in modulating how river channels interact with their floodplain reservoirs and can be used to guide future field data collection.

Finally, in the Conclusion (Chapter 5), we discuss how decadal-scale modeling has allowed us to better understand the potental legacy of dam building and removal on the sediment cascade. Remaining gaps are identified and future research directions proposed. This work increases understanding of sediment movement through human landscapes, but there is still so much to learn.

Chapter 2

A decadal-scale numerical model for low-sinuosity, cobble-bedded rivers

2.1 Summary

Even though width change is one of the most important responses of rivers to changes in governing conditions, many numerical models assume that banks are immovable. We have adapted MAST-1D, a reach-scale numerical model, to simulate the relevant decadal-scale processes for coarse (gravel-cobble bedded) multithreaded rivers. The model has separate functions for bank erosion and vegetation encroachment, allowing for width change. Bank erosion is a function of the mobility and transport capacity for large, structurally-important grains which protect the bank toe. Vegetation growth is linearly proportional to channel width and occurs during conditions of low shear stress. In addition, MAST-1D simulates local, reach-scale avulsions, which occur when aggradation causes channel depth to drop below a threshold. The behavior of MAST-1D was assessed using simple boundary conditions. When the annual hydrograph and sediment supply regime are kept constant, the channel width, migration rate, and sediment transport rate oscillate on decadal timescales. The time period between oscillations is dependent on the frequency of local avulsions, which are most sensitive to sediment supply and the size of coarse particles. Our simulations suggest that internal decadal scale variability is an inherent feature of coarse, wandering rivers and that it is closely coupled with reach-scale sediment storage and evacuation. Traditional regime approaches to characterizing channel dimensions may be too simplistic for alluvial systems where avulsion is a natural, frequent process.

2.2 Introduction

It is a well-established principle that alluvial channels are composed of self-formed boundaries that evolve in response to governing flow and sediment supply regimes. In their pioneering work, *Leopold and Maddock* (1953) introduced the idea that river dimensions are correlated with a single 'formative' discharge, which they defined as the bankfull discharge but which has also been associated with the flow responsible for most sediment transport (*Andrews*, 1980; *Wolman and Miller*, 1960). Hydraulic geometry has persisted as one of the key concepts in geomorphology and still influences the way in which many researchers approach channel width. It is an approximation of reality; channel width fluctuates through time, responding to the sequencing of flood events and natural variability in sediment supply (e.g. *Baker*, 1977; *Lisle*, 1982). This is especially true for gravel-bedded rivers with a wandering morphology, which are multi-threaded and often characterized by flashy flood regimes. The time it takes for width to recover between floods is dependent on the rate at which vegetation colonizes channel bars, which depends on climate and flood frequency (*Wolman and Gerson*, 1978). Width change can affect sediment transport and bed evolution in a variety of ways. Widening results in a higher flood conveyance, reducing the shear stress for a given flow. However, it also leads to bank erosion and a wider zone over which sediment is mobile, increasing supply. The rate of channel widening is related to channel migration and the frequency of floodplain turnover, which have implications for riparian ecology (*Kloehn et al.*, 2008; *Konrad*, 2012; *O'Connor et al.*, 2003). Despite the importance of these processes in the context of bank erosion and flood risk, many modeling projects on multi-reach, decadal scales either neglect width change (e.g. *Czuba et al.*, 2012; *Ferguson and Church*, 2009; *Gomez et al.*, 2009; *Verhaar et al.*, 2008) or assume a constant width-discharge relation (*Viparelli et al.*, 2011).

The processes that maintain active channel width in alluvial, wandering rivers can be summarized by three factors: 1) the ability of the flow to scour banks and bars, 2) activation or reactivation of floodplain surfaces via avulsion, and 3) the rate of vegetation encroachment onto bare sediment surfaces. Traditionally, the net effect of these factors have been explained by regime models. Both empirical (e.g. *Leopold and Maddock*, 1953) and analytical (e.g. *Millar and Quick*, 1993; *Eaton et al.*, 2004) approaches have successfully predicted channel dimensions on the reach scale in terms of a set of governing conditions such as a channel-forming discharge, bank strength, and sediment load. The primary caveat of these models is that they assume the channel is in equilibrium with the boundary conditions. As such, they are inappropriate tools for use on rivers that are actively adjusting to a disturbance (such as a large flood or change to sediment supply), and they do not consider the propagation of the disturbance downstream.

Numerical models offer the opportunity to assess both the spatial and temporal responses of channels to changes in the boundary conditions. Models featuring width change began appearing in the early 1990s and focused on the fluvial-driven processes leading to mass failure of banks composed of uniform sediment size (*Darby and Thorne*, 1996; *Mosselman*, 1992; *Pizzuto*, 1990). In 1993, a task force was set up by the American Society of Civil Engineers to summarize width change modeling efforts and identify areas of improvement (*ASCE Task Committee on Hydraulics and of River Width Adjustment*, 1998a,b). Since then, models have grown to incorporate a wider and more realistic set of bank erosion processes, including sediment transport of bank material (*Carroll et al.*, 2004; *Rinaldi et al.*, 2008), the effect of groundwater fluxes in reducing bank stability (*Higson and Singer*, 2015; *Rinaldi et al.*, 2008), bank protection from cohesive slumps of floodplain material (*Parker et al.*, 2011), and channel widening via incision (*Cantelli et al.*, 2007; *Cui et al.*, 2006). Many of these advances have been aided in large part by improvements in 2D modeling (*Darby and Van de Wiel*, 2003; *Nelson et al.*, 2003).

Numerical models addressing channel avulsion fall into two general types–1-3D morphodynamic models of channel bifurcations and cellular-based models of entire channel-floodplain networks (for review, see *Hajek and Wolinsky*, 2012). The former focus on the geomorphic conditions that lead to preferential flow and sediment transport in different distributary channels, including local variations in slope, complex flow at island heads, and upstream meandering and bar deposition (*Kleinhans et al.*, 2008; *Miori et al.*, 2006). To date, most assume that channel width in each distributary remains constant, although *Miori et al.* (2006) used regime relations to characterize width change as a result of channel shifting. Cellular models (e.g. *Jerolmack and Paola*, 2007) have qualitatively and quantitatively reproduced long-term avulsion behavior observed in the field, including so-called 'local' avulsion, where a segment of channel forges a new path, then rejoins the existing channel a short distance downstream.

Understanding the influence of vegetation on fluvial processes has significantly advanced our knowledge of bank and bar erosion (*Abernethy and Rutherfurd*, 2001; *Beechie et al.*, 2006; *Fetherston et al.*, 1995; *Micheli and Kirchner*, 2002; *Perona et al.*, 2012), deposition (*Friedman et al.*, 1996), and channel morphology (*Gran and Paola*, 2001; *Tsujimoto*, 1999). There has been a flurry of research on the interactions between flow, sediment transport, and riparian ecosystems (see reviews by *Camporeale et al.*, 2013; *Corenblit et al.*, 2007; *Greet et al.*, 2011; *Osterkamp and Hupp*, 2010). Particular emphasis has been put on numerically modeling the influence of hydrologic processes on riparian growth and succession (e.g. *Camporeale and Ridolfi*, 2007; *Tealdi et al.*, 2011). However, the sediment transport and bed evolution models that take vegetation into account (e.g. *Tsujimoto*, 1999; *Van De Wiel and Darby*, 2004) generally only consider what *Camporeale et al.* (2013) refers to as its 'passive' role: in other words, they simulate the effect of vegetation on flow resistance and deposition, but do not account for vegetation encroachment onto bare sediment surfaces. This is a major impediment for modeling channels longer than a couple years, after which vegetation growth becomes a major factor in width change (*O'Connor et al.*, 2003; *Williams and Wolman*, 1984). In addition, they neglect the transport and deposition of wood, which is one of the main drivers of channel morphology (*Bertoldi et al.*, 2009; *Fetherston et al.*, 1995; *O'Connor et al.*, 2003) on rivers in forested landscapes.

Despite improvements in our ability to quantify bank processes, few existing models are applicable on the annual-decadal, multi-reach scales relevant to many contemporary management issues. Two- and three-dimensional models are becoming increasingly successful in capturing river erosion and deposition, but most do not consider vegetation growth and are currently limited to rather small spatial and temporal scales. Some numerical models have been applied to decadal and longer timescales (e.g. *Eke et al.*, 2014; *Higson and Singer*, 2015), but only on the scale of a single bend. *Tunnicliffe and Church* (2015) developed a 1-D model for the multi-reach scale, but their width change function relies on an optimality criterion, which is designed to characterize channels in equilibrium. Landscape evolution and/or cellular models can be applicable to decadal timescales, but they generally either assume a constant width for the active channel belt or rely on hydraulic geometry and regime equations that are not appropriate for rivers adjusting to changing governing conditions such as sediment supply or hydrologic regime (*Jerolmack and Paola*, 2007; *Tucker and Hancock*, 2010). It is therefore unsurprising that so many projects use one-dimensional, fixed bank numerical models to simulate systems that are expected to experience width change.

We aim to fill this gap by adapting MAST-1D, a 1-dimensional, reach-scale bed evolution model, to allow for channel width change and local channel avulsion. Bank erosion and vegetation encroachment are modeled as two separate processes, following the approach used in the model by *Parker et al.* (2011) and its decendents. Our version of MAST-1D is designed for low-sinuosity, gravel-cobble bedded rivers where cohesive material constitutes a negligible portion of the bank and the channel belt is dominated by small, local avulsions rather than meander extension. Channel stability is dictated by the mobility of the largest size fractions in the alluvial deposits. Our model calculatates size-specific sediment transport, allowing for bed elevation and grainsize to evolve. It is therefore an appropriate tool for exploring gravel and cobble-bed systems undergoing changes to sediment supply or hydrology. In this chapter, we describe the model and its behavior. In Chapter 3, the model is applied to Elwha River, where two dams were emplaced and removed a century later, to examine the effect of sediment supply on channel evolution.

2.3 Model framework

MAST-1D is a one-dimensional bed evolution model designed to simulate channel and floodplain exchange over decadal and longer timescales. It is unique in that it allows for the size-specific exchange of sediment between the floodplain and the channel through both channel migration and overbank flooding. Details on the original version of MAST-1D can be found in *Lauer et al.* (2016). We have modified MAST-1D to better represent coarse, wandering rivers. Our model is limited to systems where the floodplain material is composed primarily of gravel and cobble, there is negligible cohesive material in the cutbank (Figure 2.1), and channel sinuosity is low.

Three primary changes have been made to MAST-1D: 1) hydraulics are calculated with a daily discharge series instead of a flow duration curve; 2) lateral channel change is represented by two processes–channel widening and narrowing–so that the width is allowed to change over time; and 3) a simple avulsion function acts as an additional source of channel-floodplain exchange. We have summarized the basic model procedure and provided details on the channel width change and avulsion procedures below. A full model description can be in Appendix A.

Figure 2.1: Gravel-cobble cutbank along Elwha River, Washington, USA. the bank is composed entirely of non-cohesive material and is protected by an armored toe deposit.

2.3.1 General structure and model procedure

In MAST-1D, the river is conceptualized as a linear series of model cells, each of which contains a set of reservoirs: a channel bed (active layer), point bar, floodplain, and channel and floodplain substrates (Figure 2.2). Each has a characteristic geometry, volume, and grain size distribution, which is modified as sediment is exchanged with other reservoirs due to transport, channel widening or narrowing, and avulsion. Like other 1D bed evolution models, the outgoing sediment load from an upstream model cell becomes the supply to the downstream node.

Each model cell is long enough to incorporate a reach-sized portion of channel. In other words, the sediment exchanges between reservoirs represent an average over multiple bends and bar sequences. The channel shape is assumed to be rectangular. This neglects the important influence of channel morphology on hydraulics and sediment transport. *Ferguson* (2003) has suggested that using a depth-averaged shear stress (i.e. a rectangular channel) underestimates channel-wide transport because sediment transport scales non-linearly with flow. He derived a mathematical solution for incorporating channel shape into one-dimensional sediment transport calculations. His method involves integrating a sediment transport formula over a range of depths. While this works well for simple formulae (such as the Meyer-Peter and Müller equation he used), relations designed for transport of sediment mixtures, which include hiding functions, yield significantly more complicated integrals that lose physical meaning. In addition, large floods capable of transforming channel morphology may occur multiple

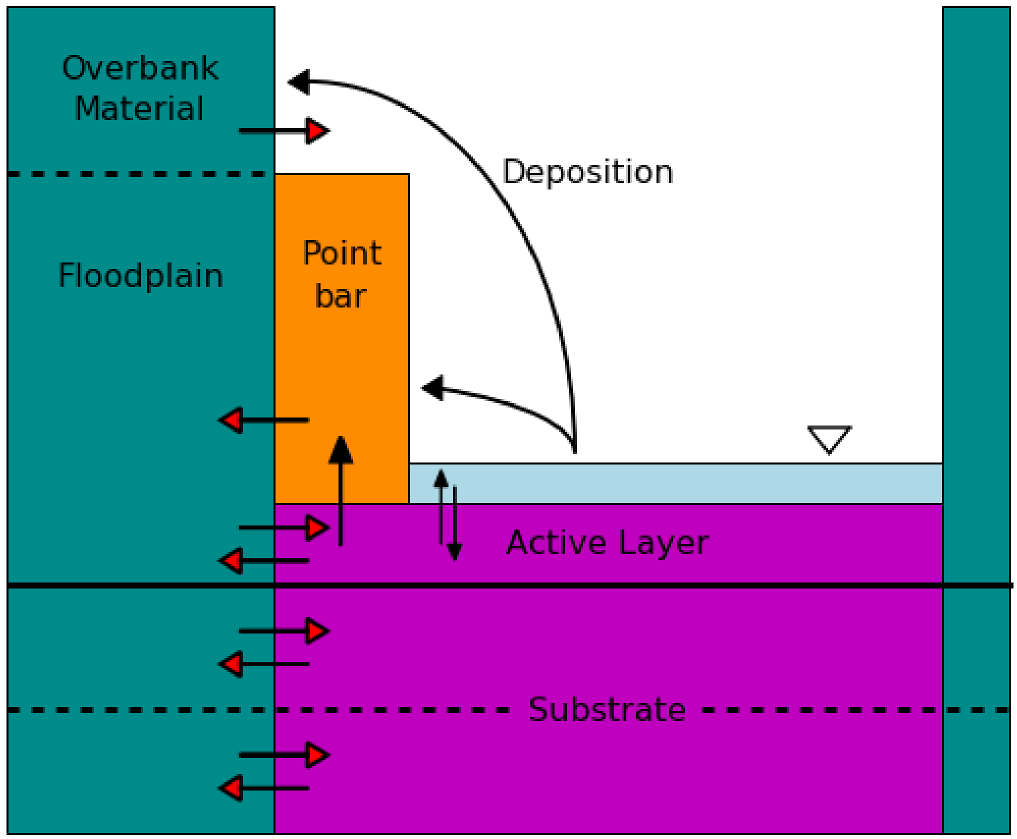

Figure 2.2: Schematic showing MAST-1D reservoirs and exchanges within one model cell. Red-filled arrows denote exchanges that are determined by width change.

times over decadal timescales, and therefore channel shape cannot be assumed constant. Furthermore, our model does not account for the transport and deposition of large wood, which can affect channel shape as much as sediment transport (*Abbe and Montgomery*, 1996). For these reasons, we believe that using a rectangular channel is justified, even though it imposes a significant loss of realism.

MAST-1D iterates through 5 main processes. First, hydraulics are calculated using the standard step method applied to the backwater equation, assuming steady, gradually-varied sub-critical flow. The flow area is divided into two segments–the channel and floodplain. Bedload is then calculated with a form of the *Wilcock and Crowe* (2003) equation that has been optimized for large, cobble-bedded rivers by *Gaeuman et al.* (2009). It is assumed that any washload in the channel passes through the system, although during flood conditions some washload and fine bed material may deposit on the floodplain. Next, lateral exchanges of sediment to and from the channel are calculated, as described below. Sediment transport and lateral exchange rates are used to calculate the change in bed elevation using a modified form

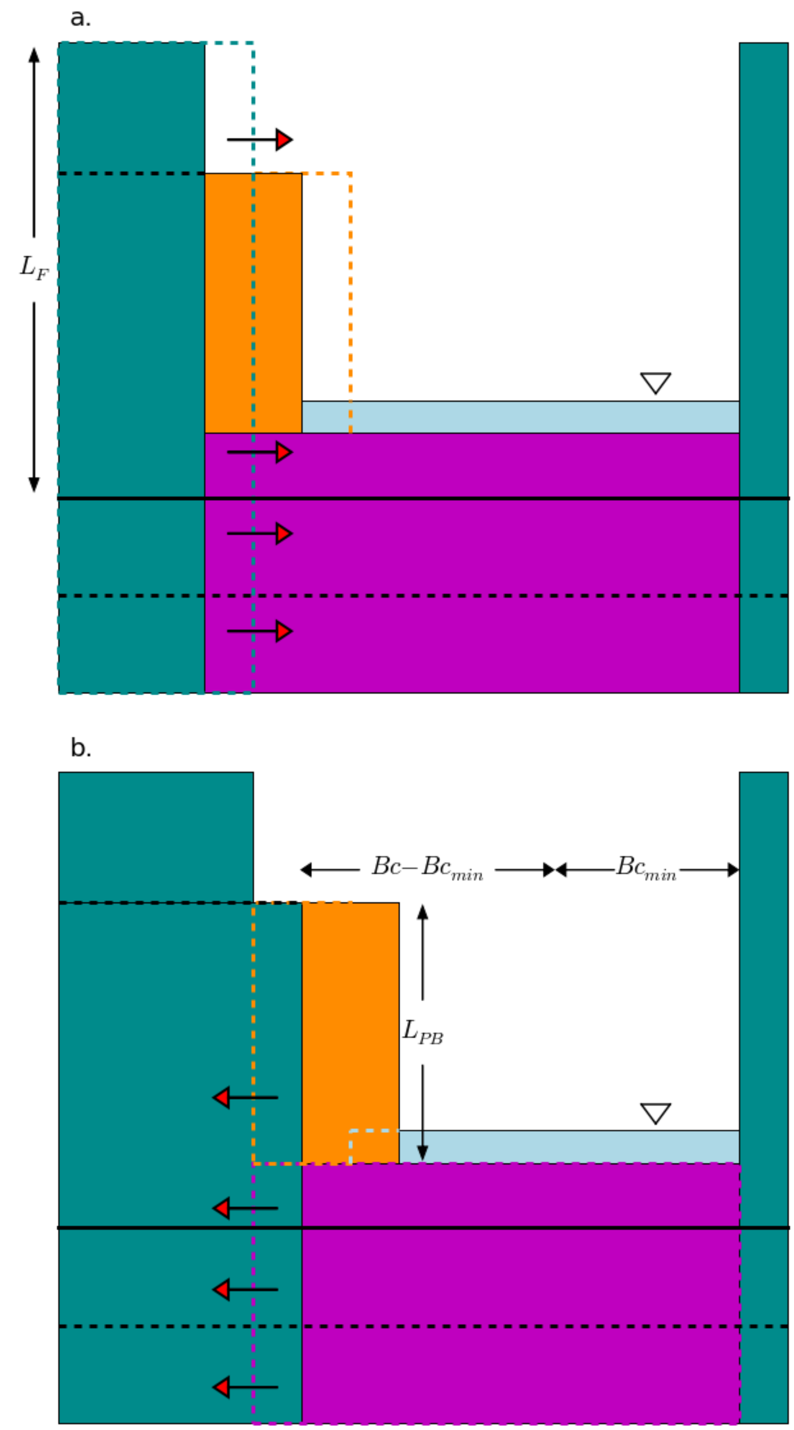

Figure 2.3: Schematic showing reservoir exchanges. Arrows and dashed boxes show sediment fluxes. Bank erosion (a.) causes material from the floodplain and floodplain substrate to be added to the channel zone, increasing the width of the channel. Vegetation encroachment (b.) leads to channel narrowing, as channel and point bar sediment is incorporated into the floodplain zone.

of the Exner equation:

$$\frac{\Delta z}{\Delta t} = \frac{1}{B_c(1-\lambda)} * \frac{I_m + Q_{s,in} - Q_{s,out}}{\Delta x} \tag{2.1}$$

where $\frac{\Delta z}{\Delta t}$ is the rate of bed elevation change, B_c is channel width, λ is bed porosity, Δx is the channel length, I_m is the incoming flux due to lateral change, and $Q_{s,in}$ and $Q_{s,out}$ are the sediment transport rates for the upstream supply and load. Mass conservation is then applied on a size-specific basis to each reservoir (active layer, channel, and substrates), and the grainsize distributions and geometries are updated to reflect incoming and outgoing sediment fluxes. If the channel aggrades beyond a threshold, avulsion occurs, transfering sediment between the channel and floodplain and lowering the bed elevation (see below).

2.3.2 Lateral exchange and width change

In alluvial rivers, active channel width is maintained by two processes: the scour of banks by the flow, which acts to widen the channel, and the encroachment of floodplain vegetation, which leads to narrowing of the active channel margin. The interaction between these two processes results in channel migration and an exchange of sediment to and from the floodplain.

In MAST-1D, lateral exchange describes the magnitude of sediment fluxes between channel and floodplain reservoirs within each model cell (see Figure 2.3; floodplain and floodplain substrate reservoirs are teal and channel reservoirs–active layer and channel substrate–are magenta). The volumes of sediment entering and exiting the channel per unit time are functions of bank erosion (E) and narrowing caused by vegetation (N), where

$$I_m = \frac{E}{\Delta t} * L_F * \Delta x \tag{2.2}$$

and

$$O_m = \frac{N}{\Delta t} * L_{PB} * \Delta x \tag{2.3}$$

where L_F is the height of the floodplain above the substrate and L_{PB} is the height of the point bar (a constant). The rate of channel width change is a function of the magnitudes of bank erosion and point bar and vegetation growth (*Parker et al.*, 2011):

$$\frac{\Delta B_c}{\Delta t} = \frac{E}{\Delta t} + \frac{N}{\Delta t} \tag{2.4}$$

where $\frac{\Delta B_c}{\Delta t}$ represents the total rate of channel width change. Note that $\frac{N}{\Delta t}$ is negative.

Bank erosion

Our simple model of channel widening only relates bank erosion to sediment transport capacity. *Parker et al.* (2011) notes how bank retreat in natural rivers is held in check by a protective

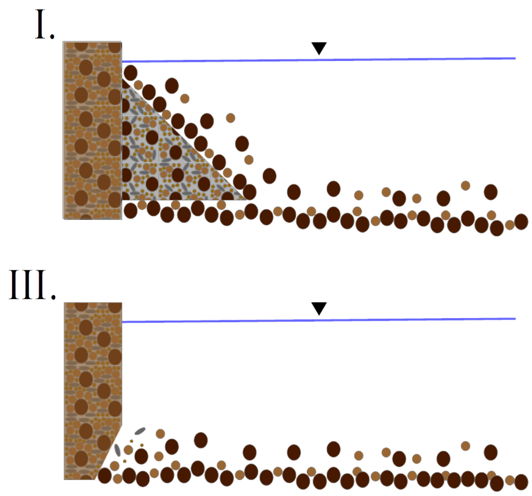

Figure 2.4: Conceptual model of bank erosion along a coarse, cohesionless bank. I. The bank is protected by flow by an unconsolidated toe deposit with an armored surface. During flows with high enough energy, the armor layer on the bank toe is entrained. II. The protective bank toe deposit is transported away. III. Bank material is eroded away, either by dislodgement and avalanching of individual particles or by slip failure. IV. When the supply of bank material exceeds the capacity to transform it, a new toe develops, over which a new armor layer forms as the flood recedes.

layer on the bank toe. In the fine-grained, lowland streams considered in their study, this protection took the form of slump blocks of cohesive material that fall into the river during bank retreat and cap the bank toe. Our hypothesis is that in coarse-bedded, non-cohesive floodplains, an armor of large grains protect the bank toe and modulate rates of bank erosion (Figure 2.1). Scour results when the shear stress of the flow is sufficient to entrain and transport particles from the near-bank region. A conceptual model for bank retreat is presented in Figure 2.4. In order for erosion to occur, the coarse surface grains armoring the bank toe must be transported (Stage I in Figure 2.4). The initiation of bank erosion is therefore a function of the entrainment condition for near-bank particles (*Nanson and Hickin*, 1986), which depend on fluid forces acting on the bed and grain-bed collisions (*Sutherland*, 1967). In particular, the largest grains must be reaching the threshold for full mobility (*MacKenzie and Eaton*, 2017) in order to break up the armor layer on the bank toe and allow it to be transported away (Stage II). Stage III is initiated once the protective toe is gone. Bank retreat occurs, by entrainment and avalanching of individual particles and by shear failure (see *ASCE Task Committee on Hydraulics and of River Width Adjustment*, 1998a). When the sediment supplied from the bank exceeds the transport capacity in the near-bank region, a new toe develops, becoming armored as the flow wanes (Stage IV; and refer to *Thorne*, 1982).

Because MAST-1D uses a rectangular cross-section, and because the spatial resolution is designed to be large (multiple channel widths and meander bends), our widening function uses channel-averaged hydraulic and sediment transport metrics to calculate bank erosion.

Both field and experimental data support this approach for self-formed channels with cohesionless banks. *Nanson and Hickin* (1986) argue that bank erosion is a function of the bed shear stress, as sediment transport on the bed leads to the undercutting and subsequent collapse of banks. They find that stream power, along with the shear force of bank material (which is a function of grainsize) explain most of the variability in channel migration rates along several Canadian rivers. In fact, stream power appears correlated to bank erosion rates on a variety of systems (*Krapesch et al.*, 2011; *Nicoll and Hickin*, 2010). These studies suggest that the magnitude of bank erosion can be related to the channel-averaged strength of flow. The disadvantage to this approach is that it does not take into account increased shear stress along the banks due to channel curvature. The model is therefore most appropriate for channels with low sinuosity, where a straight channel assumption is justifiable. In addition, MAST-1D does not account for retreat that occurs when banks become oversteepened as a result of degradation (e.g. *Cantelli et al.*, 2007), nor does it consider mass failure resulting from a build-up of pore pressure in near-bank deposits (*Higson and Singer*, 2015).

Our approach for the initiation of bank erosion stems from the work of *MacKenzie and Eaton* (2017), who find that lateral channel instability in their laboratory channel occurred when the largest grains in the sediment mixture were fully mobile on the bed. In natural, poorly-sorted cobble-bedded rivers, it is likely that full mobility of the coarse fraction is rarely, if ever, achieved. Therefore, widening in our modified version of MAST-1D is occurs when a supply-normalized unit transport rate of the upper tail of the grainsize distribution, qs_{Cmax}, exceeds a threshold, qs_{cr}. Our physical interpretation is that, beyond qs_{Cmax}, the grains on the bank toe are sufficiently mobile to break up the armor layer, allowing the toe to be scoured away (Stage II in Figure 2.4). We define the supply-normalized unit coarse transport rate as

$$qs_{Cmax} = qs_C / f_C \tag{2.5}$$

where qs_C is the unit sediment transport rate of the coarse end of the surface sediment mixture and f_C is the fraction of that group of sizes present in the bed. qs_C is calculated via the *Gaeuman et al.* (2009) version of the *Wilcock and Crowe* (2003) function, though any fractional sediment transport equation will work. It is directly proportional to f_C (see Equation 2 in *Gaeuman et al.*, 2009). Therefore, qs_{Cmax} represents the transport rate expected with an unlimited supply of coarse sediment. Equation A.43 is equivalent to the fractional transport scaled to the bed surface distribution described by *Wilcock and McArdell* (1993), who use it to identify thresholds between partial and full transport. There is currently no straightforward way to determine the threshold unit transport rate qs_{cr}. As a first step, it should be estmated for each system, ideally by comparing sediment transport calculations to field data of bank erosion.

Once bank erosion is initiated (Phase III in Figure 2.4), floodplain sediment mixes with the active layer adjacent to the bank, and the magnitude of bank erosion depends on the ability of the flow to transport this near-bank sediment. When coarse sediment supply from the bank exceeds the transport capacity, it will build up along the bank toe and protect it from further erosion. The near-bank sediment transport capacity, qs_{NB}, is a function of the grainsize distribution of the near bank region, which is defined by

$$f_{i,NB} = \alpha_f f_i + (1 - \alpha_f) f_{i,FP} \tag{2.6}$$

where $f_{i,NB}$ is the near-bank fraction of size class i, f_i is the fraction in the active layer, $f_{i,FP}$ is the fraction in the floodplain, and α_f is a mixing constant that ranges between 0 and 1. Larger values of α_f make bank erosion more dependent on the grainsize distribution of the bed and therefore more sensitive to sediment supply. qs_{NB} is calculated using the Gaeuman et al. (or other fractional) sediment transport relation, with $f_{i,NB}$ as the grainsize distribution. The portion of $qs_{i,NB}$ that transports coarse floodplain material, $qs_{C,FP}$, is

$$qs_{C,FP} = \frac{qs_{C,NB}}{f_{C,NB}} f_{C,FP} (1 - \alpha_f) \tag{2.7}$$

where $qs_{C,NB}$ is the unit coarse sediment transport rate of the near-bank mixture and $f_{C,FP}$ is the fraction of coarse material in the floodplain. The bank erosion rate is

$$\frac{E}{\Delta t} = \begin{cases} 0, & qs_{Cmax} \leq qs_{cr} \\ (qs_{C,FP}) / (L_F * f_{C,FP}), & qs_{Cmax} > qs_{cr} \end{cases} \tag{2.8}$$

where L_F is the bank (floodplain) height.

Vegetation encroachment

Channel narrowing results from multiple interrelated processes, including deposition on bars, degradation leading to the development of benches, and encroachment of vegetation onto exposed surfaces. One of the weaknesses of using a simple rectangular cross-section is that lateral variability in deposition cannot be modeled. Here we focus on channel narrowing due to vegetation encroachment. The relationship between vegetation growth and hydrology is complicated, with the germination and ultimate success of seedlings dependent on the spatial and temporal availability of soil moisture (*Camporeale et al.*, 2013; *Pasquale et al.*, 2012), flood sequencing (*Camporeale and Ridolfi*, 2007; *Perona et al.*, 2012), the availability of in-channel wood, which act as nurse logs (*Bertoldi et al.*, 2009; *Fetherston et al.*, 1995), and species (*Robertson and Augspurger*, 1999). As a first step, channel narrowing only occurs during relatively low flows in MAST-1D. We assume that the magnitude of vegetation encroachment is proportional to the area of unvegetated point bar surface (this is the same approach used by *Konrad*, 2012). The rate of encroachment is treated as a constant, α_n:

$$\frac{N}{\Delta t} = \begin{cases} -\alpha_n * (B_c - B_{min}), & \tau < \tau_r \\ 0, & \tau \geq \tau_r \end{cases} \tag{2.9}$$

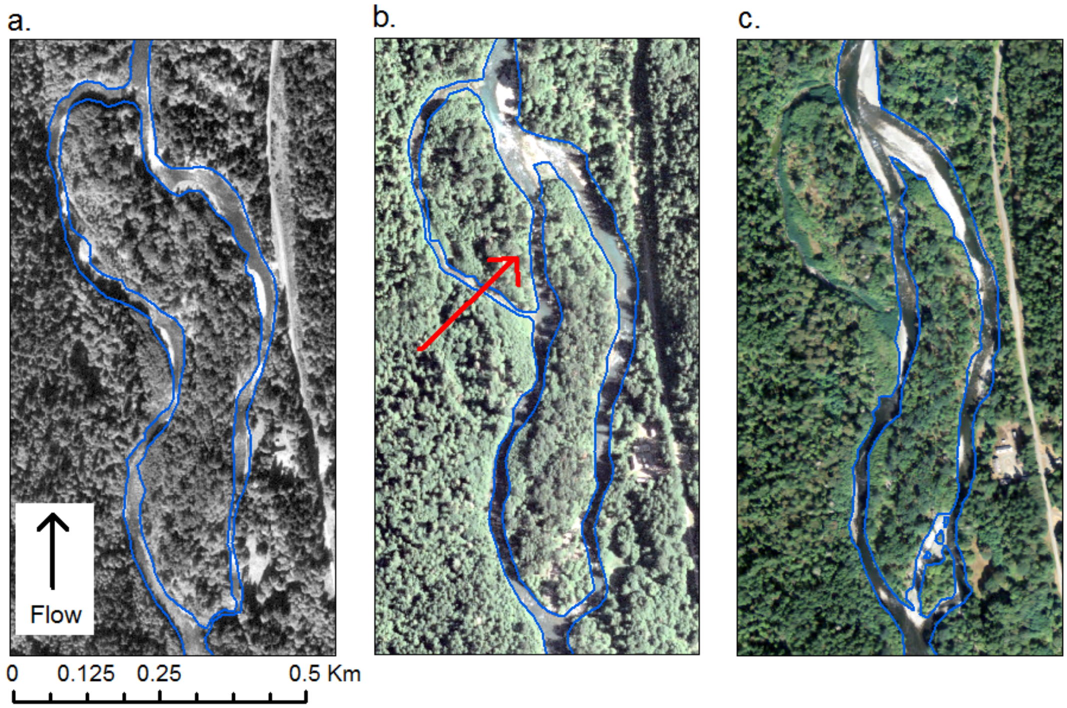

Figure 2.5: Example of a local avulsion on Elwha River, Washington roughly 2 km downstream of Glines Canyon Dam. In 1994 (a), the channel is composed of two branches. An avulsion takes place between 1994 and 2006 (b), creating a third, narrow channel about halfway down the bifurcation. By 2009 (c), the old channel has lost all flow and been colonized by vegetation. Active channel margins are outlined in blue.

B_{min} is a constant user-defined minimum width and $B_c - B_{min}$ represents the unvegetated point bar. τ_r represents a reference shear stress, below which flow is low enough to leave surfaces exposed for colonization. As theories of vegetation colonization become more advanced, this algorithm may be improved.

2.3.3 Avulsion

Avulsion is an inherent feature of river systems in which the rate of bed aggradation outpaces the timescale over which the channel can sequester that sediment into the floodplain via lateral migration (*Jerolmack and Mohrig*, 2007). In forested rivers, local avulsions occur where the channel is blocked by log jams (*Gottesfeld and Gottesfeld*, 1990; *O'Connor et al.*, 2003). A case study of a typical channel evolution sequence following a local avulsion is presented in Figure 2.5. In the period between air photos in Figures 2.5a and b, flow from the downstream half of the left fork of a bifurcating stream is captured by a new channel that cuts across a mid-channel island, joining with the right fork a few hundred meters downstream. The old channel is not abandoned immediately, although it narrows. After a few to several years (Figure 2.5), the new channel captures all flow from the left fork (at most stages), it widens, and the old channel is colonized by vegetation and incorporated into the floodplain.

In MAST-1D, we characterize avulsion in a much simpler way by treating it as an instantaneous process. It is triggered in model cells experiencing high levels of aggradation where the bed elevation approaches that of the floodplain. This is similar to the approach taken by *Jerolmack and Paola* (2007), although their cellular model accounts for levees and defines initiation of avulsion when the channel aggrades above the floodplain. A schematic of the MAST-1D algorithm is presented in Figure 2.6. The floodplain (teal) is composed of flood channels that initially lay above the primary conveyance zone (i.e. the active layer, Figure 2.6a). Note that in MAST-1D, the floodplain is treated as a single rectangular reservoir, though we show a flood channel in Figure 2.6 to clarify the process. As the channel (displayed in magenta) aggrades, the height of the bank, L_f, decreases. When L_f dips below a threshold value L_t, avulsion is initiated (Figure 2.6b). The bed elevation lowers by a spacing constant L_a as part of the channel inhabits the floodplain channel (Figure 2.6c):

$$z_{new} = z_{old} - L_a \tag{2.10}$$

z_{old} is the pre-avulsion bed elevation and z_{new} is the resulting elevation (Figure 2.6d). The surface of the new channel becomes active, so that the volume of floodplain material added to the active layer for size class i ($AL_{in,i}$) is

$$AL_{in,i} = \alpha_a * B_c * L_{AL} * f_{i,FP} * \Delta x \tag{2.11}$$

where α_a is the fraction of channel that avulses, L_{AL} is the thickness of the active layer, and $f_{i,FP}$ is the fraction of size class i in the floodplain. We make the simplification that the abandoned portion of channel becomes vegetated immediately, so that the volume of channel sediment sequestered into the floodplain reservoir ($FP_{in,i}$) is

$$FP_{in,i} = [\alpha_a * B_c * L_{AL} * f_{i,AL} + B_c * L_a * f_{i,SC}] * \Delta x \tag{2.12}$$

where $f_{i,AL}$ is the fraction of size class i in the active layer and f_{SC} is the fraction in the channel portion of the substrate. To conserve mass, we must assume that the aggraded material in the 'non-avulsed' portion of channel (the channel substrate) enters the floodplain. Therefore, even though we are assuming that the overall channel width does not change during the avulsion, slightly more sediment is sequestered into the floodplain than that which becomes new channel. It is also important to note that our avulsion threshold does not account for the very important influence of log jams, which are known to cause avulsions forested wandering rivers. We assume that the magnitude of lag jamming is proportional to the aggradation rate of sediment. This is a portion of the model that can be improved.

After the avulsion, the boundary between the floodplain, active layer, and substrate reservoirs are adjusted to reflect the new L_F (which represents channel depth). Details of this pro-

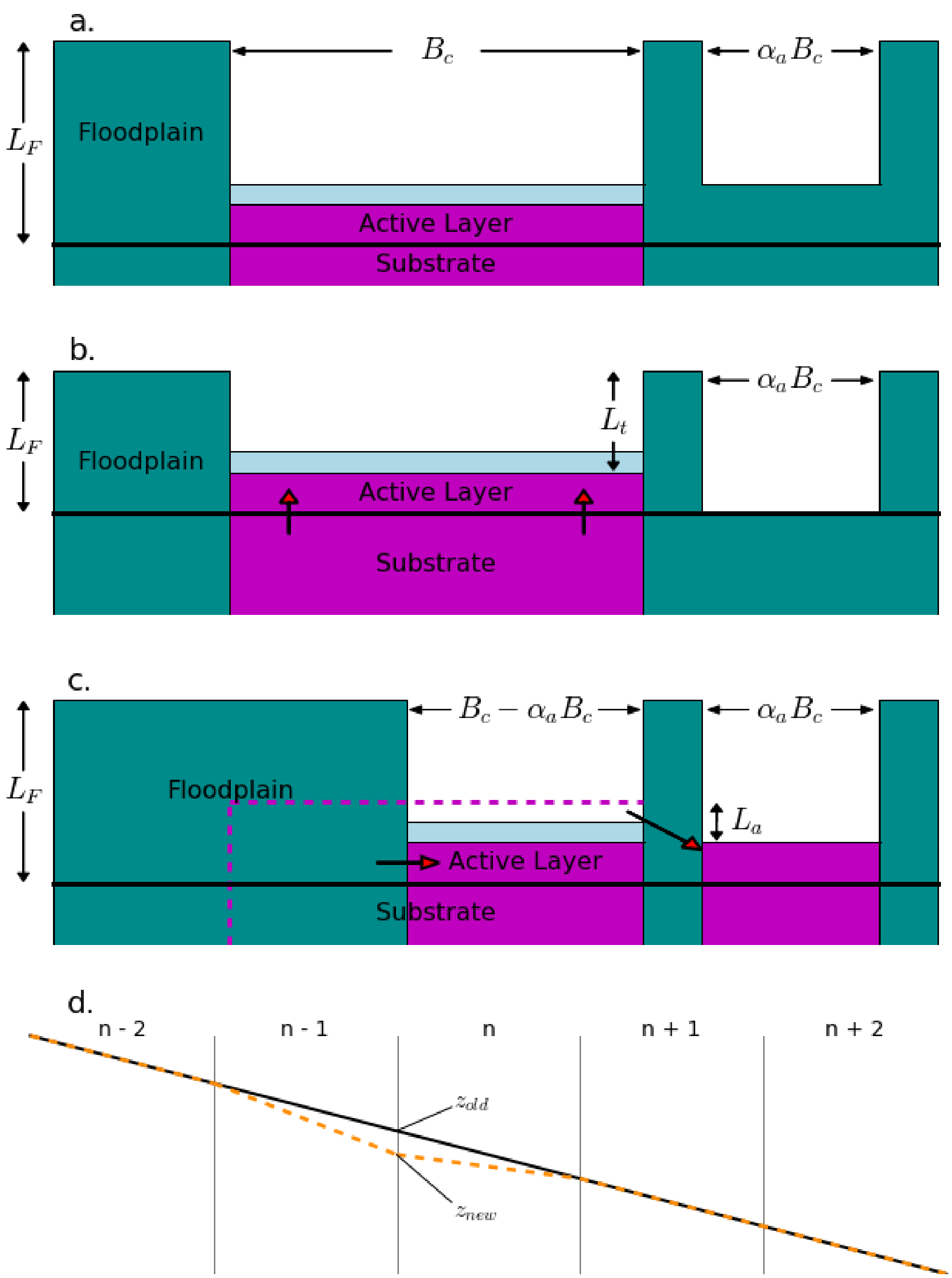

Figure 2.6: Conceptual diagram of avulsion in MAST-1D with relevant parameters. a. river setup prior to avulsion. The channel elevation is lower than that of the floodplain channel. b. river setup at the threshold for avulsion. The channel (magenta) has aggraded so that it is within a threshold length (L_t) of the floodplain height. c. river setup after avulsion. The depth of the channel has lowered by L_a. Old channel material is sequestered into the floodplain, while floodplain material is incorporated into the active layer. d. Longitudinal profile before (black line) and after (orange line) an avulsion on node n.

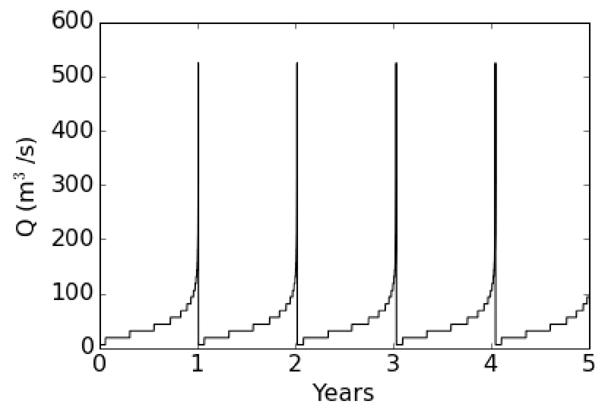

Figure 2.7: Sample of repeating hydrograph used in model runs.

Table 2.1: Select initial conditions for model runs

Parameter	Value	Source
Bank height	1.86 m	derived from *Castro and Jackson* (2001)
Width	81 m	Model calibration
Gradient	0.0069	DEM
Thickness of overbank material	0.14 m	Bank survey
D_{50}	68 mm	Bulk Sampling
D_{90}	265 mm	Bulk Sampling

cedure can be found in Appendix A.

2.4 Model behavior

Simple simulations were performed to demonstrate the general behavior of MAST-1D. The input parameters are loosely based on Elwha River, a wandering cobble-bedded stream with a drainage area of about 850 m^3/s. The primary initial conditions are listed in Table 2.1. A full list can be found in Appendix B. Sediment was supplied at capacity.

The fractions and transport rates of coarse material in the active layer and floodplain are calculated by summing the fractions for three boulder size classes:

$$f_C = f_{256-362} + f_{362-512} + f_{512-1024} \tag{2.13}$$

and

$$qs_C = qs_{256-362} + qs_{362-512} + qs_{512-1024} \tag{2.14}$$

where the subscripts refer to the bounds of the size classes used in mm. These classes approximately reflect all material including and above the channel D_{90} (Table 2.1).

When run for over two centuries with a repeating hydrograph (Figure 2.7), avulsions occur every few decades (Figure 2.8a). The other channel characteristics oscillate at the same

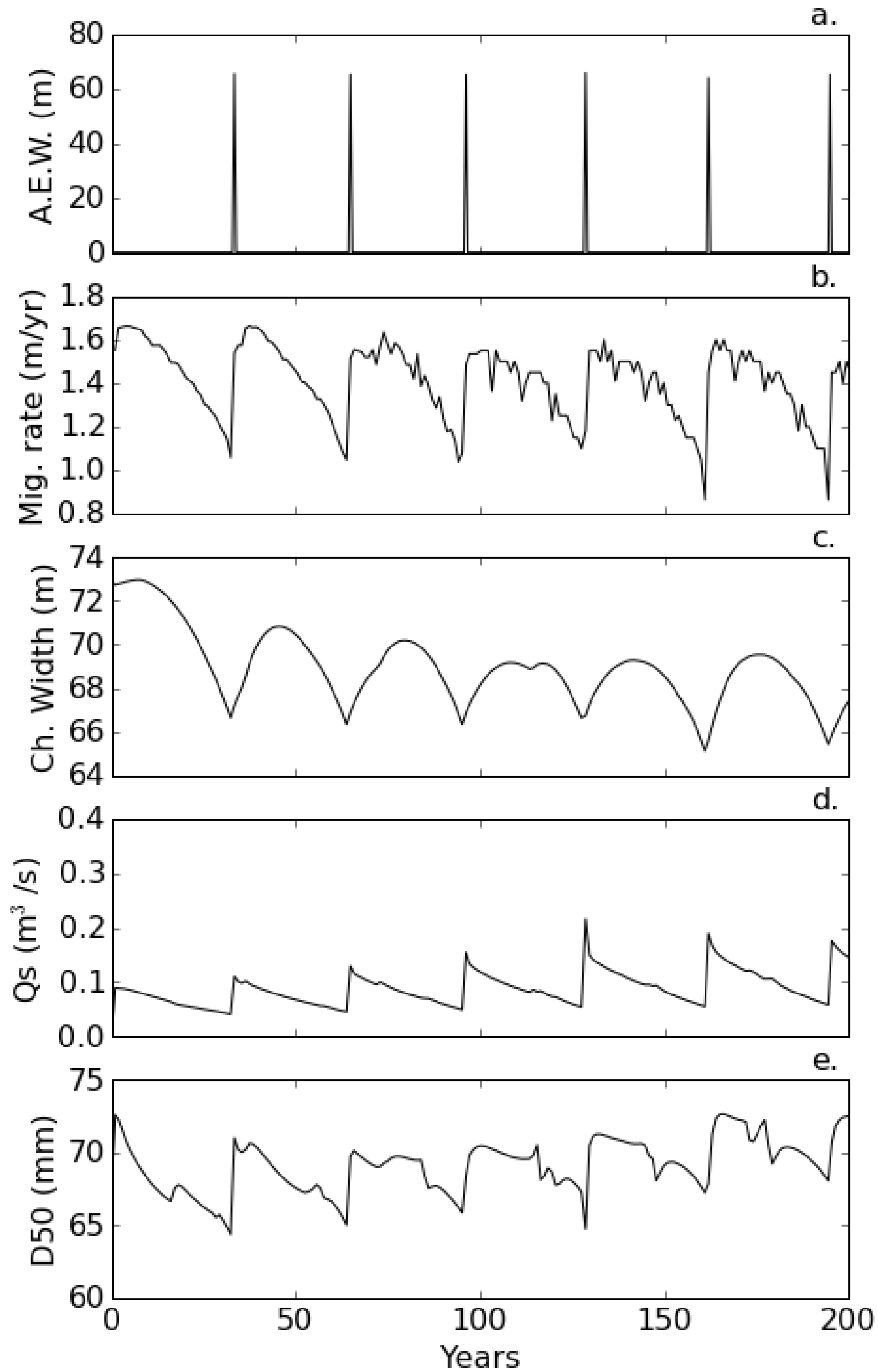

Figure 2.8: Channel characteristics over time for a single node. a) width of material exchanged during avulsion, b) annual channel migration rate, calculated as the mean of the annual rates of narrowing and widening, c) channel width, d) sediment transport rate during the maximum discharge, e) median channel grainsize. Parameters: qs_{cr}: 10^{-7}; α_f: 0.55; τ_r: 32 m^3/s; α_n: 0.055; B_{min}: 40 m; L_t: 0.75 m; α_a: 1; L_a: 1 m. See Appendix B for other parameters.

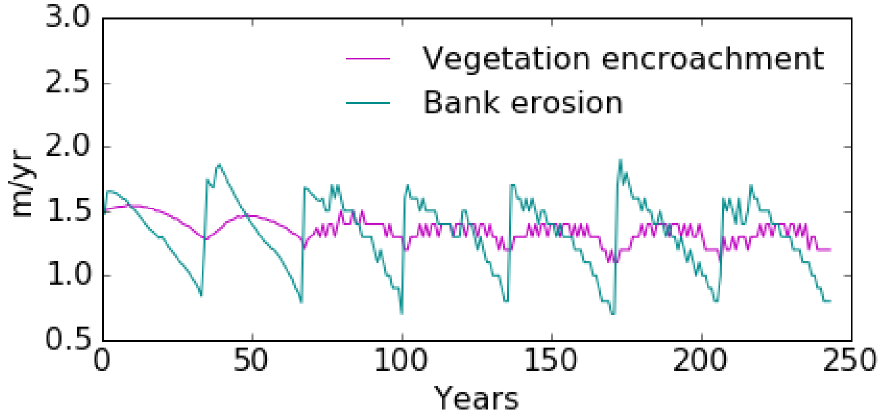

Figure 2.9: Rates of bank erosion and vegetation encroachment. See Figure 2.8 for parameters.

timescale. The migration rate (2.8b) declines gradually from around 1.5 m/yr to about 1 m/yr, then rapidly rises following an avulsion due to the increase in channel depth. Decadal variability is greater for bank erosion than vegetation encroachment, for which rates for all years fall within a 0.4 m/y range (Figure 2.9). For roughly half the time, bank erosion out-paces vegetation encroachment, and channel width is increasing (Figure 2.8c). As bank erosion declines, encroachment becomes the dominant mode of channel migration, and width declines until the next avulsion event. Spikes in the rate of sediment transport (Figure 2.8d) and bed coarsening (Figure 2.8e) occur at the same time as avulsions. In between these events, sediment transport declines slowly as channel capacity is reduced due to aggradation. The D_{50} fluctuates between a range of about 8 mm.

The trends presented in Figure 2.8 hold regardless of the initial channel dimensions. Width is plotted twice a year, during the low flow period and after the largest flow, in Figure 2.10. The three series represent runs which are identical except for the starting width. Annually, width varies by roughly a half meter as narrowing occurs during low flows and bank erosion widens the channel during the upper tail of the hydrograph. All runs evolve to a similar range of widths, which slowly declines through time.

Sediment supply affects the evolution of channel width and the frequency of avulsion (Figure 2.11). When upstream sediment is supplied at capacity, the channel avulses roughly twice as often than if there is no upstream supply, and fluctuates between a smaller range of widths. When sediment supply is cut off, width decreases slowly on centennial timescales, although avulsions cause a spike in sediment supply that lead to temporary channel widening. Our model suggests that rivers are much less sensitive to flow sequencing then they are to sediment supply. To test the effect of hydrograph shape on the evolution of channel width, MAST-1D was run using the discharge record from the 2007 water year. For one run, the actual sequence of discharges were maintained, and the hydrograph was repeated for 100 years. The same set of discharges were then ordered sequentually (similar to the hydrograph presented in Figure

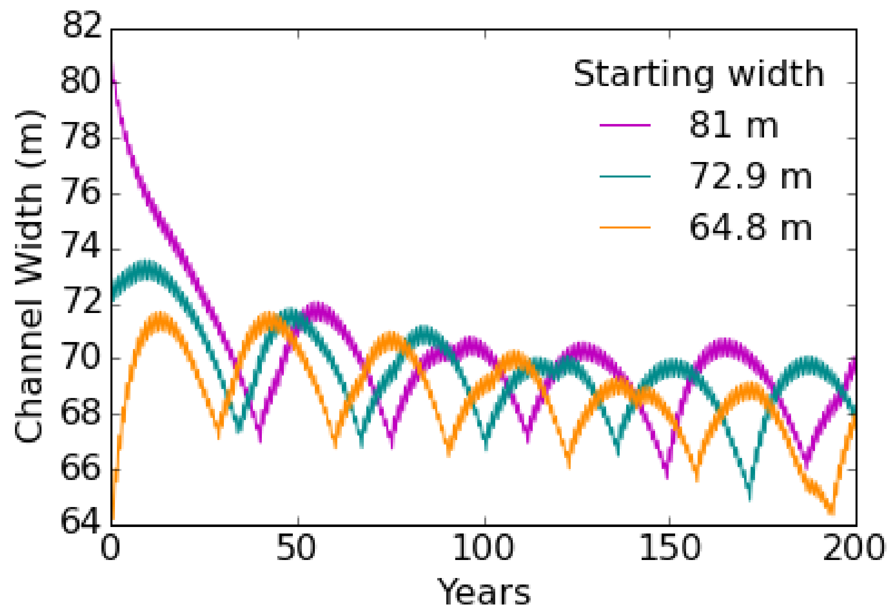

Figure 2.10: Evolution of channel width over time for different intial widths. For parameters, refer to Figure 2.8.

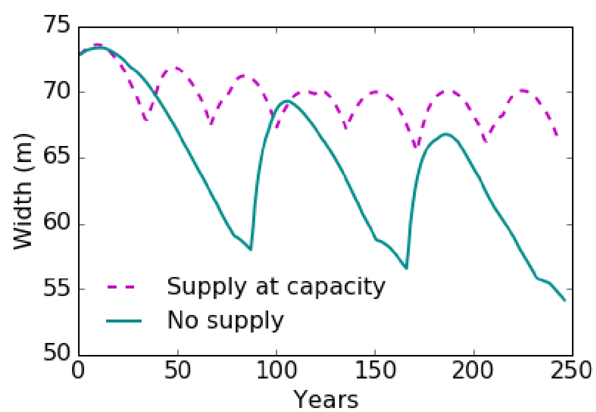

Figure 2.11: Channel width for runs with and without an upstream supply of sediment.

2.7) and repeated for the same time frame. Channel width for the two runs is plotted in Figure 2.12. The shape of the hydrograph appears to change the magnitude, but not amplitude, of the response. Even though the run with the 'natural' hydrograph evolves to a slightly lower width, avulsion occurs at a similar frequency.

In summary, MAST-1D predicts that coarse-bedded, wandering alluvial systems exhibit cyclical, autogenic behavior. The channel fills with sediment, which reduces its capacity and causes it to fill faster. Eventually, a local avulsion occurs, which deepens the channel and increases its capacity again. This process is maintained regardless of initial channel width, sediment supply, or flow sequencing.

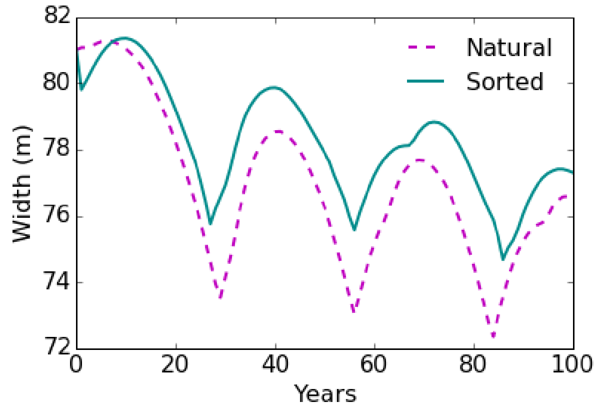

Figure 2.12: Effect of flow sequencing on channel width. Flow is calculated using by repeating daily flows from the 2007 water year. For the 'natural' run, the true order of flow events was preserved, while discharges were put in ascending order for the 'sorted' run.

2.4.1 Sensitivity analysis

A sensitivity analysis was performed for the bank erosion, vegetation encroachment, and avulsion parameters. The results are presented in Figure 2.13 for channel width and in Figure 2.14 for channel migration. Variation in most parameters has a limited impact on channel width and avulsion frequency. Only for C_{max} (the coarse particle size class) did a variation of 10% affect width by more than that amount. When the bounds of the three size classes that we have defined as the 'coarse' range are each lowered by 10%, the model evolves so that the range of channel widths is nearly 10 m higher, the migration rate is about a third higher than the base run, and avulsions occur more frequently. The opposite occurs when C_{max} is 10% coarser.

The channel migration rate is moderately sensitive to the floodplain mixing coefficient (α_f), narrowing coefficient (α_n), and minimum width (Bc_{min}), which each vary by roughly 10% when they are raised/lowered by that amount. Increasing α_f implies that less of the near-bank sediment in transport is sourced from the banks, lowering the rate of channel widening for any given flow in which bank erosion is initiated. When α_f is low, the implication is a higher bank-sediment transport rate and therefore a higher widening rate. Since channel narrowing is linearly related to α_n, increasing it causes higher migration rates, and vice versa. Vegetation encroachment rates are inversely proportional to B_{min}.

Surprisingly, neither channel width nor migration rates are sensitive to the avulsion threshold (L_t), avulsion mixing parameter (α_a), or avulsion depth (L_a). It is important to note that the upstream boundary condition was set so that sediment was supplied at capacity for the sensitivity analysis runs. The choice of parameter may become more important in conditions of sediment starvation or excess, where the difference in grainsize between the active layer and floodplain is more pronounced.

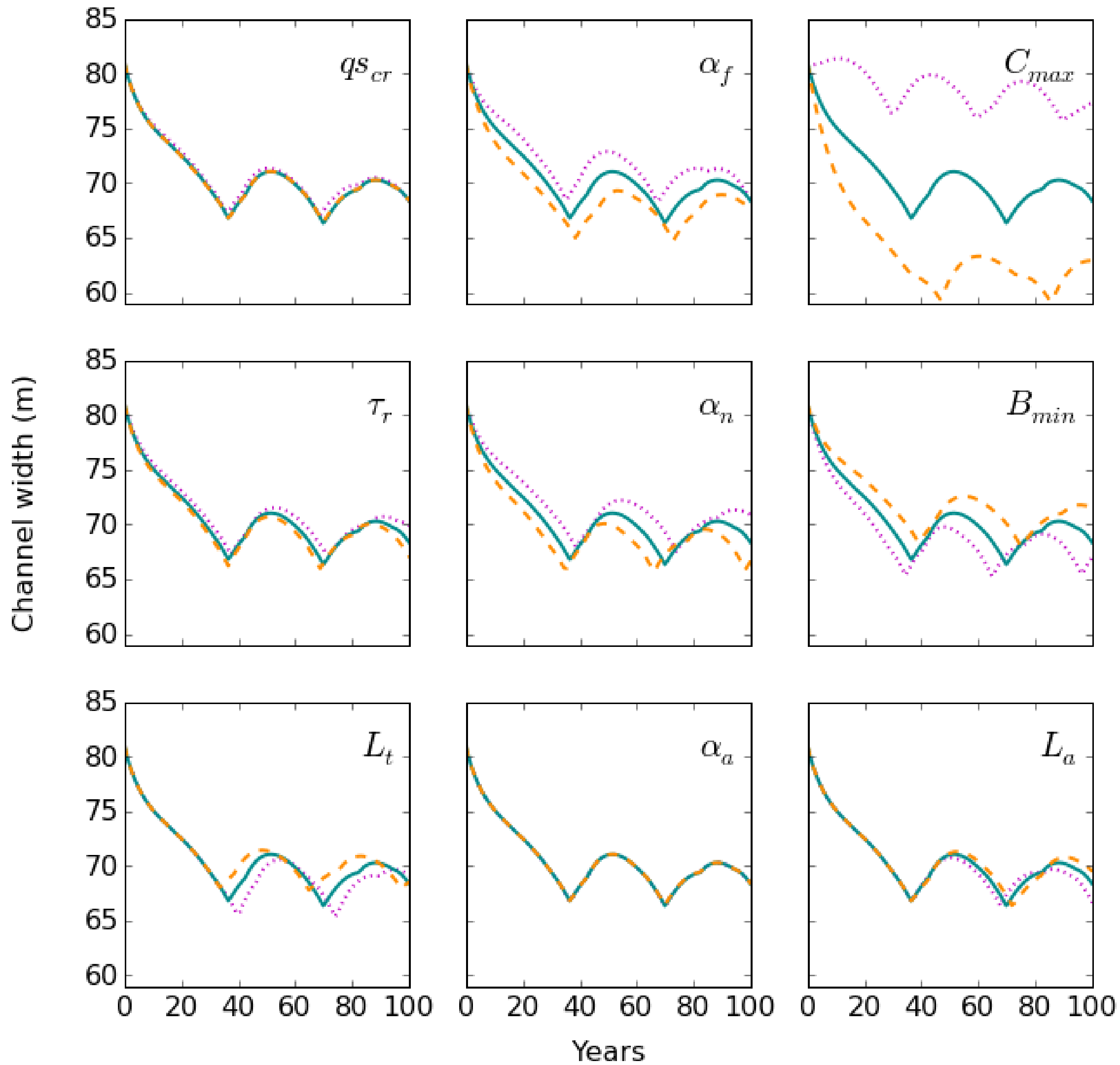

Figure 2.13: Sensitivity of channel width to model parameters. Solid teal lines represent the base run, yellow dashed line represents a 10% increase in the parameter, and magenta dotted lines denote a 10% decrease in the parameter value. Base run: qs_{cr}: 10^{-7}; α_f: 0.55; τ_r: 32 m^3/s; α_n: 0.055; B_{min}: 40 m; L_t: 0.75 m; α_a: 0.2; L_a: 1 m.

2.5 Discussion

Theories of river dynamics have traditionally favored lowland, migrating channels, yet we often apply numerical models based on these theories to rivers behaving according to a different set of processes. Conceptual models for wandering, cobble-bedded rivers indicate that bank erosion during large floods and avulsion are the key ways in which the floodplain and channel exchange sediment (*O'Connor et al.*, 2003; *Konrad*, 2012). However, there is a paucity of decadal-scale numerical models that take both of these processes into account. In MAST-1D, we have made simplifying assumptions about channel geometry, morphology, and reach-scale processes in order to explore the long-term dynamics of avulsion and width change.

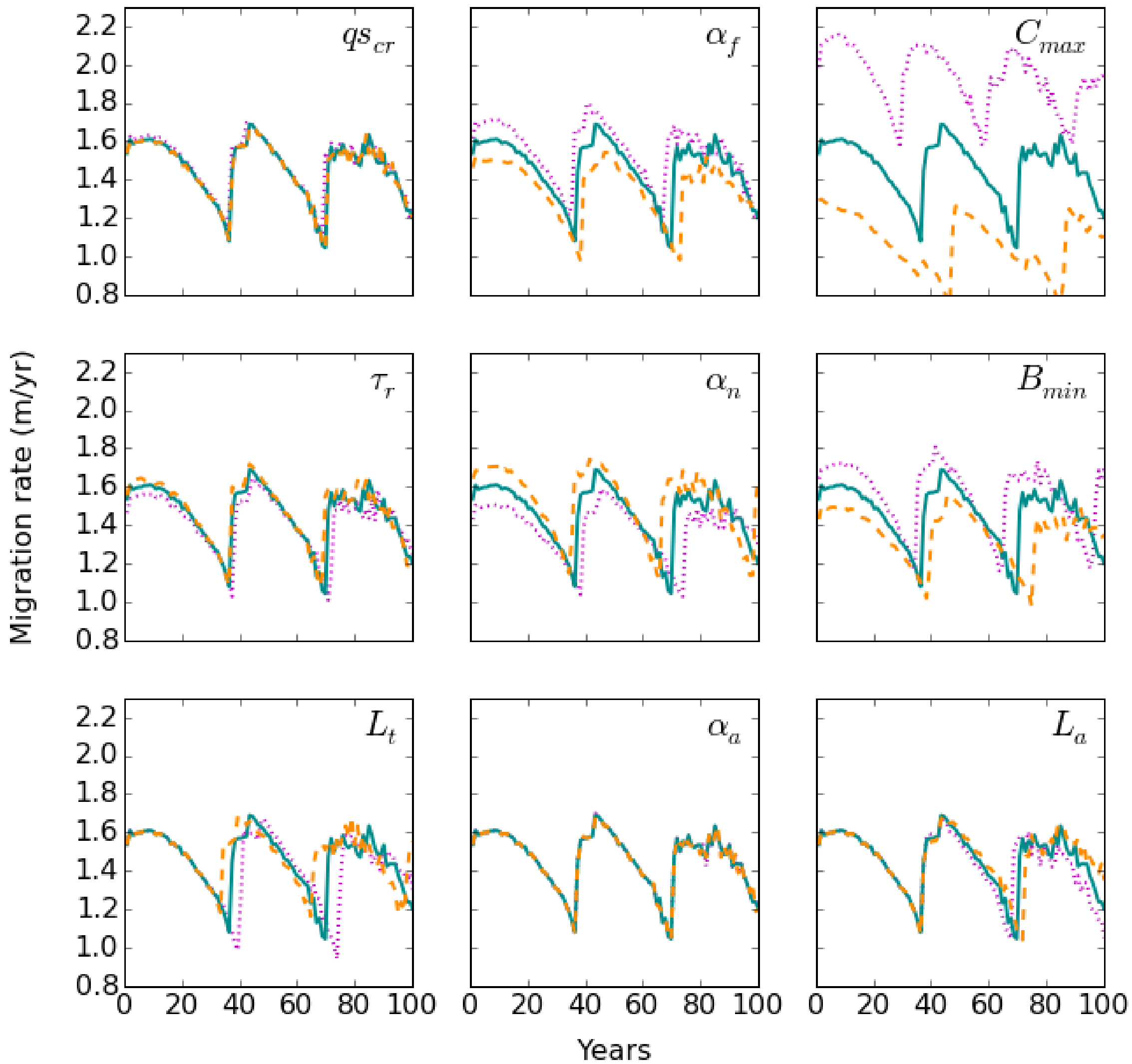

Figure 2.14: Sensitivity of migration rate to model parameters. Solid teal lines represent the base run, yellow dashed line represents a 10% increase in the parameter, and magenta dotted lines denote a 10% decrease in the parameter value. Base run: qs_{cr}: 10^{-7}; α_f: 0.55; τ_r: 32 m^3/s; α_n: 0.055; B_{min}: 40 m; L_t: 0.75 m; α_a: 0.2; L_a: 1 m.

Our model suggests that autogenic variability is inherent to rivers with erodable banks and the ability to shift channels. Decadal-scale oscillations in migration rate, sediment transport capacity, and channel width appear to be modulated by the frequency of avulsions (Figure 2.8). When the channel avulses, a fresh supply of relatively fine floodplain sediment is immediately available for transport and the channel becomes deeper, causing higher shear stresses during large flows. This increases the mobility of the channel and causes a spike in the sediment transport rate (Figure 2.8d). The bed quickly armors as the fine sediment is selectively transported (Figure 2.8e). Over a few decades, the sediment transport and migration rates slowly decline, trending to a more stable channel until the next avulsion event.

There are two major assumptions in our avulsion model that impact its behavior. The first is that floodplain sediment is mixed with the active layer following an avulsion. The physical interpretation of this is that the sediment in side channels have a high connectivity to the primary channel in the reach. Since the majority of avulsions and side channels appear to be sub-reach scale (*Jerolmack and Paola*, 2007, also see Figure 2.5), it is likely that they can readily exchange sediment. The other assumption is that floodplain channels inhabited following an avulsion are not armored. Avulsing channels tend to favor former channel locations (*Jerolmack and Paola*, 2007), so it is possible that new channels are already armored and do not provide a pulse of fresh sediment supply (Figure 2.8d). However, floodplain channels are often activated during high discharge events, and these may accumulate sediment that is readily released when the channel captures a higher percentage of flow during an avulsion.

Channel width is a function of the relative intensities of bank erosion and vegetation encroachment. Its oscillatory behavior on decadal timescales (Figure 2.8c) is a result of two processes. The abrupt increase in shear stress and mobility following avulsion leads to higher rates of bank erosion, causing widening. As the channel widens, its competence per unit channel decreases because the flow is spread over a larger surface area. In addition, lateral sediment supply via bank erosion accelerates aggradation, further reducing the capacity (and shear stress) of the channel during high flows. Bank erosion rates subsequently decrease. When they become lower than the rate of vegetation encroachment, the channel begins to narrow. A narrower channel means that there is less exposed sediment available for colonization, and the rate of encroachment declines slightly until the next avulsion event. The results shown in Figure 2.9 suggest that bank erosion is more sensitive to autogenic fluctuations in bed mobility than vegetation.

Our MAST-1D simulations suggest that sediment supply has a large impact on timescales of autogenic adjustments: when supply is high (at capacity), avulsion is more frequent than when supply is low (no upstream supply, Figure 2.11). An excess of sediment exists in the channel when upstream supply is at capacity because bank erosion also acts as a source of sediment supply. While vegetation encroachment sequesters some of this excess sediment, it does not directly lead to a change in bed elevation. Therefore, the channel is in a constant state of net aggradation. In reality, sediment supply to gravel-bed rivers can be episodic, and periods of aggradation followed by stability may be the norm. In addition, abrasion and weathering of grains, processes not accounted for in MAST-1D, may increase mobility of individual particles and counter aggradation.

Interestingly, MAST-1D predicts that the channel still aggrades (albeit at a much lower rate) when upstream supply is cut off, even though the channel armors. This is at odds with the commonly-held view that sediment starved conditions generally lead to degradation (e.g. *Galay*, 1983; *Williams and Wolman*, 1984). Much of our theory about channel profile change stems from observations of rivers with self-formed substrates. In the Pacific Northwest, many rivers are reworking floodplain surfaces that were created during glacial and para-glacial conditions, and are under-fit to transport the largest particles in the channel at rates necessary to cause substantial bed elevation change (*Hassan et al.*, 2014). Therefore, it is plausible that during conditions of sediment starvation, fine material supplied via bank erosion is quickly winnowed away while the remaining coarse floodplain gravels, cobbles, and boulders accumulate in the channel and contribute to the armor layer. The long term response of the river would then be a slow net loss of finer floodplain material instead of incision. While field studies of wandering rivers generally associate low sediment supply with channel stability (e.g. *Konrad et al.*, 2011; *Pohl*, 2004), our MAST-1D results suggest that bank erosion and avulsion do still occur during sediment starvation, though at much lower rates. This is supported by field evidence; the avulsion presented in Figure 2.5 occurred along the sediment-starved Elwha River, where a dam 2 km upstream had cut off supply to the reach for nearly 100 years.

We adapted MAST-1D with the hypothesis that coarse cobble-boulder sized sediment forms an armor layer on the bank toe that protects the bank from frequent erosion. Our model qualitatively mimics the behavior of the experimental channels described in *MacKenzie and Eaton* (2017): increasing the size of the largest grains in the sediment mixture leads to less lateral migration and a narrower channel (Figures 2.13 and 2.14). In fact, model behavior is more sensitive by a large margin to the coarse grainsize fraction (C_{max}) than any of the other parameters tested. Our simplistic conceptual model of non-cohesive banks may leave out key components that contribute to the initiation and magnitude of bank erosion. In particular, we neglect the role of vegetation and its interaction with bank material. Both field (*Beechie et al.*, 2006) and numerical (*Eaton and Giles*, 2009) evidence suggest that vegetation plays little role in bank strength for larger channels, whose bank toes extend much deeper than the rooting depth. However, MAST-1D will overestimate bank erosion in channels narrower than about 15 m (*Beechie et al.*, 2006), where vegetation becomes significant. In addition, improvements could be made to MAST-1D to include the important role of woody debris in initiating channel avulsion and providing suitable terrain for vegetation growth.

2.6 Conclusion

Traditionally, geomorphologists have operated under the assumption that rivers can be adequately characterized by a single 'regime' width, and it is common to numerically model channel processes without dynamically linking them to the floodplain. We developed MAST-1D to simulate coarse-bedded, wandering rivers, where width changes are frequent and morphologically important. These types of rivers are unique in that local, reach-scale avulsions and bank erosion both act as sources of sediment to the channel. The model suggests that the dominant discharge concept overlooks inherent decadal-scale variability, even when flow and sediment supply regimes are in a steady state. Channel aggradation leads to avulsion, which locally increases channel depth (and shear stress), increases sediment mobility, and affects channel migration rates. Changes to boundary conditions, such as a reduction in sediment supply, alter the timescale and magnitude at which wandering rivers operate but do not fundamentally change the dominant fluvial processes.

MAST-1D serves as a tool for analyzing and predicting river behavior on the scale of decades to centuries. While we have included most relevant parameters for this timescale, future effort should be focused on modeling the role of vegetation, particularly as it relates to log-jam formation and colonization of point bar surfaces, and to including algorithms for abrasion and floodplain weathering, which impact long-term sediment mobility. In addition, our understanding of long-term channel evolution would benefit from more observations of local avulsion events. Future field and laboratory campaigns should focus on quantifying the fluctuation of channel depth following channel reorganization.

Chapter 3

The impact of sediment supply on channel stability along Elwha River, Washington following dam emplacement and removal

3.1 Summary

Two hydropower dams, which had been in place on Elwha River for nearly one hundred years, were removed beginning in 2011. The channel, which had coarsened and become more stable as a result of sediment starvation, experienced increased rates of bank erosion and new channel activation following the removal. Our research attempts to understand the impact of sediment supply on channel stability. We are especially interested in whether the same geomorphic processes that led to increased stability following dam emplacement can explain patterns of channel change in the opposite trajectory after the removal. We used MAST-1D, a one-dimensional size-specific bed evolution model which accounts for bank erosion, vegetation encroachment, and local channel avulsion to simulate reach-scale evolution of Elwha River over its entire history of dam emplacement and removal. The model treats bank erosion as a function of sediment mobility, but does not account for hydraulic changes related to bar formation. MAST-1D was able to reproduce field data of particle size, channel width, and rates of channel widening and narrowing over the period in which the dams were in place. Our observations and modeling suggest that channel armoring led to decreased rates of bank erosion, and that reductions in channel width slowed the rate of vegetation encroachment, as less bar space was available for colonization. Reductions in sediment supply decreased the frequency of avulsion. These factors combined to increase the overall stability of the channel. Simulations in MAST-1D are consistent with increased rates of bank erosion and avulsion that were observed in the field following dam removal, but the model underestimated the ability

of Elwha River to export the pulse of sediment released from the upstream reservoir. It is likely that local channel morphology, especially the impact of bar deposition and curvature on lateral variability in flow strength, play an important role in characterizing channel instability in this period. Information on the caliber of sediment supply from the upstream reservoir, as well as a better understanding of vegetation processes, can increase the success of future modeling studies and improve our understanding of landscape recovery from dams.

3.2 Introduction

The Glines Canyon and Elwha Dams, which had cut off sediment supply to Elwha River for nearly a century, were torn down between 2011 and 2014, releasing several million cubic meters of sediment downstream. Within the span of a few years, the reaches between the dams underwent a regime shift from a sediment starved, armored system to a supply-rich, unstable configuration (*Draut et al.*, 2011; *East et al.*, 2015; *Kloehn et al.*, 2008; *Konrad*, 2009; *Pohl*, 2004). Elwha River may take decades to recover from the sediment pulse (*East et al.*, 2015) and to adjust to a regime with a higher sediment supply. While other unregulated regional rivers offer a glimpse of how the Elwha may evolve (*Kloehn et al.*, 2008), it is unclear how long recovery will take and how dynamic it will be in the future (*Draut et al.*, 2011).

While the case of Elwha River is unusual in its scale, the geomorphic processes related to sediment supply reductions and pulses are observed on many gravel and cobble-bed rivers. Streams respond to adjustments in governing conditions with changes in particle size, width, and depth. These factors affect the capacity of the channel and its ability to transport sediment. Most river bed surfaces coarsen as a result of low sediment supply (e.g. *Hassan et al.*, 2006; *Williams and Wolman*, 1984), and many experience channel narrowing due to flood peak reduction and encroachment of vegetation onto formally active channel surfaces (e.g. *Gordon and Meentemeyer*, 2006; *Swanson et al.*, 2011). The Piave and Brenta Rivers in Italy narrowed as a result of declining sediment supply due to gravel mining, then widened after mining stopped (*Kaless et al.*, 2014). Similarly, *Kondolf et al.* (2002) found that land use changes in rivers of vastly different scales resulted in width change–again, increased sediment load to the river led to widening, and decreased load resulted in narrowing.

Pulses of sediment from dam removals, landslides, and other disturbances can increase sediment transport rates, change the texture of the bed surface, and alter channel morphology on timescales of several months to decades and longer (*Czuba et al.*, 2012; *Major et al.*, 2012; *Wilcox et al.*, 2014). While ample research has focused on the evolution of sediment pulses through translation and dispersion (e.g. *Cui et al.*, 2003; *East et al.*, 2015; *Lisle et al.*, 2001), much less is known about the feedbacks between sediment supply and channel stability during extreme events. Large inputs of sediment can lead to deposition on channel bars, which constricts flow near the banks and can lead to bank erosion. In addition, if a sediment pulse is composed of fine material, it can increase the mobility of the bed surface, leading to instability (*Wilcock and Crowe*, 2003). While *Madej et al.* (2009) observed channel widening on Redwood

Creek, California following a sediment pulse caused by a large flood, *Tullos and Wang* (2014) found that little widening occurred on Dahan River, Taiwan after a dam failure. More work is needed on the factors that lead to channel instability during extreme sediment supply events.

Assessing the impact of sediment supply on channel stability in the field is challenging for a number of reasons. Geomorphic processes often operate on timescales much longer than available field observations. Decadal-scale studies generally rely on aerial photographs, which vary widely in quality and are not always available at convenient time intervals. It can be difficult to distinguish the impact of sediment supply from that of hydrology, when both lead to morphologic changes observed in photographs. It is for this reason that many researchers and managers turn to numerical modeling to explain field observations.

Here we use MAST-1D, a reach-scale, one-dimensional bed evolution model, to assess the feedbacks between sediment supply and channel stability on Elwha River over its century-long history of dam emplacement and subsequent removal. Our objectives are twofold: we first assess whether MAST-1D can adequately reproduce observed geometric and textural changes both over the period of sediment starvation when the dams were in place and during the sediment pulse following removal. We then analyze how these changes in sediment supply have impacted channel evolution. Our focus is on changes to rates of floodplain-channel interaction. While channel coarsening and narrowing has been observed on many dammed channels, most previous research on the subject (e.g. *Konrad et al.*, 2011; *Williams and Wolman*, 1984) considers rivers where the flow regime has been significantly altered; therefore, the influence of sediment supply cannot be separated from that of the flow regime. The Glines Canyon Dam removal is the largest to date in the United States, and the magnitude of the sediment pulse is unique among other projects. As we usually lack detailed before-and-after observations on natural sediment pulses, feedbacks between channel stability and events of this magnitude are largely still open questions. While the results of our study are only strictly applicable to Elwha River between Glines Canyon Dam and Elwha Dams, they should be relevant to those interested in the effects of sediment supply on channels, particularly in gravel-bedded, mountain rivers. In addition, they may prove useful for improving channel geometry algorithms for landscape evolution models.

3.3 Study location

Elwha River drains 833 km^2 of primarily steep terrain from the northern flanks of the Olympic Mountains to the Strait of Juan de Fuca (Figure 3.1). The basin straddles the Hurricane Ridge Fault, which separates two major Eocene-aged terranes (*Tabor and Cady*, 1978). The upper portion of the basin drains the highly deformed Olympic Sedimentary Complex, containing metasedimentary rocks, while downstream the river flows through the Coast Range Terraine, composed primarily of basalt and sandstone (*Brandon et al.*, 1998; *Tabor and Cady*, 1978). The region is uplifting at a rate of 0.28 mm/yr (*Brandon et al.*, 1998), providing steep terrain susceptible to landsliding and debris flows (*Montgomery and Brandon*, 2002). During the Last Glacial

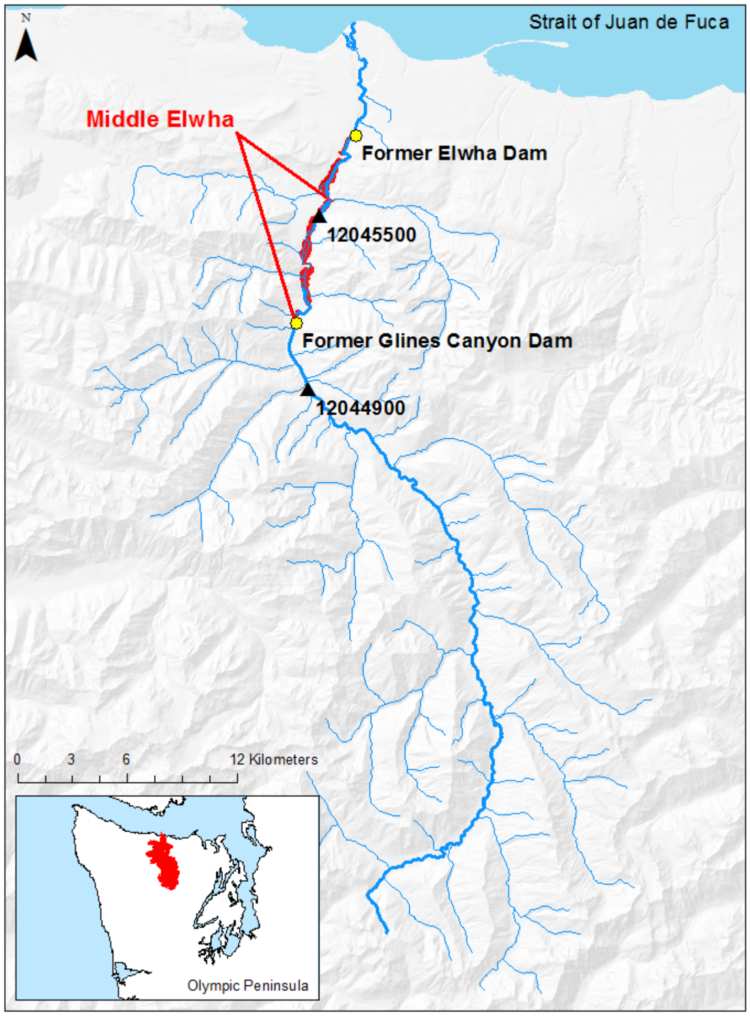

Figure 3.1: Map of Elwha River basin showing locations detailed in the text. Black trianges denote US Geological Survey stream gauges. Red shading in the main map delineates alluvial surfaces (channel and floodplain) between Glines Canyon and Elwha Dams. Shading in the inset shows the entire Elwha Basin.

Maximum, the valley was overrun by both an alpine glacier from the south and from the Juan de Fuca Lobe of the Cordilleran Ice Sheet from the north. Retreat began about 14.5k years ago, after which glacio-lacustrine and outwash deposits filled much of the lower valley (*Easterbrook*, 1986; *Polenz et al.*, 2004). Elwha River incised during the Early Holocene following isostatic rebound along the coast (*Mosher and Hewitt*, 2004), leaving local bluffs that act as major sediment sources to the delta. Modern alluvial clasts are composed of a variety of lithologies, sourced from both the local bedrock and from granitic sources within the former glacial extent.

Annual precipitation in the basin varies between ∼5600 mm in the headwaters and ∼1500

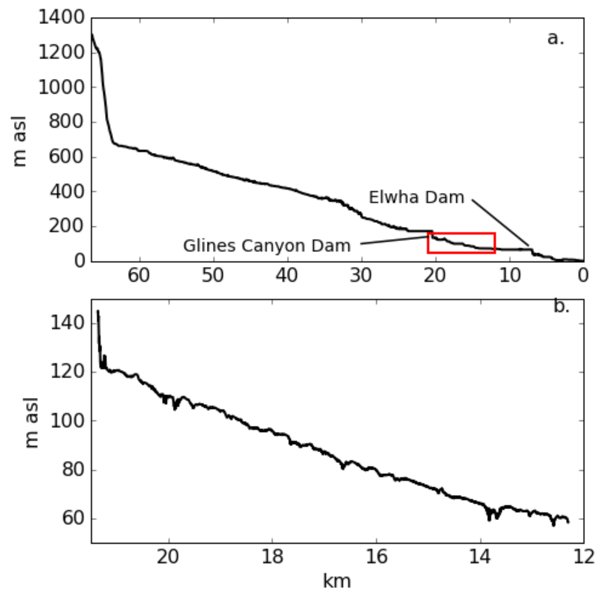

Figure 3.2: Longitudinal profile of a. Elwha River and b. the study area extracted from DEMs collected prior to dam removal. Red box in a. denotes the study area.

mm in the rainshadow at the mouth (*Munn et al.*, 1999). Elwha River has a rainfall-dominated hybrid hydrologic regime with a bimodal hydrograph (*Reidy-Liermann et al.*, 2012). Peak flows range between ~130 and 1200 m^3/s and generally occur in late autumn or winter. A secondary runoff peak occurs during the spring snowmelt season. Mean discharge over the period of record (1896-2015) is 43 m^3/s.

The upper 83% of the watershed is within Olympic National Park and is nearly pristine. During the early 20th century, two hydropower dams were constructed on the lower portion of the river to accomodate growth of nearby Port Angeles, WA. The 33 m Elwha Dam, forming Lake Aldwell, was completed in 1913 and was followed in 1927 by the 64 m tall Glines Canyon Dam and adjacent Lake Mills reservoir. The reservoirs trapped 3 ± 0.8 and 16 ± 2 million m^3 of sediment, respectively (*Bountry et al.*, 2011). Prior to 1975, hydrograph alteration for power generation would have influenced peak flows but likely had a minor impact on daily discharge. From 1977-2011, the dams were primarily managed as run-of-the-river (see *Duda et al.*, 2011b). Both dams were removed between 2011-2014.

Our study focuses on the Middle Elwha, the set of reaches between the two former dams (Figure 3.1). A 1.5 km bedrock canyon confines the channel immediately downstream of Glines Canyon Dam, except for an ~700 m long reach where a small floodplain has developed. Gradient is steep, at about 0.011 (Figure 3.2). The next 3 km are less steep (gradient is about 0.008) and have a gravel-dominated, laterally-active anabranching morphology (*Knighton*, 1998). The last 4 km are nearly straight with a gradient of about 0.006, and bedrock outcrops limit floodplain development and migration in localized reaches.

Apart from the dams, human alteration has been limited to minor projects on residential properties. Prior to dam removal, the sediment-starved bed was coarse and stable (*Draut et al.*, 2011; *Pohl*, 2004), although floodplain-channel interaction continued on a reduced scale (*Kloehn et al.*, 2008). Removal of both dams began in September 2011. Elwha Dam was removed incrementally during a six-month period. The Glines Canyon Dam occurred over a longer period that extended from 2011-2014. The full removal schedule can be found in *Randle et al.* (2015) and *East et al.* (2015) and is only briefly summarized here. Pieces of the dam were demolished in stages, and during the first year, only suspended sediment passed downstream into the study area. In October 2012, the first pulse of bed material spilled over the dam. It was composed primarily of sand and fine gravel (*Draut and Ritchie*, 2015). The pulse reduced surface particle size, and was associated with minor channel widening (*East et al.*, 2015). Peak flows during the first two years following the removal were abnormally low; even so, 90% of the 5 million m^3 of sediment released from the two reservoirs in that time was transported into the Strait of Juan de Fuca (*Magirl et al.*, 2015; *Randle et al.*, 2015; *Warrick et al.*, 2015). Dam removal was halted between November 2012 and September 2013. A second pulse of bed material entered the study area when removal re-commenced and the final blast occurred. Removal was completed in summer 2014. The first major flow events following dam removal occurred in the winter of the 2015 water year. Two floods with recurrence intervals of about 2 years caused extensive flooding, despite their modest magnitudes. We observed that the elevation of flow on the floodplain locally reached levels recorded during the largest flood on record in the pre-removal period. Early in the 2016 water year, a 30 year flood passed through the system, causing additional flooding and infrastructure damage.

3.4 Methods

3.4.1 MAST-1D setup

MAST-1D is a one-dimensional bed evolution model designed to simulate channel and floodplain exchange over decadal and longer timescales. The model space is divided into a series of nodes. Every node contains a set of reservoirs, each with an evolving geometry and grain size distribution. Size-specific vertical and lateral exchanges of sediment occur between reservoirs. Aggradation and degradation lead to exchanges between the channel bed, underlying substrate, and sediment load. Lateral mixing between the floodplain and channel occurs via migration, overbank flooding, and avulsion. Sediment is exchanged between model nodes via downstream variability in sediment transport capacity.

MAST-1D iterates through 5 main processes. First, hydraulics are calculated for a two-part cross-section that includes rectangular channel and floodplain units. We use the standard step method applied to the backwater equation, assuming steady, gradually-varied sub-critical flow. Bedload is then calculated with the set of equations presented by *Gaeuman et al.* (2009), which were calibrated to a large, cobble-bedded river. Next, lateral exchanges of sediment to and from the channel are calculated. Two processes contribute to migration–bank erosion and

Table 3.1: Boundary conditions for model runs

	Pre-Glines 1918-1927	Pre-Removal 1927-2011	Post-Removal 2011-2016
Between dams			
Upstream sediment supply	Sediment rating curve	0	Decay function
Downstream WSE	30 m	30 m	Linear reduction/stage-discharge rating curve
Control run			
Upstream sediment supply	Sediment rating curve	Sediment rating curve	Sediment rating curve
Downstream WSE	Stage-discharge rating curve	Stage-discharge rating curve	Stage-discharge rating curve

vegetation encroachment. Bank erosion is initiated when the mobility of the coarse (boulder-sized) fraction of the channel surface exceeds a threshold, and its magnitude is a function of the sediment transport rate of coarse particles in the channel surface and floodplain. Vegetation encroachment occurs during periods of low shear stress, and its rate is proportional to channel width. Sediment transport and lateral exchange rates are used to calculate the change in bed elevation using a 1-D form of the Exner equation. Mass conservation is then applied on a size-specific basis to each reservoir (active layer, channel, and substrates), and the grain size distributions and geometries are updated to reflect incoming and outgoing sediment fluxes. If the channel aggrades to the extent that it is approaching the height of the banks, avulsion occurs, lowering the bed elevation and exchanging sediment between the channel and floodplain. Full details on MAST-1D can be found in Chapter 2 and in Appendix A.

There are several potentially important processes not accounted for in our implementation of MAST-1D. Lateral variability in flow hydraulics due to curvature and bar growth is disregarded, as is temporal variability in channel sinuosity. In addition, the model does not include the influence of large woody debris and log jams, which can be instrumental in trapping sediment and initiating avulsion.

Boundary conditions and run sequences

MAST-1D requires a flow record and two boundary conditions–an upstream sediment supply and a downstream water surface elevation. For the flow, we use daily discharge data for 1918-2016 from the USGS Gauge at McDonald Bridge (12045500), located in a bedrock canyon roughly halfway between the former Glines Canyon and Elwha dams (Figure 3.1). We divide the record into three periods, which are summarized in Table 3.1. The first, which we term the 'Pre-Glines period,' spans between 1918-1927 and includes the period between emplacement of Elwha and Glines Canyon Dams. We do not simulate the first five years of backwater effects caused by the Elwha Dam (1913-1918) because the discharge record does not exist for that period. For the Pre-Glines period, the downstream water surface elevation is set at the height of the Elwha Dam, 30 m above the initial bed elevation. The upstream bedload was supplied at capacity, which we calculated using a 2-zone channel/floodplain cross-section with dimensions that have been calibrated to field measurements of long-term sediment supply (this is explained further below). The suspended sediment load was determined by an emperical relation developed for Elwha River by *Konrad* (2009):

$$Q_{s,s} = 10^{-5} * (0.78Q)^{2.5} \tag{3.1}$$

where $Q_{s,s}$ is the suspended transport rate in kgs^{-1} and Q is the discharge at the McDonald Bridge gauge in m^{3}s^{-1}. We assume that grains smaller than 0.5 mm always travel in suspension, which is generally the case in samples collected by *Curran et al.* (2009). During overbank flooding, larger particles may become suspended and deposit on the floodplain. We set the trapping efficiency of the floodplain at 20% for both coarse and fine grains. All fine (<5 mm) sediment not deposited on the floodplain is supplied to the next downstream node. Coarse grains that are not deposited on the floodplain are assumed to re-enter the channel and are accounted for in the bedload calculation.

The second, or Pre-Removal period, starts when Glines Canyon Dam is installed in 1927 and lasts until dam removal begins in 2011. We assume that all sediment was trapped behind the dam, and set the sediment supply to zero (*Curran et al.* (2009) estimates that 14% of suspended sediment flows past the dam, but we assume this has negligible influence on the bed).

The third (Post-Removal) period commences following initiation of dam removal in September 2011. We simulated the removal of Elwha Dam in the model by incrementally lowering the downstream water surface elevation over the 6 month period over which the removal took place. After that, a stage-discharge rating curve was developed to set the boundary. The stage is calculated for each flow using the 2-zone cross section and assuming normal flow.

In our model, the pulse of upstream sediment supply following removal of Glines Canyon Dam is released in October 2012, when bed material began spilling over the dam site. We do not account for sediment released during the period between September 2011 and October 2012, which was exclusively washload and most of which passed through the study area without depositing (*East et al.*, 2015). To simulate the pulse, an exponential decay function of the form

$$Q_{s,i} = Q_{c,i}(1 + Ce^{\frac{-t}{\lambda}}) \tag{3.2}$$

is used. $Q_{s,i}$ is the sediment feed for bedload size class i, $Q_{c,i}$ is the size-specific sediment transport capacity (see below), t is the time elapsed since the dam removal, and C and λ are constants that determine the shape of the curve.

C and λ were calibrated using measured rates of Lake Mills reservoir denudation and sediment load estimates upstream of Lake Mills provided by the US Bureau of Reclamation and US Geological Survey for the 2012-2016 water years. The rates represent the total sediment load, so assumptions must be made on the partitioning of sediment sizes. Sedimentology work by *Draut and Ritchie* (2015) indicates that most sediment deposited before October 2013 was under 8 mm. However, the load coarsened over time; a subsurface sample collected on a bar just upstream of the dam site in August 2015 show that grains as large as 181 mm were available for transport, and cobble-size pieces of dam were observed throughout the study area. To mimic this coarsening, the sediment pulse is divided into two phases. Between October 2012 and October 2013, the size-specific transport capacity (Q_c) is truncated at 8 mm, so only sand and fine gravel is supplied. The value of C (hereafter C_1) is adjusted accordingly. After October 2013, the full grain size distribution of $Q_{c,}$ is used, and a new value of C (C_2) is calibrated.

The partitioning of the sediment pulse between suspended load and bedload is another source of uncertainty. No information is available on the percentage of sand that traveled in suspension. To capture the range of possible responses, we perform three runs with different values for the percent of suspended sediment supplied during the Post-Removal period (Table 3.2). The parameters and boundary conditions for the Pre-Glines and Pre-Removal periods are identical for each of these runs (see 'Between Dams' in Table 3.1). In the first scenario, run R1, 77% of the total load is suspended. This is the ratio reported by *Curran et al.* (2009), who collected suspended and bedload samples upstream of Lake Mills from 2006-2007. In their assessment of Lake Mills denudation, *Randle et al.* (2015) divided the deposit into fine (silt and clay) and coarse (sand and coarser) material and found that the former only constituted 29% of material evacuated between 2012 and 2013. Therefore, for the second scenario (R2), we assume that the suspended load is 29% of the total load. This is likely an underestimate, since sand travels in suspension along Elwha River. For the third scenario (R3), we use stratigraphic data collected from the Lake Mills reservoir between 1989 and 1994 by *Gilbert and Link* (1995). They estimated volumes and size distributions for each delta unit. We are assuming that the delta topset (the uppermost layer, which is composed of coarse sediment) represents the bed material captured in Lake Mills. The fraction of bedload is calculated as the volume of the delta topset divided by the total volume of all reservoir deposits (excluding tributary fans). This comes out to 16% bedload and 84% suspended load and is likely an underestimate, since it does not consider bed material sediment available from tributaries. While the uncertainty in our estimates of sediment supply following the dam removal is high, the three scenarios should provide a sense of the range of possible responses.

For each sediment supply scenario, sediment supply was calculated using Equation 4.2 for the 2013-2016 water years. C and λ were adjusted until the time series of calculated sediment supply was similar to that provided by the USGS/USBR. A plot of the calibrations is presented in Appendix B.

To separate the influence of the dams from hydrologic variability, a control simulation, C4, is run using the same initial conditions as the other three runs but supplying upstream sediment using a rating curve (see below). In C4, the downstream water surface elevation is calculated via a stage-discharge rating curve (see above and refer to Table 3.1).

Table 3.2: Summary of model runs

Run	% sus.*	Source**	C_1	C_2	τ***
R1	77	Average of measurements by *Curran et al.* (2009)	100	42	365
R2	29	Coarse/fine partition by *Randle et al.* (2015)	310	140	365
R3	84	Pre-removal Lake Mills reservoir measurements	70	30	365
C4	varies	Control run, supply determined by rating curves	-	-	-

*Percent of load comprised of suspended sediment during Post-Removal period
**Source used to determine the partitioning between suspended and bedload during the Post-Removal period
***In days

Initial conditions and model calibration

The study area is divided into 21 cells, each with unique valley widths and sinuosities measured from air photos. In MAST-1D, sinuosity is assumed to remain constant through time, and each cell should incorporate several meander bends. The small length of our study area, as well as the need to capture longitudinal variability in the response of the dams, necessitated a relaxation of this rule, and our cells are roughly 5 channel widths long, shorter than what would be considered 'reach scale.'

Model cells fall into one of two types: 'canyon' and 'alluvial.' Canyon cells, which represent bedrock canyon reaches, have fixed banks (the channel cannot migrate or avulse). To simulate bedrock, these cells are not allowed to degrade 0.2 m lower than the initial elevation (potential aggradation is unlimited). Channel width was measured from air photos (see below), and initial slope was calculated from a 0.5 meter resolution DEM provided by the US Geological Survey. The initial channel depth was set at an arbitrary value high enough to prevent overbank flooding.

For alluvial cells, lateral channel fluxes and unlimited aggradation and/or degradation may occur. The study area was divided into two sections based on slopes measured from the DEM. Model cells in the upstream segment, which stretches from 2 km downstream of the former Glines Canyon Dam to river km 17 (Figure 3.2), were given initial slopes of 0.0081. Alluvial cells downstream of river km 17 were assigned an initial slope of 0.0069. For each section, the initial channel width was calibrated using the Lake Mills reservoir survey data of *Gilbert and Link* (1995, see above). An annual bedload sediment supply was calculated from the reservoir data using volumes of the delta topset and tributary fan deposits. These sediments represent the long-term natural bed material supply to Elwha River. We computed bedload sediment transport capacity for the period between 1927 and 1994 using the 2-part cross-section and *Gaeuman et al.* (2009) equation, and adjusted channel width until the annual average sediment yield was within 5% of that measured in the reservoir. The grain size distribution used in the calculation is adapted from a composite of bulk subsurface sediment samples of bank toe and collapse deposits collected between Glines Canyon Dam and the Strait of Juan de Fuca. We found that the grain size distributions of coarse-layer bank deposits are similar to those of point bar heads within the channel (Figure 3.3). We added a 1% lag of sediment in the 512-1024 mm size range to account for large boulders observed on riffle crests but not collected in the bank samples. A comparison of the grain size distributions of the modeled load and reservoir bed material is presented in Appendix B. The two distributions are similar, indicating that the calibration is adequate. Initial channel widths are plotted in Figure 3.4. They represent the width that which is able to transport the observed sediment load given the measured flow regime and assuming static banks and is roughly analogous to an emperically derived regime width. All alluvial cells were assigned the same initial channel depth of 1.86 m, which was determined using a regional hydraulic geometry relation developed by *Castro and Jackson* (2001).

The initial channel geometry and grain size distribution were used to derive a sediment rating curve for the upstream boundary condition. We used the dimensions of the downstream alluvial section (81 m channel width and slope of 0.0069) for numerical stability, although calculations using the upstream alluvial section yields similar results. The rating curve was calculated using a 2-part channel/floodplain cross-section, using daily discharge data from the USGS gauge at McDonald Bridge (Figure 3.1). $Q_{c,i}$ was extracted from the rating curve for each day.

All model cells start with the same initial grain size distributions. The channel GSD is the same used to calculate incoming bedload supply and calibrate initial channel width (see above). The initial floodplain grain size distribution is a function of both channel material sizes and the thickness of fine overbank deposits. The overbank thickness on the floodplain was estimated from measurements of bank stratigraphy collected along eroding banks during low flow (see Appendix C). The thickness of bed material in the banks was calculated as the difference between the channel depth and overbank thickness and was held as a constant. MAST-1D calculates the inital floodplain grain size so that the system is at perfect steady state between lateral deposition and lateral erosion in all size classes, given duration-averaged flow data and a constant migration rate (see the Appendix A for details).

A detailed list of the initial conditions and model parameters, as well a description of the calibration procedure, can be found in Appendix B.

3.4.2 Model confirmation

Airphoto analysis

In order to assess the performance of MAST-1D, channel width and rates of channel-floodplain exchange were calculated from aerial photographs. Channel and valley margins were delineated. Table 3.3 lists the available photos. The channel is defined here as unvegetated surfaces within the floodplain (wetted channel plus bars and visible paleochannels), which provided consistency over photos captured during different discharges. All photos were viewed at a resolution of 1:1500 during the digitization process to ensure consistency. The resolution and quality of the air photos improved over time, and this likely introduced systematic error, as

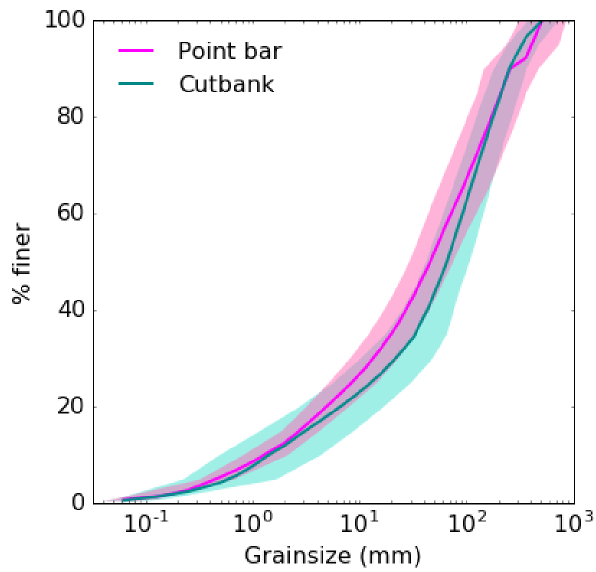

Figure 3.3: Composite subsurface grain size distributions of Elwha River cutbank and point bar head deposits. Shading represents the standard deviation of all samples for each landform.

Table 3.3: Air photos used in the analysis with available accompanying data

Photo date	Source	R/S	RE (m)	TE (m)
1976**	National Park Service*	-	7	12.2
1981	National Park Service*	-	15	18
1994-09-21	USGS DOQ	1:12000	3.9	10.7
2006-04-01	USDA NAIP	1 m	5	11.2
2009-10-08	USDA NAIP	1 m	5	11.2
2013-08-31	USDA NAIP	1 m	5	11.2
2014-12-03	USGS/National Park Service	0.05 m	-	-
2015-06-04	USGS/National Park Service	0.05 m	-	-
2016-08-11	USGS/National Park Service	0.05 m	-	-

*Air photos digitized by author.
**Coverage of air photo does not extend to whole study area
R/S Resolution or scale
RE Registration error
TE Total error (registration + digitization)

more floodplain channels are visible in the most recent, high resolution photos (*Draut et al.*, 2011). In addition, identifying the break between vegetated and unvegetated surfaces can be difficult, both in shadowed areas and on point bars where vegetation density varies. For these reasons, we conservatively estimate that digitization error is 10 m. To calculate total error (TE), we follow the method of *Draut et al.* (2008), where

$$TE = \sqrt{RE^2 + DE^2} \tag{3.3}$$

RE is the registration error and DE is the digitization error. TE is listed in Table 3.3 for photos where the registration error is available. Floodplain margins were delineated using a combination of air photos, digitized geological maps (*Tabor and Cady*, 1978), and, where available, LiDAR data.

The digitized air photos were divided into segments that aligned with the MAST-1D model cells. Channel and valley centerlines were produced for each photo. The sinuosity of each river segment was calculated for each photo, and the average of all available years was input into MAST-1D. Channel widths for each segment were calculated as the quotient of the channel area and centerline length on each photo. The area of floodplain eroded or created between sets of air photos was measured by using the Union tool in ESRI ArcMap. No attempt was made to distinguish channel widening via bank erosion in the air photos from new channel created following an avulsion or activation of a floodplain channel. In other words, an avulsion that results in a bare gravel/cobble surface would appear to have led to widening in our analysis. Therefore, when comparing the output of MAST-1D to channel change measured from the air photos, the area of new channel creation calculated from the air photos is equivalent to the sum of the areas of modeled bank erosion and avulsed channel, and the area of vegetation encroachment is the sum of areas of channel narrowing and avulsion.

3.4.3 Other confirmation data

Other field data were collected and acquired from outside sources to calibrate and verify the model. Wolman pebble counts of point bar head deposits collected near the end of the Pre-Removal period were provided by the US Geological Survey (USGS) and National Atmospheric and Oceanic Administration (NOAA). To quantify Post-Removal particle sizes, digital photographs of point bar heads were taken using a GoPro camera in September-October 2015. Particle size information was extracted from the images at Seattle University using Digital Gravelometer software. The size distributions extracted from the photos were truncated at about 32 mm as recommended by the software. Details on the field and lab procedure are provided in Appendix C.

Details on the post-removal sediment budget through the 2016 water year were provided by the USGS. This information included sediment flux exiting the Lake Mills reservoir, storage within the sediment area, and flux out of the reach. In addition, reach storage between 2011 and 2013 was provided in *East et al.* (2015). Details on the calculation methods are found in *East et al.* (2015). The sediment budget is presented in metric tons. To convert the MAST-1D volumes (in m^3) into tons, we assume a sediment density of 2.7 tm^{-3}.

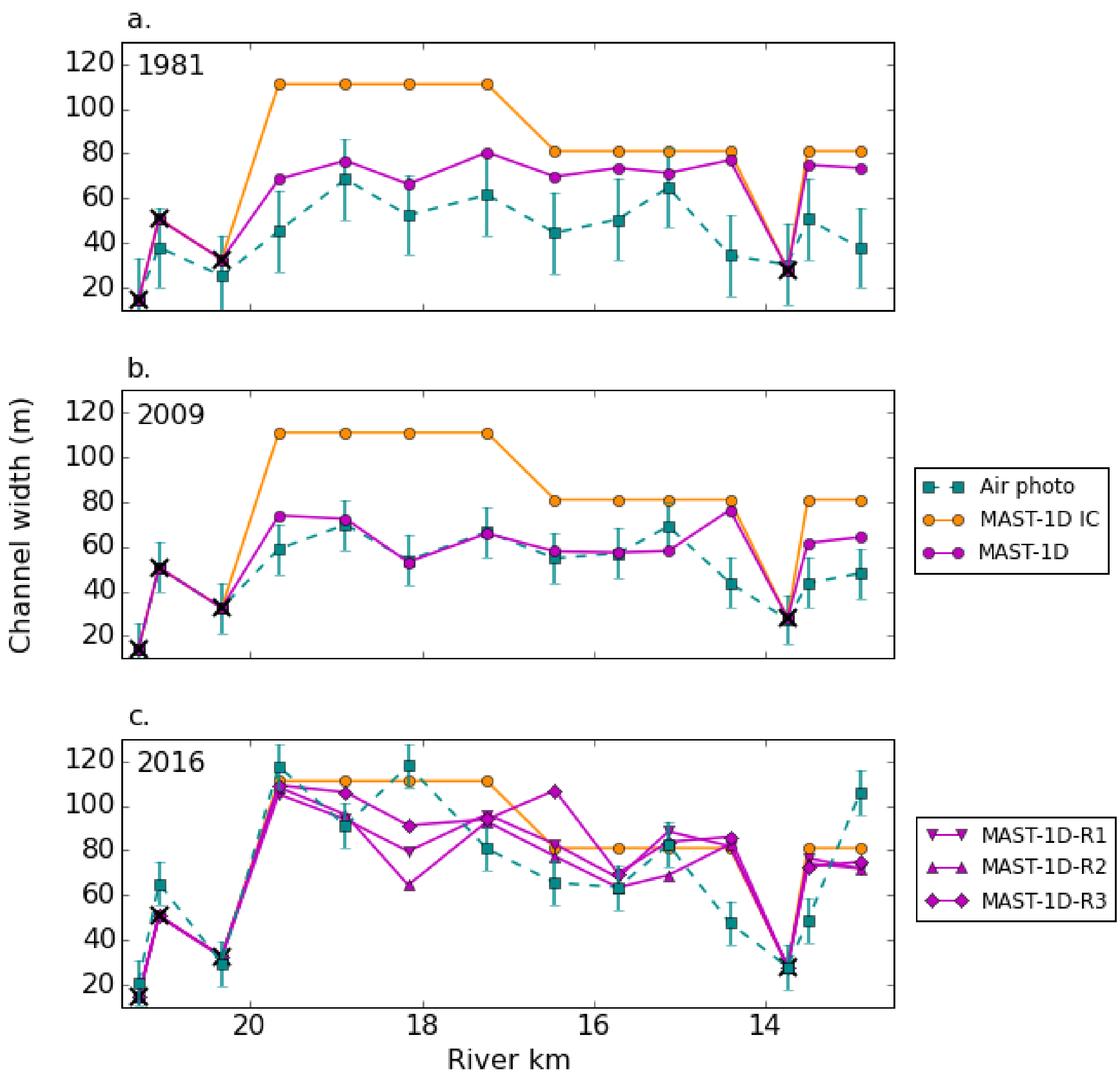

Figure 3.4: Channel width plotted against channel coordinate as measured from air photos and calculated in MAST-1D for a) 1981, b) 2009, and c) 2016. The initial model condition (i.e. channel width in 1919) is plotted in orange for comparison. 'X' marks refer to bedrock canyons and were modeled with fixed banks in MAST-1D. Glines Canyon Dam is at river km 21.5.

3.5 Results

The results are divided into two parts. First, MAST-1D output is compared to the air photo and field data to assess the performance of the model. Then, rates of modeled channel evolution are presented.

3.5.1 Model performance

Here we compare evolution of Elwha River simulated by MAST-1D to field and air photo data to assess its success in replicating observed spatial and temporal patterns of geomorphic change. We focus on metrics of channel width, widening and vegetation encroachment, grain size, and channel storage. Modeled and measured channel width as a function of channel coordinate is presented in Figure 3.4 for select years, along with the initial model condition for comparison. MAST-1D replicates the spatial pattern well for the Pre-Removal period (Figures 3.4b and c). While width is overestimated for most reaches in 1981, the longitudinal trend holds over the majority of the study channel. MAST-1D does not perform well between river kms 12.5 and 15, where a bedrock canyon around river km 13.5 and the upstream end of the Lake Aldwell delta affect hydraulics and channel evolution. During the Post-Removal period (Figure 3.4d), all runs show similar trends in width, which match the air photo data in most reaches, with exceptions being at river km 18, where MAST-1D neglected to predict a 60 m increase in width, and at river km 14.5, just upstream of a bedrock canyon.

The creation of new channel falls under two categories: bank erosion in the current channel and activation/re-activation of former floodplain channels. Both processes were relevant on Elwha River, especially following dam removal. Channel outlines derived from the airphotos are presented in Figure 3.5 for the post-removal period. Most channel change occurred in the upstream half of the study area, which was characterized both by creation of new channel via re-activation of floodplain surfaces and by widening of the main channel. In the downstream half of the study area, bank erosion occurred, but the channel remained primarily single-threaded.

Widening (bank erosion plus avulsion) rates from run R3 is compared to net change measured from the air photos in Figure 3.6 (the trends were similar for all dam removal scenarios). Each point represents the spatially-averaged annual rate of channel widening or narrowing over the time interval between sequential air photos, which ranges between under 1 to 13 years (see Table 3.3). Error bars denote the standard deviation of rates for each model cell/air photo reach, which range between 240 and 918 m in valley length. The predictive success of MAST-1D is very different for widening and narrowing. While there is a large amount of scatter in the spatial variability of widening, the majority of the rates are within an order of magnitude of aerial photo measurements, and a trend between modeled and measured data is visible. MAST-1D overpredicts channel widening for most years. Errors are smaller for the Pre-Removal period than they are Post-Removal; the percent difference for the former ranges between 7 and 77%, while modeled Post-Removal rates are 26-121% different from estimates from the air photos.

Our implementation of MAST-1D does not replicate channel narrowing with high success (Figure 3.6b). While Pre-Removal spatially-averaged narrowing rates measured from the aerial photos span nearly two orders of magnitude, modeled rates all fall between 1 and 3 m/yr. In addition, while there is a lot of spatial variability in air photo measurements (as

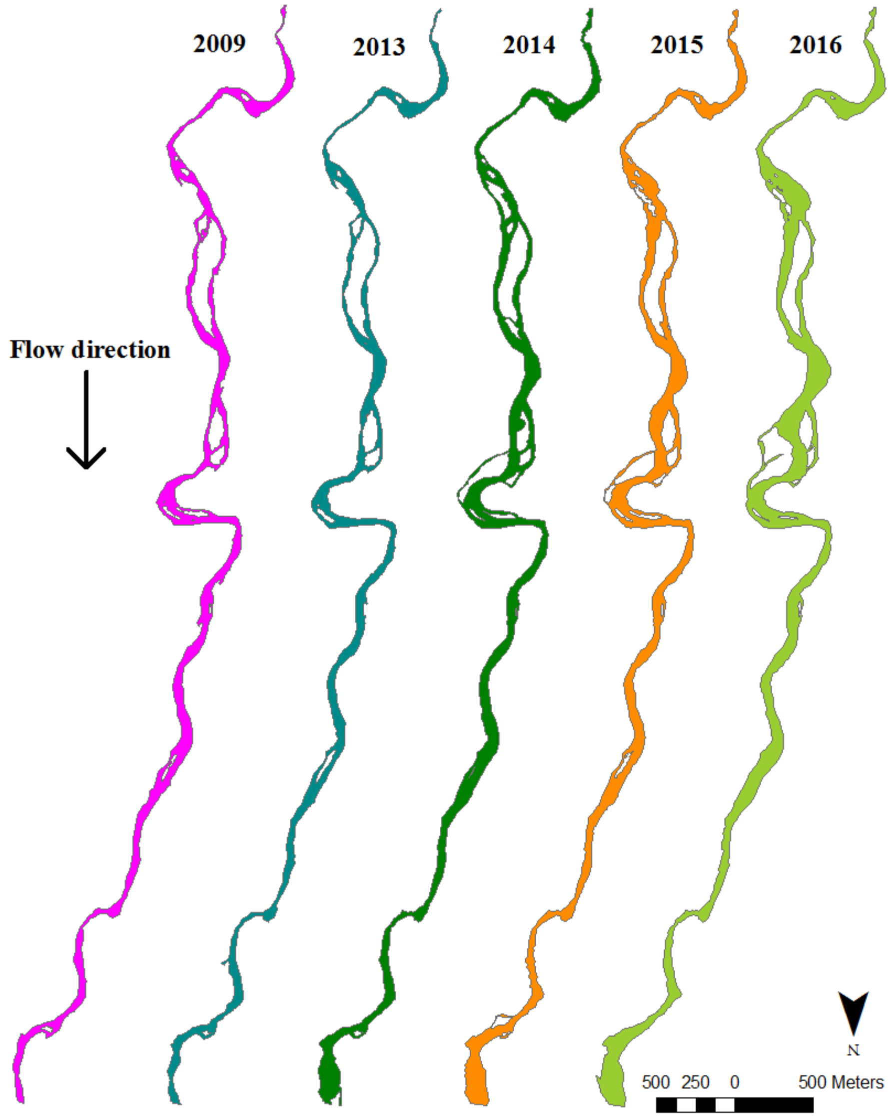

Figure 3.5: Channel outlines for Elwha River just before (2009) and following dam removal

depicted by the large horizontal error bars), MAST-1D predicts very little longitudinal variability in vegetation encroachment. The model predicts much higher spatial variability in Post-Removal narrowing than the air photos show, mainly due to a higher occurrence of narrowing due to avulsion than is observed in the latter.

The MAST-1D simulation adequately replicated bed coarsening due to sediment starvation following the closure of Glines Canyon Dam and fining due to the progradation of the Lake Aldwell delta at river km 12 during the Pre-Removal period (Figure 3.7a). Apart from the bedrock canyons at the upstream end of the study area (river kms 19-21), where the D_{50} is underestimated by over a factor of 4, model output is within the range of USGS and NOAA

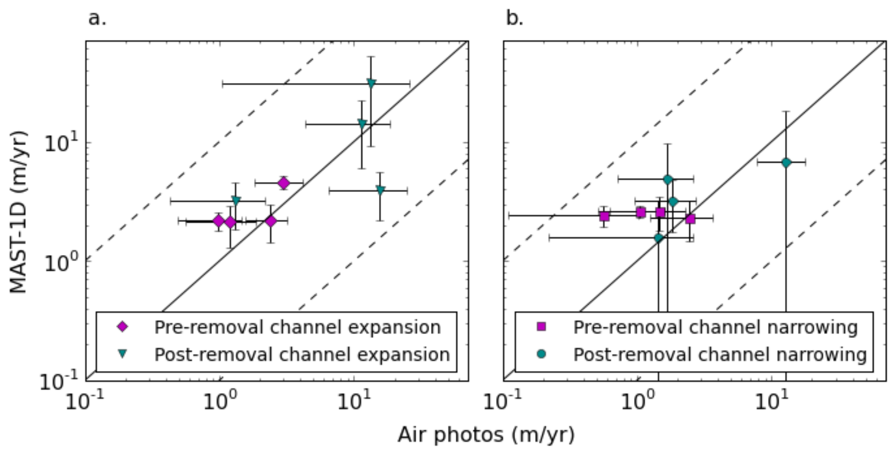

Figure 3.6: The relationship between a) annual widening (bank erosion plus new channel creation) and b) vegetation encroachment as predicted in model run R3 vs those measured from air photos. Each marker represents the mean rate of all model cells over one pair of dates, while the error bars delineate the standard deviation. Some error bars have been cut off for display. Dotted lines are one order of magnitude away from the 1:1 (solid) line.

pebble counts. As is apparent from Figure 3.7b, the truncated 2015 D_{50} for all three MAST-1D predictions is slightly lower than that calculated from photosieving for the upstream reaches. At the downstream half of the study area, runs R1 and R3 are within the lower end of observed values and predict the recovery of bed material grain size following the sediment pulse released from Lake Mills.

Total (channel plus floodplain) sediment storage between the former Glines Canyon Dam and the upstream end of the former Lake Aldwell deposit during the Post-Removal period is plotted for runs R1-R3 in Figure 3.8 along with field and remotely sensed data from the USGS and US Bureau of Reclamation. All three modeled post-removal sediment supply scenarios overpredict reach storage by at least a factor of 4. However, in R1 and R3, much of the stored material consists of fine sediment sourced from the suspended load, which has little influence on channel geomorphology. While the general temporal pattern of sediment storage is similar for all runs, the model is highly sensitive to the supply of bed material. Total storage scales with the proportion of the incoming sediment pulse consisting of bedload.

According to the field data, channel storage increased between 2012 and 2014, then decreased slightly between 2014 and 2016. All three model runs show an increase in storage up to 2014, but none are able to replicate the subsequent net export of sediment. R3 provides the best fit to the data; the projected amount of sediment exported from the study area is 13 million t, 20% lower than the USGS/USBR calculations, but simulated bed material storage is within the error range in 2013 and just above it in 2016.

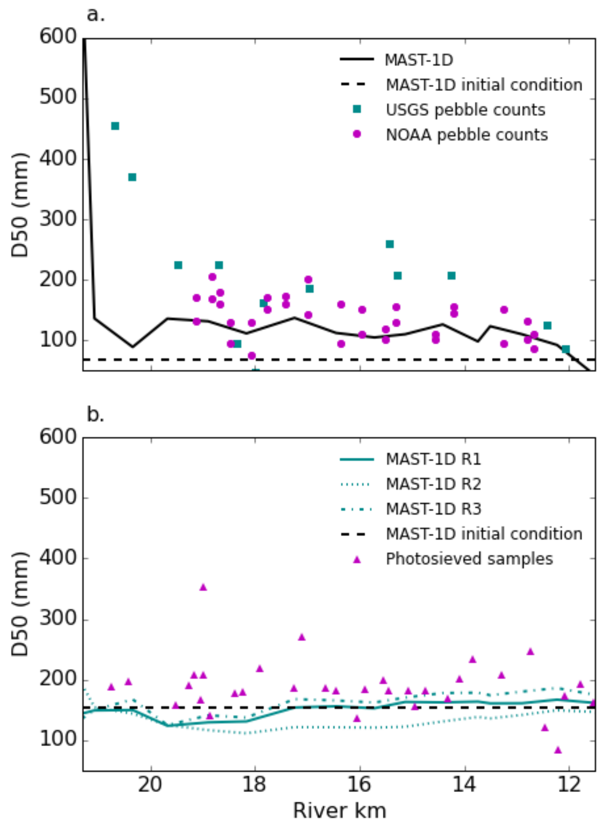

Figure 3.7: D_{50} for a) the end of the Pre-Removal period and b) 2015, four years after dam removal. Markers represent a) Wolman counts provided by the USGS and NOAA and b) photosieved samples. MAST-1D output was truncated at 32 mm in b) to make it comparable to the photosieved samples.

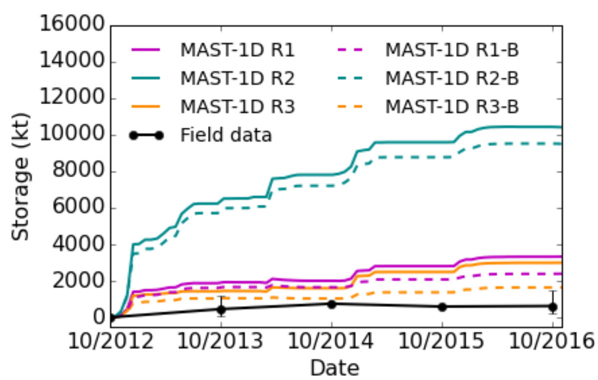

Figure 3.8: Total (channel and floodplain) storage within the study area. For the model runs, solid lines represent storage for all material (fine material and bed material), while the dotted lines show storage of bed material (sizes >0.5 mm) only. Storage measured from field data (black line) is sourced from *East et al.* (2015) for 2013 and from unpublished data from the USGS/USBR for all other dates. It represents total storage of all size classes. Uncertainty estimates, where available, are represented by error bars. The contribution of bed material to total storage has not been quantified in the field.

3.5.2 Channel evolution

Here we present output from the MAST-1D simulations that show the effect of sediment supply on channel evolution. In runs R1-R3, the sediment supply regime is impacted by dam emplacement and removal. Run C4 represents the control case where there is no disturbance to sediment supply. We focus on the surface particle size and channel widening and narrowing processes.

The sediment supply regime imposed by the dam impacted the transport rate and calibre of bed surface material (Figure 3.9). A comparison of the annual sediment yield between the dammed and control run for the Pre-Glines and Pre-Removal period (Figure 3.9a) reveals that, as expected, the removal of upstream sediment supply following dam emplacement leads to a reduction in the sediment load. It takes about 15 years for the sediment regime to adjust, after which the yield for the dammed simulation remains under 20% of the control run. The channel surface particle size evolves on a similar timescale (Figure 3.9c); the dammed reach coarsened rapidly until 1935 then continued to increase slowly throughout the rest of the run, while the control fluctuated within a range of less than 10 mm throughout the entire run, fining slightly after the 1970s.

During the Post-Removal period (Figure 3.9b and d), the sediment yield declined exponentially, mimicking the sediment supply for R1 and R3. The total mass of sediment exiting the modeled channel is inversely proportional to the amount of bedload supplied; runs R1 and R3 each experience yields approaching 2.5 million m^3, while yields in R2 are less than half that. The particle size for all three runs drops into the sand/fine gravel range during the first (fine) sediment pulse, then coarsens during the second pulse. While the D_{50} for runs R1 and R3 approach that of the control run by 2015, R2 does not recover.

Bank erosion and vegetation encroachment as calculated by the model were impacted by sediment supply disturbances caused by the dam. Average rates for runs R3 and C4 are presented in Figure 3.10. The trends for the other runs are similar to R3. The bank erosion rates for both runs are variable on an annual timescale and are dependent on the magnitude of peak flow events. They were highest during the 1970s-1990s, when a greater proportion of large flood events occurred compared to the mid-20th century. After about 1945, slightly less erosion is predicted during any given flow in R3 than in C4 during the Pre-Removal period.

Annually-averaged erosion rates are compared with annual peak daily discharges in Figure 3.11 (runs R3 and C4 are presented). The control data (grey points) represent the range of bank erosion that could be expected in a system with sediment supplied at capacity. During the Pre-Removal period, the modeled erosion rates are within the range of those expected in a system that is not supply-limited, despite the fact that rates in R3 are lower for any given flood (Figure 3.10). However, avulsion is much less common in the sediment starved system. Time-averaged annual widening rates are presented in Figure 3.12. The solid teal series represent the total widening rate, which can be divided into widening via bank erosion (the magenta dotted series) and avulsion. In the dam run (R3), nearly all widening is due to bank erosion,

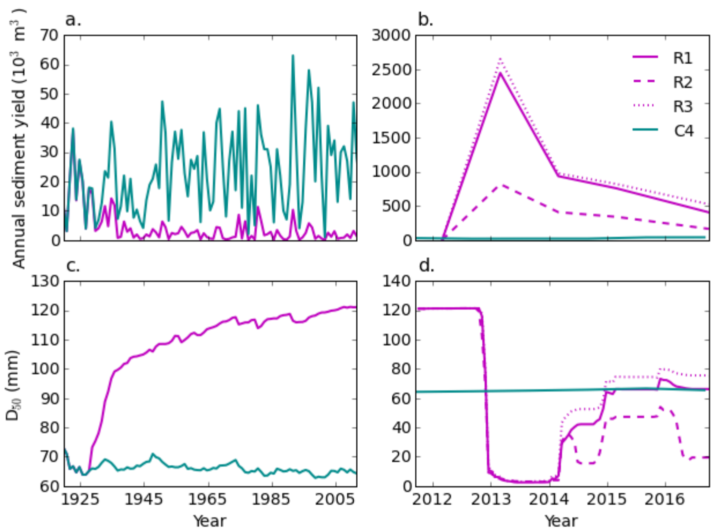

Figure 3.9: Evolution of channel characteristics over time. Magenta series denote the simulations modeling the dams (R1-R3), while teal series represent the control run C4. a) annual sediment yield during the Pre-Glines and Pre-Removal periods, b) yield for the Post-Removal period, c) reach-average channel surface D_{50} for the Pre-Dam and Pre-Removal periods, and d) reach-average channel surface D_{50} for the Post-Removal period. Sediment yield is defined as the total sediment (suspended plus bedload) passing into the upstream end of the former Lake Aldwell reservoir.

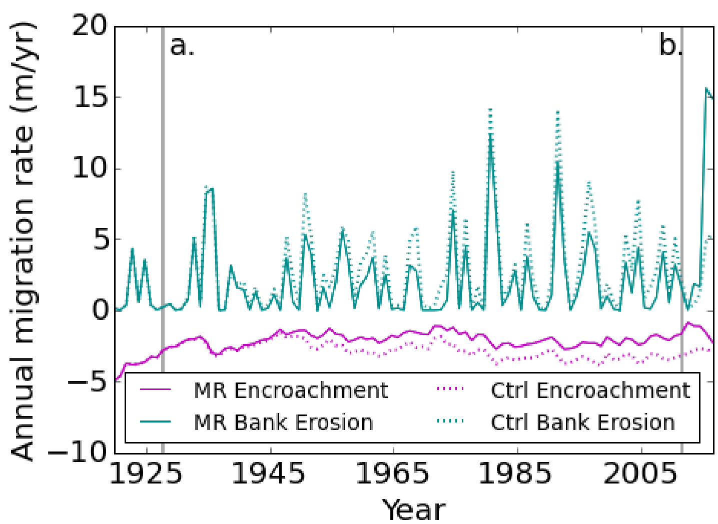

Figure 3.10: Average annual bank erosion and encroachment rates for simulations with and without dam emplacement/removal. Channel narrowing is represented as negative for display. Line a. delineates 1927, the year Glines Canyon Dam was closed, while line b. denotes the introduction of bedload sediment into the Middle River in late 2012.

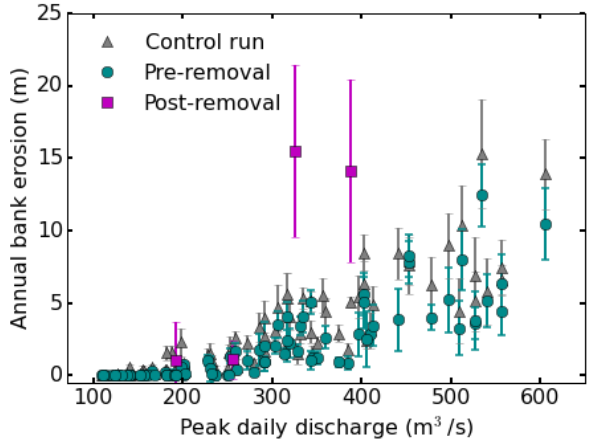

Figure 3.11: Total bank erosion compared to annual peak daily discharge for each water year. Data are calculated from the 1919-2016, 1927-2011, and 2012-2016 water years for the control, pre-removal period, post-removal period, respectively. Points represent the median bank erosion of all model cells, and error bars delineate the standard deviation. Run R3 is used for the dam simulations. The trends in the other runs are similar.

while avulsion accounts for about a quarter of new channel in C4.

Following dam removal , annual erosion rates increase to over 15 m/yr for R3, while they remain below 5 m/yr for C4 (Figure 3.10). For the first two years following release of the bed material sediment pulses, peak flows were lower than the annual flood. These flows appear to have been near the threshold of bank instability and the erosion rate is within the range expected for the low and at capacity sediment supply regime. (Figure 3.11). Rates are much higher for the next two years; spatially averaged bank erosion exceeds 12 m and is within the range expected for flows nearly twice as high in the supply-limited and at-capacity systems .

Averaged over the entire Post-Removal period, the bank erosion rates range between 2.5 and 11 m/yr, 1.25-5x higher than the control run (Figure 3.12b). In most reaches, rates are similar for R1, R2, and R3, suggesting that the proportion of bed material in the pulse has only a marginal impact on rates of bank erosion. However, the avulsion rate varies both longitudinally within individual runs and between them. For all simulations, avulsion rates are at a maximum at the first alluvial model cell downstream of the dam (river km 19.7) then decrease until about river km 16, after which the rates are negligible. The avulsion rate in R2 is over twice high as in the other two runs; avulsion accounts for nearly all the new channel formation in the upstream half of the channel in that run, while in R1 and R3 avulsion and bank erosion are roughly equally dominant.

Annually-averaged rates of channel narrowing (Figure 3.10) exhibit much less year-to-year variability than widening. In run C3, simulated annual narrowing rates range between 0 and 4 m/yr. Narrowing rates for the dammed and control run begin to diverge about 20 years after

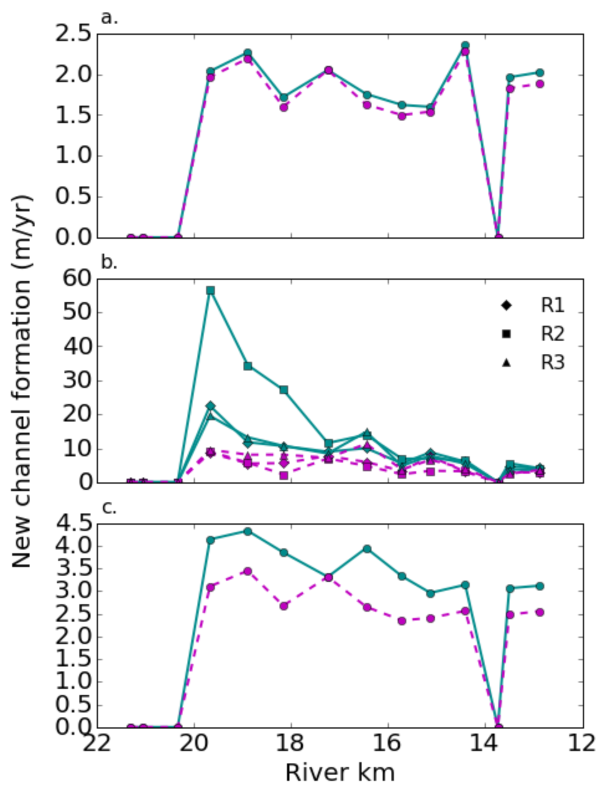

Figure 3.12: Temporally-averaged rates of new channel formation a) the Pre-Removal period b) the Post-Removal period, and c) the control simulation with sediment supplied at capacity (run C4). Solid teal series denote the total widening, while bank erosion rates are plotted in dashed magenta.

dam emplacement, with the former leveling off at a rate roughly 1 m/yr lower than the latter due to a narrower channel and less bar space for colonization. The narrowing rate increases following dam removal, but at a lower magnitude than bank erosion.

3.6 Discussion

The closure of Glines Canyon Dam in 1927 marked the beginning of a regime shift for the downstream reaches of Elwha River from a system that was connected to frequent sources of sediment to one that was sediment-starved and geomorphically stable. Following dam removal, the river has both responded to a large disturbance–in the form of a 16-million ton sediment pulse–and begun its transition into a new, more supply-rich regime. Our goal was to characterize these transitions by identifying the key spatial and temporal adjustments to channel stability. By using MAST-1D to simulate different sediment supply scenarios, we were able to compare the modeled evolution of Elwha River to a hypothetical scenario where sediment supply remained consistent through time to quantify the effect of supply on geomorphic behavior. Numerical modeling is also useful in that it can shed light on the relative importance of various channel behaviors which may be fundamentally different in process but lead to similar landform adjustments. Identifying areas where MAST-1D is successful in replicating field data and areas where it fails leads to insight on the range of geomorphic responses to variability in sediment supply.

3.6.1 MAST-1D confirmation–successes and failures

One fundamental assumption of MAST-1D (and other 1D models) is that channel evolution can be characterized by reach-average sediment fluxes that are calculated using channel-average hydraulics. This simplified representation appears adequate for the Pre-Removal period. The model predicted channel D_{50} values that are within the range of field data for all reaches except for a series of bedrock canyons immediately downstream of the dam (Figure 3.7). The canyons have slopes and channel morphologies outside of the range of what the sediment transport equation was designed for.

MAST-1D also successfully replicated pre-removal channel width (Figure 3.4) and, to a lesser extent, channel widening (Figure 3.6). Scatter between model and air photo data in the latter may be partially due to systematic error in the air photo measurements. Rivers are more likely to reoccupy portions of channel that were recently abandoned, meaning that over decadal timescales the net movement of the channel margin is less than the total movement (*Konrad*, 2012). Comparing channel margins between sets of aerial photographs generates the net channel change, while MAST-1D is only able to calculate the total change. Therefore, all else being equal, the difference between narrowing and widening for the two methods should increase over time. To test this, we plotted the average migration rate calculated via air photos as a function of the length of time between sequential air photos (Figure 3.13). The photos depict Elwha River upstream of Glines Canyon Dam and were chosen because the pattern of sediment supply in the study area (between the dams) is similar to that which we expect to observe from the systematic error. Details on these photos can be found in Appendix D. There appears to be a weak exponential relationship between the rate of channel movement and the length of time between air photos, especially with regards to channel widening. The significance of the relations cannot be tested because they are non-linear.

If this error is significant over the reach between the two dams, then MAST-1D should overpredict rates of widening and narrowing compared to the air photos during periods with long gaps between photos. Residuals of the data in Figure 3.6 are plotted in Figure 3.14. They are exclusively negative for air photo measurements spanning four years or more, as would be expected if channel and floodplain deposits reoccupied their former territory between air photos. However, there is no relation for photos taken fewer than four years apart. While using rates of channel change calculated from aerial photography to calibrate MAST-1D probably introduces systematic error, it is likely small in comparison to the uncertainty related to characterizing sediment supply.

MAST-1D replicated channel characteristics in the Post-Removal period with limited success. Our air photo analysis shows that Elwha River widened in two ways following the initial

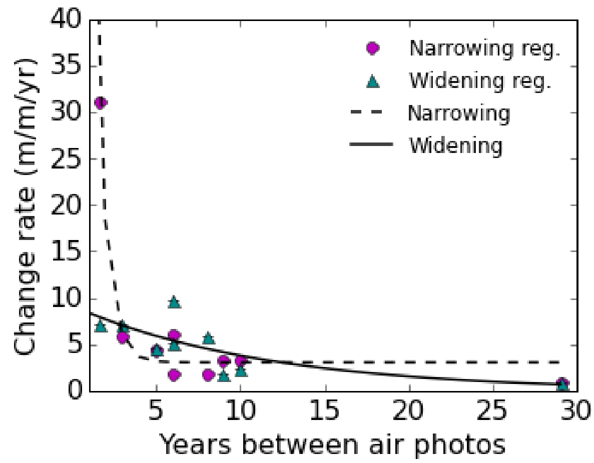

Figure 3.13: Annual rates of channel widening and narrowing plotted against the length of time between air photo pairs. Markers show the mean rate for all model cells/reaches and error bars mark the standard deviation. Regression lines were fitted with least-squares non-linear regression to the mean values.

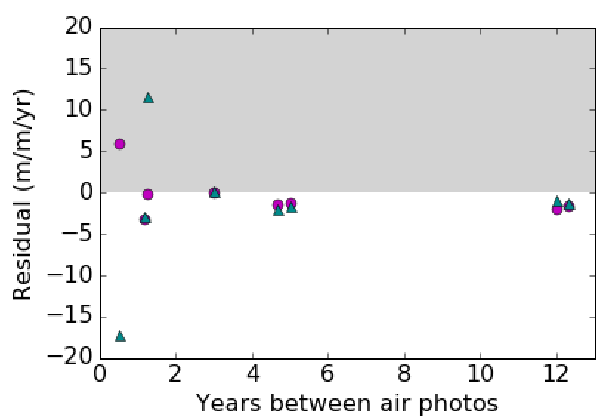

Figure 3.14: Residuals between modeled rates of channel widening and narrowing and those measured from air photos for the study area. Magenta circles represent channel narrowing, while teal triangles show widening.

pulse of bedload sediment released past Glines Canyon Dam in 2012 (Figure 3.5). Aggradation in the main channel caused flow and sediment to be diverted into floodplain channels, reactivating them (*East et al.*, 2015). Then, significant bank erosion occurred following low-moderate flood events in 2014-2015. Most channel widening–both via floodplain activation and bank erosion–occurred in the alluvial reaches in the upstream half of the study area (river kms 17-20). While width increased 10-20 m downstream of river km 17 (and about 60 m just upstream of the Lake Aldwell delta), the channel remained primarily single-threaded. MAST-1D captures the correct spatial pattern. The equivalent of floodplain activation in the model is avulsion. It is initiated by the same process–channel aggradation–although in MAST-1D, avulsion does not immediately lead to net width change, because the assumption is made that activation of floodplain surfaces leads to an equal amount of channel abandonment. In the field, post-removal floodplain activation was not necessarily accompanied by an equal rate of channel abandonment. For the most part, channel width five years after removal was initiated is predicted correctly (Figure 3.4), although the contribution of bank erosion to channel widening is overestimated in reaches with significant floodplain channel reactivation.

The model performs poorly in two places. The first is at river km 13, where MAST-1D overpredicts width by an order of 2. The reach is just upstream of a bedrock canyon, and a small part of its outer bend flows adjacent to a bedrock outcrop. This may have limited bank erosion. The model also fails near river km 18 where sinuosity increased following dam removal.

Reachwide, MAST-1D overpredicts the total amount of post-removal widening up to 2016 and fails to capture the timing (hence the scatter in Figure 3.6). It also underestimates the ability of Elwha River to export the pulse of sediment out of the system, leading to levels of system storage that are too high (Figure 3.8) and a grain size distribution slightly too fine in the upstream upstream portion of the channel (Figure 3.7). The severity of this failing depends on whether excess sediment stored in the modeled system is composed primarily of washload or bed material. In MAST-1D, suspended sediment cannot be deposited in the channel; any storage of washload material is constrained to the floodplain overbank zone. As the floodplain reservior is very large, it should be able to sequester the excess sediment without having a significant impact on modeled rates of channel change. Underestimating the competence of the channel to evacuate bed material may have a large impact on the modeled measures of stability. Channel storage leads to aggradation, and thus more avulsion. Finer sediment in the channel would also lead to increased sediment mobility on the near-bank (*Wilcock and Crowe*, 2003), presumably increasing bank erosion. These processes may partially explain the overestimation of widening presented in Figure 3.6.

Part of the reason for the discrepancy between modeled and measured storage may be because the sediment transport equation we selected (*Gaeuman et al.*, 2009) was calibrated to a reach downstream from a dam, and may be ill-equipped to deal with large sand loads. It is also possible that cross-section variability not accounted for in MAST-1D impacts post-removal evolution. The model does not account for the influence of channel morphology, which will have a first-order impact on sediment transport dynamics. Flow concentration in the thalweg will locally increase the sediment transport rate and may increase the total competence of the channel. *Ferguson* (2003) estimates that gravel bed rivers with one or more deep thalwegs may have transport rates at least five times higher than rectangular channels because of the non-linear relationship between shear stress and sediment transport rate. Flow concentration along thalwegs will also increase shear stress along the channel margin, leading higher rates of bank erosion. This effect is enhanced by deposition of bars on the opposite bank. In fact, part of the reason MAST-1D underestimates grain size several years after dam removal may be because it does not account for the role that channel morphology plays in partitioning sediment into coarse patches on bar heads and in the thalweg and fine patches on bar tails.

It is more likely that the discrepancy between modeled and measured storage is due to an inadequate representation of sediment supply at the upstream boundary condition. The primary source of error in our model is due to the large uncertainty surrounding the grain size of sediment supplied from Lake Mills. *Randle et al.* (2015) estimated that 71% of the material evacuated from the former Lake Mills was sand size or larger between 2012 and 2013. However, it is unclear how much of the sand traveled in suspension. Our simulations are very sensitive to the partitioning of supply between the bed and the suspended loads because the former is more likely to end up stored within the system. The results presented in Figure 3.8 suggest that most material traveled in suspension; run R3, for which we assumed that 84% of the total load is suspended, matched the field data best. In fact, if we assume that most sediment stored in the mainstem and floodplain channels is composed of bed material, then R3 replicates the system quite well; bed material storage is only slightly higher than the range of variability in the field data.

The error bars around the field data presented in Figure 3.8 may underestimate the actual uncertainty regarding sediment storage in the study area. *Warrick et al.* (2015) used the reach storage analysis performed by *East et al.* (2015), among other data, to compile a sediment budget for Elwha River between 2011 and 2013. They found a 1.7 Mt disparity between measurements of sediment stored between Glines Canyon and Elwha Dams (the *East et al.* (2015) data) and calculations of storage for the same area derived from DEM differencing estimates (for incoming supply from the reservoir) and sediment monitoring stations (for incoming flux upstream of Glines Canyon dam and outgoing flux downstream of the dams). Sediment flux out of the study area as calculated using the *East et al.* (2015) data is 40% higher than measured at the downstream gauge. A new range of error reflecting this discrepancy is shaded in grey in Figure 3.15b. We assumed that it remained at 40% for all years. Total storage from R1 fits well within the range. *Warrick et al.* (2015) suggests that the discrepancy relates to error in data from the sediment monitoring stations rather than the *East et al.* (2015) data. Still, the possibility remains that at least part of the disparity between modeled and measured storage is due to underestimation of the latter.

To our knowledge, no data apart from that presented in *Randle et al.* (2015) exists regarding the caliber of sediment supplied to Elwha River downstream of Glines Canyon Dam. In order to assess the sensitivity of the model to the grain size distribution of the sediment supply, we re-ran simulation R1 with a slightly finer sediment pulse (hereafter termed 'Finer GSD'). The method described in Section 3.4.1 was used to determine the upstream boundary condition. However, instead of inputing the size distribution derived from bank material (Figure 3.3) into the sediment transport capacity calculation, we used the distribution from a bulk sample collected on a point bar head just upstream of the former Glines Canyon Dam (Figure 3.15a; also see Appendix C). The values for C_1 and C_2 input into Equation 4.2 were 44 and 17, respectively. The fractions of sand and fine gravel supplied to the system was similar for 'Finer GSD' and

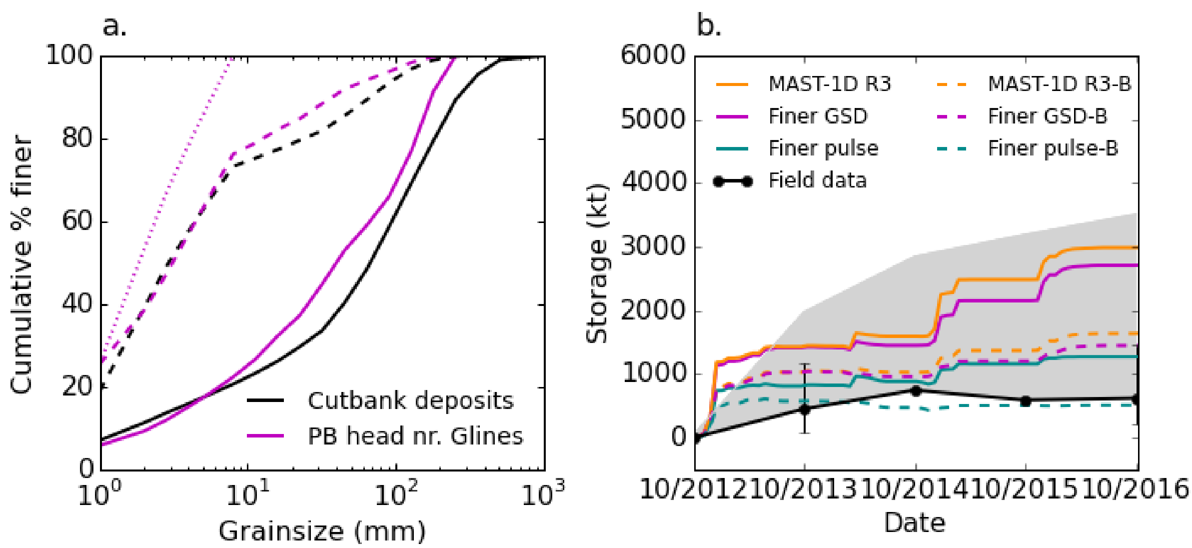

Figure 3.15: Impact of sediment supply caliber on storage within the study area. a. Subsurface grain size distribution for the composite cutbank sample (black solid line) and sample of a point bar head immediately upstream of the Glines Canyon Dam collected in September 2015 (solid magenta line). Dotted lines represent the time-averaged GSD of upstream sediment supply. The dotted black line refers to model run R3, the dotted magenta line to run 'Finer GSD' and the dashed magenta line to 'Finer pulse.' b. Sediment storage. 'Finer GSD' represents a run that was identical to R3, except a finer grain size distribution was used to calibrate the sediment pulse. 'Finer pulse' is similar to the 'Finer GSD' run, except the grainsize distribution of the upstream boundary condition was truncated at 8 mm for the entire post-removal period, instead of just the first year. See Figure 3.8 and the text for further details.

R3, but the fractions of coarse gravel and cobble in the former were slightly finer (Figure 3.15a). This difference between the two runs is marginal in terms of channel storage (Figure 3.15b). However, if we assume that the sediment load for 'Finer GSD' remains truncated at 8 mm (and C_1 is used in Equation 4.2 for the entire duration of the run), then the temporal pattern of bed material storage closely resembles that of the field data. This seems to suggest that, at least for the first five years following dam removal, bed material evacuated from the former Lake Mills reservoir was primarily composed of sand and fine gravel, although cobble-size chunks of concrete from Glines Canyon Dam were observed throughout the study area. Constraining upstream sediment supply is crucial for determining whether our sediment flux calculations are reliable.

Another impediment to modeling width change on decadal timescales appears to be the lack of a reliable, simple framework for characterizing vegetation dynamics. For MAST-1D, the assumption was made that narrowing occurred at low shear stresses. While the overall timescale of response to the emplacement of Glines Canyon Dam seems reasonable compared to the response time of other systems (see below), the narrowing function was not able to replicate rates of vegetation encroachment measured from the aerial photographs (Figure 3.6).

3.6.2 Impact of sediment supply on channel stability

Bank erosion and avulsion

The MAST-1D modeling suggests that upstream sediment supply has a first-order impact on channel stability. Rates of both bank erosion and avulsion were lower in the runs simulating dam emplacement compared to the control run (Figures 3.11 and 3.12). A coarsening of the bed texture during the Pre-Removal period (Figure 3.9c) reduces the mobility of near-bank channel sediment, so that the armor layer protecting bank toe deposits are less likely to be broken and that, if removed, the flow is not able to move as much sediment away from the bank. This means that large flow events contribute to less bank erosion (Figure 3.10). While this response is conditioned by the way bank erosion is characterized in the model, *Konrad et al.* (2011) made a similar observation while analyzing aerial photos taken before and after emplacement of a dam on Green River. They found that the discharges that best correlated with floodplain turnover increased following emplacement of the dam and suggested that higher flows were necessary to destabilize the banks because the bed had armored. However, damming on the Green River led to a reduction in peak flows, which *Konrad et al.* (2011) suggest were more important in reducing migration rates than armoring. The results depicted in Figure 3.10 suggest that a reduction in bank erosion can occur even when the hydrograph undergoes minimal alteration.

Sediment starvation also lowers the magnitude of channel deposition, which decreases the frequency of avulsion (Figure 3.12). Since new channels act as a source of sediment supply, a reduction in avulsion further decreases the amount of available sediment to the reach. Our modeling suggests that emplacement of Glines Canyon Dam led to increased channel stability on Elwha River by armoring the channel (therefore leading to lower mobility in the near-bank region) and by reducing the occurrence of destabilizing depositional features in the channel. Both of these processes act as a positive feedback, because they further reduce sediment supply from the floodplain. Our findings complement those of *Draut et al.* (2011), who observed that Elwha River showed little geomorphic response just downstream of the Elwha Dam to a 40 year flood in 2007, even though the same flood led to significant channel change both upstream of both dams and near the river mouth, where till bluffs on the channel margins act as an additional source of sediment supply.

The relationship between sediment supply and channel widening is less straightforward during the Post-Removal period. The pulse of sediment reduced grainsize (Figure 3.9), increasing the mobility of the near-bank region (Figure 3.11 and leading to channel widening (Figure 3.4). However, as discussed above, the processes by which this occurred are more complicated than can be explained by reach-wide patterns of channel mobility and deposition, and they are highly sensitive to the upstream boundary conditions. Our modeling suggests that the river is most sensitive to incoming sediment supply on the alluvial reaches closest to the dam (Figure 3.12). While comparable increases in rates of bank erosion were experienced throughout the study channel, the amount of avulsed channel increased with proximity to the dam. It was in the upstream half of the study area that the runs R1-R3 differed most; the higher the supply of bedload, the more avulsion that occurred. This suggests that the reaches closest to the dam act as the primary sinks for excess bed material sediment. Consistent deposition will lead to more avulsion but also keep bank heights relatively low, so that flooding is more frequent. This partitioning of shear stress between the channel and floodplain further decreases the transport capacity of the channel, acting as a positive feedback mechanism that encourages more deposition.

The proximity of alluvial channel reaches to the source of the sediment pulse likely impacts the influence of the pulse on channel stability. Of particular importance, as suggested by Figure 3.12, is the presence of active floodplain surfaces accessible via avulsion, which can act as loci of deposition. This may partially explain why the response of the banks to dam removals has been less noticeable (or not mentioned) on other mountain rivers. Bank erosion was not reported on the White Salmon River up to two years following removal of Condit Dam (*Wilcox et al.*, 2014) or on the Sandy River after Marmot Dam was removed (*Major et al.*, 2012). Both of these rivers flow through at least 3 km of bedrock canyon, which may have acted as a buffer to the initial sediment pulse. Elwha River flows through broad alluvial valleys within 2 km of the dam.

Vegetation encroachment

Modeled rates of channel narrowing are not as sensitive to sediment supply or decadal-scale hydrologic variability as rates of bank erosion. During the Pre-Removal period, the modeled narrowing rate gradually lowered, eventually stabilizing after about two or three decades (Figure 3.10). It did not begin to significantly diverge from the control run until a couple decades after dam emplacement. Drought in the 1930s may have been the primary cause of channel narrowing during this period. It is also possible that the model is responding to the initial condition. While there is scant data on channel margins for this period along Elwha River, evidence from other rivers suggests they narrow on a similar timescale. *Williams and Wolman* (1984) found that channels experiencing narrowing following dam emplacement tended to adjust after a few decades, although they found that most change occurred within the first decade. *Merritt and Cooper* (2000) similarly found that the initial width adjustment took about a decade. The difference between these studies and Elwha River is that the reductions in channel width in the latter were caused mainly by a temporary *increase* in the rate of vegetation encroachment due to a reduction in peak flows, which left more channel surface area available for colonization. The rate of vegetation encroachment *decreases* in our simulations as the total amount of point bar available for colonization decreases. This suggests that channel width change on Elwha River, which did not experience major flow alteration, was driven more by stabilization or destabilization of the eroding banks than by any major change in vegetation dynamics.

That being said, MAST-1D is not particularly successful in reproducing the rates of vegetation encroachment observed in air photos for the study reach (Figure 3.6a). The model assumes that channel narrowing occurs solely as a result of low shear stress, which is contradicted by a number of studies (e.g. *Bertoldi et al.*, 2009; *Camporeale et al.*, 2013; *Perona et al.*, 2009). One option is to ignore the dependence of vegetation growth on discharge and set channel narrowing as a linear function of available bar space, the approach taken by *Davidson* (2016) and *Konrad* (2012). However, this ignores the importance of flow variability–particularly the ability of low-moderate flood events to scour fresh vegetation (*Perona et al.*, 2012). Perhaps stochastic approaches, such as that adopted by *Camporeale and Ridolfi* (2007) can prove useful. In addition, MAST-1D (as well as nearly all bed evolution models) fail to consider the importance of in-channel wood, whose distribution impacts bar stability, seedling germination, and avulsion.

3.7 Conclusion

Decadal-scale numerical modeling of Elwha River demonstrates the impact of sediment supply disturbances imposed by the emplacement and removal of Glines Canyon Dam on channel stability, which we characterize in terms of bank erosion and avulsion. We have shown that the reduction in bed mobility and channel deposition caused by sediment starvation can explain the reach-scale increase in channel stability following emplacement of the dam. It is clear that the sediment pulse following dam removal led to channel instability, which manifested itself in increases in width and avulsion. But the geomorphic processes responsible for the increase in instability are more complex than those for the decrease. Local effects of channel morphology on the flow field likely play just as large a role in initiating bank erosion and avulsion as reach-wide patterns of bed mobility and channel storage.

Dam removal is becoming an increasingly popular form of river restoration. Decadal-scale numerical experiments of dam-influenced systems like Elwha River offer valuable insight on how to interpret geomorphic adjustments following large-scale anthropogenic disturbances and can identify missing pieces of the puzzle. Our modeling efforts have suggested that quantifying the caliber of sediment supply, and how it evolves over time, should be prioritized, as uncertainty related to sediment mobility precluded us from explaining observed patterns in sediment yield. In addition, while our ability to predict bank erosion on the reach scale is improving, much work is still needed to successfully quantify vegetation processes. On a whole, this study demonstrates the importance of considering the impact of sediment supply on lateral exchange processes, particularly on decadal timescales.

Chapter 4

Elwha in the 21st century: can we use the past to predict the future?

4.1 Summary

The question of whether or not Elwha River, and other medium-large streams undergoing dam removal, will evolve to resemble 20th century rivers not affected by direct anthropogenic alteration is relevant to water resource managers. We consider two questions: how will Elwha River respond to the pulse of sediment following dam removal on decadal timescales? and is it appropriate to assume hydrologic stationarity in light of decadal-scale climatic variability and ongoing climate change?

We present a brief literature review of decadal-scale climatic and sediment supply regimes in the Pacific Northwest to put Elwha River in context. Elwha is a rainfall-dominated hybrid stream with a secondary nival peak that varies in strength over time. Three large-scale climate phases have been identified in Elwha River discharge data between 1925 and 2016 that align well with phases of the Pacific Decadal Oscillation and with regional trends in flood magnitude. Phase 1, which lasts between 1925 and 1946, is characterized by low annual water yields and flood events. During Phase 2 (1947-1976), abundant precipitation and cool temperatures lead to a hydrologic regime characterized by high overall water yield and a strong snowmelt period in the spring. In Period 3 (1977-2016), the strength of the nival period decreases and overall water yield decreases, with a concurrent increase in the magnitude of flood events. Pacific Northwest rivers have high sediment loads due to abundant supply from uplifting mountains, relict glacial sediments, and, locally, extensive floodplains. In high-order trunk streams, supply can be considered primarily continuous, but high-magnitude events may release pulses into the system.

We use a Monte Carlo modeling approach to explore how dam removal and hydrologic regimes affect sediment transport and channel stability over the course of decades. Simulations with sediment supply regimes representing dam emplacement and removal are com-

pared to model runs in which sediment was supplied at capacity. While the channel grainsize of the post-removal channel recovered within a few decades, channel width and migration rate were significantly higher than the capacity run because the pulse of sediment released during the dam removal deposited in the floodplain, creating a fine sediment reservoir that was more easily erodible. Both sediment transport and channel stability were sensitive to climate, with Period 3 being more flood-driven than Periods 1 and 2. Channel stability is linked to the strength of the snowmelt season. In hybrid streams with abundant sediment supply and coarse banks, nival flows are able to efficiently transport sediment without leading to bank instability. With declining snowpack projected for the future, we expect the strength of the nival flow to decrease on Elwha River, making it even more laterally unstable and flood-driven. Using channel measurements from regional rivers dating to the 20th century will likely underestimate future channel width and migration.

4.2 Introduction

In many resource management and restoration projects, it is necessary to predict future sediment loads and bank stability in order to plan for flood and erosion risk and to maintain ecosystem health. Often, projects involve catchments in which the sediment supply and/or the flow regime are subject to anthropogenic alteration, so that the previous sediment transport regime will not be a good predictor of future behavior. Elwha River represents one such case. After almost 100 years of sediment starvation following emplacement of Glines Canyon Dam, more than 9 million tons of sediment were released during the largest dam removal in history (*Warrick et al.*, 2015). One of the important questions–both on Elwha River and for other dam removal projects–is how long the pulse of sediment will affect channel dynamics.

Analysis of recent medium to large scale dam removals in the Pacific Northwest seem to suggest that the majority of reservoir sediment can be evacuated without extreme aggradation downstream. The White Salmon River, Washington aggraded when Condit dam was removed, but the channel subsequently incised nearly to its pre-removal elevation within 15 days (*Wilcox et al.*, 2014). Aggradation downstream of Sandy River in Oregon was confined to the first 2 km downstream of Marmot Dam, and deposition elsewhere was limited primarily to pool-filling and bar accretion (*Major et al.*, 2012). Accumulation was also limited to pools along the Rogue River, Oregon, following removal of the Savage Rapids Dam (*Bountry et al.*, 2013). In the latter two cases, at least half of the reservoir sediment was evacuated during the year following the removal, even though no peak flow events reached the 2-yr recurrence interval. This has led *Major et al.* (2012) to suggest that the sequencing of flow events does not have a significant effect on the evolution of the reservoir, which is largely driven by slope. Indeed, based on elevation measurements taken on the channel thalweg, Elwha River recovered from the initial pulse of sediment within two years, despite abnormally low peak flows during the dam removal (*East et al.*, 2015).

However, on larger rivers with active floodplains, there is evidence that sediment pulses travel more slowly. For example, *Czuba et al.* (2012) suggests that a pulse of sediment originating from a series of rockfalls and debris avalanches on Mt. Rainier in 1963 is still causing aggradation along the White River in Washington. Since dam removal (especially on medium to large streams) is a recent restoration technique, the impact of former reservoir deposits on long-term sediment supply is still unclear.

In addition, predicting future channel behavior is confounded by climatic variability. Sediment transport is dependent on the amount of excess force applied to the river bed and banks by the flow. Therefore, determining the characteristic hydrologic regime is an essential step for assessing any fluvial system. It is common practice to use relations developed from flow frequency analyses to predict future discharge conditions. Frequency anaysis is often based on the assumption of stationarity, the condition in which the mean and variance of the data record are constant through time. The magnitude of annual peak flows are treated as independent events, when in reality persistent climatic cycles and trends influence the magnitude and frequency of floods.

Hydrologists acknowledge that flood frequency records are non-stationary on decadal timescales because of natural variability and global climate change (*Khaliq et al.*, 2006; *Milly et al.*, 2008; *Salas and Obeysekera*, 2014). Some researchers (e.g. *Kiem et al.*, 2003; *Cunderlik and Burn*, 2003; *Whitfield et al.*, 2010, c.f. *Villarini et al.*, 2009) warn against extrapolating records encompassing only a single climatic phase or using historical data to predict flow in future climates. However, others argue that stationarity is an acceptable assumption given the uncertainty in flow frequency analysis (e.g. *Serinaldi and Kilsby*, 2015). *Matalas* (1997) defends the usefulness of stationarity by noting that while the frequency of events is likely to change in the future, their magnitudes will not. But what are the implications of non-stationary flow frequencies on sediment transport regimes? While climate variability has been acknowledged in the context of bed material sediment transport (*McLean and Church*, 1999), we are not aware of a study that quantifies its effect, even though bed material transport affects channel morphology. *Ferrer-Boix and Hassan* (2015) have found that, in an experimental channel, the frequency of large discharge events affects the amount of fine sediment winnowing and thus the sediment transport rate. Flood frequencies also characterize the effective discharge, a geomorphologic metric often used in place of a full hydrograph (*Basso et al.*, 2015).

The purpose of this chapter is to speculate on whether Elwha River will evolve to resemble regional rivers not subject to direct anthropogenic disturbance. In order to do so, we must consider both the future sediment supply and flow regimes. This leads to two questions: what is the decadal-scale impact of dam removal on Elwha River? and does climatic variability have a large impact on the sediment transport regime and stability of the channel? Our approach is twofold. First, we contextualize Elwha River with a brief review of decadal-scale climate and sediment supply in the Pacific Northwest. We then use a Monte Carlo approach to examine the range of geomorphic responses to dam removal as compared to 'natural' sediment supply conditions. We impose observed 20th century climate regimes and reflect on whether future sediment transport and channel stability can adequately be predicted using past hydrologic data.

4.3 Elwha River in context: a review of the decadal-scale climatology and sediment supply regimes on Pacific Northwest rivers

4.3.1 Decadal-scale climate variability in the Pacific Northwest and its effects on hydrology

Climate in the Pacific Northwest (PNW) is driven largely by energy fluxes to and from the North Pacific Ocean. Much of the interannual variability is explained by the well-known El-Niño-Southern Oscillation (ENSO) phenomenon, where relatively warm, dry winters are characteristic of El Niño years and the opposite occur during La Niña events. A lower-frequency climatic pattern was identified in the 1990s (e.g. *Trenberth*, 1990; *Ebbesmeyer et al.*, 1991; *Hare and Francis*, 1995; *Zhang et al.*, 1997). *Mantua et al.* (1997) performed the Emperical Orthogonal Functions (EOF) technique on a North Pacific sea surface temperature anamoly (SSTA) dataset to indentify individual modes of variability. He found that the first principle component, which he termed the Pacific Decadal Oscillation (PDO), was correlated with trends in river discharge and salmon productivity in the Pacific Northwest and Alaska. Since then, the PDO has been used widely as a decadal-scale climatic metric and correlated with regional temperature, precipitation, runoff, and streamflow (for reviews, see *Mantua and Hare*, 2002, and *Whitfield et al.* 2010). Unlike ENSO, in which El Niños and La Niñas occur between periods of 'neutral' conditions, the PDO is a bimodal index that switches between two regimes. During positive phases, the PNW is warmer and drier, while a cooler, wetter climate is characteristic of negative phases. Only two full cycles have been identified over the modern period; negative phases lasted between the 1890s and 1925 and from 1947-1977, and positive phases lasted from 1925-1947 and 1977-~1998 (*Mantua and Hare*, 2002; *Zhang et al.*, 1997).

Over the last few years, it has become clear that the PDO signal captures elements of several coupled atmospheric and oceanic processes, comprising white noise from atmospheric forcing and red noise caused by ocean 'memory' (*Newman et al.*, 2003, 2016). The atmospheric forcing comes from stochastic fluctuations of the Aleutian Low, a persistent low pressure system around the convergence of the Polar and Ferrell Cells, and from atmospheric teleconnections of ENSO. A decadal periodicity emerges partially because these signals are reddened by the thermal inertia of the ocean and from the seasonal height variation of its mixed surface layer. In addition, ocean temperature and pressure are affected by fluctuations at the boundary of the major gyres in the North Pacific, which create oceanic Rossby waves that take a few years to a decade to cross the ocean (*Newman et al.*, 2016). Despite evidence of PDO-correlated regime shifts in many biophysical data, including marine ecosystems (*Mantua et al.*, 1997; *Litzow*, 2006), snowpack (*Mote*, 2003), drought (*McCabe et al.*, 2004) and streamflow (*Slaymaker*, 1972; *Mantua et al.*, 1997; *Pagano and Garen*, 2005; *Whitfield et al.*, 2010; *Fleming et al.*, 2007; *Bowling et al.*, 2000; *Moore*, 1996; *Reidy-Liermann et al.*, 2012), climate scientists are increasingly critical of the notion that phase shifts actually occur in the ocean. The PDO index only captures a portion of North Pacific variability (*Overland et al.*, 2008), and some believe that regime shifts are merely coincidences arising from representing multiple processes using a single metric (*Newman et al.*, 2016). *Overland et al.* (2008) argues that North Pacific variability is inherently random with a regime-like character and autocorrelation that cause multi-year deviations from a single century-long mean, but found that the 1945 and 1977 shifts are statistically significant.

Despite its flaws, the PDO index has been a useful tool for linking climate to decadal variability in streamflow. Temperature appears to be the most important determinant of discharge patterns during the winter and in low-elevation mountain basins, with warmer periods resulting in less precipitation contributing to the snowpack (*Liu et al.*, 2013; *Mote*, 2006). *Moore* (1996) found that temperature was the primary control on discharge response to the Pacific/North American teleconnection pattern (which is highly correlated to the PDO); during strong (warm) phases of the PNA, there was significantly less snow-water equivalent, leading to more discharge during the winter and weaker spring freshets. The response of precipitation to PDO-captured processes varies more widely than temperature regionally but is relatively consistent on local scales, with the response of streams complicated by the interplay between glacial dynamics, land use patterns, and hydrologic regime (*Whitfield et al.*, 2010). *Fleming et al.* (2007) compared discharge patterns between different states of the PDO for many rivers in coastal northwest Washington and southwest British Columbia. They found that the effects of precipitation anomalies manifest most strongly during the freshet; in pluvial streams, negative PDO years experience more discharge in the winter than positive PDO periods, while in nival streams the signal is lagged until the snowmelt season. Hybrid streams are affected during both seasons and the effect on these systems is the largest, as they are more sensitive to snowpack fluctuations. In fact, Fleming and his collegues found that some pluvial streams became hybrid systems during the negative PDO because of the accumulation of snowpack at higher elevations.

A climatic regime shift occurred between 1976 and 1977, which resulted in the transition from a negative to positive PDO but also seemed to reflect different patterns of oceanic spatial and temporal variability. *Bond et al.* (2003) did principle component analysis on North Pacific SSTA data and found that since the late 1980s, the time series has been dominated by the second PC (termed the 'Victoria Pattern'), not the PDO (the first PC). Fish catch data from *Litzow* (2006) shows that, after 1976-77, marine ecosystems in the Gulf of Alaska had a spatio-temporal structure similar to that predicted by *Bond et al.* (2003). *Piechota et al.* (1997) found that the signature of ENSO events in streamflow records after 1976 are distinguishable from those before the regime shift, and *Hamlet and Lettenmaier* (2007) have suggested that climatic variability since around 1973 has led to increased variance in runoff and that these trends may

Table 4.1: Hydrological parameters for three climatic periods.

	Annual Yield (m^3/yr)	σ/μ	2-year flood* (m^3/s)
Period 1 (1925-1946)	$1.2*10^9$	$5.3*10^7$	310
Period 2 (1947-1976)	$1.5*10^9$	$4.1*10^7$	377
Period 3 (1977-2016)	$1.3*10^9$	$5.7*10^7$	480

σ Variance of annual water yield
μ Mean of annual water yield
*See Figure 4.3 for details on flood frequency analysis.

lead to higher flood risks.

Streamflow is also correlated to large-scale increases in temperature that are not (directly) related to the PDO. In general, hemispheric-scale hydrologic models show that snowpack has decreased with rising temperatures throughout the Western US since the early 20th century, albeit with some decadal fluctuations (*Mote et al.*, 2005). Principle component analysis on drought indices by *McCabe et al.* (2004) suggest that both the PDO and North American temperature explain variance during dry periods, corroborating model findings. In the PNW, both numerical modeling (*Hamlet and Lettenmaier*, 2007) and time series analysis (*Luce and Holden*, 2009; *Mote*, 2003) reveal that increasing temperatures since the mid-20th century have contributed to reduced spring snowpack, more runoff in the cool season, and lower discharges during the dry season. EOF analysis on outputs from Global Circulation Models (GCMs) with mid-range levels of greenhouse gas emissions suggest that an increase in SST will become the leading principle component in all regions of the North Pacific sometime within the first half of the 21st century (*Overland and Wang*, 2007). In the PNW, snowpack will become more sensitive to temperature, and April snowpack is expected to decrease up to 70% by the 2080s (*Elsner et al.*, 2010; *Mote*, 2006). Some lower-elevation nival streams are expected to transition to hybrid regimes, while other hybrid streams will likely become purely pluvial (*Reidy-Liermann et al.*, 2012).

Elwha River hydrology

Elwha River drains temperate rainforest on the north face of the Olympic Mountains. Most of the catchment is contained within Olympic National Park and is unaffected by land use change. Annual precipitation in the basin varies between ~5500 mm in the headwaters and ~1500 mm in the rainshadow at the mouth (*Munn et al.*, 1999). Snow is the primary form of precipitation during winter in the headwater areas, but precipitation quickly transitions to rain with declining elevation. As such, the river has a rainfall-dominated hybrid hydrologic regime with a bimodal hydrograph (*Reidy-Liermann et al.*, 2012). Peak flows range between ~130 and 1200 m^3/s and generally occur in late autumn or winter. A secondary runoff peak occurs during the spring snowmelt season. Mean discharge over the period of record (1896-2015) is 43 m^3/s.

Elwha River discharge patterns have been influenced by decadal-scale climatic variability

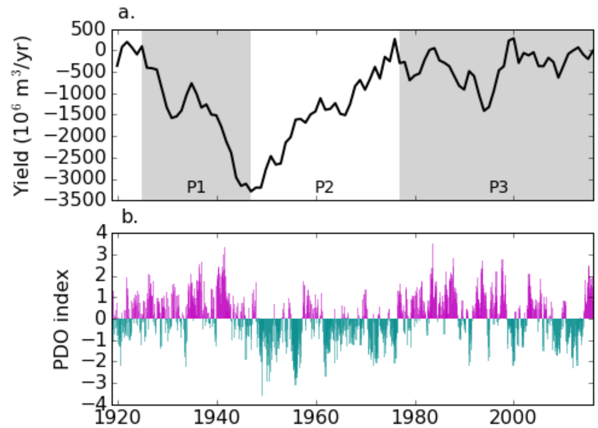

Figure 4.1: Metrics of hydrologic change. a. cumulative departure of Elwha River annual water yield from the mean. The three hydrologic periods listed in Table 4.1 are highlighted with shading. Yields were calculated from daily discharge data from USGS gauge 12045500 at McDonald Bridge (https://waterdata.usgs.gov/usa/nwis/uv?12045500). b. the monthly Pacific Decadal Oscillation index. Data was downloaded from the Joint Institute for the Study of the Atmosphere and Ocean (http://research.jisao.washington.edu/pdo/PDO.latest.txt)

(Table 4.1). The cumulative departure from the mean of annual water yield for the period of continuous daily recording, 1919-2016, is presented alongside the PDO index in Figure 4.1. Inflection points correlate well with regional shifts in the PDO, and the record can be divided into three periods. During Period 1, which aligns with the positive PDO phase between 1925 and 1946, the average annual yield was $1.2*10^9$ m^3, 11% lower than the 1925-2016 average. Water yields in the winter and nival seasons were roughly equal (Figure 4.2a). The flow regime abruptly shifted between Periods 1 and 2 as the PDO entered a negative phase (see the inflection point in Figure 4.1a). During this phase (1947-1976) average annual water yields were $1.5*10^9$ m^3, 8% higher than average. Much of the increased flow originated from snowmelt and was released in June (Figure 4.2b). After the climatic shift of 1976-1977, annual yields decreased as a whole (mean yield is $1.3*10^9$ m^3/s) but display greater interannual variability (Figure 4.1). Average monthly flow in Period 3 is similar to Period 2 during the winter, but nival flows are considerably lower (Figure 4.2c).

Over half of the annual peak flows occurred during December or January in all three climatic phases. But the timing and magnitude of flood events differ between the three periods. 10-14% of peak flow events occurred during the nival period (April-June) in Periods 1 and 2, while all peak events fell between October and March in Period 3. In addition, peak flow magnitude increases through time (Figure 4.3): the two-year flood is over 100 m^3/s higher in Period 3 than in Periods 1 and 2 (Table 4.1). Both annual peak flows and annual peak daily flows in Period 3 are statistically different from Periods 1 and 2 at the 90% confidence level using the students' t test (Period 3 is only different from Period 1 at the 95% level). Peak flows

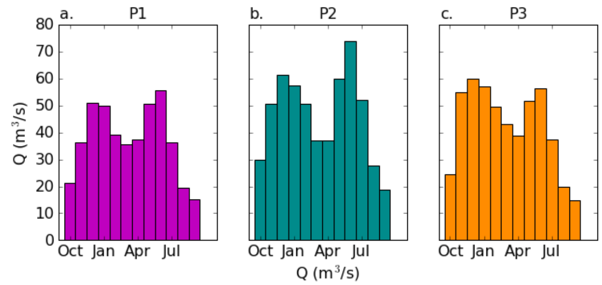

Figure 4.2: Monthly mean daily discharge for a. Period 1 (1925-1946), b. Period 2 (1946-1976), and c. Period 3 (1977-2016).

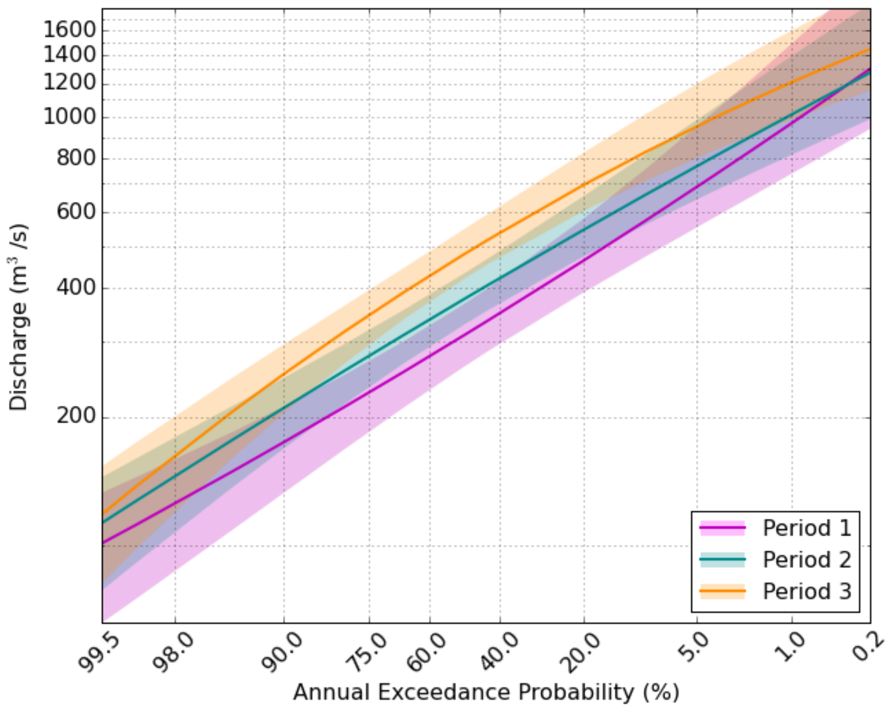

Figure 4.3: Flood frequency plot for the three hydrologic periods (refer to Table 4.1). Frequency analysis was done with the US Geological Survey 'PeakFQ' software (https://water.usgs.gov/software/PeakFQ/). A log-Pearson type III distribution was used to define the flood series. Further details on the methods are described in IACWD (1982).

during Periods 1 and 2 are not statistically different.

In summary, Elwha River is a hybrid stream with peak flows occuring primarily in winter but with a significant nival period that was slightly stronger before the 1976-1977 climatic shift. Period 1 (1925-1946) is characterized by low water yields and flood events. Discharges during Period 2 (1947-1976) reflect the negative phase of the PDO, and average annual water yields are greatest during this period. Flows following 1977 (Period 3) have been more variable with larger flood events than the other two periods.

4.3.2 Sediment supply of large Pacific Northwestern rivers draining mountainous catchments

The Pacific Northwest is adjacent to a subduction zone at the margin of the North American and Juan de Fuca plates. Most streams in the region originate in the tectonically-active Cascade, Olympic, or Coast mountain ranges. High denudation rates caused by uplift are expressed primarily in the frequency of debris flows, which are efficient in transporting sediment from areas of high relief into storage and eventual transport at lower elevations (*Montgomery and Brandon*, 2002). In addition, outwash from both Pleistocene-age and modern glaciers add to the high sediment loads in northern portions of the region and in basins with high relief. In many catchments, high-order (trunk) streams have been aggrading in the long term due to increased sediment supply from easily erodable volcanic material (*Czuba et al.*, 2012; *Guthrie et al.*, 2012; *Jordan and Slaymaker*, 1991). All of these conditions have created supply-rich streams where channels have low armor ratios and have evolved to transport large amounts of sediment (*Pfeiffer et al.*, 2017).

Sediment flux entering high-order streams has been filtered by storage zones within the catchments. *Benda and Dunne* (1997a,b) used numerical modeling to characterize the nature of sediment routing within channel networks in Oregon. They show that random pulses of sediment supplied to the stream network via debris flows are conditioned by differential rates of transport and storage. In high order streams, stochastic pulses originating throughout the basin merge so that supply is nearly continuous. Local storage zones also provide consistent sources of sediment in rivers with high rates of floodplain turnover (e.g. *Beechie et al.*, 2006; *O'Connor et al.*, 2003) or where rivers erode into bluffs composed of Pleistocene-age glacial landforms (*Draut et al.*, 2011). However, fluctuations in supply are noticable in trunk streams when disturbance events such as forest fires or heavy storm events affect large portions of the basin (*Benda and Dunne*, 1997a) or where single sediment pulses are high enough in magnitude to disrupt the system for a long period of time (*Czuba et al.*, 2012).

Large-scale fluctuations in sediment supply may also be correlated to climate variability. More chronic wet and stormy conditions or increases in the occurrence of forest fire could both increase the frequency of landslides and debris flows (*Benda and Dunne*, 1997a; *Cannon and DeGraff*, 2009), but differences in recharge rate may complicate the relationship (*Jakob et al.*, 2005). Long-term records of debris flows from the Alps show that their frequency has been sensitive to decadal-scale climate variability in the past, although future temperature and precipitation projections for the region favor increases in debris flow magnatude rather than frequency (*Stoffel et al.*, 2008, 2014). Increased flow and exposed sediment resulting from melting glaciers is another possible source, but *Czuba et al.* (2012) did not find a correlation between glacial retreat and sediment supply on Mt. Rainier. The influence of decadal-scale climate variability and change on sediment supply is still largely uncertain, and it is likely than any signals are masked by the episodic nature of sediment delivery in headwater areas. *Naik and Jay* (2011) and *Inman and Jenkins* (1999) have both found that suspended sediment loads during climatically cool periods were larger than during warm phases on the Columbia River and in California rivers, respectively. Both studies relied on sediment rating curves, so the signals reflect changes in discharge and may have little to do with sediment supply. However, in large, high order streams, sediment supply sources may be extensive enough that supply correlates more closely to discharge than in higher areas of the catchment.

Sediment supply on Elwha River

The 833 km^2 Elwha River basin drains the rugged northern slopes of the tectonically-active Olympic Mountains. Uplift occurs at a rate of 0.28 mm/yr (*Brandon et al.*, 1998), providing steep terrain susceptible to frequent landsliding and debris flows (*Montgomery and Brandon*, 2002). The basin is dissected by the Hurricane Ridge Fault, which separates the highly deformed Olympic Sedimentary Complex, containing metasedimentary rocks, from the Coast Range Terraine, which is composed primarily of basalt and sandstone (*Brandon et al.*, 1998; *Tabor and Cady*, 1978). Only a small portion of the basin is glaciated, and pro-glacial material likely acts as a negligible source of sediment. Elwha River is divided into a series of subbasins, each separated by steep bedrock canyons. Within each subbasin, the river flows within both narrow and broad floodplains, which act as continuous sources of sediment supply (except for localized reaches, where the channel flows against bedrock outcrops at the valley margins). In the lower portions of the valley, till, glacio-lacustrine, and outwash deposits underly bluffs ranging from a few to tens of meters high. These are significant sources of sediment in the localized reaches where they occur (*Draut et al.*, 2011).

Since Elwha River is a high order stream, and because supply from the actively migrating channel receives ample supply from the banks, it is likely that the supply rate relative to discharge is rather consistent. However, disturbance events can provide pulses of sediment. In 1967, a landslide dam breach several km upstream of Glines Canyon released a wave of sediment that deposited a 0.25 km^2 fan in the channel (*Tabor*, 1987). The influence of the deposit on modern sediment loads is unknown, although it was reworked locally for at least 15 years following the breach (*Acker et al.*, 2008). The time-averaged sediment supply rate has increased over the last three decades: *Bountry et al.* (2011) found that the mean annual sedimentation rate in the Lake Mills reservoir was 47% higher from 1994-2010 than from 1927-1994. Whether the increase is related to climate, either directly or indirectly, is unclear.

The largest disturbance to Elwha River's sediment supply regime was from the emplacement and removal of the Glines Canyon and Elwha Dams, which cut off supply to downstream reaches from the early 20th century until 2011. Between 2011 and 2013, 10.5 million tons of sediment were released from behind the dams (*Warrick et al.*, 2015). Terraces of a few to several meters remain in the former reservoirs. The deposits have become vegetated and more stable; however, they will likely act as a continuous source of sediment for decades to centuries.

Table 4.2: Monte Carlo simulation sets. Each set is comprised of 200 runs of 150 years.

Discharge scenario	Sediment supply scenario S1 (with dam)	S2 (at capacity)	S3 (episodic)
P1 (1925-1946)	S1-P1	S2-P1	S3-P1
P2 (1947-1976)	S1-P2	S2-P2	S3-P2
P3 (1977-2016)	S1-P3	S2-P3	S3-P3
Pall (1925-2016)	S1-Pall	S2-Pall	S3-Pall
P123 (cycles through P1-P3)	S1-P123	-	-

4.4 Elwha past and future: Monte Carlo simulations of channel evolution with varying sediment supply and climatic regimes

4.4.1 Methods

A numerical modeling campaign was designed to answer the two main questions of this study: 1) will the post-dam Elwha River evolve to the same state as it would if the dam never existed, and 2) in the context of geomorphic modeling, does an assumption of hydrologic stationarity adequately represent historical time periods with different mean climates? We adopt a Monte Carlo approach to simulate the range of possible river responses to different sediment supply and hydrologic regimes.

Channel evolution between Glines Canyon and Elwha Dams was modeled using MAST-1D. Verification of the model is presented in Chapter 3. In order to minimize computation time, we assume that the reach is fully alluvial and longitudinally homogenous. The model parameters can be found in Appendix B. We performed 13 sets of model runs, each comprised of 200 individual simulations spanning 150 years (1918-2068). To add stochasticity to the model, the daily discharge record was created by randomly sampling annual hydrographs from different climatic periods (see below). The sets are listed in Table 4.2.

Sediment supply scenarios

Three different sediment supply regimes are used (Figure 4.4). For each, the sediment transport capacity is calculated using a form of the *Wilcock and Crowe* (2003) equation modified for large, cobble-bedded streams by *Gaeuman et al.* (2009). Hydraulics are calculated assuming normal flow in a two-part cross-section that includes a rectangular channel and floodplain. The sediment supply is a function of the capacity:

$$Q_{s,i} = CQ_{c,i} \tag{4.1}$$

where $Q_{s,i}$ is the sediment supply for size class i, $Q_{c,i}$ is the sediment transport capacity for that class, and C is a supply modifier. The first scenario (S1) represents emplacement and removal of Glines Canyon Dam. Sediment supply is set at capacity ($C = 1$) for 9 years and then reduced

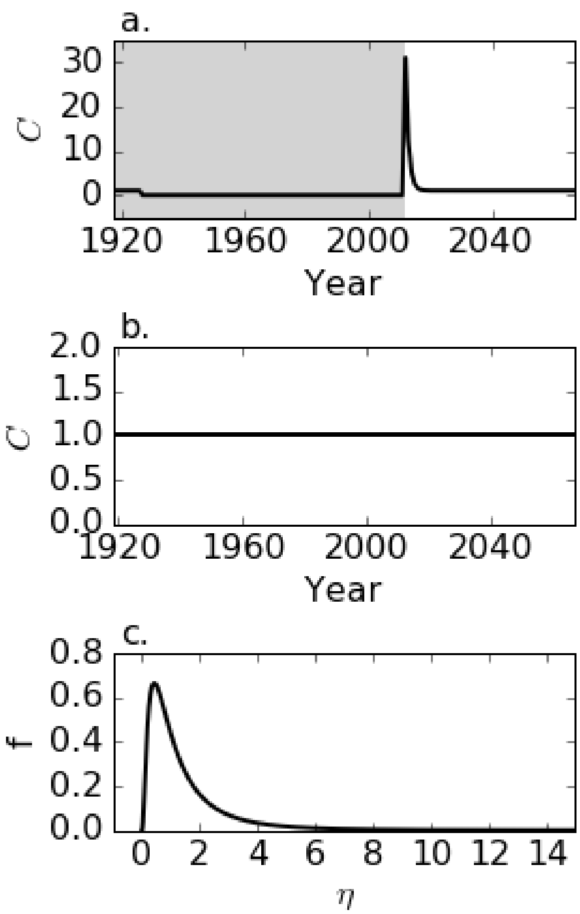

Figure 4.4: Sediment supply boundary conditions for the Monte Carlo simulations. a) S1. The supply coefficient C becomes zero following dam emplacement in 1927 (S1-D) and jumps to 30 before declining exponentially to simulate the pulse of post-removal bed material beginning in 2012 (S1-PD). b) S2. Constant feed; C remains at 1 throughout the run. c) S3. Stochastic sediment supply. The value of C is selected at random from a positively-skewed log-normal distribution with a mean value of 1.

to zero in 1927 to simulate emplacement of the dam. The pulse following removal is modeled using an exponential decay curve

$$Q_{s,i} = Q_{c,i}(1 + C_r e^{\frac{-t}{\lambda}}) \tag{4.2}$$

where t is the time in days since the removal, C_r = 30, and λ = 365 days. (Figure 4.4a). See Chapter 3 for a description of the calibration and grainsize distribution of the pulse.

For the second set of model runs (S2), sediment supply is set at capacity ($C = 1$, Figure 4.4b). These simulations represent evolution of Elwha River without influence from the dams. We are assuming that sediment is supplied at capacity. While this is probably reasonable given the decadal timescale of the study and since Elwha River is a high-order stream in a supply-rich basin (*Benda and Dunne*, 1997b; *Montgomery and Brandon*, 2002), we also perform a third set of runs (S3) where sediment is supplied episodically to see whether the mode of sediment delivery impacts channel evolution. For each discharge, the value of C is selected randomly from a log-normal distribution with a mean of 1 and standard deviation of 0.9 (Figure 4.4c). With this distribution, sediment is supplied below capacity most of the time, but pulses of sediment periodically pass through the system. This sediment supply scenario likely overestimates the period of time that the channel is sediment-starved but will provide an end-member case.

Discharge scenarios

To examine the impact of historic climate regimes on channel evolution, each sediment supply scenario was run with four different discharge regimes. The first three (P1-P3) correspond to the three periods outlined in Section 4.3.1. For each run, a discharge record is created using observed flow data from the USGS gauge at McDonald bridge. Water years within each period (i.e. 1925-1946 for P1, 1947-1976 for P2, and 1977-2016 for P3) are selected at random and composited to create a 150 year record. Flow sequences within each water year remain intact, so that the annual hydrograph is maintained. A fourth scenario, Pall, is run with water years selected from all three climatic periods (1925-2016). Pall represents the condition of hydrologic stationarity.

To examine the response time of the simulated channels to changes in climate regime, discharge scenario P123 was run with supply scenario S1 (with the dam). In P123, the climate state shifts over the course of the run. Modeled time was divided into three periods. For the first 29 modeled years (1918-1946), discharges were sampled from the water years occurring in P1. Discharges were extracted from P2 between 1947 and 1976. For the final 91 years (1977-2068), water years from P3 are used.

Geomorphic metrics

The effective discharge, bankfull discharge, and migration rate are used to quantify the modeled sediment transport regime and degree of channel stability. The effective discharge (Q_{eff}), introduced by *Wolman and Miller* (1960), is defined as the flow that, when integrated over long timescales, transports the most sediment. Wolman and Miller, as well as many others after them (e.g. *Andrews*, 2015; *Emmett and Wolman*, 2001; *Torizzo and Pitlick*, 2004), have found that the effective discharge typically occurs frequently and is less than or close to the bankfull discharge, suggesting that it is related to the channel-forming flow. However, others have found that plots of sediment transport against flow frequency tend to have a bimodal distribution–in other words, both frequent and more rare (recurrence intervals on the order of years-decades) flows are geomorphically important (e.g. *Lenzi et al.*, 2006; *Phillips*, 2002). To fully appreciate how the dominant flow responds to changes in the flow regime, the Q_{50} is also calculated. It is the discharge below which half of the duration-averaged sediment is transported (*Sichingabula*, 1999) and is a more useful metric than Q_{eff} when the frequency/transport relationship is

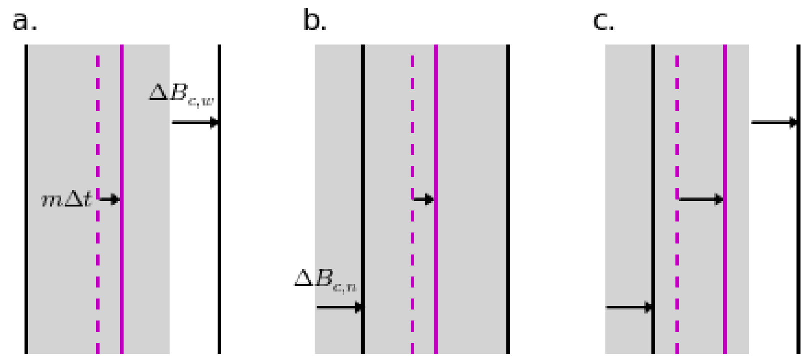

Figure 4.5: Schematic showing the relationship between the migration rate (m) and a. a widening channel, b. a narrowing channel, and c. a channel where widening and narrowing is occurring concurrently. The solid lines show the channel position and centerline at time t, while the shading and dotted line represent the channel at $t-1$.

bimodal. To calculate Q_{eff} and Q_{50}, discharge data must be binned. So as not to underestimate the importance of extreme flood events, we follow the method of *Hassan et al.* (2014) and choose bins that are the resolution of our discharge data (100 ft^3/s or 2.8 m^3/s).

To see how the Q_{50} relates to channel-forming conditions, it is also normalized by the bankfull discharge Q_b (*Emmett and Wolman*, 2001), which we calculate using the Manning Equation

$$Q_b = \frac{1}{n} A R^{2/3} S^{1/2} \tag{4.3}$$

where n is the Manning roughness coefficient, A is channel area, R is the hydraulic radius, and S is slope. Manning's n is calculated with a modified form of the Strickler relation that accounts for roughness from form drag and sinuosity

$$n = k_1(0.013 D^{1/6} + k_2) \tag{4.4}$$

where D is a characteristic grainsize which we set to $2D_{65}$, following *Wilcock et al.* (2009), k_1 is a sinuosity multiplier and k_2 is a form drag factor. Using a D_{65} of 112 mm (from the initial grainsize distribution) and setting k_1 to 1.15 and k_2 to 0.0066 yields an n value of 0.044, which is close to values measured on similar rivers in the field by *Barnes* (1967). We are assuming for these calculations that D is constant, but since it is taken to the 1/6 power in Equation 4.4, Q_b is not very sensitive to it.

We define the channel migration rate m as the lateral movement of the channel centerline over a defined period of time. Migration can occur as a result of channel widening, narrowing, or both (Figure 4.5). MAST-1D does not keep track of left and right banks. We assume that all widening occurs on one bank and all narrowing on the other. The migration rate is simply the average of movement from widening and narrowing:

$$m = 0.5\left(-\frac{\Delta B_{c,n}}{\Delta t} + \frac{\Delta B_{c,w}}{\Delta t}\right) \tag{4.5}$$

where $\frac{\Delta B_{c,n}}{\Delta t}$ is the rate of channel narrowing (which is negative by definition) and $\frac{\Delta B_{c,w}}{\Delta t}$ is the rate of widening.

To test whether or not geomorphic processes on Elwha River can be considered stationary despite changes in the governing climatic conditions, metrics of effective and bankfull discharge from runs with the three climatic periods (P1-P3) are each tested for equal central tendency with Pall using Welch's t-test.

4.4.2 Results

The results are divided into two parts. First, the results from S1-Pall and S2-Pall are presented to demonstrate the differences in channel evolution between dammed and constant sediment supply conditions. Then, we focus on the impact of climate on the effective discharge and migration rate for all sediment supply scenarios.

Evolution of dammed and at-capacity channel-floodplain systems

S1-Pall behaved differently from S2-Pall, both before and after the dam removal. Evolution of several key variables is presented in Figure 4.6. Following dam emplacement, both runs have similar width ranges for about 15 years, when the dammed channel begins to narrow at a faster rate (Figure 4.6a). By the time dam removal occurs, the two populations are nearly distinct. Following dam removal, channel widening occurs. While width for individual runs fluctuates based on the flow record, the median width for all runs stabilizes at just under 100 m after about 15 years. It never evolves back to the pre-disturbance condition (represented by the at capacity supply scenario); S2-Pall very gradually narrows, finally reaching a median width that is 30% lower than the post-dam channel.

The range of widths after 150 years is much wider for S1-Pall than for S2-Pall. Channel width is negatively correlated to the grainsize distribution of the post-removal floodplain (Figure 4.6c), which is in turn dependent on flow sequencing during the dam removal. The relationship between channel width, floodplain D_{50}, and flow sequencing is presented in Figure 4.7 for S1-Pall. Both parameters were averaged for each run from the years after 2040, for which the median of all runs is stable. 35% of the variability in channel width can be explained by the grainsize distribution of the floodplain ($p << 0.001$). The correlation of floodplain grainsize and channel width to geomorphically-significant flows over time is shown in Figure 4.7b. The y-axis shows the r^2 value for least-squares linear regression for channel width and floodplain D_{50} as functions of the cumulative volume of flow above 150 m^3/s. In other words, flows occuring between 2012 and 2013 were summed for 2013, flows occuring between 2012 and 2014 were summed for 2014, and so on so that at the end of the run in 2068, the

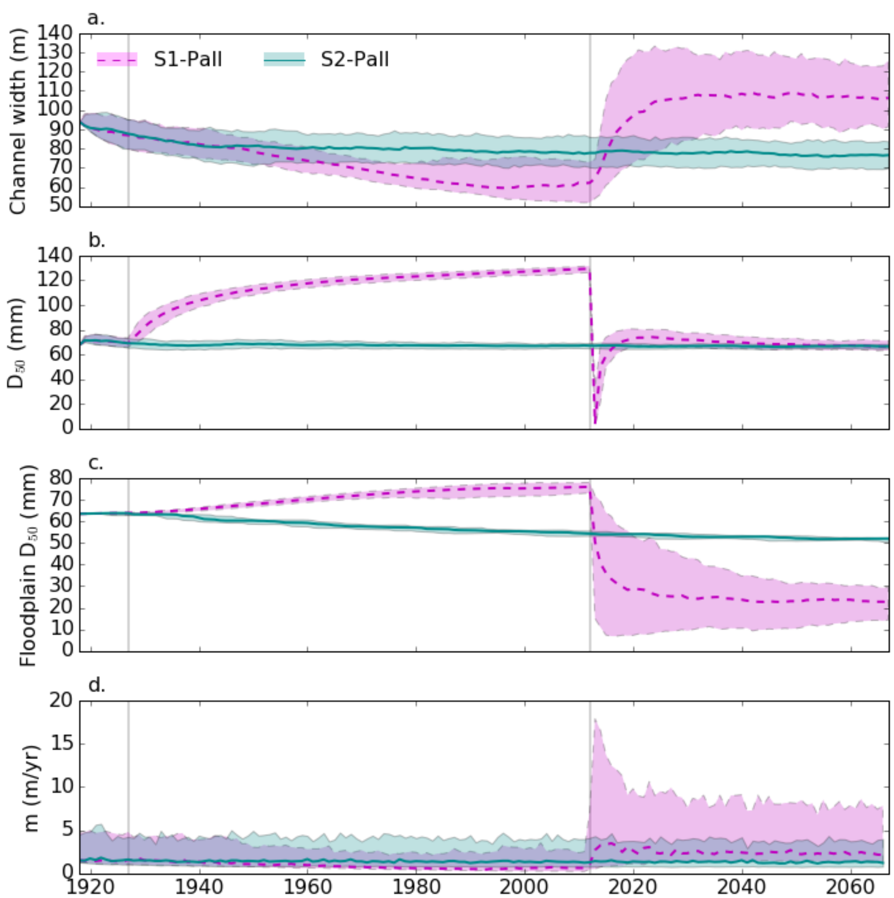

Figure 4.6: Evolution over time of the channel and floodplain for runs with dam emplacement/removal (S1-Pall) and sediment supplied at capacity (S2-Pall). The shading delineates the 5th-95th percentile of all 200 runs, while the line denotes the median. Grey horizontal lines delineate dam emplacement in 1927 and removal in 2012. a. channel width. b. channel D_{50}. c. floodplain D_{50}. d. channel migration rate.

regression is performed against all flows >150 m^3/s during the post-removal period. With a constant source of sediment (S2-Pall), the correlation between both channel width and floodplain grainsize increases as the regression considers more recent flows. When all >150 m^3/s flows between 2012 and 2068 are considered, they explain 30 and 50% of the variability in floodplain D_{50} and width, respectively. In contrast, the high flow events just after dam removal had a lasting impact on channel form for S1-Pall. The sequence of flows during the first two years following dam removal explain almost 70% of the variability in floodplain D_{50}. The correlation declines over time, and flows after 2030 have virtually no impact on floodplain sediment. The correlation between flow and channel width rises with increasingly recent flow history after 2015, but unlike in S2-Pall, channel width is more correlated to the two years following dam removal than it is to the following 30 years.

The channel migration rate is less correlated with floodplain grainsize (r^2 = 0.20, $p << .001$). Migration rates for the Monte Carlo simulations are similar for S1-Pall and S2-Pall,

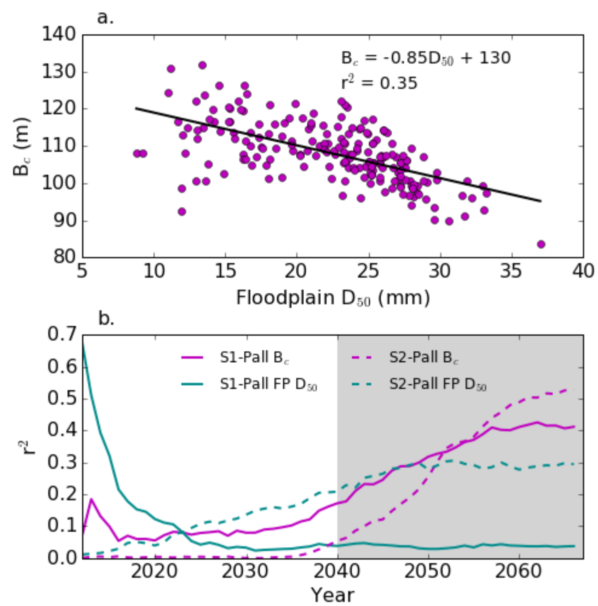

Figure 4.7: Correlation between floodplain D_{50}, channel width (B_c), and high flow events. a. Regression for channel width as a function of floodplain D_{50} for S1-Pall. Each point represents one model simulation. Channel width and floodplain D_{50} were both averaged over all nodes. Values for both variables are averaged for the period after 2040. b. Regression of channel width and floodplain (FP) D_{50} as a function of cumulative volume of flow >150 m^3/s. See text for details. Grey shading shows the period over which Bc and FP D_{50} were averaged.

although the range of values is lower during the dammed period and higher after the removal (Figure 4.6d). Unlike the floodplain, the grainsize of the channel (Figure 4.6b) recovered to the dam-free, constant supply state within 50 years after the removal.

Effect of climate on sediment transport and channel stability

Differences in the hydrologic regime led to unique regime conditions for all three climatic periods (Figure 4.8). P1, which has the lowest average annual water yield and peak flows (Table 4.1), has the lowest sediment yield and migration rate in all sediment supply scenarios. The channel is much more dynamic in P2; it has the highest annual sediment yield in all sediment supply scenarios except for the dammed period in S1, and its median migration rate is 10-35% higher than P1. Channels under the P3 climate regime experience the highest rates of lateral instability; the migration rate is nearly double that in P1. In addition, channels in P3 maintain a higher width/depth ratio than P1 and P2 (Figure 4.8i-l), although the ranges for all hydrology scenarios overlap quite a bit within each sediment supply scenario. The largest difference occurs in the sediment-starved post-dam channel, where over 75% of model runs in P3 had width-depth ratios higher than the other discharge groups. However, despite differences in lateral stability and sediment transport competence, bankfull discharges for the three periods

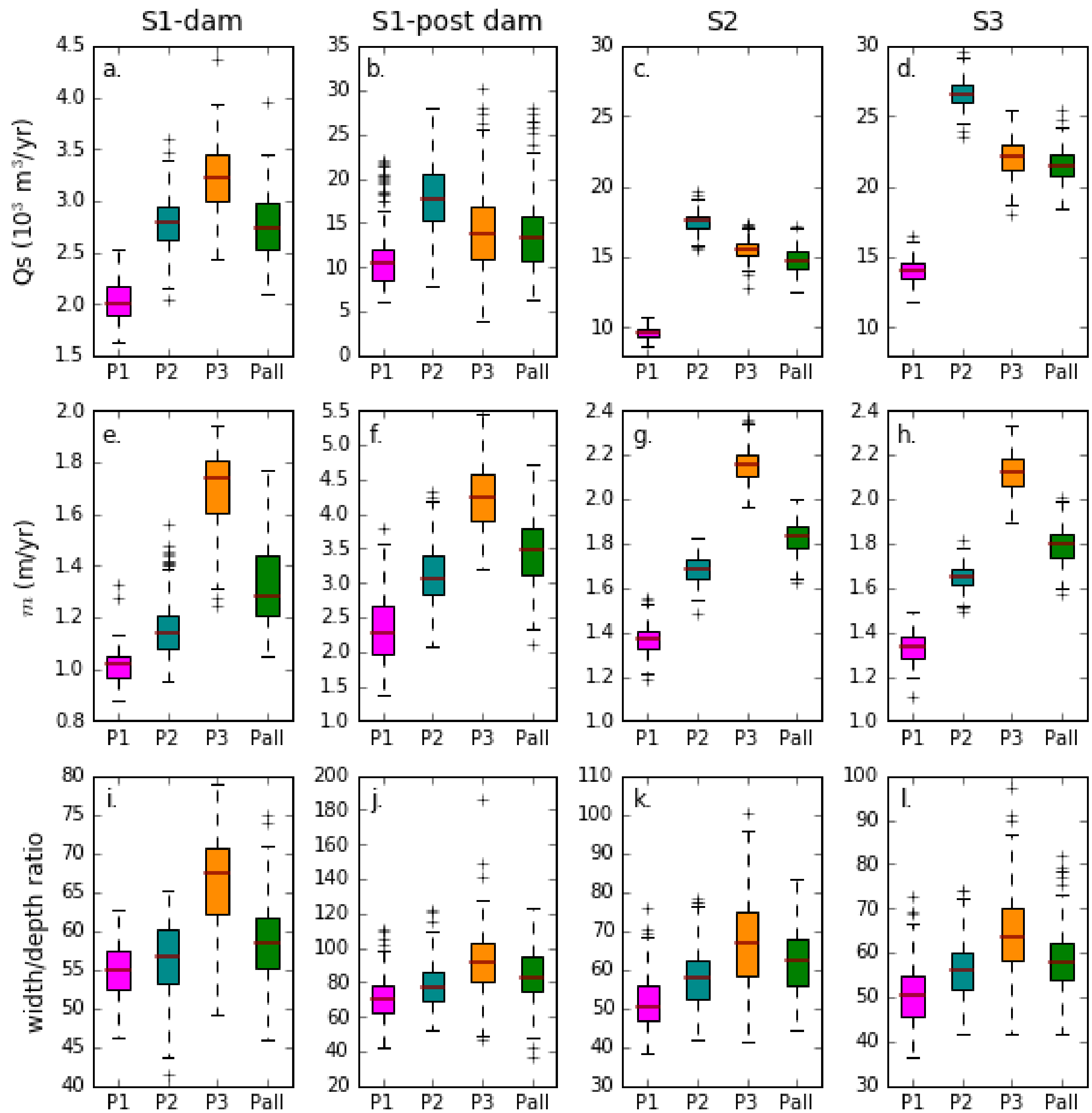

Figure 4.8: Geomorphic metrics as a function of sediment supply and hydrologic regime. Note the scale differences on the y-axis. Upper headings refer to the sediment supply regime: S1-dam is the pre-dam removal period (1919-2011) and S1-post dam is the post-removal period (2012-2068). For S2 and S3 (sediment supplied at capacity and episodically, respectively), the whole model period is used. a-d. Average annual sediment yield, e-h. Average annual channel migration rate. i-l. Channel width/depth ratio at the end of the modeled period.

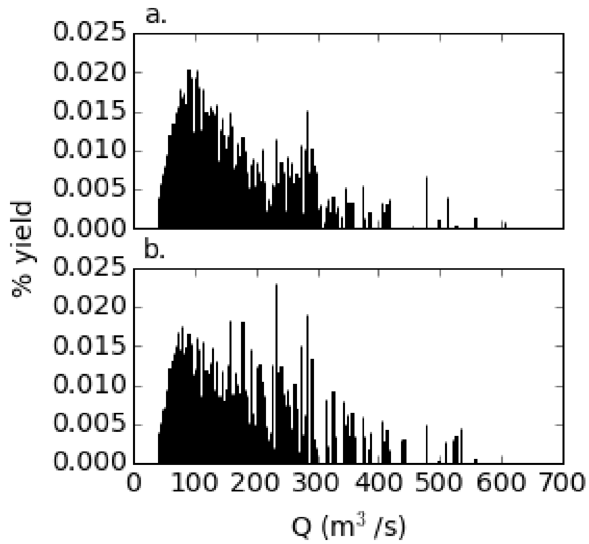

Figure 4.9: Examples of effective discharge plots with bimodal distributions. a. A single run from S3-Pall. Effective discharge is 103 m^3/s. b. A single run from S3-P3. Effective discharge is 231 m^3/s.

occur between 1-4 times per year (Figure 4.10). The ranges of bankfull recurrence intervals overlap for all climate periods in each sediment supply scenario except for the dammed period in S1 (based on a oneway ANOVA test, they are only statistically indistinguishable for S1-PD).

The relationship between discharge and cumulative decadal-scale transport in the MAST-1D simulations has a bimodal distribution as described by *Phillips* (2002). Examples of effective discharge plots from two simulations are presented in Figure 4.9. Much of the sediment is transported during flows of around 100 m^3/s, which occur on average around 18 times a year (Figure 4.10d). However, large peaks also occur at bankfull and flood discharges. In Figure 4.9a, the former peak is more dominant and the effective discharge is low. In Figure 4.9b a single flood flow bin transports the largest percentage of sediment, and the effective discharge only occurs about once a year, even though more sediment as a whole is transported during frequent events.

Metrics of effective discharge are presented in Table 4.3. Under undisturbed sediment supply conditions (S2 and S3), discharge/yield relations for most runs in P1 and P2 are similar to that presented in Figure 4.9a; the effective discharge is around 100 m^3/s and it occurs roughly 3-20 days per year (Figure 4.10). P2 has a slightly higher Q_{50} than P1, but the Q_{50}/Q_b ratio is nearly identical for both periods, with the Q_{50} occurring at about half bankfull flow. On the other hand, the sediment transport regime for P3 resembles that of Figure 4.9b. The effective discharge is over twice that of P1 and P2, and it has a recurrence interval of about 1 year. The Q_{50} for P3 represents conditions closer to bankfull than in the other two periods.

Since P1/P2 and P3 show distinct patterns of effective discharge, the simulation assuming

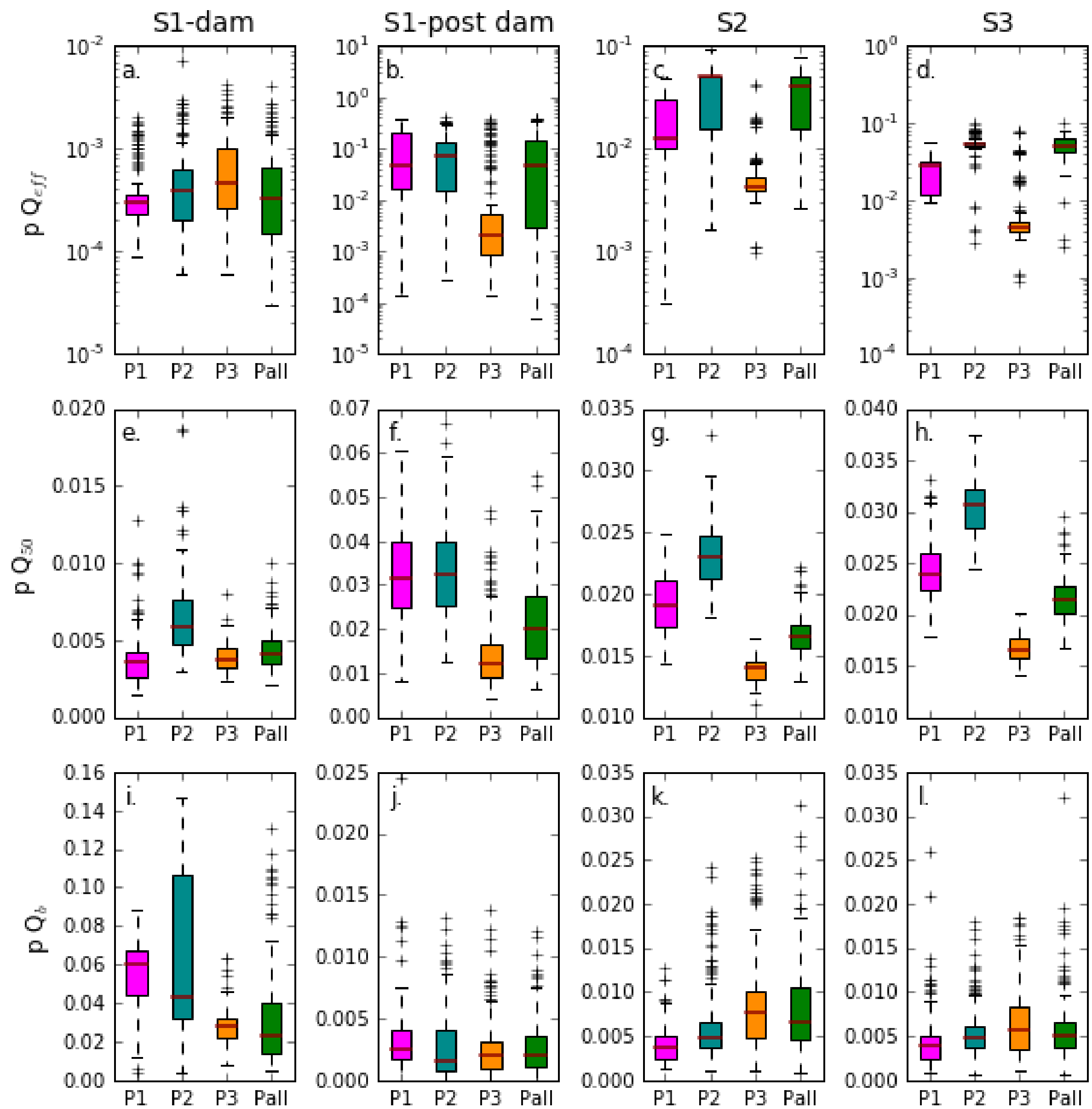

Figure 4.10: Frequency that flow exceeds effective discharge metrics for the effective discharge (a-d), discharge over which 50% of sediment is transported (e-h), and the bankfull discharge (i-l). See Figure 4.8 for a description of the sediment supply regimes. Note differences in y-axis scaling. A p value of 0.003 corresponds to the event occurring once a year.

Table 4.3: Metrics of effective discharge. The value listed is the median of the individual simulations. Bold values for P1-P3 denote populations that are significantly different from Pall at the 99.9% confidence level.

	Sediment supply scenario			
Run	**P1**	**P2**	**P3**	**Pall**
S1 D				
Q_{eff}	**452**	511	508	477
Q_{50}	**206**	**200**	**290**	252
Q_b	**84**	**113**	133	132
Q_{50}/Q_b	**2.40**	1.90	**2.17**	1.89
S1 PD				
Q_{eff}	**92**	95	**355**	103
Q_{50}	**101**	**125**	**185**	140
Q_b	**224**	300	**365**	312
Q_{50}/Q_b	0.46	0.43	**0.50**	0.46
S2				
Q_{eff}	**140**	106	**282**	111
Q_{50}	**117**	**135**	**175**	149
Q_b	202	220	**232**	204
Q_{50}/Q_b	**0.58**	**0.61**	0.75	0.72
S3				
Q_{eff}	103	106	**282**	101
Q_{50}	**111**	**127**	**161**	136
Q_b	**201**	224	**257**	231
Q_{50}/Q_b	0.55	0.55	**0.63**	0.58

D Prior to dam removal (1919-2011)
PD Post-dam removal (2012-2068)

hydrologic stationarity (Pall) is a poor representation of the sediment transport regime. For undisturbed sediment supply regimes (S2 and S3), Pall aligns most closely with a transport regime dominated by frequent flow events; it is statistically indistinguishable from P1 and P2 for about half the effective discharge metrics. It fails to characterize the high-flow dominated regime of P3. Performance is worse in supply regime S1. The effective discharge for Pall is somewhat similar to P2, but is statistically different from both P1 and P3 in nearly all metrics.

Our modeling suggests that channels respond to changes between the three hydrologic regimes within a decadal timescale. The median migration rates and channel widths from simulation set S1-P123 are plotted against time. The other hydrologic scenarios are shown for comparison. The channels responded to the change from P1 to P2 rapidly. The median migration rate for S1-P123 reached that of the P2 run immediately, and channel width adjusted in less than 10 years. The response time from P2 to P3 was longer, with the S1-P123 migration rate and channel width both taking a couple decades to reach that of P3.

In our simulations, dam emplacement has a large impact on channel regime characteristics and on the effective discharge. When sediment supply is low, larger, less frequent flood events are the dominant form of sediment transport. Q_{eff} for the dammed S1 period is up to 5 times

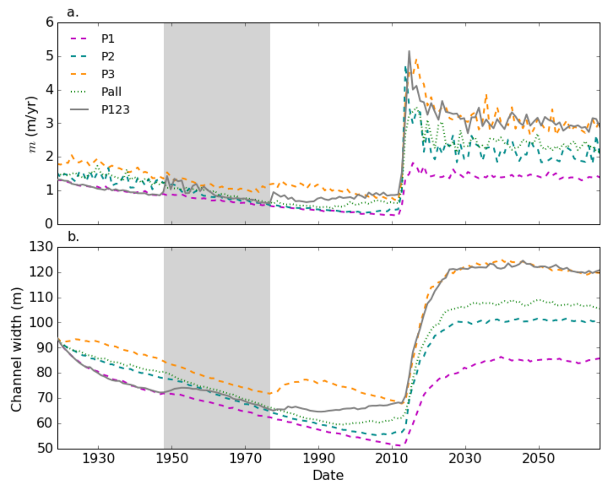

Figure 4.11: Response time of a. the channel migration rate and b. channel width to changes in hydrologic regime for sediment supply scenario S1 (dam emplacement and removal). Series represent the median from each Monte Carlo run. In P1-P3 and Pall, a single hydrologic regime spanned the entire run. In P123, the hydrologic regime switched from P1-P2 and P2 to P3. Shading represents the division between the three hydrologic periods.

higher than for 'natural' S2 and S3 sediment supply regimes (Table 4.3). It is similar for all three climate regimes, but occurs most frequently during P3, for which large floods are more common (Figure 4.10a; also see Figure 4.3). As a result, sediment yield for P3 surpasses that of P2, whose discharge regime is less efficient at transporting large grains (Figure 4.8a). Dam emplacement also led to a reduction in the bankfull discharge (Table 4.3); our simulations suggest that flooding occurred more frequently by almost an order of magnitude (Figure 4.10i-j). Following dam removal, the sediment transport regime adjusted so that patterns of sediment yield during the post-dam period in S1 more closely resemble those of S2 and S3 (Figure 4.8b). However, channel geometry does not fully recover to pre-dam conditions; the width/depth ratio remains higher (Figure 4.8j) and flooding occurs slightly less frequently (Figure 4.10b).

4.5 Discussion

Dams have left a geomorphic legacy on the landscape by fragmenting the routing of sediment through basins and creating storage loci behind reservoirs. As an increasing number of dams are removed, basin continuity will be restored, but the former reservoir deposits may persist for decades or centuries. Whether rivers will fully recover from damming, or whether they will adopt a new steady state, is still largely an open question, especially in the context of global climate change.

Our Monte Carlo simulations suggest the latter, at least on decadal timescales. One of the assumptions of our implementation of MAST-1D is that sediment in the floodplain composes a single, homogenous reservoir. In other words, any sediment entering the floodplain adjusts the grainsize distribution of the entire floodplain, including the banks. During the period when Glines Canyon Dam was in place, the channel became armored, and sediment entering the floodplain via channel migration was coarser. A coarse floodplain and channel bottom impeded erosion of the protective bank toe, causing a drop in channel migration rate and a narrower channel (Figure 4.6). Following dam removal, bed material was finer than the bulk floodplain mixture, at least for the first year following the release of bed material from the former reservoir (*Draut and Ritchie*, 2015). Much of the sediment went into secondary storage on the floodplain, via overbank deposition, avulsion and floodplain channel reactivation (see Chapter 3). We predicted that the floodplain becomes finer and that the banks become more erodable. With lower bank strength, the flow is able to maintain a wider channel (*Eaton et al.*, 2004; *Millar and Quick*, 1993, Figure 4.6a). Since floodplain turnover is much slower than turnover in the channel, the grainsize in the former did not recover after 50 years while the channel active layer adjusted to reflect the long-term sediment supply caliber after a few decades (Figure 4.6b and c).

The reservoir model is an oversimplification of floodplain dynamics. In reality, the size distribution of existing eroding banks does not change, and any increase in erodability on these deposits is due to rising channel mobility that enables erosion of the bank toe and an increase in local shear stress caused by bar growth on the opposite bank. In addition, our simulations overestimate post-removal storage, particularly of fine material (see discussion of this issue in Chapter 3). The major drop in floodplain particle size shown in Figure 4.6c is primarily due to deposition of suspended sediment during overbank flooding. Suspended sediment lowers the overall grainsize distribution of the floodplain, but has little geomorphic influence. However, because the bank erosion algorithm depends on the fraction of coarse material in the floodplain (see Chapter 2), the fine fraction will have increased modeled rates of bank erosion. This likely explains why the channel width and migration rate fail to return to pre-dam levels.

However, rivers tend to re-occupy recently abandoned surfaces more frequently than they erode older floodplain material (*Jerolmack and Paola*, 2007; *Konrad*, 2012). Therefore, bank stability in the decades following dam removal is dependent on the particle size of the deposits that are stored in the modern channel. Suspended material does deposit on channel margins and point bars (an example is provided in Figure 4.12). If current bar deposits contain predominately fine material and are incorporated into the floodplain, they may create patches of floodplain with lower bank strength than older deposits, changing the regime channel dimensions and contributing to increased instability on decadal timescales. While our simulations certainly overestimate the magnitude of floodplain fining, our results generate a hypothesis that can be tested in the field. Indeed, a channel survey conducted in 2015 revealed that Elwha River is already cutting into fresh bar deposits (refer to Appendix C) which appear to lack boulder-sized sediment currently found in modern cutbank deposits.

As shown in Figure 4.7, our simulations suggest that the amount of floodplain fining, and

Figure 4.12: Deposition of fine material on new point bar surfaces. Much of the material originated as suspended load and is much finer than the adjacent eroding bank.

as a consequence the long-term effects on channel width and migration, is directly related to the magnitude of high flow events in the couple years following dam removal. Equation 4.2 implies that, the higher the flow during the initial phase of dam removal, the more reservoir sediment that is eroded. Increased sediment supply leads to more overbank deposition and higher avulsion rates (see Chapter 3), which introduce more fine sediment into the floodplain. This contradicts the findings of *Major et al.* (2012), who postulate that the flow magnitude during dam removal affected short-term timing of sediment flux to Sandy River, Oregon following removal of Marmot Dam, but had little impact on the long-term evolution of the reservoir. However, Marmot Dam was removed in one stage and eroded primarily through knickpoint retreat. The Glines Canyon Dam was removed in stages over the course of two years, which allowed the channel to migrate across the reservoir deposit (*Randle et al.*, 2015). The migration rate, which is proportional to flow strength, will have affected the net amount of sediment released from the reservoir.

The three years following dam removal on Elwha River were abnormally dry, with peak flows all below the two year flood. The Elwha channel was able to export about 90% of the sediment released from Lake Mills, and *East et al.* (2015) have predicted that around 0.3 Mt remain in the channel and roughly 0.2 Mt were deposited in the floodplain. This sediment will likely have a limited effect on future floodplain dynamics, and the decadal-scale width and migration rate will probably lower than our modeled range, particularly since we overestimated the amount of fine channel storage. However, we hypothesize that the hydrologic regime during dam removal does affect the evolution of the channel. A large flood during or shortly after dam removal can erode large swaths of the former reservoir deposit. Most of the bedload component of the pulse will enter long-term storage on bars downstream of the dam and may eventually become incorporated into the floodplain, altering its composition.

We have shown that decadal-scale channel stability is sensitive to large inputs of fine sediment into the floodplain. However, there is still uncertainty regarding the actual supply of this sediment from upstream reservoirs. Little is known about the partitioning of sediment between the suspended and bed loads, or about how the caliber of sediment supply evolves over time as fine reservoirs are exhausted. These factors will control how the river behaves on decadal timescales, and future field campaigns should prioritize characterizing the caliber of deposits remaining within the former reservoir as well as on point bars downstream.

The range of migration rates we calculated for Elwha River are somewhat lower than those found on other regional rivers. While we predicted migration rates of between 1-2 m/yr for the at capacity (S2) and stochastic (S3) supply scenarios (Figure 4.8e-h), *O'Connor et al.* (2003) found that migration rates for rivers draining the western side of the Olympic peninsula were 2-12 times higher. It is true that our numerical model does not account for many local bank erosion processes. But Elwha River is also straighter and steeper than other regional rivers, and local climate is slightly different. These factors may partially explain the discrepancy.

Even if the governing factors were more similar, Elwha River today cannot be expected to have the same channel exchange rates to those measured over the course of the 20th century because the flow regime will reflect a different climate. *O'Connor et al.* (2003) used historic maps and photos that go as far back as the late 1800s and incorporate multiple phases of the Pacific Decadal Oscillation. Our modeling shows that small adjustments to the hydrologic regime can have a moderate impact on sediment transport. In all cases except for S1-dam, the channel geometry appears to be adjusted to the flow regime. For S1-post dam, S2, and S3, median bankfull discharge occurs 1-2 times per year for all discharge scenarios (Figure 4.10j-l). This approximately corresponds to the one year peak flow event (see Figure 4.3), which aligns with regional bankfull flow frequencies for maritime mountains in the Pacific Northwest (*Castro and Jackson*, 2001).

Our modeling suggests that adjustment to new hydrologic regimes can occur within a few years, which is short enough time to make the change relevant on decadal timescales (Figure 4.11). Metrics of channel forming discharge are different for the three periods and reflect unique geomorphic regimes. The bankfull discharge scales with the frequency of large floods which are capable of mobilizing the banks, regardless of sediment supply regime. But

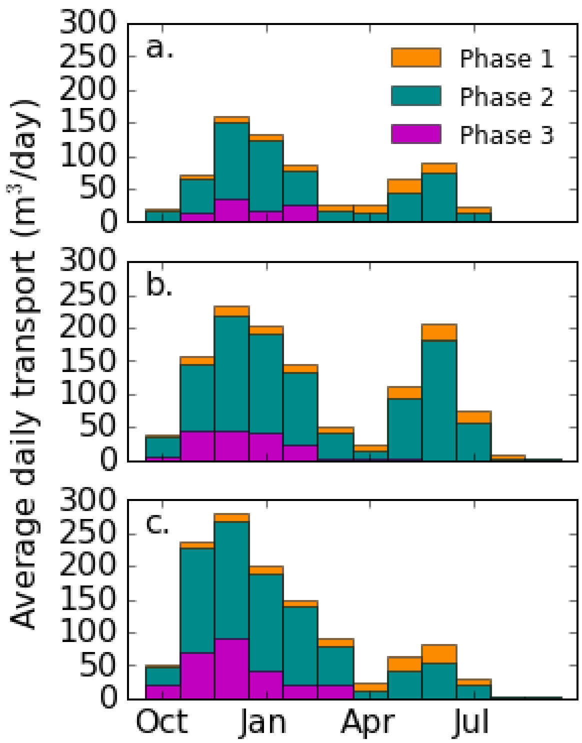

Figure 4.13: Average daily sediment transport by month, divided into phases of transport described by *Carling* (1988). Phase 1 represents movement of fine sediment winnowed from the bed surface. During Phase 2, most of the active layer is in transport, but the coarsest grains are mostly immobile and maintain channel stability. The entire bed is in transport during Phase 3. See text for details. a. Period 1; b. Period 2; c. Period 3.

the relationship between bankfull flow and effective discharge is different for P3 than for the earlier two periods (Table 4.3), representing a shift in the nature of the sediment transport regime from one driven by modest, frequent flow events to one dominated more by large flood events (except in the case of sediment-starved S1-D, for which exceptionally high flows are required to mobilize the bed).

In order to see the significance of this shift on channel stability, it is useful to divide sediment transport events by their ability to mobilize the active layer. *Carling* (1988) identified three different phases of sediment transport. During Phase 1 transport, most of the bed is static, and mobilized sediment is comprised of fine grains winnowed from the bed surface. Phase 2 transport occurs when most grains are at least partially mobile, but the largest particles do not move. Significant transport occurs within the active layer, but there is little geomorphic change. Only during Phase 3, when flow is strong enough to mobilize the structural grains, does the bed become restructured. Distributions of transport phases, averaged by month for runs with supply scenario S3, are presented in Figure 4.13 for the three climatic periods. We defined the threshold between Phase 1 and Phase 2 as the point at which channel shear stress is 1.5 times that needed to entrain a 54 mm particle, which roughly corresponds to the the D_{50}. This implies that the D_{50} is well above the entrainment threshold, but not fully mobile, which *Wilcock and McArdell* (1993) found occurs at roughly twice the shear stress required to mobilize the particle. For our calculations, Phase 3 occurs when the channel shear stress exceeds 1.5 times the entrainment threshold for a 300 mm particle, which roughly corresponds to the D_{90}. In our simulations, most sediment transport occurs during Phase 2, regardless of the climatic period. But Phase 3 transport constitutes a slightly higher percentage of the total load for P3 (10% as opposed to 7% for both P1 and P2). Q_{eff} describes Phase 3 transport for P3, while it occurs during Phase 2 for P1 and P2.

The increased importance of high-magnitude flood events manifests itself in greater geomorphic instability. Even though the average annual water and sediment yield are both lower in P3 than P2 (Table 4.1 and Figure 4.8b-d), P3 maintains a significantly higher width-depth ratio and migration rate. It is also possible that scour-and-fill episodes are more intense during P3, although the spatial and temporal resolution of MAST-1D is too coarse to characterize these processes well. *Battin et al.* (2007) suggest that larger peak flows may increase bed scour in the winter, jeopardizing salmon eggs during the incubation period. *McKean and Tonina* (2013) point out that only small portions of the bed are mobile during floods and that larger floods will not put salmon redds at risk. Neither studies considered the effect of increasing flood peaks on channel width and bank erosion, which act as a control on channel competence and a source of sediment supply.

The difference in channel stability between the three climatic periods is due in large part to the distribution of annual water yield between the winter and nival seasons. During the cool phase of the PDO (P2), much of the winter precipitation that would lead to high floods is captured in the basin as snow and released more slowly in the spring. While nival flows are efficient in transporting sediment (Figure 4.13b), in Elwha River's hybrid regime, they are not powerful enough to lead to Phase 3 transport. The ratio between mean annual sediment yield and migration rate is plotted as a function of average discharge during the nival period in Figure 4.14. In the two sediment supply scenarios without Glines Canyon Dam, P2 transports roughly 50% more sediment for every unit of bank movement. P1 and P3, which are both characterized by weak snowmelt flows, have nearly the same flux/migration ratio, despite the fact that P3 is more driven by low-frequency flood flows. Large floods were rare during P1, but frequent events were smaller as well, so that the reduction in channel migration is matched by a low sediment yield. In P2, a winter season with abundant transport and bank erosion is followed by nival flows that convey sediment through the channel without leading to bank instability.

The implication is that, at least for hybrid streams with high sediment supply, the bed material sediment transport regime is essentially de-coupled from the channel forming discharge. The channel is shaped by the magnitude and frequency of flood peaks, while sediment transport is more closely related to total water yield. The relationship between the two is dependent on temperature, which dictates the partitioning of precipitation between rain and snow. However, the importance of the snowmelt season varies depending on sediment availability and landscape history. For supply scenario S1, the difference in flux/migration ratio between P2 and the other hydrologic regimes is much lower than in S2 and S3. During the dammed period, nival flows contribute little to overall sediment transport because the bed surface is armored and only winter flood flows are able to mobilize the coarse fraction. Following dam removal, near-bank sediments are more mobile, and nival flows can feasibly lead to bank erosion.

It appears that the assumption of hydrologic stationarity is problematic in the context of decadal-scale geomorphic processes. The range of output for the Pall simulations fell between the three climate periods and acts as an average for the historic period. However, there was no cyclic pattern; each period had a unique set of governing parameters which led to differences in the flows responsible for transporting the most sediment, the amount of channel instability, and the relationship between sediment yield and bank erosion. There is no evidence to indicate that the future hydrologic regime will resemble any of the periods captured in the historic record. *Reidy-Liermann et al.* (2012) predicts that many basins in the region may experience larger flood peaks in the future as the result of decreasing snowpack and the consequent transition to more flashy, rainfall-dominated hydrologic regimes. They anticipate that by 2040, Elwha River will have transitioned into a completely pluvial system. Our analysis suggests that the future channel will be dominated even more by flood flows and that it will be less laterally stable. Using the 20th century to predict the 21st may lead to an underestimation of flood and erosion risk.

4.6 Conclusion

Our objective was to consider whether Elwha River, and other hypothetical systems undergoing dam removal, will evolve to resemble past undisturbed systems. Our analysis suggests that, at least for high-order trunk streams with active channel/floodplain coupling, the answer may depend on the amount of sediment that is sequestered into the floodplain while the initial pulse of reservoir sediment is moving through the system. When the sediment pulse is much finer than the floodplain, it can create patches that are easily erodible, leading to higher channel widths and migration rates that may persist for decades. While it is common to quantify the movement of the sediment pulse through the system by measuring elevation change in the thalweg, it may be more appropriate on decadal timescales to consider the material deposited on bars and in floodplain channels. To do so, more information is also needed on the caliber of sediment supply.

Hybrid streams in the Pacific Northwest will likely behave differently in the 21st century than in the 20th. On Elwha River, the sediment transport regime transitioned over the course of the 20th century from being dominated by modest, very frequent flows, to being shaped more by flood events. Our simulations show that this transition would probably have occurred to some extent even if the dams had not been in place. It appears that as snowpack decreases

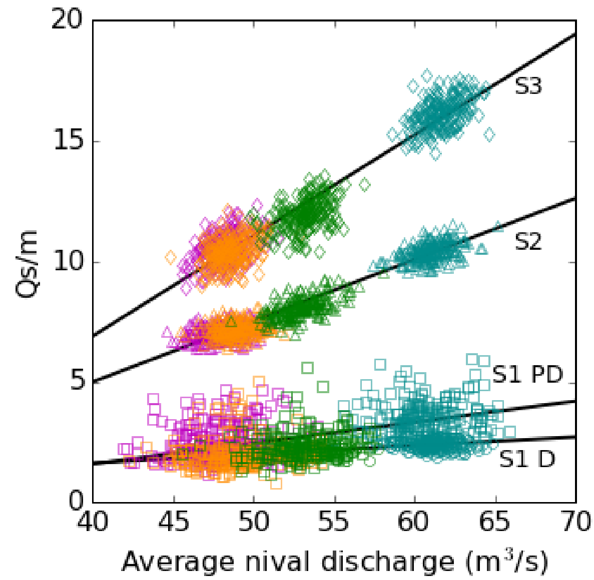

Figure 4.14: The ratio of average annual sediment transport (in thousands of m^3) to channel migration (in m/y) as a function of the average nival discharge. Pre- and post-dam removal periods in S1 are denoted by circles and squares, respectively. Triangles represent S2, and S3 is plotted in diamonds. Colors represent the climatic periods and are the same as Figures 4.8 and 4.10.

and disappears, channel instability and coupling with the floodplain will increase.

Geomorphologists have a long tradition of conceptualizing rivers as being governed by a relatively static set of environmental forcings, where channels are fluctuating around regime dimensions that are characterized by a single channel-forming discharge and homogeneous particle size. Our analysis suggests that this framework is questionable on human timescales, in the context of natural and anthropogenically altered sediment supply and streamflow variability.

Chapter 5

Conclusion

Over the past century, dams and the reservoirs behind them have become one of the most pervasive features of Earth's landscapes. One of the new frontiers in geomorphology is learning how landscapes evolve after dams have been removed. The purpose of this thesis was to explore the decadal-scale legacy of dams on Elwha River. In particular, we were interested in examining processes related to channel/floodplain coupling, which determine how material of various sizes travels through the sediment cascade. To do so, a numerical model was adapted that we suggest captures the most relevant processes operating on large, wandering, low-sinuosity cobble-bedded streams over decadal timescales. Our hypothesis, explained in Chapter 2, was that bank stability is determined by the ability of the flow to mobilize the large structural grains near the channel margins. Non-cohesive banks are protected by a bank toe, and when that toe is scoured away, bank erosion continues while the channel has the capacity to transport large grains. A crucial element to our model is the assumption that the channel-wide shear stress is an adequate proxy for near-bank flow conditions. Widening via bank erosion is countered by channel narrowing due to vegetation growth on exposed channel surfaces. We use channel-wide shear stress as a proxy for river flow, and assume that narrowing occurs when the shear stress is low. Even given the simplest characterization of governing conditions–steady sediment supply and hydrologic regimes–channel width and migration rate are not constant. Instead, they fluctuate within a narrow range. This is because wandering rivers often avulse, reoccupying old locations and scouring floodplain channels that once carried only flood flow. Our modeling in Chapter 2 suggests that when the river avulses, the deeper channel becomes more effective at scouring banks.

As is demonstrated in Chapter 3, this model of mobility-driven bank erosion appears to adequately describe channel-floodplain coupling on the sediment-starved Elwha River when Glines Canyon and Elwha Dams were in place. Comparison between model output and field data show that the former is able to reproduce observed channel width and grainsize. Glines Canyon Dam blocked sediment supply to the study area, creating a new reservoir behind the dam. The exchange of sediment between the channel and floodplain slowed, both due to a decrease in the number of avulsions and because channel coarsening led to a reduction in the frequency and magnitude of bank erosion events. We found in Chapter 4 that sediment transport was dominated by large, winter flood events during this period. While flows during the snowmelt period transport up to about a third of the annual yield in supply-rich conditions, they are unable to mobilize the coarse bed during the dammed period.

According to our model, channel-floodplain exchange increases significantly during the first decade following dam removal. The primary flux is due to increases in floodplain storage caused by avulsion. This is corroborated by air photo analysis, which reveals that for the upstream half of the study area, most widening was due to the activation of floodplain channels. Channel width and rates of bank erosion also increased. However, the poor fit between modeled and field rates of channel movement and sediment flux during the post-removal period suggests that our assumption that channel-wide hydraulics are suitable proxies for near-bank flow strength is not justified during periods of exceptionally high sediment supply.

Unlike other shorter-term studies (*East et al.*, 2015; *Major et al.*, 2012), our decadal-scale perspective from Chapter 4 seems to suggest that future channel evolution can be dependent on the flow regime during the first two years of dam removal if large flood events during sediment pulses result in ample deposition of sediment on the floodplain. If this sediment is finer than the underlying material, it can increase the mobility of the floodplain, leading to higher magnitudes of channel instability on decadal timescales. However, our analysis is based on major assumptions about the caliber of sediment supply and the efficiency of the floodplain in trapping suspended sediment. Regardless of the impact of sediment supply, future flow regimes will influence how stable channels are in the future; declining snowpack and increasing winter peak flows expected for many Pacific Northwest basins will likely lead to higher rates of migration and more transport events that break up surface layers in the channel.

Our study revealed that a rather simple characterization of lateral flux, using channel-wide flow metrics, is sufficient to explain quite a bit of the variablility in observed channel width and migration, especially during periods of low sediment supply. However, the current model is missing key reach-scale processes that affect performance during periods of sediment excess. This includes the role of log jams, which can act as in-channel storage reservoirs and cause avulsion. In the future, the influence of channel morphology in partitioning flow and sediment should be considered. In addition, more realistic algorithms for vegetation growth will help quantify the important effect of channel narrowing on sequestering sediment within the floodplain.

Numerical models are only as good as the data that back them. As we have shown in Chapter 2, our model is highly sensitive to grain size. Its underestimation of the competence of Elwha River to evacuate the pulse of sediment following dam removal (see Chapter 3) may reflect uncertainty in the upstream boundary condition more than any process deficiencies in the model. Quantifying sediment supply and particle size is one of the most important–and most challenging–tasks for any geomorphic study. We suggest that future field studies on dam removals prioritize campaigns to quantify the magnitude and, more importantly, the size, of sediment pulses.

It appears that dams leave a lasting legacy on the sediment cascade. They divide natural storage centers into two parts: a fine reservoir behind the dam composed of sediment reflecting the long-term sediment load, and a coarser channel/floodplain system downstream of the dam that is starved of fine material. Remixing of the reservoirs following dam removal is a process that occurs over decadal timescales. Overbank deposition, avulsion, and vegetation growth all reintroduce reservoir sediment back into the downstream floodplain. Most adjustment occurs within the few years after the removal, but patches of old and new material might persist on the order of decades. This means that rates of bank erosion and sediment supply to the channel can be affected over long timescales. Channel-floodplain coupling is ultimately determined by channel processes, which are highly sensitive to sediment supply and channel morphology.

So far, most studies of dam removals have focused on the short-term impact of the initial sediment pulse on the channel profile and planform. There has been little consideration to sediment exchange between the channel and floodplain–neither in terms of additional sediment supply via bank erosion or with regards to the long-term sequestration of sediment. We have shown that the legacy of dams does not end after the initial wave of sediment has dissipated. Our 1-D reservoir-based approach has generated general hypotheses about how channel-floodplain coupling may impact channel stability. More observations are needed to quantify how dam emplacement and removal affect the patchiness of sediment deposits–and whether erosion of these deposits conform to existing conceptual and numerical models of bank stability. In addition, our research has only touched on the many responses of rivers to sediment pulses. We have considered the characteristics of one reservoir. Future work should explore the various responses of channel stability to sediment inputs of different magnitudes and calibers.

Bibliography

Abbe, T. B., and D. R. Montgomery (1996), Large woody debris jams, channel hydraulics and habitat formation in large rivers, *Regulated Rivers Research & Management*, *12*(23), 201–221.

Abernethy, B., and I. D. Rutherfurd (2001), The distribution and strength of riparian tree roots in relation to riverbank reinforcement, *Hydrological processes*, *15*(1), 63–79.

Acker, S. A., T. J. Beechie, and P. B. Shafroth (2008), Effects of a natural dam-break flood on geomorphology and vegetation on the elwha river, washington, usa.

Andrews, E. D. (1980), Effective and bankfull discharges of streams in the yampa river basin, colorado and wyoming, *Journal of Hydrology*, *46*(3-4), 311–330.

Andrews, E. D. (1986), Downstream effects of flaming gorge reservoir on the green river, colorado and utah, *Geological Society of America Bulletin*, *97*(8), 1012–1023.

Andrews, S. G. C., E. Mortenson (2015), Evaluation of alternative streamflows to improve aquatic and riparian habitat in the walker river basin, nevada, *Journal of the Nevada Water Resources Association*.

ASCE Task Committee on Hydraulics, B. M., and M. of River Width Adjustment (1998a), River width adjustment. i: Processes and mechanisms, *Journal of Hydraulic Engineering, ASCE*, *124*.

ASCE Task Committee on Hydraulics, B. M., and M. of River Width Adjustment (1998b), River width adjustment. ii: Modeling., *J. Hydr. Engrg., ASCE*, *124*.

Baker, V. R. (1977), Stream-channel response to floods, with examples from central texas, *Geological Society of America Bulletin*, *88*(8), 1057–1071.

Barnes, H. H. (1967), Roughness characteristics of natural channels, *Tech. rep.*, US Govt. Print. Off.,.

Basso, S., A. Frascati, M. Marani, M. Schirmer, and G. Botter (2015), Climatic and landscape controls on effective discharge, *Geophysical Research Letters*, *42*(20), 8441–8447.

Battin, J., M. W. Wiley, M. H. Ruckelshaus, R. N. Palmer, E. Korb, K. K. Bartz, and H. Imaki (2007), Projected impacts of climate change on salmon habitat restoration, *Proceedings of the national academy of sciences*, *104*(16), 6720–6725.

Beechie, T. J., M. Liermann, M. M. Pollock, S. Baker, and J. Davies (2006), Channel pattern and river-floodplain dynamics in forested mountain river systems, *Geomorphology*, *78*(1), 124–141.

Benda, L., and T. Dunne (1997a), Stochastic forcing of sediment routing and storage in channel networks, *Water Resources Research*, *33*(12), 2865–2880.

Benda, L., and T. Dunne (1997b), Stochastic forcing of sediment supply to channel networks from landsliding and debris flow, *Water Resources Research*, *33*(12), 2849–2863.

Bertoldi, W., A. Gurnell, N. Surian, K. Tockner, L. Zanoni, L. Ziliani, and G. Zolezzi (2009), Understanding reference processes: linkages between river flows, sediment dynamics and vegetated landforms along the tagliamento river, italy, *River Research and Applications*, *25*(5), 501–516.

Bledsoe, B. P., and C. C. Watson (2001), Effects of urbanization on channel instability, *JAWRA Journal of the American Water Resources Association*, *37*(2), 255–270.

Bond, N., J. Overland, M. Spillane, and P. Stabeno (2003), Recent shifts in the state of the north pacific, *Geophysical Research Letters*, *30*(23).

Bountry, J., R. Ferrari, K. Wille, and T. Randle (2011), Survey report for lake mills and lake aldwell on the elwha river, washington, *Tech. rep.*, SRH-2010-23, US Department of the Interior, Bureau of Reclamation, Denver, CO.

Bountry, J. A., Y. G. Lai, and T. J. Randle (2013), Sediment impacts from the savage rapids dam removal, rogue river, oregon, *Reviews in Engineering Geology*, *21*, 93–104.

Bowling, L. C., P. Storck, and D. P. Lettenmaier (2000), Hydrologic effects of logging in western washington, united states, *Water Resources Research*, *36*(11), 3223–3240.

Brandon, M. T., M. K. Roden-Tice, and J. I. Garver (1998), Late cenozoic exhumation of the cascadia accretionary wedge in the olympic mountains, northwest washington state, *Geological Society of America Bulletin*, *110*(8), 985–1009.

Brunner, G. W. (2016), Hec-ras river analysis system. hydraulic reference manual. version 5.0., *Tech. rep.*, US Army Corps of Engineers Hydrologic Engineering Center.

Bunte, K., and S. R. Abt (2001), Sampling surface and subsurface particle-size distributions in wadable gravel-and cobble-bed streams for analyses in sediment transport, hydraulics, and streambed monitoring.

Burroughs, B. A., D. B. Hayes, K. D. Klomp, J. F. Hansen, and J. Mistak (2009), Effects of stronach dam removal on fluvial geomorphology in the pine river, michigan, united states, *Geomorphology*, *110*(3), 96–107.

Camporeale, C., and L. Ridolfi (2007), Noise-induced phenomena in riparian vegetation dynamics, *Geophysical Research Letters*, *34*(18).

Camporeale, C., E. Perucca, L. Ridolfi, and A. Gurnell (2013), Modeling the interactions between river morphodynamics and riparian vegetation, *Reviews of Geophysics*, *51*(3), 379–414.

Cannon, S. H., and J. DeGraff (2009), The increasing wildfire and post-fire debris-flow threat in western usa, and implications for consequences of climate change, in *Landslides–disaster risk reduction*, pp. 177–190, Springer.

Cantelli, A., M. Wong, G. Parker, and C. Paola (2007), Numerical model linking bed and bank evolution of incisional channel created by dam removal, *Water Resources Research*, *43*(7).

Carling, P. (1988), The concept of dominant discharge applied to two gravel-bed streams in relation to channel stability thresholds, *Earth Surface Processes and Landforms*, *13*(4), 355–367.

Carroll, R., J. Warwick, A. James, and J. Miller (2004), Modeling erosion and overbank deposition during extreme flood conditions on the carson river, nevada, *Journal of Hydrology*, *297*(1), 1–21.

Castro, J. M., and P. L. Jackson (2001), Bankfull discharge recurrence intervals and regional hydraulic geometry relationships: patterns in the pacific northwest, usa, *JAWRA Journal of the American Water Resources Association*, *37*(5), 1249–1262.

Church, M. (2002), Fluvial sediment transfer in cold regions, in *Landscapes of transition*, pp. 93–117, Springer.

Church, M. (2008), *Gravel Bed Rivers 6, Volume 11*, chap. Multiple scales in rivers, pp. 3–32, Elsevier.

Church, M., and O. Slaymaker (1989), Disequilibrium of holocene sediment yield in glaciated british columbia, *Nature*, *337*(2), 452–454.

Church, M. A., D. McLean, and J. Wolcott (1987), River bed gravels: sampling and analysis, *Sediment Transport in Gravel-Bed Rivers. John Wiley and Sons New York. 1987. p 43-88, 17 fig, 3 tab, 50 ref.*

Constantine, J. A., T. Dunne, J. Ahmed, C. Legleiter, and E. D. Lazarus (2014), Sediment supply as a driver of river meandering and floodplain evolution in the amazon basin, *Nature Geoscience*, *7*(12), 899–903.

Corenblit, D., E. Tabacchi, J. Steiger, and A. M. Gurnell (2007), Reciprocal interactions and adjustments between fluvial landforms and vegetation dynamics in river corridors: a review of complementary approaches, *Earth-Science Reviews*, *84*(1), 56–86.

Cui, Y., G. Parker, J. Pizzuto, and T. E. Lisle (2003), Sediment pulses in mountain rivers: 2. comparison between experiments and numerical predictions, *Water Resources Research*, *39*(9).

Cui, Y., G. Parker, C. Braudrick, W. E. Dietrich, and B. Cluer (2006), Dam removal express assessment models (dream). part 1: model development and validation, *Journal of Hydraulic Research*, *44*(3), 291–307.

Cunderlik, J. M., and D. H. Burn (2003), Non-stationary pooled flood frequency analysis, *Journal of Hydrology*, *276*(1), 210–223.

Curran, C. A., C. P. Konrad, J. L. Higgins, and M. K. Bryant (2009), Estimates of sediment load prior to dam removal in the elwha river, clallam county, washington, *Tech. rep.*, US Geological Survey.

Czuba, J. A., C. S. Magirl, C. R. Czuba, C. A. Curran, K. H. Johnson, T. D. Olsen, H. K. Kimball, and C. C. Gish (2012), *Geomorphic analysis of the river response to sedimentation downstream of Mount Rainier, Washington*, US Department of the Interior, US Geological Survey.

Darby, S. E., and C. R. Thorne (1996), Development and testing of riverbank-stability analysis, *Journal of hydraulic engineering*, *122*(8), 443–454.

Darby, S. E., and M. J. Van de Wiel (2003), Models in fluvial geomorphology, *Tools in fluvial geomorphology*, pp. 501–537.

Davidson, S. (2016), Modeling disturbance and channel evolution in mountain streams, Ph.D. thesis, University of British Columbia.

Department of the Interior (1995), Elwha river ecosystem restoration implementation, final environmental impact statement. nps d-271a.

Dietrich, W. E., T. Dunne, N. F. Humphrey, L. M. Reid, et al. (1982), Construction of sediment budgets for drainage basins, *Sediment Budgets in Forested Drainage Basins. United States Forest Service Gen. Tech. Rep. PNW-141. p5-23.*

Doyle, M. W., E. H. Stanley, and J. M. Harbor (2002), Geomorphic analogies for assessing probable channel response to dam removal, *JAWRA Journal of the American Water Resources Association*, *38*(6), 1567–1579.

Draut, A., and A. C. Ritchie (2015), Sedimentology of new fluvial deposits on the elwha river, washington, usa, formed during large-scale dam removal, *River Research and Applications*, *31*(1), 42–61.

Draut, A. E., J. B. Logan, R. E. McCoy, M. McHenry, and J. A. Warrick (2008), Channel evolution on the lower elwha river, washington, 1939-2006, *Tech. rep.*, Geological Survey (US).

Draut, A. E., J. B. Logan, and M. C. Mastin (2011), Channel evolution on the dammed elwha river, washington, usa, *Geomorphology*, *127*(1), 71–87.

Duda, J., H. J. Coe, S. Morley, and K. Kloehn (2011a), Establishing spatial trends in water chemistry and stable isotopes (δ15n and δ13c) in the elwha river prior to dam removal and salmon recolonization, *River research and applications*, *27*(10), 1169–1181.

Duda, J. J., J. A. Warrick, and C. S. Magirl (2011b), Coastal habitats of the elwha river, washington-biological and physical patterns and processes prior to dam removal, *Tech. rep.*, US Geological Survey.

East, A. E., G. R. Pess, J. A. Bountry, C. S. Magirl, A. C. Ritchie, J. B. Logan, T. J. Randle, M. C. Mastin, J. T. Minear, J. J. Duda, et al. (2015), Large-scale dam removal on the elwha river, washington, usa: River channel and floodplain geomorphic change, *Geomorphology*, *228*, 765–786.

Easterbrook, D. J. (1986), Stratigraphy and chronology of quaternary deposits of the puget lowland and olympic mountains of washington and the cascade mountains of washington and oregon, *Quaternary Science Reviews*, *5*, 145–159.

Eaton, B. C., and T. R. Giles (2009), Assessing the effect of vegetation-related bank strength on channel morphology and stability in gravel-bed streams using numerical models, *Earth Surface Processes and Landforms*, *34*(5), 712–724.

Eaton, B. C., M. Church, and R. G. Millar (2004), Rational regime model of alluvial channel morphology and response, *Earth Surface Processes and Landforms*, *29*(4), 511–529.

Ebbesmeyer, C. C., D. R. Cayan, D. R. McLain, F. H. Nichols, D. H. Peterson, and K. T. Redmond (1991), 1976 step in the pacific climate: forty environmental changes between 1968-1975 and 1977-1984.

Eke, E., G. Parker, and Y. Shimizu (2014), Numerical modeling of erosional and depositional bank processes in migrating river bends with self-formed width: Morphodynamics of bar push and bank pull, *Journal of Geophysical Research: Earth Surface*, *119*(7), 1455–1483.

Elsner, M. M., L. Cuo, N. Voisin, J. S. Deems, A. F. Hamlet, J. A. Vano, K. E. Mickelson, S.-Y. Lee, and D. P. Lettenmaier (2010), Implications of 21st century climate change for the hydrology of washington state, *Climatic Change*, *102*(1-2), 225–260.

Emmett, W. W., and M. G. Wolman (2001), Effective discharge and gravel-bed rivers, *Earth Surface Processes and Landforms*, *26*(13), 1369–1380.

Ferguson, R. (2003), The missing dimension: effects of lateral variation on 1-d calculations of fluvial bedload transport, *Geomorphology*, *56*(1), 1–14.

Ferguson, R., and M. Church (2009), A critical perspective on 1-d modeling of river processes: Gravel load and aggradation in lower fraser river, *Water Resources Research*, *45*(11).

Ferrer-Boix, C., and M. A. Hassan (2015), Influence of the sediment supply texture on morphological adjustments in gravel-bed rivers, *Water Resources Research*, *50*(11), 8868–8890.

Fetherston, K. L., R. J. Naiman, and R. E. Bilby (1995), Large woody debris, physical process, and riparian forest development in montane river networks of the pacific northwest, *Geomorphology*, *13*(1-4), 133–144.

Fleming, S. W., P. H. Whitfield, R. Moore, and E. J. Quilty (2007), Regime-dependent streamflow sensitivities to pacific climate modes cross the georgia–puget transboundary ecoregion, *Hydrological Processes*, *21*(24), 3264–3287.

Foley, M. M., J. J. Duda, M. M. Beirne, R. Paradis, A. Ritchie, and J. A. Warrick (2015), Rapid water quality change in the elwha river estuary complex during dam removal, *Limnology and Oceanography*, *60*(5), 1719–1732.

Friedman, J. M., W. R. Osterkamp, and W. M. Lewis (1996), Channel narrowing and vegetation development following a great plains flood, *Ecology*, *77*(7), 2167–2181.

Gaeuman, D., E. Andrews, A. Krause, and W. Smith (2009), Predicting fractional bed load transport rates: Application of the wilcock-crowe equations to a regulated gravel bed river, *Water resources research*, *45*(6).

Galay, V. (1983), Causes of river bed degradation, *Water resources research*, *19*(5), 1057–1090.

Gilbert, J., and R. Link (1995), Alluvium distribution in lake mills, glines canyon project and lake aldwell, elwha project, washington, *Elwha Technical Series PN-95-4, August, Boise, ID*.

Gomez, B., B. J. Rosser, D. H. Peacock, D. M. Hicks, and J. A. Palmer (2001), Downstream fining in a rapidly aggrading gravel bed river, *Water Resources Research*, *37*(6), 1813–1823.

Gomez, B., Y. Cui, A. Kettner, D. Peacock, and J. Syvitski (2009), Simulating changes to the sediment transport regime of the waipaoa river, new zealand, driven by climate change in the twenty-first century, *Global and Planetary Change*, *67*(3), 153–166.

Gordon, E., and R. K. Meentemeyer (2006), Effects of dam operation and land use on stream channel morphology and riparian vegetation, *Geomorphology*, *82*(3), 412–429.

Gottesfeld, A. S., and L. M. J. Gottesfeld (1990), Floodplain dynamics of a wandering river, dendrochronology of the morice river, british columbia, canada, *Geomorphology*, *3*(2), 159–179.

Graf, W. L. (1999), Dam nation: A geographic census of american dams and their large-scale hydrologic impacts, *Water resources research*, *35*(4), 1305–1311.

Graf, W. L. (2006), Downstream hydrologic and geomorphic effects of large dams on american rivers, *Geomorphology*, *79*(3), 336–360.

Gran, K., and C. Paola (2001), Riparian vegetation controls on braided stream dynamics, *Water Resources Research*, *37*(12), 3275–3283.

Grant, G. (2001), Dam removal: Panacea or pandora for rivers?, *Hydrological Processes*, *15*(8), 1531–1532.

Grant, G. E., and S. L. Lewis (2015), The remains of the dam: What have we learned from 15 years of us dam removals?, in *Engineering Geology for Society and Territory-Volume 3*, pp. 31–35, Springer.

Greet, J., J. Angus Webb, and R. D. Cousens (2011), The importance of seasonal flow timing for riparian vegetation dynamics: a systematic review using causal criteria analysis, *Freshwater Biology*, *56*(7), 1231–1247.

Gregory, K., and C. Park (1974), Adjustment of river channel capacity downstream from a reservoir, *Water Resources Research*, *10*(4), 870–873.

Guthrie, R., P. Friele, K. Allstadt, N. Roberts, S. Evans, K. Delaney, D. Roche, J. Clague, and M. Jakob (2012), The 6 august 2010 mount meager rock slide-debris flow, coast mountains, british columbia: characteristics, dynamics, and implications for hazard and risk assessment., *Natural Hazards & Earth System Sciences*, *12*(5).

Hajek, E. A., and M. A. Wolinsky (2012), Simplified process modeling of river avulsion and alluvial architecture: Connecting models and field data, *Sedimentary Geology*, *257*, 1–30.

Hamlet, A. F., and D. P. Lettenmaier (2007), Effects of 20th century warming and climate variability on flood risk in the western us, *Water Resources Research*, *43*(6).

Hare, S., and R. Francis (1995), Climate change and salmon production in the northeast pacific ocean, *Canadian Special Publication of Fisheries and Aquatic Sciences*, pp. 357–372.

Hassan, M., L. Roberge, M. Church, M. More, S. Donner, J. Leach, and K. Ali (2017), What are the contemporary sources of sediment in the mississippi river?, *Geophysical Research Letters*, *44*(17), 8919–8924.

Hassan, M. A., R. Egozi, and G. Parker (2006), Experiments on the effect of hydrograph characteristics on vertical grain sorting in gravel bed rivers, *Water Resources Research*, *42*(9).

Hassan, M. A., D. Brayshaw, Y. Alila, and E. Andrews (2014), Effective discharge in small formerly glaciated mountain streams of british columbia: Limitations and implications, *Water Resources Research*, *50*(5), 4440–4458.

Heller, P. L., P. E. Beland, N. F. Humphrey, S. K. Konrad, R. M. Lynds, M. E. McMillan, K. E. Valentine, Y. A. Widman, and D. J. Furbish (2001), Paradox of downstream fining and weathering-rind formation in the lower hoh river, olympic peninsula, washington, *Geology*, *29*(11), 971–974.

Higson, J. L., and M. B. Singer (2015), The impact of the streamflow hydrograph on sediment supply from terrace erosion, *Geomorphology*, *248*, 475–488.

Hoey, T. B., and R. Ferguson (1994), Numerical simulation of downstream fining by selective transport in gravel bed rivers: Model development and illustration, *Water resources research*, *30*(7), 2251–2260.

Hooke, R. L. (1994), On the efficacy of humans as geomorphic agents, *GSA Today*, *4*(9), 217.

Hooke, R. L. (2000), On the history of humans as geomorphic agents, *Geology*, *28*(9), 843–846.

Inman, D. L., and S. A. Jenkins (1999), Climate change and the episodicity of sediment flux of small california rivers, *The Journal of geology*, *107*(3), 251–270.

Interagency Advisory Committee on Water Data (1982), *Guidelines for determining flood flow frequency: Bulletin 17B of the Hydrology Subcommittee*, Office of Water Data Coordination, Reston, VA.

Jakob, M., M. Bovis, and M. Oden (2005), The significance of channel recharge rates for estimating debris-flow magnitude and frequency, *Earth Surface Processes and Landforms*, *30*(6), 755–766.

James, L. A., and M. B. Singer (2008), Development of the lower sacramento valley flood-control system: Historical perspective, *Natural Hazards Review*, *9*(3), 125–135.

Jenkins, K. J., N. Chelgren, K. Sager-Fradkin, P. Happe, and M. J. Adams (2015), Occupancy patterns of mammals and lentic amphibians in the elwha river riparian zone before dam removal, *River research and applications*, *31*(2), 193–206.

Jerolmack, D. J., and D. Mohrig (2007), Conditions for branching in depositional rivers, *Geology*, *35*(5), 463–466.

Jerolmack, D. J., and C. Paola (2007), Complexity in a cellular model of river avulsion, *Geomorphology*, *91*(3), 259–270.

Jordan, P., and O. Slaymaker (1991), Holocene sediment production in lillooet river basin, british colombia: A sediment budget approach, *Géographie physique et Quaternaire*, *45*(1), 45–57.

Kaless, G., L. Mao, and M. Lenzi (2014), Regime theories in gravel-bed rivers: models, controlling variables, and applications in disturbed italian rivers, *Hydrological Processes*, *28*(4), 2348–2360.

Khaliq, M., T. Ouarda, J.-C. Ondo, P. Gachon, and B. Bobée (2006), Frequency analysis of a sequence of dependent and/or non-stationary hydro-meteorological observations: A review, *Journal of hydrology*, *329*(3), 534–552.

Kiem, A. S., S. W. Franks, and G. Kuczera (2003), Multi-decadal variability of flood risk, *Geophysical Research Letters*, *30*(2).

Kleinhans, M., H. Jagers, E. Mosselman, and C. Sloff (2008), Bifurcation dynamics and avulsion duration in meandering rivers by one-dimensional and three-dimensional models, *Water resources research*, *44*(8).

Kloehn, K. K., T. J. Beechie, S. A. Morley, H. J. Coe, and J. J. Duda (2008), Influence of dams on river-floodplain dynamics in the elwha river, washington, *Northwest Science*, *82*(sp1), 224–235.

Knighton, D. (1998), Fluvial forms and processes: London, *Edward Arnold*.

Kondolf, G., H. Piégay, and N. Landon (2002), Channel response to increased and decreased bedload supply from land use change: contrasts between two catchments, *Geomorphology*, *45*(1), 35–51.

Konrad, C., H. Berge, R. Fuerstenberg, K. Steff, T. Olsen, and J. Guyenet (2011), Channel dynamics in the middle green river, washington, from 1936 to 2002, *Northwest Science*, *85*(1), 1–14.

Konrad, C. P. (2009), Simulating the recovery of suspended sediment transport and river-bed stability in response to dam removal on the elwha river, washington, *Ecological Engineering*, *35*(7), 1104–1115.

Konrad, C. P. (2012), Reoccupation of floodplains by rivers and its relation to the age structure of floodplain vegetation, *Journal of Geophysical Research: Biogeosciences (2005–2012)*, *117*(G4).

Krapesch, G., C. Hauer, and H. Habersack (2011), Scale orientated analysis of river width changes due to extreme flood hazards, *Natural Hazards and Earth System Sciences*, *11*(8), 2137.

Lane, E. (1955), Design of stable channels, *Transactions of the American Society of Civil Engineers*, *120*, 1234–1279.

Lauer, J., and G. Parker (2008a), Modeling framework for sediment deposition, storage, and evacuation in the floodplain of a meandering river: Theory, *Water Resources Research*, *44*.

Lauer, J. W., and G. Parker (2008b), Net local removal of floodplain sediment by river meander migration, *Geomorphology*, *96*(1), 123–149.

Lauer, J. W., E. Viparelli, and H. Piégay (2016), Morphodynamics and sediment tracers in 1-d (mast-1d): 1-d sediment transport that includes exchange with an off-channel sediment reservoir, *Advances in Water Resources*, *93*, 135–149.

Lauer, J. W., C. Echterling, C. Lenhart, P. Belmont, and R. Rausch (2017), Air-photo based change in channel width in the minnesota river basin: Modes of adjustment and implications for sediment budget, *Geomorphology*, *297*, 170–184.

Lenzi, M., L. Mao, and F. Comiti (2006), Effective discharge for sediment transport in a mountain river: computational approaches and geomorphic effectiveness, *Journal of Hydrology*, *326*(1), 257–276.

Leopold, L., and T. J. Maddock (1953), The hydraulic geometry of stream channels and some physiographic implications.

Lisle, T. E. (1982), Effects of aggradation and degradation on riffle-pool morphology in natural gravel channels, northwestern california, *Water Resources Research*, *18*(6), 1643–1651.

Lisle, T. E., Y. Cui, G. Parker, J. E. Pizzuto, and A. M. Dodd (2001), The dominance of dispersion in the evolution of bed material waves in gravel-bed rivers, *Earth Surface Processes and Landforms*, *26*(13), 1409–1420.

Litzow, M. A. (2006), Climate regime shifts and community reorganization in the gulf of alaska: how do recent shifts compare with 1976/1977?, *ICES Journal of Marine Science: Journal du Conseil*, *63*(8), 1386–1396.

Liu, M., J. C. Adam, and A. F. Hamlet (2013), Spatial-temporal variations of evapotranspiration and runoff/precipitation ratios responding to the changing climate in the pacific northwest during 1921-2006, *Journal of Geophysical Research: Atmospheres*, *118*(2), 380–394.

Luce, C. H., and Z. A. Holden (2009), Declining annual streamflow distributions in the pacific northwest united states, 1948–2006, *Geophysical Research Letters*, *36*(16).

MacKenzie, L. G., and B. C. Eaton (2017), Large grains matter: contrasting bed stability and morphodynamics during two nearly identical experiments, *Earth Surface Processes and Landforms*.

Madej, M. A., D. G. Sutherland, T. E. Lisle, and B. Pryor (2009), Channel responses to varying sediment input: A flume experiment modeled after redwood creek, california, *Geomorphology*, *103*(4), 507–519.

Magilligan, F. J., and K. H. Nislow (2005), Changes in hydrologic regime by dams, *Geomorphology*, *71*(1), 61–78.

Magirl, C. S., R. C. Hilldale, C. A. Curran, J. J. Duda, T. D. Straub, M. Domanski, and J. R. Foreman (2015), Large-scale dam removal on the elwha river, washington, usa: Fluvial sediment load, *Geomorphology*, *246*, 669–686.

Major, J. J., J. E. OConnor, C. J. Podolak, M. K. Keith, G. E. Grant, K. R. Spicer, S. Pittman, H. M. Bragg, J. R. Wallick, D. Q. Tanner, et al. (2012), *Geomorphic response of the Sandy River, Oregon, to removal of Marmot Dam*, US Geological Survey.

Mantua, N. J., and S. R. Hare (2002), The pacific decadal oscillation, *Journal of oceanography*, *58*(1), 35–44.

Mantua, N. J., S. R. Hare, Y. Zhang, J. M. Wallace, and R. C. Francis (1997), A pacific interdecadal climate oscillation with impacts on salmon production, *Bulletin of the american Meteorological Society*, *78*(6), 1069–1079.

Mapes, L. (2013), *Elwha: A river reborn*, Mountaineers Books.

Martin, R. L., D. J. Jerolmack, and R. Schumer (2012), The physical basis for anomalous diffusion in bed load transport, *Journal of Geophysical Research: Earth Surface (2003–2012)*, *117*(F1).

Matalas, N. C. (1997), Stochastic hydrology in the context of climate change, in *Climate Change and Water Resources Planning Criteria*, pp. 89–101, Springer.

McCabe, G. J., M. A. Palecki, and J. L. Betancourt (2004), Pacific and atlantic ocean influences on multidecadal drought frequency in the united states, *Proceedings of the National Academy of Sciences*, *101*(12), 4136–4141.

McKean, J., and D. Tonina (2013), Bed stability in unconfined gravel bed mountain streams: With implications for salmon spawning viability in future climates, *Journal of Geophysical Research: Earth Surface*, *118*(3), 1227–1240.

McLean, D. G., and M. Church (1999), Sediment transport along lower fraser river: 2. estimates based on the long-term gravel budget, *Water Resources Research*, *35*(8), 2549–2559.

Merritt, D. M., and D. J. Cooper (2000), Riparian vegetation and channel change in response to river regulation: a comparative study of regulated and unregulated streams in the green river basin, usa, *River Research and Applications*, *16*(6), 543–564.

Micheli, E., and J. Kirchner (2002), Effects of wet meadow riparian vegetation on streambank erosion. 2. measurements of vegetated bank strength and consequences for failure mechanics, *Earth Surface Processes and Landforms*, *27*(7), 687–697.

Millar, R. G., and M. C. Quick (1993), Effect of bank stability on geometry of gravel rivers, *Journal of Hydraulic Engineering*, *119*(12), 1343–1363.

Milly, P. C., J. Betancourt, M. Falkenmark, R. M. Hirsch, Z. W. Kundzewicz, D. P. Lettenmaier, and R. J. Stouffer (2008), Stationarity is dead: Whither water management?, *Science*, *319*(5863), 573–574.

Miori, S., R. Repetto, and M. Tubino (2006), A one-dimensional model of bifurcations in gravel bed channels with erodible banks, *Water Resources Research*, *42*(11).

Montgomery, D. R., and M. T. Brandon (2002), Topographic controls on erosion rates in tectonically active mountain ranges, *Earth and Planetary Science Letters*, *201*(3), 481–489.

Moore, R. (1996), Snowpack and runoff responses to climatic variability, southern coast mountains, british columbia, *Northwest Science*, *70*(4), 321–333.

Morley, S. A., J. J. Duda, H. J. Coe, K. K. Kloehn, and M. L. McHenry (2008), Benthic invertebrates and periphyton in the elwha river basin: current conditions and predicted response to dam removal, *Northwest Science*, *82*, 179–196.

Mosher, D. C., and A. T. Hewitt (2004), Late quaternary deglaciation and sea-level history of eastern juan de fuca strait, cascadia, *Quaternary International*, *121*(1), 23–39.

Mosselman, E. (1992), Mathematical modeling of morphological processes in rivers with erodible banks, *Unpublished Ph. D. Thesis, Delft University of Technology*.

Mote, P. W. (2003), Trends in snow water equivalent in the pacific northwest and their climatic causes, *Geophysical Research Letters*, *30*(12).

Mote, P. W. (2006), Climate-driven variability and trends in mountain snowpack in western north america*, *Journal of Climate*, *19*(23), 6209–6220.

Mote, P. W., A. F. Hamlet, M. P. Clark, and D. P. Lettenmaier (2005), Declining mountain snowpack in western north america*, *Bulletin of the American meteorological Society*, *86*(1), 39–49.

Munn, M. D., R. Black, A. Haggland, M. Hummling, and R. Huffman (1999), An assessment of stream habitat and nutrients in the elwha river basin: implications for restoration, *Tech. rep.*, US Dept. of the Interior, US Geological Survey; Branch of Information Services [distributor],.

Naik, P. K., and D. A. Jay (2011), Distinguishing human and climate influences on the columbia river: changes in mean flow and sediment transport, *Journal of hydrology*, *404*(3), 259–277.

Nanson, G. C., and E. J. Hickin (1986), A statistical analysis of bank erosion and channel migration in western canada, *Geological Society of America Bulletin*, *97*(4), 497–504.

Nelson, J. M., J. P. Bennett, and S. M. Wiele (2003), Flow and sediment-transport modeling, *Tools in fluvial geomorphology*, *18*, 539–576.

Newman, M., G. P. Compo, and M. A. Alexander (2003), Enso-forced variability of the pacific decadal oscillation, *Journal of Climate*, *16*(23), 3853–3857.

Newman, M., M. A. Alexander, T. R. Ault, K. M. Cobb, C. Deser, E. Di Lorenzo, N. J. Mantua, A. J. Miller, S. Minobe, H. Nakamura, et al. (2016), The pacific decadal oscillation, revisited, *Journal of Climate*, (2016).

Nicoll, T. J., and E. J. Hickin (2010), Planform geometry and channel migration of confined meandering rivers on the canadian prairies, *Geomorphology*, *116*(1), 37–47.

Nones, M., P. Ronco, and G. Di Silvio (2013), Modelling the impact of large impoundments on the lower zambezi river, *International journal of river basin management*, *11*(2), 221–236.

O'Connor, J. E., M. A. Jones, and T. L. Haluska (2003), Flood plain and channel dynamics of the quinault and queets rivers, washington, usa, *Geomorphology*, *51*(1), 31–59.

O'Connor, J. E., J. J. Duda, and G. E. Grant (2015), 1000 dams down and counting, *Science*, *348*(6234), 496–497.

Osterkamp, W., and C. Hupp (2010), Fluvial processes and vegetationglimpses of the past, the present, and perhaps the future, *Geomorphology*, *116*(3), 274–285.

Overland, J., S. Rodionov, S. Minobe, and N. Bond (2008), North pacific regime shifts: Definitions, issues and recent transitions, *Progress in Oceanography*, *77*(2), 92–102.

Overland, J. E., and M. Wang (2007), Future climate of the north pacific ocean, *Eos, Transactions American Geophysical Union*, *88*(16), 178–182.

Pagano, T., and D. Garen (2005), A recent increase in western us streamflow variability and persistence, *Journal of Hydrometeorology*, *6*(2), 173–179.

Parker, G., Y. Shimizu, G. Wilkerson, E. Eke, J. Abad, J. Lauer, C. Paola, W. Dietrich, and V. Voller (2011), A new framework for modeling the migration of meandering rivers, *Earth Surface Processes and Landforms*, *36*(1), 70–86.

Pasquale, N., P. Perona, R. Francis, and P. Burlando (2012), Effects of streamflow variability on the vertical root density distribution of willow cutting experiments, *Ecological engineering*, *40*, 167–172.

Perona, P., P. Molnar, M. Savina, and P. Burlando (2009), An observation-based stochastic model for sediment and vegetation dynamics in the floodplain of an alpine braided river, *Water Resources Research*, *45*(9).

Perona, P., P. Molnar, B. Crouzy, E. Perucca, Z. Jiang, S. McLelland, D. Wüthrich, K. Edmaier, R. Francis, C. Camporeale, et al. (2012), Biomass selection by floods and related timescales: Part 1. experimental observations, *Advances in Water Resources*, *39*, 85–96.

Pess, G. R., M. L. McHenry, T. J. Beechie, and J. Davies (2008), Biological impacts of the elwha river dams and potential salmonid responses to dam removal, *Northwest Science*, *82*, 72–90.

Pfeiffer, A. M., N. J. Finnegan, and J. K. Willenbring (2017), Sediment supply controls equilibrium channel geometry in gravel rivers, *Proceedings of the National Academy of Sciences*, *114*(13), 3346–3351.

Phillips, J. D. (2002), Geomorphic impacts of flash flooding in a forested headwater basin, *Journal of Hydrology*, *269*(3), 236–250.

Piechota, T. C., J. A. Dracup, and R. G. Fovell (1997), Western us streamflow and atmospheric circulation patterns during el niño-southern oscillation, *Journal of Hydrology*, *201*(1), 249–271.

Pizzuto, J. E. (1990), Numerical simulation of gravel river widening, *Water Resources Research*, *26*(9), 1971–1980.

Poff, N. L., J. D. Olden, D. M. Merritt, and D. M. Pepin (2007), Homogenization of regional river dynamics by dams and global biodiversity implications, *Proceedings of the National Academy of Sciences*, *104*(14), 5732–5737.

Pohl, M. (2004), Channel bed mobility downstream from the elwha dams, washington, *The Professional Geographer*, *56*(3), 422–431.

Polenz, M., K. W. Wegmann, and H. W. Schasse (2004), *Geologic map of the Elwha and Angeles Point 7.5-minute quadrangles, Clallam County, Washington*, Washington State Division of Geology and Earth Resources.

Randle, T. J., J. A. Bountry, A. Ritchie, and K. Wille (2015), Large-scale dam removal on the elwha river, washington, usa: Erosion of reservoir sediment, *Geomorphology*, *246*, 709–728.

Reidy-Liermann, C., J. D. Olden, T. Beechie, M. J. Kennard, P. Skidmore, C. Konrad, and H. Imaki (2012), Hydrogeomorphic classification of washington state rivers to support emerging environmental flow management strategies, *River Research and Applications*, *28*(9), 1340–1358.

Rinaldi, M., B. Mengoni, L. Luppi, S. E. Darby, and E. Mosselman (2008), Numerical simulation of hydrodynamics and bank erosion in a river bend, *Water Resources Research*, *44*(9).

Robertson, K. M., and C. K. Augspurger (1999), Geomorphic processes and spatial patterns of primary forest succession on the bogue chitto river, usa, *Journal of Ecology*, *87*(6), 1052–1063.

Rubin, Z. K., G. M. Kondolf, and P. A. Carling (2015), Anticipated geomorphic impacts from mekong basin dam construction, *International Journal of River Basin Management*, *13*(1), 105–121.

Salas, J. D., and J. Obeysekera (2014), Revisiting the concepts of return period and risk for nonstationary hydrologic extreme events, *Journal of Hydrologic Engineering*, *19*(3), 554–568.

Serinaldi, F., and C. G. Kilsby (2015), Stationarity is undead: Uncertainty dominates the distribution of extremes, *Advances in Water Resources*, *77*, 17–36.

Sichingabula, H. M. (1999), Magnitude-frequency characteristics of effective discharge for suspended sediment transport, fraser river, british columbia, canada, *Hydrological processes*, *13*(9), 1361–1380.

Sklar, L. S., W. E. Dietrich, E. Foufoula-Georgiou, B. Lashermes, and D. Bellugi (2006), Do gravel bed river size distributions record channel network structure?, *Water resources research*, *42*(6).

Slaymaker, H. O. (1972), Recent fluctuations in the mean discharge of the fraser river, *Contemporary Geography: Research Trends. BC Geographical Series*, (16).

Stoffel, M., D. Conus, M. A. Grichting, I. Lièvre, and G. Maître (2008), Unraveling the patterns of late holocene debris-flow activity on a cone in the swiss alps: chronology, environment and implications for the future, *Global and Planetary Change*, *60*(3), 222–234.

Stoffel, M., T. Mendlik, M. Schneuwly-Bollschweiler, and A. Gobiet (2014), Possible impacts of climate change on debris-flow activity in the swiss alps, *Climatic change*, *122*(1-2), 141–155.

Sutherland, A. J. (1967), Proposed mechanism for sediment entrainment by turbulent flows, *Journal of Geophysical Research*, *72*(24), 6183–6194.

Swanson, B. J., G. A. Meyer, and J. E. Coonrod (2011), Historical channel narrowing along the rio grande near albuquerque, new mexico in response to peak discharge reductions and engineering: magnitude and uncertainty of change from air photo measurements, *Earth Surface Processes and Landforms*, *36*(7), 885–900.

Tabor, R. W. (1987), *Geology of Olympic National Park*, Pacific Northwest National Parks & Forests Association.

Tabor, R. W., and W. M. Cady (1978), Geologic map of the olympic peninsula, washington, *Tech. rep.*

Tealdi, S., C. Camporeale, and L. Ridolfi (2011), Modeling the impact of river damming on riparian vegetation, *Journal of hydrology*, *396*(3), 302–312.

Thorne, C. (1982), *Gravel-bed rivers*, chap. Processes and mechanisms of river bank erosion, pp. 227–271, John Wiley & Sons, Inc.

Torizzo, M., and J. Pitlick (2004), Magnitude-frequency of bed load transport in mountain streams in colorado, *Journal of Hydrology*, *290*(1), 137–151.

Trenberth, K. E. (1990), Recent observed interdecadal climate changes in the northern hemisphere, *Bulletin of the American Meteorological Society*, *71*(7), 988–993.

Tsujimoto, T. (1999), Fluvial processes in streams with vegetation, *Journal of hydraulic research*, *37*(6), 789–803.

Tucker, G. E., and G. R. Hancock (2010), Modelling landscape evolution, *Earth Surface Processes and Landforms*, *35*(1), 28–50.

Tullos, D., and H.-W. Wang (2014), Morphological responses and sediment processes following a typhoon-induced dam failure, dahan river, taiwan, *Earth Surface Processes and Landforms*, *39*(2), 245–258.

Tunnicliffe, J. F., and M. Church (2015), A 1-d morphodynamic model of postglacial valley incision, *Journal of Geophysical Research: Earth Surface*, *120*(11), 2253–2279.

Van De Wiel, M. J., and S. E. Darby (2004), Numerical modeling of bed topography and bank erosion along tree-lined meandering rivers, *Riparian vegetation and fluvial geomorphology*, pp. 267–282.

Verhaar, P. M., P. M. Biron, R. I. Ferguson, and T. B. Hoey (2008), A modified morphodynamic model for investigating the response of rivers to short-term climate change, *Geomorphology*, *101*(4), 674–682.

Villarini, G., F. Serinaldi, J. A. Smith, and W. F. Krajewski (2009), On the stationarity of annual flood peaks in the continental united states during the 20th century, *Water Resources Research*, *45*(8).

Viparelli, E., D. Gaeuman, P. Wilcock, and G. Parker (2011), A model to predict the evolution of a gravel bed river under an imposed cyclic hydrograph and its application to the trinity river, *Water Resources Research*, *47*(2).

Warrick, J. A., J. A. Bountry, A. E. East, C. S. Magirl, T. J. Randle, G. Gelfenbaum, A. C. Ritchie, G. R. Pess, V. Leung, and J. J. Duda (2015), Large-scale dam removal on the elwha river, washington, usa: source-to-sink sediment budget and synthesis, *Geomorphology*, *246*, 729–750.

Whitfield, P. H., R. Moore, S. W. Fleming, and A. Zawadzki (2010), Pacific decadal oscillation and the hydroclimatology of western canadareview and prospects, *Canadian Water Resources Journal*, *35*(1), 1–28.

Wilcock, P., J. Pitlick, and Y. Cui (2009), Sediment transport primer: estimating bed-material transport in gravel-bed rivers.

Wilcock, P. R., and J. C. Crowe (2003), Surface-based transport model for mixed-size sediment, *Journal of Hydraulic Engineering*, *129*(2), 120–128.

Wilcock, P. R., and B. W. McArdell (1993), Surface-based fractional transport rates: Mobilization thresholds and partial transport of a sand-gravel sediment, *Water Resources Research*, *29*(4), 1297–1312.

Wilcox, A. C., J. E. O'Connor, and J. J. Major (2014), Rapid reservoir erosion, hyperconcentrated flow, and downstream deposition triggered by breaching of 38 m tall condit dam, white salmon river, washington, *Journal of Geophysical Research: Earth Surface*, *119*(6), 1376–1394.

Williams, G. P., and M. G. Wolman (1984), Downstream effects of dams on alluvial rivers.

Wolman, M., and J. Miller (1960), Magnitude and frequency of forces in geomorphic processes, *Journal of Geology*, *68*, 54–74.

Wolman, M. G., and R. Gerson (1978), Relative scales of time and effectiveness of climate in watershed geomorphology, *Earth Surface Processes and Landforms*, *3*(2), 189–208.

Zhang, Y., J. M. Wallace, and D. S. Battisti (1997), Enso-like interdecadal variability: 1900-93, *Journal of climate*, *10*(5), 1004–1020.

Appendix A

MAST-1D model description

A.1 Introduction

MAST-1D (morphodynamic and sediment tracers in 1-D) is a bed evolution model where the channel and floodplain are coupled. Details can be found in the original publications (*Lauer and Parker*, 2008a,b; *Lauer et al.*, 2016).

MAST-1D is designed to model long spatial (10s to 100s km) and temporal (decades-millenia) timescales where bank erosion and channel migration allow for channel sediment to be sourced and stored within the floodplain. The channel (active layer), substrate, and floodplain are treated as a set of reservoirs, each with a characteristic geometry, volume, and grainsize distribution. Mass is conserved within each reservoir on a size-specific basis. Channel exchange occurs between reservoirs via longitudinal sediment transport, bank erosion, channel narrowing, avulsion, and bed elevation change, all of which are functions of an imposed water discharge.

A model schematic is presented in Figure A.1. The model space is structured into a series of nodes aligned in the longitudinal direction. During each time step, the outgoing sediment load in the upstream node is calculated. It is a function of the sediment transport capacity of the active layer reservoir and the depositional properties of the floodplain. When the flow is high enough to overtop the banks, some sediment is deposited in the floodplain reservoir as overbank material. The rest is transported downstream and becomes the incoming flux to the next node. Once transport is calculated, lateral exchanges of sediment between reservoirs are characterized for each node. When flow strength is low, we assume that the bed is stable and that vegetation is able to grow on channel surfaces. This leads to transfer of sediment into the floodplain from a point bar deposit, which is composed of material from the active layer reservoir and the sediment load. The point bar is assumed to have a single constant height. Floodplain sediment is transferred to the active layer reservoir via bank erosion when flow is strong enough to mobilize bank material. Net fluxes to and from the active layer, from the incoming and outgoing sediment load and from bank erosion, are calculated to de-

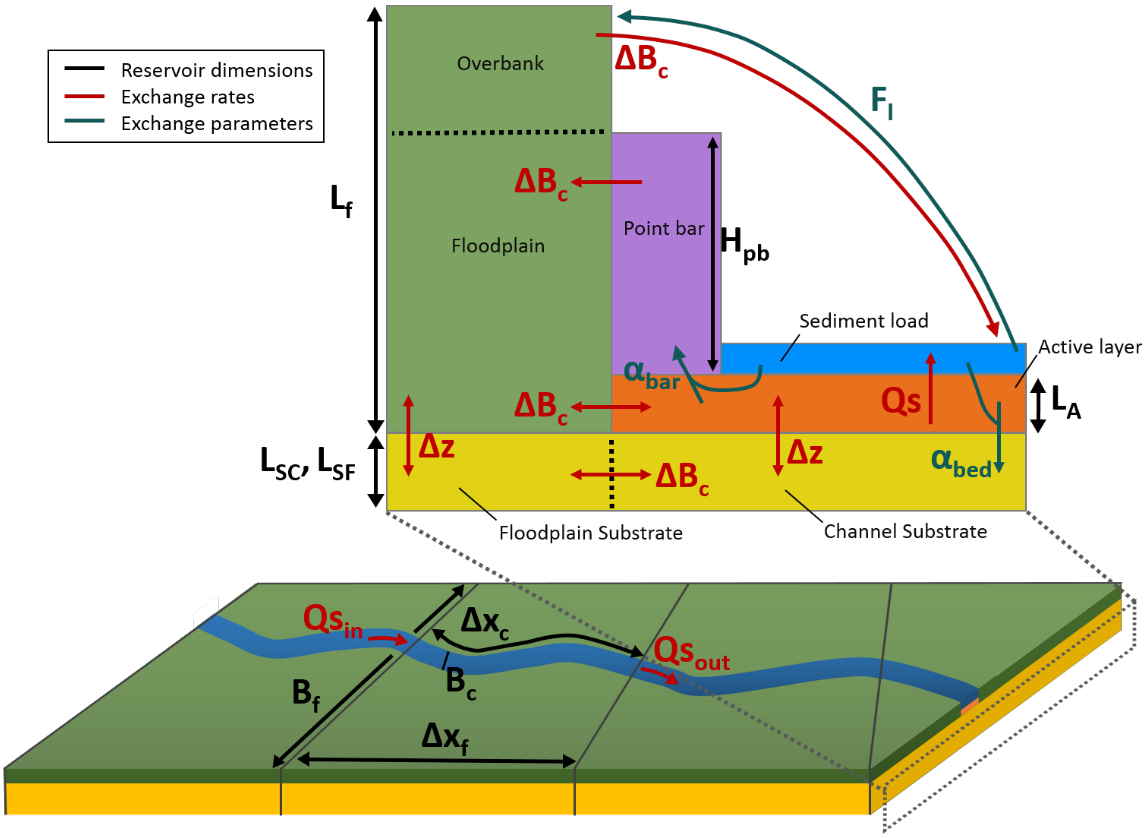

Figure A.1: Model schematic

termine changes in bed elevation (z) and channel width (B_c). When input to the active layer exceeds output, aggradation occurs and the underlying channed substrate increases in thickness. When sediment transport capacity is greater than supply to the active layer, the channel degrades and substrate material is incorporated into the active layer.

In MAST-1D, flow strength is calculated from an imposed discharge, which can be represented either by a stepped flow duration curve or a hydrograph. When using a the latter, flow strength, sediment transport, and reservoir exchanges are determined using each discharge value in turn. Each flow is imposed over a number of timesteps that cumulatively equal the temporal resolution of the discharge record (e.g. if a daily discharge record is used and each model time step is 0.25 days, then 4 time steps will be performed for each discharge). When a flow duration curve is used, the discharge record is divided into bins that are assigned a time-averaged duration. Flow strength, sediment transport capacity, and reservoir exchanges are determined for each discharge in turn, and the total flux for each exchange is the duration-weighted average of all imposed flows. While the flow duration curve does not account for temporal variability in the hydrologic regime, it is more numerically stable and allows MAST-1D to run much faster. For both flow algorithms, we assume that the channel is rectangular and that sediment distribution within each reservoir is spatially homogenous.

Full details of the model are divided into three sections. First, the model steps are listed in order with references to the equations used. Then, the governing equations for flow, sediment transport, and reservoir exchange are presented in detail. Finally, methods for determining initial model conditions are highlighted.

A.2 Model procedure

The model steps proceed as follows:

1. Boundary conditions are set using Equations A.88-A.90. The upstream boundary is an imposed size-specific sediment load. The downstream water surface elevation is imposed, either as a constant (i.e. in the case of a downstream control such as a dam) or as a function of discharge.

2. The floodplain number (*Lauer and Parker*, 2008a), which is a parameter that determines the ability of the floodplain to trap overbank material, is either calculated with Equations A.91-A.92 or set by the user. The initial floodplain grainsize distribution is set to reflect long-term steady-state conditions with Equations A.93-A.94.

3. Hydraulics are calculated for the entire reach using the standard step backwater method (Equations A.1-A.16).

4. Bedload transport for the upstream-most node is determined with Equations A.17-A.25.

5. Equations A.43-A.47 are used to calculate rates of channel widening and narrowing.

6. Lateral reservoir exchange rates are calculated with Equations A.48-A.49 and A.51-A.58. These include exchanges between the floodplain and active layer due to bank erosion and channel narrowing.

7. The Exner equation (Equation A.59) is solved to determine whether the channel is aggrading or degrading. Vertical exchange rates between the substrate, active layer, and floodplain reservoirs are determined using Equations A.60-A.64.

8. The suspended sediment concentration and deposition rate is determined with Equations A.26-A.28 and A.40.

9. Volumes and grainsize distributions of the reservoirs are updated using Equations A.70-A.72.

10. Equations A.74-A.78 are used to update channel geometry. If the conditions for avulsion are met, Equations A.83-A.87 are used to adjust reservoir dimensions and grainsizes.

11. Equations A.79-A.82 are used to split or combine substrate layers. If the thickness of the uppermost substrate layer becomes thicker than a threshold, it is split into two stratigraphic units. If the thickness dips below a threshold, it is combined with the stratigraphic unit below it.

12. If the net amount of channel degradation drops below a critical value and the node designated as bedrock-influenced, then the node becomes partly alluvial. In future steps, partly alluvial transport is calculated as a function of the bed that is alluvial. When the volume of sediment in the active layer of the partly-alluvial node reaches its capacity, then the node becomes fully alluvial.

13. The sediment transport rates $Q_{s,i}$ and $Q_{s,w}$ are set as the feed for the next node in the downstream direction. Steps 4-12 are repeated for all nodes.

14. The boundary conditions are changed if needed by the user. Steps 3-13 are repeated for the specified number of timesteps or discharges.

A.3 Governing equations

A.3.1 Hydraulics

Hydraulics are calculated using the standard-step method applied to the backwater equation, assuming steady, gradually-varied, subcritical flow. The water surface elevation (WSE) of the downstream-most node is provided as a boundary condition (see Section A.4.1), and conservation of energy is used to determine the WSE of the next node upstream. The WSE of the second node is then used to calculate the third node upstream, and so on. The procedure was adapted from that used in the HEC-RAS model (*Brunner*, 2016).

Calculation of flow depth and velocity

Hydraulics between each node are calculated using the 1-dimensional form of the Bernoulli Equation:

$$z_2 + y_2 + \frac{\alpha_{v,2}\bar{v}_2^2}{2g} = z_1 + y_1 + \frac{\alpha_{v,1}\bar{v}_1^2}{2g} + h_e \tag{A.1}$$

The subscript 1 denotes the downstream node, while 2 represents the upstream node. z and y are bed elevation and flow depth, respectively, and WSE = $z + y$. $\bar{v}$ is average velocity over the node cross-section, g represents gravitational acceleration, α_v is a weighting coefficient that accounts for the partitioning of average velocity between the channel and floodplain, and h_e denotes the energy loss between the upstream and downstream nodes.

The channel cross-section is divided into two parts: the channel and the floodplain, each with a characteristic roughness. The mean kinetic energy head ($\alpha_v \frac{\bar{v}_2^2}{2g}$) is defined as the discharge-weighted average between the velocity heads of the two sections:

$$\alpha_v \frac{\bar{v}^2}{2g} = \frac{Q_c \frac{v_c^2}{2g} + Q_f \frac{v_f^2}{2g}}{Q_c + Q_f} \tag{A.2}$$

where Q_c and Q_f are the discharges over the channel and floodplain zones, respectively, and v_c and v_f are the corresponding velocities. If we rewrite v in terms of Q and flow area A:

$$v = \frac{Q}{A} \tag{A.3}$$

and

$$\bar{v} = \frac{Q}{A_c + A_f}, \tag{A.4}$$

then we can use the Manning Equation:

$$Q = KS_f^{1/2} \tag{A.5}$$

to reformulate equation A.2 in terms of area and conveyance K, which is defined as

$$K = \frac{1}{n} AR^{2/3} \tag{A.6}$$

R is the hydraulic radius, estimated as the flow depth y (assuming a wide channel) and n is the Manning coefficient. For the channel, it is calculated using a modified form of the Strickler relation:

$$n_c = C_{n,m}(0.0146 D_{65}^{1/6} + C_{n,a}) \tag{A.7}$$

where D_{65} is the 65th percentile of the bed material grainsize distribution and $C_{n,a}$ and $C_{n,m}$ are user-defined constants that account for roughness due to form drag and sinuosity. The Manning coefficient for the floodplain in each node is a user-defined constant.

The energy slope (S_f) is assumed to be constant between the two nodes and is defined as:

$$S_f = \Big(\frac{Q_1 + Q_2}{K_{c,1} + K_{f,1} + K_{c,2} + K_{f,2}}\Big)^2 \tag{A.8}$$

Using values of A and K calculated for the channel and floodplain, we can solve for α:

$$\alpha_v = \frac{(A_c + A_f)^2 [\frac{K_c^3}{A_c^2} + \frac{K_f^3}{A_f^2}]}{(K_c + K_f)^2} \tag{A.9}$$

The energy loss (h_e) between the upstream and downstream nodes is a function of both friction and expansion/contraction. We are ignoring the effects of expansion and contraction so that

h_e depends on friction only:

$$h_e = \frac{\Delta x(Q_{c,1} + Q_{c,2}) + \Delta x \chi (Q_{f,1} + Q_{f,2})}{Q_{c,1} + Q_{f,1} + Q_{c,2} + Q_{f,2}} \tag{A.10}$$

where Δx is the length of channel in the node and χ is the channel sinuosity. Finally, Equations A.4, A.9, and A.10 can be substituted into Equation A.1 to solve for the WSE of the upstream node, $z_2 + y_2$.

Iteration procedure

Equation A.1 cannot be solved using direct methods, so iteration must be used to converge on the proper WSE. An initial guess is made for y_2 (usually as the flow depth from the previous timestep). Then the respective channel area for both the upstream and downstream nodes are calculated as

$$A_c = y * B_c \tag{A.11}$$

and the floodplain areas are

$$A_f = B_f[y - (L_f - L_a)] \tag{A.12}$$

where B_c is the channel width, B_f is the width of the floodplain, L_f is the height of the floodplain, and L_a is the thickness of the active layer.

Equation A.1 is solved for y_2, and the error is calculated as the difference between the input and output y_2 values. The error divided by a user-defined stabilizing term is subtracted from the input y_2 term to create the y_2 for the next iteration. This continues until the error is less than .001 m.

Finally, the values from the final iteration are input into the Manning Equation, resulting in the friction slope and discharge for the node:

$$S_f = (\frac{Q}{K_c + K_f})^2, \tag{A.13}$$

$$Q_c = Q(\frac{K_c}{K_c + K_f}), \tag{A.14}$$

$$Q_f = Q - Q_c, \tag{A.15}$$

and

$$y_f = y_c - (L_f + L_a) \tag{A.16}$$

where y_f is the flow depth on the floodplain. Channel velocity (V_c) is calculated using Equation A.3, with the Q_c and A_c.

A.3.2 Sediment transport

There are two forms of sediment transport in MAST-1D, bedload transport and suspended load. In this implementation, it is assumed that all silt and clay (termed washload here) travels as suspension, regardless of discharge. Sand and gravel may also travel in suspension and be deposited on the floodplain depending on the flow conditions.

Bedload

Bedload transport is calculated using the *Gaeuman et al.* (2009) equations, which are a form of the Wilcock and Crowe equations that are suitable for large, cobble-bed streams. The sediment transport rate is a function of the excess channel-wide shear stress over a grainsize-dependent threshold. The shear stress exerted on the sediment grains (the skin friction, or τ') is calculated following the method in the BAGS Primer (*Wilcock et al.*, 2009) as

$$\tau' = 0.00148\rho * g * (2S_f * D_{65})^{0.25} V_c^{1.5} \tag{A.17}$$

where ρ is the density of water, set at 1000 kg/m^3 and V_c is channel velocity. The dimensionless reference shear stress for the mean particle size τ^*_{rm} is

$$\tau^*_{rm} = 0.03 + \frac{0.022}{1 + e^{7.1\sigma_{SG} - 1.66}} \tag{A.18}$$

σ_{SG} is the standard deviation of the sediment grainsize on the psi scale. This is converted into a dimensional reference shear stress (τ_{rm}) using the Shields equation:

$$\tau_{rm} = \tau^*_{rm}(\rho_s - \rho) g D_g \tag{A.19}$$

where ρ_s is sediment density and D_g is the mean particle size. A hiding function is used to calculate the reference shear stress for each particle size:

$$\tau_{ri} = \tau_{rm} \left(\frac{D_i}{D_{50}}\right)^b \tag{A.20}$$

where τ_{ri} is the reference shear stress and D_i is the grain diameter for size class i and

$$b = \frac{0.7}{1 + e^{1.9 - D_i/3D_g}} \tag{A.21}$$

where D_g is the mean grain size. The dimensionless transport rate for each size class i depends on ϕ_i, the ratio between the shear stress and the reference shear stress for that size, where

$$\phi_i = \frac{\tau'}{\tau_{ri}} \tag{A.22}$$

The equation is

$$w_i^* = \begin{cases} 0.002\phi_i^{7.5}, & \phi_i < 1.35 \\ 14(1 - \frac{0.894}{\phi_i^{0.5}})^{4.5}, & \phi_i \geq 1.35 \end{cases} \tag{A.23}$$

The fractional transport rate is then put into dimensional form and multiplied by its fraction in the bed:

$$q_{s,i} = f_i \frac{w_i^* u^{*3} B_c \rho}{g(\rho_s - \rho)} \tag{A.24}$$

where $q_{s,i}$ is the sediment transport rate for size class i and u^* is the shear velocity, which is

$$u^* = \left(\frac{\tau}{\rho}\right)^{0.5} \tag{A.25}$$

Washload

Sediment can enter the suspended load in two ways: 1) via bank erosion, and 2) as incoming load from upstream. It is assumed that washload sediment is neither entrained from nor deposited on the channel bed. It may be deposited on the point bar and thus transferred to the floodplain through lateral migration, or it may be deposited directly on the floodplain through overbank deposition (see Section A.3.4). Washload sediment is not entrained from the floodplain; the only mechanism for moving washload from the floodplain to the channel is through bank erosion. The amount of deposition on the floodplain is a function of the sediment concentration in the overbank flow scaled by a constant floodplain number (Section A.4.2):

$$d_w = \frac{FCQ_f}{B_f} \tag{A.26}$$

where d_w is the average amount of washload sediment deposited on the floodplain per unit channel length, F is the floodplain number and C is the suspended sediment concentration,

$$C = \frac{q_{w,in}}{Q_c} \tag{A.27}$$

where $q_{w,in}$ is the incoming suspended sediment from the upstream node or boundary feed. The suspended sediment transport rate (q_w) is calculated via conservation of mass:

$$q_w = (f_{SAL,w} I_{v,SAL,w} + f_{FP,w} \frac{E}{\Delta t} + f_{PB,w} \frac{N}{\Delta t} + q_{w,in} - d_w \Delta x) \tag{A.28}$$

where $I_{v,SAL,w}$ is the incoming substrate sediment due to vertical channel change (Section A.3.4), $\frac{E}{\Delta t}$ and $\frac{N}{\Delta t}$ are rates of widening and narrowing, respectively, and Δx is the length of the node. ($f_{SAL,w}$, $f_{FP,w}$, and $f_{PB,w}$ refer to the fractions of mud in the active layer, floodplain, and point bar, respectively). Note that $\frac{N}{\Delta t}$ is negative.

Suspended sand and gravel

If flooding occurs and turbulence is strong enough so that the diffusive forces lifting particles exceed gravitational forces, some sediment travels in suspension and is deposited on the floodplain. The gravitational forces acting on the grain are characterized by its settling velocity, which is calculated using the emperical formulation derived by *Dietrich et al.* (1982). The velocity is determined via a dimensionless parameter, $D*$, which quantifies the ratio between the gravitational force acting on the particle and the viscous properties of the flow:

$$D* = \frac{(\rho_s - \rho)(D * 10^{-3})^3 g}{\rho \nu^2} \tag{A.29}$$

where ν is the kinematic viscosity. The dimensionless velocity, W_i^*, is

$$W_i^* = \begin{cases} 10^a, & D*^2 > 0.5 \\ \frac{D*^2}{5832}, & D*^2 \leq 0.05 \end{cases} \tag{A.30}$$

where a is

$$a = 10^{-3.76715+1.92944 log(D*) - 0.09815[log(D*)]^2 - 0.00575[log(D*)]^3 + 0.00056[log(D*)]^4} \tag{A.31}$$

The settling velocity $v_{b,i}$ is

$$v_{b,i} = \Big(\frac{(\rho_s - \rho)}{\rho} W_i^* g \nu\Big)^{1/3} \tag{A.32}$$

To determine the amount of sediment that deposits on the floodplain, the proportion of total suspended sediment that is transported overbank must be calculated. To do so, a Rouse profile is created. We assume that sediment in the bottom 5% of the profile travels as bedload. By this definition, the suspended sediment transport rate within the channel that occurs below the top of the bank is

$$q_{s,b,i} = \int_{0.05}^{(L_F - L_{AL})/y} \frac{0.05(1-z)}{0.95z} Z dz \tag{A.33}$$

where y is the flow depth in the channel and Z is the Rouse number,

$$Z = \frac{v_{b,i}}{\kappa u^*} \tag{A.34}$$

where κ is the von Karman constant (0.4). The sediment transport rate above the level of the floodplain is

$$q_{s,o,i} = \int_{(L_F - L_{AL})/y}^{1} \frac{0.05(1-z)}{0.95z} Z dz \tag{A.35}$$

The total proportion of overbank suspended sediment that is transported above the level of the banks (P_o) is

$$P_o = \frac{0.95}{1 - (L_F - L_{AL})/y} * \frac{q_{s,o,i}}{q_{s,o,i} + q_{s,b,i}} \tag{A.36}$$

Equations A.33 and A.35 are discretized into 20 segments.

Only a portion of sand and gravel in any given size class travels in suspension. The rest saltates along the bed. We define the former portion with a constant, α_{FS}, which ranges between 0 and 1. The sediment concentration of size class i in the overbank water column is

$$C_i = \frac{q_{s,i,in}\alpha_{FS}P_o}{Q_c} \tag{A.37}$$

where $q_{s,i,in}$ is the incoming sediment feed in size class i. The fraction of overbank sediment that deposits on the floodplain per unit channel length is

$$d_i = \frac{F_{bed}C_iQ_f}{B_f} \tag{A.38}$$

where F_{bed} is the floodplain number for bed material, a constant.

Calculation of total transport and floodplain deposition

For each timestep, the total bedload sediment transport rates per size class, $Q_{s,i}$, is the weighted sum of the rates for each flow in the duration curve, so that

$$Q_{s,i} = \sum_{j=1}^{n} q_{i,j}p_j \tag{A.39}$$

where $q_{i,j}$ is the size-specific transport rate and p_j is the flow frequency for flow j, and n is the number of discharges in the flow duration curve. When running MAST-1D with a hydrograph, $n = 1$. $Q_{s,i}$ is calculated using Equation A.24. The total suspended sediment transport rate (Q_w) is

$$Q_{s,w} = \sum_{j=1}^{n} q_{w,j} \tag{A.40}$$

Equation A.28 is used to calculate $q_{w,j}$.

The overbank deposition rates d_w and d_i are also duration-averaged sums:

$$d_w = \sum_{j=1}^{n} d_{w,j}p_j \tag{A.41}$$

and

$$d_i = \sum_{j=1}^{n} d_{i,j}p_j \tag{A.42}$$

where $d_{w,j}$ and $d_{i,j}$ are solved for using Equations A.26 andA.38, respectively.

A.3.3 Width change

There are two components to width change that result in sediment exchanges: channel widening via erosion and narrowing from vegetation encroachment onto bars. When rates of erosion and vegetation growth are not equal, width change occurs. When they are equal, there is migration but no net change in width. The governing equations are briefly described here. Full details on the theory and rationale can be found in Chapter 2.

Channel widening

Our simple model of channel widening only relates bank erosion to sediment transport capacity. Channel widening occurs when a supply-normalized unit transport rate of the upper tail of the grainsize distribution, qs_{Cmax}, exceeds a threshold, qs_{cr}. We define the supply-normalized unit coarse transport rate as

$$qs_{Cmax} = qs_C / f_C \tag{A.43}$$

where qs_C is the unit sediment transport rate of the coarse end of the surface sediment mixture and f_C is the fraction of that group of sizes present in the bed. qs_C is calculated via the equations in Section A.3.2. qs_{Cmax} represents the transport rate expected with an unlimited supply of coarse sediment. There is currently no straightforward way to determine the threshold unit transport rate qs_{cr}, and for now it is a user-defined constant.

Once bank erosion is initiated ($qs_{Cmax} > qs_{cr}$, floodplain sediment mixes with the active layer adjacent to the bank, and the magnitude of bank erosion depends on the ability of the flow to transport this near-bank sediment. When coarse sediment supply from the bank exceeds the transport capacity, it will build up along the bank toe and protect it from further erosion. The near-bank sediment transport capacity, qs_{NB}, is a function of the grainsize distribution of the near bank region, which is defined by

$$f_{i,NB} = \alpha_f f_i + (1 - \alpha_f) f_{i,FP} \tag{A.44}$$

where $f_{i,NB}$ is the near-bank fraction of size class i, f_i is the fraction in the active layer, $f_{i,FP}$ is the fraction in the floodplain, and α_f is a mixing constant that ranges between 0 and 1. qs_{NB} is calculated using the bedload relations outlined in Section A.3.2, with $f_{i,NB}$ as the grainsize distribution. The portion of $qs_{i,NB}$ that transports coarse floodplain material, $qs_{C,FP}$, is

$$qs_{C,FP} = \frac{qs_{C,NB}}{f_{C,NB}} f_{C,FP} (1 - \alpha_f) \tag{A.45}$$

where $qs_{C,NB}$ is the unit coarse sediment transport rate of the near-bank mixture and $f_{C,FP}$ is the fraction of coarse material in the floodplain. The bank erosion rate ($E/\Delta t$) is

$$\frac{E}{\Delta t} = \begin{cases} 0, & qs_{Cmax} \leq qs_{cr} \\ (qs_{C,FP})/(L_F * f_{C,FP}), & qs_{Cmax} > qs_{cr} \end{cases} \tag{A.46}$$

Channel narrowing

The narrowing function is: Channel narrowing results from multiple interrelated processes, including deposition on bars, degradation leading to the development of benches, and encroachment of vegetation onto exposed surfaces. We assume that channel narrowing only occurs during relatively low flows. The rate of vegetation enroachment is treated as a constant, α_n:

$$\frac{N}{\Delta t} = \begin{cases} -\alpha_n * (B_c - B_{min}), & \tau < \tau_r \\ 0, & \tau \geq \tau_r \end{cases} \tag{A.47}$$

B_{min} is a constant user-defined minimum width and $B_c - B_{min}$ represents the unvegetated point bar. τ_r represents a reference shear stress, below which flow is low enough to leave surfaces exposed for colonization.

A.3.4 Sediment reservoir exchanges

There are five sediment reservoir types in MAST-1D: the load, active layer, floodplain, channel substrate, and floodplain substrate. There are multiple layers of substrate, and layers may be added, removed, and combined, depending on the evolution of the bed. Substrate is accounted for in two zones: one under the channel region and the other beneath the floodplain. The size-specific amount of sediment for all reservoirs except the load is determined by a conservation of mass equation:

$$\frac{\Delta V_r, i}{\Delta t} = (1 - \lambda)\frac{\Delta S_{r,i}}{\Delta t} \tag{A.48}$$

where V_r is the new volume of material size class i in reservoir r, λ is porosity, and $\Delta S_{r,i}$ is the change in storage of sediment in a given size class. $\Delta S_{r,i}$ is calculated as the difference between the inputs (I) and the outputs (O) during each timestep. For the floodplain and substrate types,

$$\Delta S_{r,i} = (I_{m,r,i} + I_{v,r,i}) - (O_{m,r,i} + O_{v,r,i}) \tag{A.49}$$

where $I_{m,r,i}$ and $O_{m,r,i}$ are inputs and outputs due to net erosion and $I_{v,r,i}$ and $O_{v,r,i}$ are inputs and outputs due to the vertical change in the position of the bed. The active layer has additional terms because it exchanges material with the sediment load:

$$\Delta S_{AL} = (I_{m,r,i} + I_{v,r,i} + Q_{s,in,i}) - (O_{m,r,i} + O_{v,r,i} + Q_{s,i}) \tag{A.50}$$

$Q_{s,in,i}$ is the bedload feed and $Q_{s,i}$ is the bedload for size i.

The mass balance for the sediment load is described in terms of suspended sediment discharge, Equations A.28 and A.40. I and O terms for each reservoir are described in more detail below.

Lateral exchanges

Lateral reservoir exchanges are driven by channel migration. The size distribution of substrate underlying the channel may be different from that below the floodplain because of selective deposition onto the channel and point bar and the size-specific supply of sediment from upstream nodes. Therefore, there are two substrate reservoirs, one each for the channel and floodplain. As the channel moves across the floodplain, it lay above old floodplain substrate, which becomes incorporated into the channel substrate. It also abandons a portion of both its underlying substrate, which mixes into the floodplain substrate reservoir. For each grainsize class i in the substrate,

$$I_{m,SF,i} = O_{m,SC,i} = -(1-\lambda)\frac{N}{\Delta t} L_S f_{SC,i} \Delta x \tag{A.51}$$

and

$$O_{m,SF,i} = I_{m,SC,i} = (1-\lambda)\frac{E}{\Delta t} L_S f_{SF,i} \Delta x \tag{A.52}$$

L_S is the height of the substrate. The subscript SF represents the floodplain portion of the substrate and SC denotes the channel substrate. Washload from the floodplain (subscript FP) goes straight into the sediment load (subscript L) and does not interact with the active layer:

$$O_{m,FP,w} = I_{m,L,w} = (1-\lambda)\frac{E}{\Delta t} L_F f_w \Delta x \tag{A.53}$$

where the subscript w denotes the size class traveling as suspended load. Bed material-sized sediment that erodes from the floodplain is exchanged directly with the active layer:

$$O_{m,FP,i} = I_{m,AL,i} = (1-\lambda)\frac{E}{\Delta t} L_S f_{FP,i} \Delta x \tag{A.54}$$

The subscript AL refers to the active layer.

Inputs to the floodplain from the active layer and load occur in two ways: from overbank deposition and from channel narrowing. The latter is modulated by a point bar reservoir, which has a grainsize distribution and height, L_{PB}. The fraction of pointbar that is composed of washload sediment is

$$f_{PB,w} = 1 - \left(1 + \frac{\bar{k} Q_{s,w}}{Q_{s,b}}\right)^{-1} \tag{A.55}$$

where $Q_{s,b}$ is the duration-averaged bed material load ($\sum Q_{s,i}$) and $\bar{k}$ is a user-defined relationship between the proportion between suspended and bedload in the load and that proportion on the point bar. The export of suspended sediment from the load and the input into the floodplain via vegetation encroachment and overbank deposition becomes

$$O_{m,AL,w} = I_{m,FP,w} = (1-\lambda) f_{PB,w} L_{PB} \frac{N}{\Delta t} \Delta x + d_w \Delta x \tag{A.56}$$

The input of each size class of bed material into the floodplain due to vegetation encroachment and overbank deposition is described as

$$O_{m,AL,i} = I_{m,FP,i} = (1-\lambda) f_{PB,i} L_{PB} \frac{N}{\Delta t} \Delta x + d_i \Delta x \tag{A.57}$$

where

$$f_{PB,i} = (1 - f_{PB,w})[\alpha_{bar} f_{AL,i} + (1-\alpha_{bar}) f_{Qs,i}] \tag{A.58}$$

and α_{bar} is the proportion of point bar bed material sediment that is sourced from the active layer as opposed to the load.

Vertical exchanges

Vertical reservoir exchanges (subscript v) are driven by the Exner equation, where

$$\frac{\Delta z}{\Delta t} = \frac{1}{B_c(1-\lambda)} * \frac{(\sum(I_{m,AL,i} + Q_{s,f}) - Q_s}{\Delta x} \tag{A.59}$$

$\frac{\Delta z}{\Delta t}$ is the rate of bed elevation change and $Q_{s,f}$ is the total incoming bedload feed and Q_s is the computed load, with is exported to the next downstream node. If the channel is aggrading ($\frac{\Delta z}{\Delta t} > 0$), then the uppermost substrate channel and floodplain layers receive bed material sediment from the active layer and floodplain, respectively:

$$I_{v,SC,i} = O_{v,AL,i} = \begin{cases} \frac{\Delta z}{\Delta t} B_c \Delta x (1-\lambda)(\alpha_{bed} f_{AL,i} + (1 - \alpha_{bed} f_{L,i}), & z > 0 \\ 0, & z \leq 0 \end{cases} \tag{A.60}$$

where α_{bed} is the proportion of sediment entering the substrate from the bed vs. the bedload, the subscript v refers to vertical exchange, and

$$I_{v,SF,i} = O_{v,FP,i} = \begin{cases} \frac{\Delta z}{\Delta t} \frac{\Delta x}{\chi} B_f (1-\lambda) f_{FP,i}, & z > 0 \\ 0, & z \leq 0 \end{cases} \tag{A.61}$$

If the bed is degrading ($\frac{\Delta z}{\Delta t} < 0$), then the uppermost substrate layers provides sediment to the active layer and active floodplain:

$$O_{v,SC,i} = I_{v,AL,i} = \begin{cases} -\frac{\Delta z}{\Delta t} B_c \Delta x (1-\lambda) f_{SC,i}, & z < 0 \\ 0, & z \geq 0 \end{cases} \tag{A.62}$$

and

$$O_{v,SF,i} = I_{v,F,i} = \begin{cases} -\frac{\Delta z}{\Delta t} \frac{\Delta x}{\chi} B_c (1-\lambda) f_{SF,i}, & z < 0 \\ 0, & z \geq 0 \end{cases} \tag{A.63}$$

It is assumed that washload sediment does not infiltrate into the bed during aggradation (i.e. $I_{v,SC,w} = O_{v,AL,w} = 0$). However, during degradation, fine sediment from the uppermost substrate layer is entrained and enters the load:

$$O_{v,SC,w} = I_{v,L,w} = \begin{cases} -\frac{\Delta z}{\Delta t} B_c \Delta x (1-\lambda) f_{SC,w}, & z < 0 \\ 0, & z \geq 0 \end{cases} \tag{A.64}$$

Fine sediment in the floodplain is exchanged with the uppermost floodplain substrate in the same way as bed material, using Equations A.61 and A.63, but replacing i with w.

Exchanges in bedrock channels

The user may specify nodes that are underlain by non-erodable material such as bedrock. The channel is only allowed to degrade to a user-defined threshold, after which $\frac{\Delta z}{\Delta t}$ is set at 0 and the channel becomes 'partly alluvial.' Conservation of mass is maintained by adjusting the total volume of the active layer instead of sourcing material from the substrate. In partly-alluvial nodes, washload sediment may be evacuated from the active layer when total sediment inputs exceed outputs:

$$Q_{s,adj,w} = Q_{s,in,w} - f_{w,AL} * (Q_{s,in} - Q_s) \tag{A.65}$$

Equation A.65 ensures that the active layer grainsize distribution of a partly-alluvial node does not become dominated by fine sediment. The change in washload volume in the active layer ($\Delta S_{AL,w}$) is

$$\Delta S_{AL,w} = (I_{m,r,w} + Q_{s,in,w}) - (O_{m,r,w} + Q_{s,adj,w}) \tag{A.66}$$

When the inputs to a partly-alluvial node exceed outputs, the size-specific bedload exiting the node is adjusted to fill the active layer with bed material sediment:

$$\Delta S_{AL,i} = (I_{m,r,i} + Q_{s,in,i}) - (O_{m,r,i} + Q_{s,adj,i}) \tag{A.67}$$

where

$$Q_{s,adj,i} = Q_{s,in,i} - (Q_{s,in} - Q_s)[f_{i,AL}\alpha_{pa} + f_{i,L}(1-\alpha_{pa})] \tag{A.68}$$

$Q_{s,adj,i}$ is the adjusted sediment load for size class i, $Q_{s,in}$ and $Q_{s,out}$ are the total sediment feed and load, respectively, and α_{pa} is the ratio between the volume of a fully alluvial active layer and the current volume:

$$\alpha_{pa} = \frac{V_{AL}}{L_{AL} Bc \Delta x} \tag{A.69}$$

Equations A.67 and A.66 replace Equation A.50 in partly alluvial nodes. When α_{pa} is greater than or equal to 1, the bed is no longer partially alluvial, and bed elevation changes may occur again.

Reservoir geometry and grainsize distributions

For each timestep, the volume for each reservoir size class (including the suspended load) is calculated by multiplying the result from Equation A.48 by the length of the timestep and adding it to the initial volume:

$$V_{r,i} = V_{0,r,i} + \frac{\Delta V_{r,i}}{\Delta t}\Delta t \tag{A.70}$$

where $V_{0,r,i}$ is the volume after the previous timestep of length t (and, in the case of the fine sediment fraction, i is replaced with w). The total volume V_r is

$$V_r = \sum_{i=1}^{n} V_{r,i} + V_{r,w} \tag{A.71}$$

and the size fractions are

$$f_{r,i} = \frac{V_{r,i}}{V_r} \tag{A.72}$$

for the bed material load and

$$f_{r,w} = \frac{V_{r,w}}{V_r} \tag{A.73}$$

for the washload. Reservoir volumes and size fractions are updated during each timestep for the active layer (AL), floodplain (F), and substrate layers (S). Channel width is calculated based on the encroachment and erosion rates:

$$B_c = B_{c,0} + \left(\frac{N}{\Delta t} + \frac{E}{\Delta t}\right)\Delta t \tag{A.74}$$

where $B_{c,0}$ is the previous channel width. The floodplain width is

$$B_f = B_{f,0} - \left(\frac{N}{\Delta t} + \frac{E}{\Delta t}\right)\chi\Delta t \tag{A.75}$$

where $B_{f,0}$ is the previous floodplain width. The floodplain height then becomes

$$L_f = V_F\left(B_f\frac{\Delta x}{\chi}\right)^{-1} \tag{A.76}$$

The height of the uppermost substrate layer is a function of the vertical bed change:

$$L_s = L_{s,0} + \frac{\Delta z}{\Delta t}\Delta t \tag{A.77}$$

where $L_{s,0}$ is the previous upper substrate height. The heights of deeper substrate layers do not change. The new bed elevation z is

$$z = z_0 + \frac{\Delta z}{\Delta t}\Delta t \tag{A.78}$$

where z_0 is the previous bed elevation.

A.3.5 Substrate maintenance

All substrate layers are initially set at a uniform thickness, $L_{S,0}$. Substrate layers are split or combined when the thickness of the uppermost layer, L_S, exceeds or drops below thickness thresholds or when aggradation begins to approach the height of the floodplain.

Stratigraphy

In order to preserve the stratigraphy of subsurface deposits, the substrate reservoirs are modified as the river aggrades and degrades. If the river aggrades over a defined threshold (L_{sp}), the uppermost substrate layer is split in two, creating a new stratigraphic layer. The thickness of this new layer is

$$L_{s,new} = L_s - L_{s,0} \tag{A.79}$$

and the thickness of the old layer becomes $L_{s,0}$. New volumes are calculated for the layers as

$$V_r = L_s B_c \Delta x \tag{A.80}$$

where r represents the channel (SC) and floodplain (SF) substrate reservoirs. The grainsize distribution of the new layers is the same as in the respective parent layers.

If the uppermost substrate layer thickness is reduced below a threshold due to degradation, that layer is combined with the layer below it. The thickness of the new layer becomes

$$L_{s,new} = L_s + L_{s,-1} \tag{A.81}$$

where $L_{s,-1}$ is the thickness of the lower layer. The grainsize distribution of the combined layer is a weighted average of the two layers

$$f_{S,i} = f_{S,i} L_s + f_{S,-1,i} L_{S,-1} \tag{A.82}$$

where $f_{S,i}$ and $f_{S,-1,i}$ are the fractions for size i of the upper and lower layers, respectively. The volume of the reservoir is solved using Equation A.80.

Avulsion

Avulsion (the rapid shift of the dominant channel to a new location) is common in alluvial rivers when the channel is blocked by sediment, large wood, or other obstructions. In MAST-1D, avulsion is triggered in model nodes experiencing high levels of aggradation where the bed elevation approaches that of the floodplain. The implication is that avulsions occur in areas of persistent sediment deposition (such as deltas). When the floodplain height (L_f) dips below a user-defined threshold value, the bed elevation lowers by a spacing constant (L_{av}):

$$z_{new} = z_{old} - L_{av} \tag{A.83}$$

where z_{old} is the pre-avulsion bed elevation and z_{new} is the resulting elevation. The surface of the new channel becomes active, so that the volume of floodplain material added to the active layer for size class i ($AL_{in,i}$) in the avulsed node is

$$AL_{in,i} = \alpha_a * B_c * L_{AL} * f_{i,FP} * \Delta x \tag{A.84}$$

where α_a is the fraction of channel that avulses, L_{AL} is the thickness of the active layer, and $f_{i,FP}$ is the fraction of size class i in the floodplain. We make the simplification that the abandoned portion of channel becomes vegetated immediately. Channel substrate and the avulsed portion of the active layer are incorporated into the floodplain. Floodplain material is mixed into the active layer to represent the surface material forming the base of the new channel. The volume of channel sediment sequestered into the floodplain reservoir ($FP_{in,i}$) is

$$FP_{in,i} = [\alpha_a * B_c * L_{AL} * f_{i,AL} + B_c * L_a * f_{i,SC}] * \Delta x \tag{A.85}$$

The grainsize distribution of the active layer is adjusted to incorporate floodplain material under the new channel:

$$f_{AL,i} = \alpha_a f_{FP,i} + (1 - \alpha_a) f_{AL,i} \tag{A.86}$$

Sediment from the substrate and the old active layer are incorporated into the floodplain to conserve mass and a new floodplain volume is calculated:

$$V_{FP,i} = V_{FP,old,i} + V_{SC,i} + V_{SF,i} + V_{AL,old,i} - V_{AL,new,i} \tag{A.87}$$

where $V_{AL,old,i}$ and $V_{AL,new,i}$ are the old and new active layer size-specific volumes, respectively and $V_{FPold,i}$ is the old floodplain volume. If the uppermost substrate layer is lower or higher than L_{av}, then it is either split or combined using the methodology in Section A.3.5 before performing EquationA.87 so that $L_{FP} = L_{av}$.

A.4 Initial and boundary conditions

A.4.1 Boundary conditions

As a 1-dimensional model, MAST-1D requires two boundary conditions: an upstream sediment supply, and a downstream hydraulic boundary.

Sediment supply

By default, the upstream sediment feed is a user-defined proportion of the bedload sediment capacity, where

$$Q_{s,i,in} = C_{f,b} Q_{s,i,cap} \tag{A.88}$$

and

$$Q_{s,w,in} = C_{f,w} \sum_{j=1}^{n} Q_{s,i,in} \tag{A.89}$$

$Q_{s,i,in}$ and $Q_{s,w,in}$ are the total size-specific feed rates for the bedload and suspended load, respectively, $Q_{s,i,cap}$ is the size-specific bedload transport capacity, calculated using Equations A.17-A.25 and a user-specified size distribution, and $C_{f,b}$ is proportion of capacity that is input as bedload feed. Suspended feed is assumed to be a set multiple of initial beload capacity, modulated by the constant $C_{f,w}$.

The user may allow $C_{f,b}$ and $C_{f,w}$ to change over time, either directly or via a function. When a flow duration curve is used, $Q_{s,i,cap}$ is determined using the duration-weighted sum of sediment transport rate for all flows in the curve. When hydraulics are calculated using a hydrograph, $Q_{s,i,cap}$ is recalculated for each new flow, using the initial geometric and sediment conditions. In other words, a sediment capacity rating curve is used.

Hydraulics

The water surface elevation is set at the downstream boundary. The user has the option of setting the boundary as a constant or changing it manually (for example, if the modeled reach ends at a reservoir or shoreline). If the water surface elevation is not known, it is calculated assuming normal flow conditions and a wide channel with the Manning equation:

$$z + y = z + \left(\frac{n_c Q}{B_c S_c^{0.5}} \right)^{3/5} \tag{A.90}$$

where S_c is the channel bed slope. If y is greater than the channel depth ($L_f - L_a$), then the flow depth is solved for iteratively using Equations A.1-A.10. Δx is set at 100 m, and iterations continue until the upper and lower channel depths (y_1 and y_2) converge.

When a flow duration curve is known, the boundary water surface elevation is solved for each flow at the beginning of the run. If a hydrograph is used, then the boundary condition is solved for each discharge using the initial channel geometry and sediment conditions.

A.4.2 Initial conditions

The initial channel geometry and grainsize distribution of the active layer are supplied by the user. Given these conditions, as well as the upstream sediment boundary and sediment mixing parameters, the floodplain grainsize distribution and floodplain number are calculated so that the model river would be in equilibrium if channel width and migration rate were constant.

Floodplain number

The floodplain number F determines the proportion of the suspended load that is deposited during each timestep. The depth of fine sediment on the floodplain during the initial condition (L_w) is assumed to be equivalent to the depth during equilibrium and is calculated as

$$L_{w,0} = L_f - (L_a + L_{pb}) \tag{A.91}$$

The floodplain number then is the proportion that the sediment concentration would have to be reduced to reproduce L_w within an average floodplain reworking time (B_f/m), assuming that mud is being transported at the capacity determined in Equation A.89 and given a constant user-defined migration rate m:

$$F = \frac{L_{w,0}m}{d_{full}} \tag{A.92}$$

where d_{full} is the average suspended sediment deposition rate per unit floodplain if the entire sediment load were deposited. The floodplain number can also be set manually by the user.

Initial floodplain grainsize distribution

The initial grainsize distribution for the floodplain and floodplain substrate reservoirs is a combiniation of the distributions of the active layer and point bar:

$$f_{F,i,0} = \frac{f_{AL,i,0}L_{al} + f_{PB,i,0}L_{pb}}{L_f} \tag{A.93}$$

and

$$f_{F,i,0} = \frac{f_{AL,w,0}L_{al} + f_{PB,w,0}L_{pb} + L_{w,0}}{L_f} \tag{A.94}$$

The subscript 0 refers to the values of the variables at the initial condition.

A.5 Variable list

Table A.1: MAST-1D list of variables

Variable	Unit	Description
A	m^2	total area of flow
A_c	m^2	area of flow for channel
A_f	m^2	area of flow for floodplain
AL	-	active layer
B_c	m	channel width

Table A.1: MAST-1D list of variables

Variable	Unit	Description
B_f	m	floodplain width
B_{min}	m	minimum channel width
C	-	washload sediment concentration
$C_{f,b}$	-	bedload sediment feed boundary capacity parameter
$C_{n,a}$	-	addition constant for Manning's n
$C_{n,m}$	-	multiplier for Manning's n
$C_{f,w}$	-	suspended sediment feed boundary capacity parameter
C_i	-	concentration of size class i in overbank flow
C_{max}	-	size classes of 'coarse' particles, roughly greater than the D_{90}
d_w	m^2/s	average washload deposition rate per unit length on floodplain
d_i	m^2/s	average suspended sand/gravel deposition rate per unit length on floodplain for size class i
d_{full}	m^2/s	average suspended sediment deposition rate per unit length on floodplain if entire sediment load were deposited
D_g	m	mean grain size
D_i	m, mm	grain size at percentile i
E	m	bank erosion
F	-	floodplain number
F_{bed}	-	floodplain number for bed material
FP	-	floodplain
f_i	-	fraction of size i in sediment mixture
$f_{i,NB}$	-	fraction of size i in near-bank sediment mixture
f_w	-	fraction of suspended-size sediment in mixture
g	m/s^2	gravitational acceleration
h_e	m	energy head loss
I	-	reservoir inputs
$\bar{k}$	-	coefficient of suspended and bedload sediment in the load and on the point bar
K	-	conveyance

Table A.1: MAST-1D list of variables

Variable	Unit	Description
K_c	-	conveyance for channel
K_f	-	conveyance for floodplain
L_a	m	thickness of active layer
L_{av}	m	bed lowering during avulsion
L_f	m	floodplain height
L_{pb}	m	thickness of point bar
L_s	m	substrate thickness
L_w	m	thickness of fine sediment on floodplain during initial condition
N	m	vegetation encroachment
n_c	-	Manning's n for channel
n_f	-	Manning's n for floodplain
O	-	outputs
PB	-	point bar
p_j	-	flow frequency for flow j
P_o	-	proportion of suspended load for size class i that is overbank
$q_{s,b,i}$	-	Rouse integral for in-channel portion of flow
$q_{s,b,i}$	-	Rouse integral for overbank portion of flow
qs_{Cmax}	m^3/s	transport rate for the coarse fraction
qs_{cr}	-	mobility threshold for bank erosion
Q	m^3/s	total discharge
Q_c	m^3/s	channel discharge
Q_f	m^3/s	floodplain discharge
$Q_{s,adj,i}$	m^3/s	adjusted fractional sediment load for partially-alluvial channel
$Q_{s,b,i}$	m^3/s	proportion of suspended sand/gravel traveling within the banks
$Q_{s,f}$	m^3/s	total bedload sediment feed
$Q_{s,i}$	m^3/s	total sediment load for size i over duration curve
$Q_{s,in,i}$	m^3/s	total sediment feed for size i over duration curve
$Q_{s,o,i}$	m^3/s	proportion of suspended sand/gravel traveling above the banks

Table A.1: MAST-1D list of variables

Variable	Unit	Description
$Q_{s,w}$	m^3/s	total suspended sediment load over duration curve
$q_{s,i}$	m^3/s	channel-wide sediment load for size class i
q_w	m^3/s	suspended sediment load
$q_{w,in}$	m^3/s	suspended sediment feed
S	m^3	storage of sediment in reservoir
SC	-	channel substrate
S_c	-	channel bed slope
S_f	-	energy slope
SF	-	floodplain substrate
u^*	m/s	shear velocity
$\bar{v}$	m/s	cross-sectional average velocity
v_c	m/s	flow velocity in channel
v_f	m/s	flow velocity on floodplain
V	m^3	volume
w_i^*	-	dimensionless transport for size i
x	m	channel-wise coordinate
y	m	flow depth in the channel
z	m	bed elevation
Z	$-$	Rouse number
α_a	-	portion of channel that avulses
α_{bar}	-	fraction of point bar bed material sediment sourced from active layer
α_{bed}	-	fraction of sediment entering substrate from bed vs. bedload
α_e	-	channel widening coefficient
α_f	-	proportion of active layer transport in near-bank region
α_n	-	channel narrowing coefficient
α_{pa}	-	fraction between volume of partly-alluvial fully alluvial active layer
α_v	-	weighting coefficient for average velocity
λ	-	porosity
ν	m^2/s	kinematic viscosity
ρ	kg/m^3	density of water

Table A.1: MAST-1D list of variables

Variable	Unit	Description
ρ_s	kg/m^3	sediment density
σ_{SG}	-	standard deviation of sediment mixture on psi scale
τ'		skin friction (shear stress on grains)
τ_{cr}	N/m^2	shear stress needed to entrain reference D84
τ_r	N/m^2	reference shear stress below which vegetation encroachment occurs
τ^*_{rm}	-	dimensionless reference shear stress for the mean particle size
τ_{rm}	N/m^2	reference shear stress for the mean particle size
τ_{ri}	N/m^2	reference shear stress for size class i
ϕ_i	-	ratio between skin friction and reference shear stress of size class
χ	-	channel sinuosity

Appendix B

MAST-1D parameters and calibration

Here we present initial conditions and constants for the MAST-1D simulations. For Chapters 2 and 4, all nodes are initially homogenous. For Chapter 3, the study area was broken into 21 segments that correspond to morphologically similar portions of channel (Figure B.1). Initial conditions are presented in Tables B.1 to B.3. Reaches with 'Canyon' designations do not migrate and cannot degrade by more than 0.2 m. Slopes were extracted from a DEM from before dam removal. Sinuosity is kept constant in MAST-1D. Values are averages of sinuosities calculated from available air photos (see Chapter 3). Valley widths presented in Table B.2 represent valley area divided by the valley centerline for each node. Valley margins were digitized using a LiDAR DEM in conjunction with air photos. Valley widths in Tables B.1 and B.3 were assumed spatially constant.

Initial channel widths were calibrated so that the average annual sediment transport capacity, calcuated using a duration curve derived from daily discharge from Elwha River between 1927 and 1994, matched the annually-averaged sediment load derived from measurements of accumulation in Lake Mills from 1994. The calibrations, along with a comparision of sediment load GSDs calculated via MAST-1D and measured in the reservoir, are presented in Figures B.2-B.4.

Other initial conditions that are eqivalent for all runs are presented in Table B.4. The initial floodplain depth was taken from an emperical hydrologic geometry relation for coastal Pacific Northwest rivers presented by *Castro and Jackson* (2001). The initial thickness of overbank sediment on the floodplain is averaged from measurements from a bank survey conducted in 2015 (see Appendix C). Other constants and calibration parameters are in Table B.5.

Calibrations of the dam removal sediment supply paramter C for various sediment supply scenarios described in see Chapter 3 are presented in Figure B.5. Field data were extracted from unpublished structure-from-motion analysis of air photos of the former reservoir and were provided by the US Geological Survey.

Table B.1: Initial conditions for simulations from Chapter 2

Node	Valley length (m)	Valley width (m)	Canyon	B_c (m)	$\Delta x (m)$	Sinuosity	Slope
0	4902	581	No	81	5000	1.02	0.0069
1,	4902	581	No	81	5000	1.02	0.0069
2	4902	581	No	81	5000	1.02	0.0069
3	4902	581	No	81	5000	1.02	0.0069
4	4902	581	No	81	5000	1.02	0.0069

Table B.2: Initial conditions for simulations from Chapter 3

Node**	Valley length (m)	Valley width (m)	Canyon	B_c (m)	$\Delta x (m)$	Sinuosity	Slope
0	237	25	Yes	14.4	238	1.01	0.022
1,	680	180	Yes	50.6	731	1.08	0.0081
2	592	41	Yes	32.5	663	1.12	0.015
3	737	340	No	111	779	1.06	0.0081
4	662	397	No	111	731	1.10	0.0081
5	871	523	No	111	918	1.05	0.0081
6	616	187	No	111	790	1.28	0.0081
7	686	504	No	81	735	1.07	0.0069
8	538	502	No	81	587	1.09	0.0069
9	704	361	No	81	718	1.02	0.0069
10	704	358	No	81	671	0.95	0.0069
11	223	61	Yes	28	235	1.06	0.0069
12	574	344	No	81	608	1.06	0.0069
13	647	334	No	81	668	1.03	0.0069
14	653	427	No	81	-	1.07	0.0069
15	502	516	No	81	-	1.07*	0.0069
16	614	439	No	81	-	1.07*	0.0069
17	502	316	No	81	-	1.07*	0.0069
18	819	92	Yes	81	-	1.07*	0.0069
19	741	209	No	81	-	1.07*	0.0069
20	797	189	No	81	-	1.07*	0.0069

*Aldwell sinuosities are average of all upstream nodes
**Node count begins at Glines Canyon Dam and increase downstream

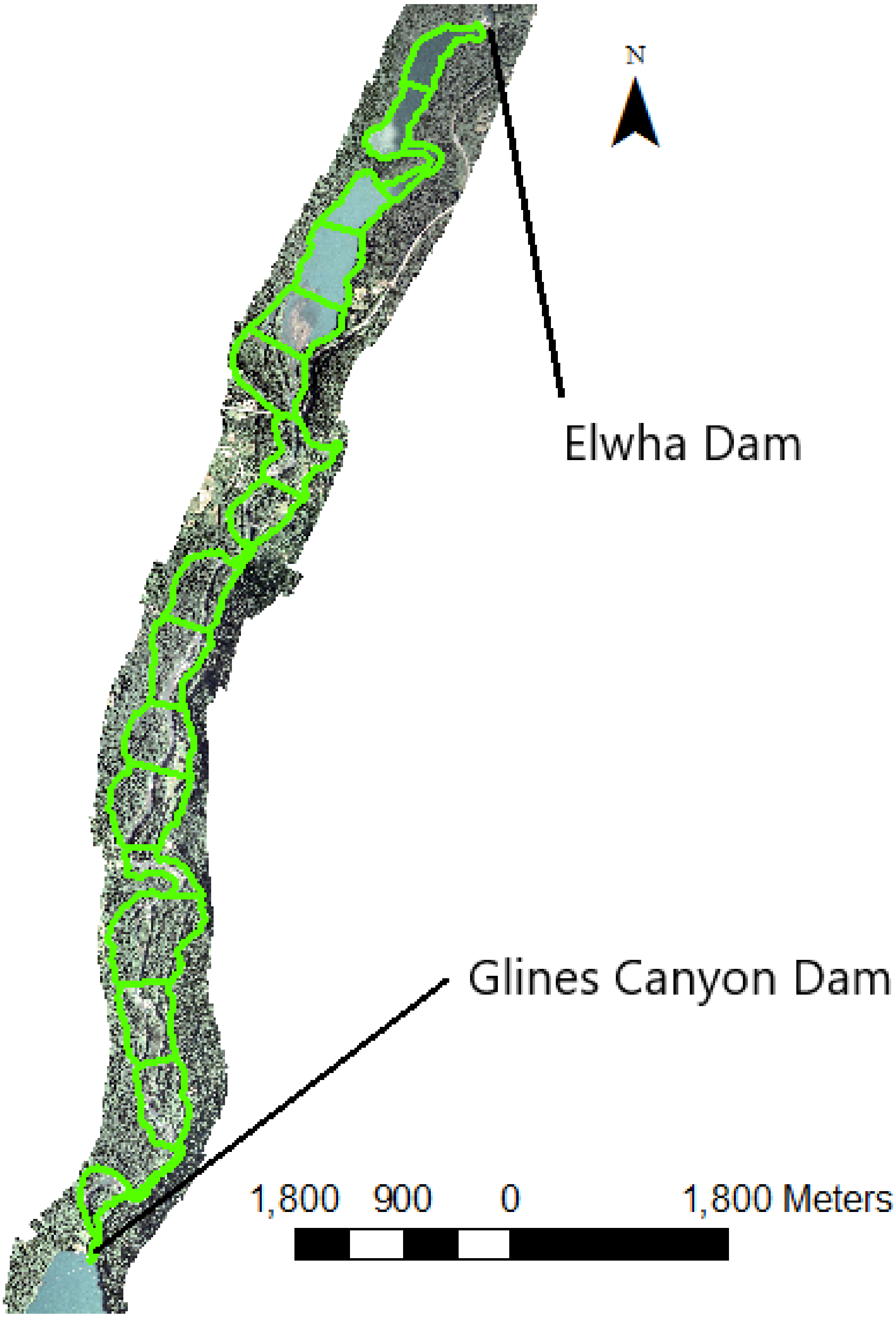

Figure B.1: Map with node locations for simulations in Chapter 3

Table B.3: Initial conditions for simulations from Chapter 4

Node	Valley length (m)	Valley width (m)	Canyon	B_c (m)	$\Delta x(m)$	Sinuosity	Slope
0	2234	594	No	94	2279	1.02	0.0074
1,	2234	594	No	94	2279	1.02	0.0074
2	2234	594	No	94	2279	1.02	0.0074
3	2234	594	No	94	2279	1.02	0.0074
4	2234	594	No	94	2279	1.02	0.0074
5	2234	594	No	94	2279	1.02	0.0074

Table B.4: Floodplain and substrate initial conditions

Variable	Unit	Description	Value
L_f	m	floodplain height	2.26
L_s	m	substrate thickness	1.0
L_w	m	thickness of fine sediment on floodplain during initial condition	0.14

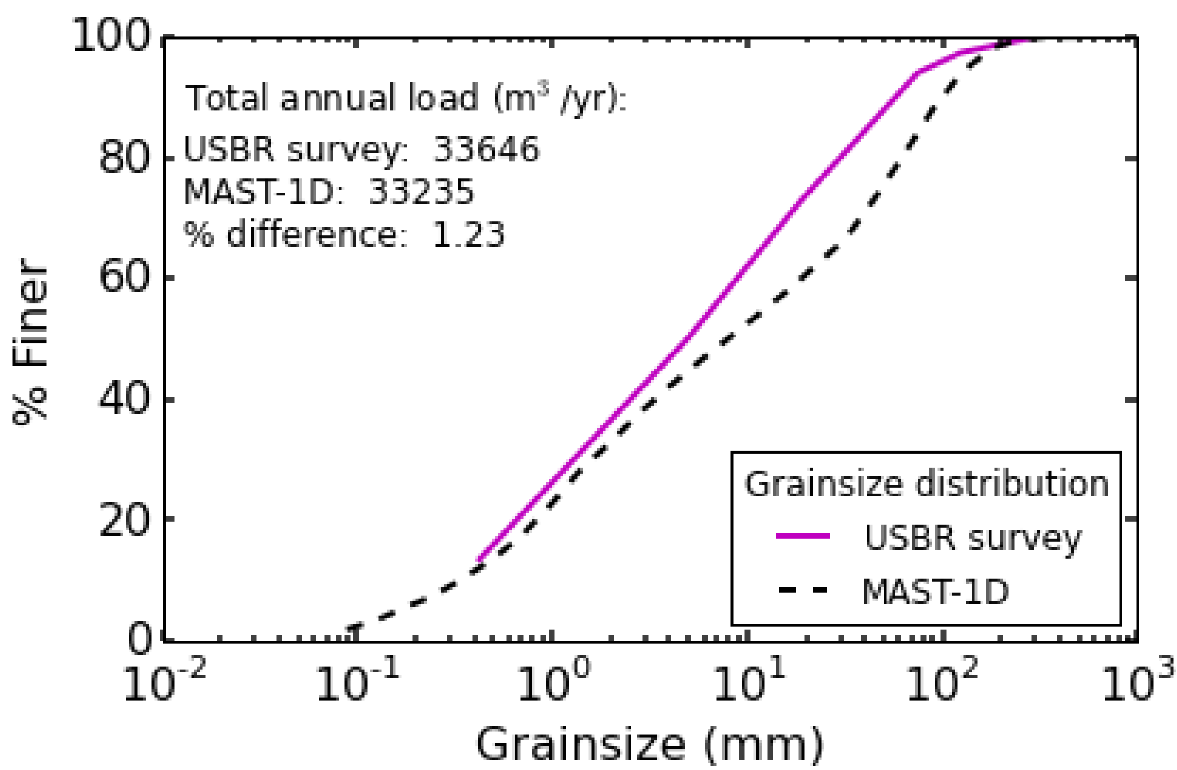

Figure B.2: Calibration of B_c for nodes with a slope of 0.0069 in Chapters 2 and 3

Table B.5: Calibration parameters and other constants. These values were used for all runs unless stated otherwise in the text.

Variable	Unit	Description	Value
B_{min}	m	minimum channel width	40
$C_{n,a}$	-	addition constant for Manning's n	0.0066
$C_{n,m}$	-	multiplier for Manning's n	1.15
C_{max}	-	coarse size classes for bank erosion algorithms	256-1024 mm
F	-	floodplain number for mud	0.2
F_{bed}	-	floodplain number for bed material	0.75
g	m/s^2	gravitational acceleration	9.81
$\bar{k}$	-	coefficient of suspended and bed-load sediment in the load and on the point bar	$10 * * -6$
L_a	m	thickness of active layer	0.4
L_{av}	m	bed lowering during avulsion	1.0
L_c	m	critical floodplain height for avulsion	0.75
L_{pb}	m	thickness of point bar	1.72
L_w	m	thickness of fine sediment on floodplain during initial condition 0.14	
n_f	-	Manning's n for floodplain	0.1
qs_{cr}	-	mobility threshold for bank erosion	10^{-6}
α_a	-	avulsion exchange parameter	0.1
α_{bar}	-	fraction of point bar bed material sediment sourced from active layer	1.0
α_{bed}	-	fraction of sediment entering substrate from bed vs. bedload	0.4
α_e	-	bank mobility coefficient	$10 * * -6$
α_f	-	fraction of channel contribution to transport in near-bank zone	0.55
α_n	-	channel narrowing coefficient	0.05
α_{pa}	-	fraction between volume of partly-alluvial fully alluvial active layer	0.5
λ	-	porosity	0.5
ν	m^2/s	kinematic viscosity	1/1300000
ρ	kg/m^3	density of water	1000
ρ_s	kg/m^3	sediment density	2650
$\tau_{c,n}$	N/m^2	critical shear stress for channel narrowing	32.0

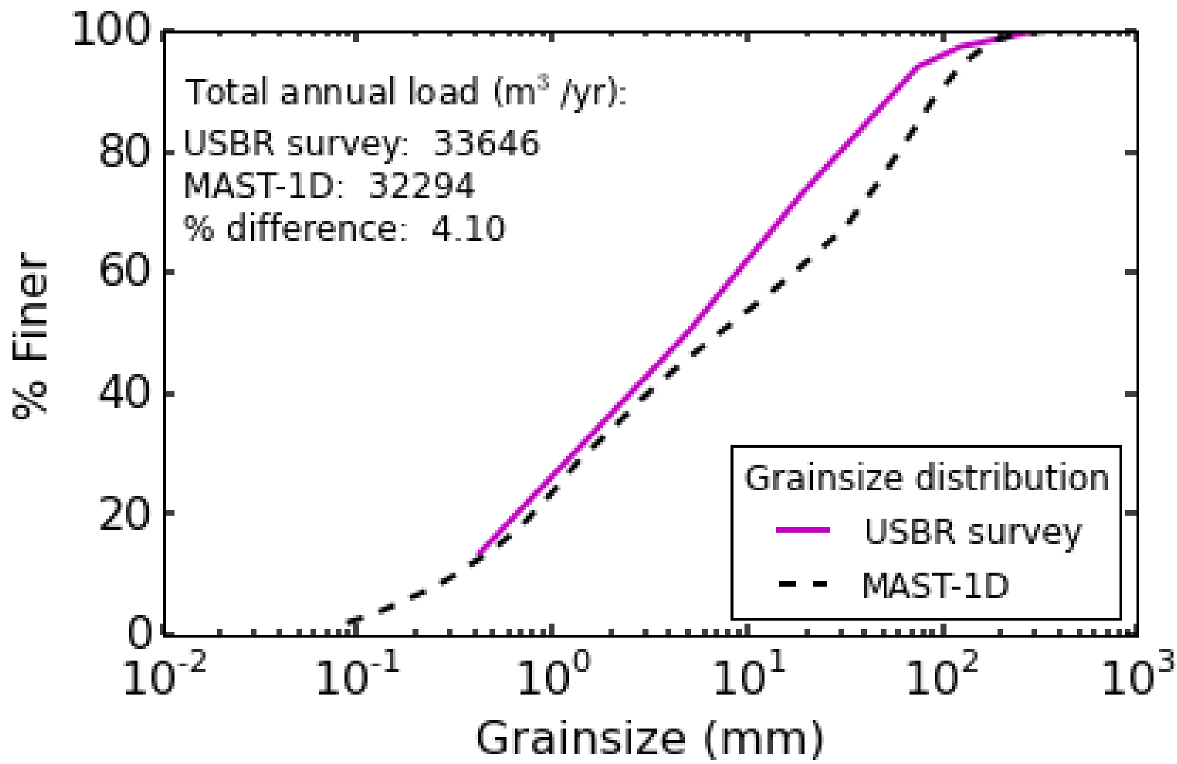

Figure B.3: Calibration of B_c for nodes with a slope of 0.0081 in Chapter 3

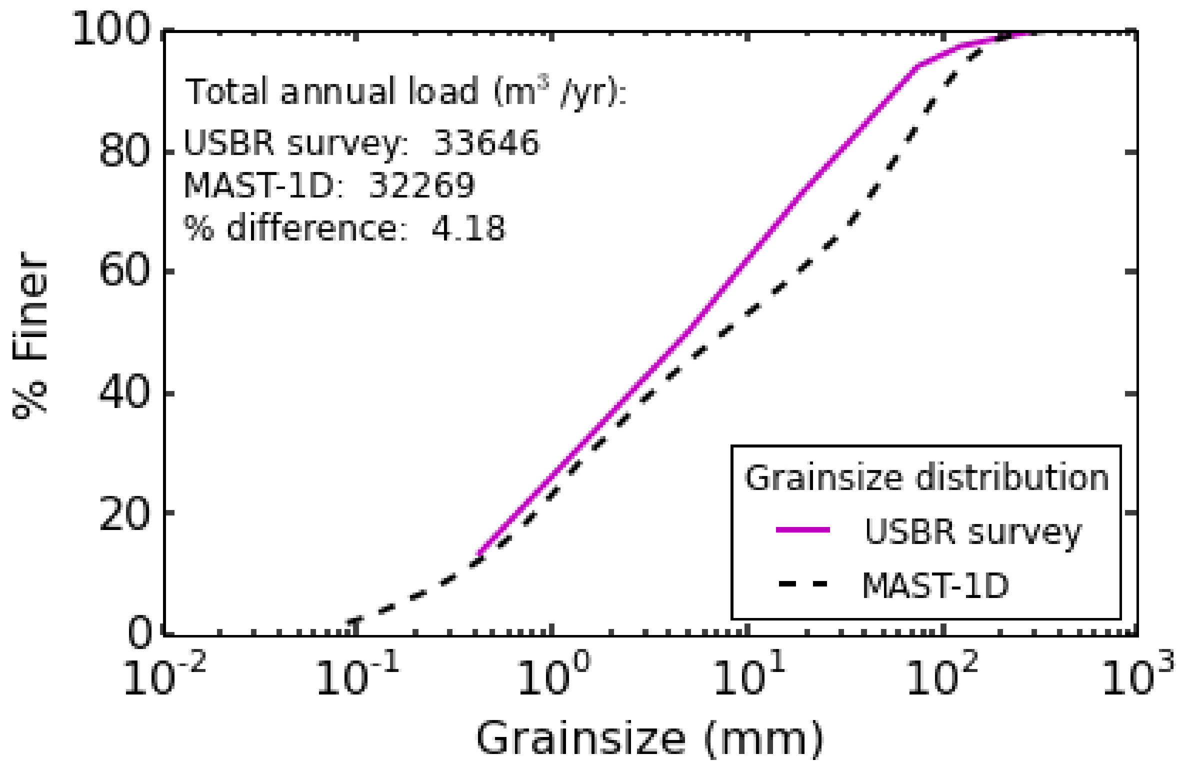

Figure B.4: [Calibration of B_c for nodes with a slope of 0.0074 in Chapter 4

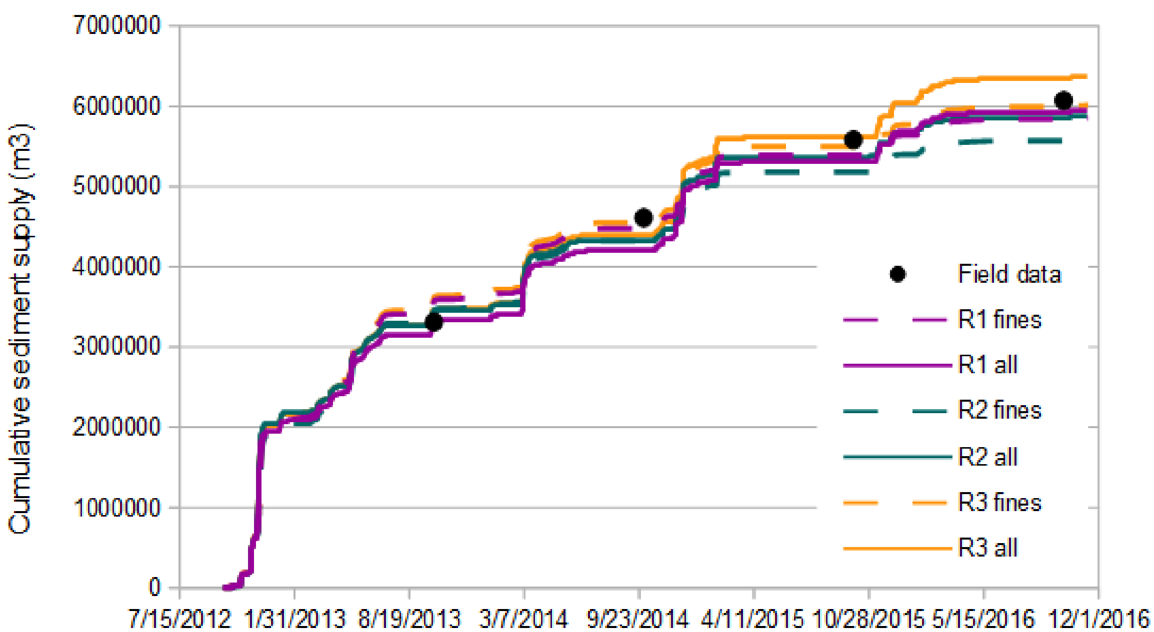

Figure B.5: Calibration of C for dam removal simulations

Appendix C

Field data

C.1 Introduction

Bank surveying and sediment sampling were conducted August-September 2015 to characterize the amount and size of sediment supplied from the floodplain. Elwha River discharge during the period ranged between 6 and 27 m^3/s but were typically around 7 m^3/s. Figure C.1 shows the locations of the samples. Both subsurface bulk sampling and photosieving are used to characterize the grainsize of the channel and floodplain. Sampling methods and results are presented in Sections C.2 and C.3, respectively. Surveying of the bank stratigraphy is described in Section C.4.

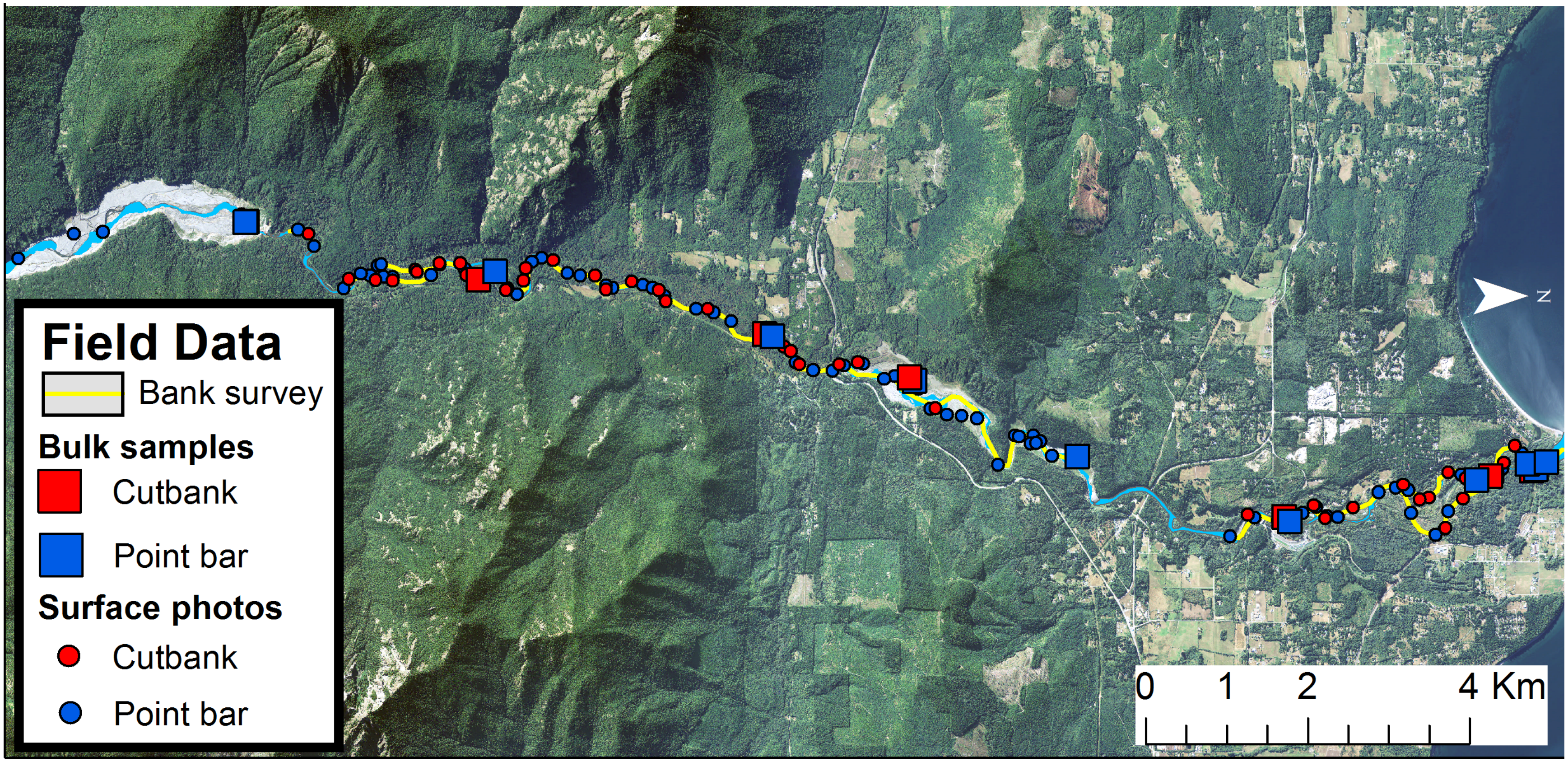

Figure C.1: Map with locations of sediment samples and survey line

C.2 Subsurface bulk sampling

Bulk subsurface sediment samples were collected at 8 point bar heads, 6 cutbank collapse deposits/toes, and on other point bar locations from immediately above Glines Canyon Dam to the Strait of Juan de Fuca. 1 sample of Lake Mills reservoir material was also extracted. We followed the guidelines outlined in *Church et al.* (1987) and *Bunte and Abt* (2001) as closely as possible. *Church et al.* (1987) recommends that samples sizes are large enough so that the coarsest size class constitutes no more than 5% of the samples mass for rivers with grains $>$128 mm. This was not feasible on the cobble-bedded Elwha, and our individual samples typically contain ˜20% of the coarsest grains. Samples sizes were typically about 500 kg. When all point bar head subsurface samples are composited, the largest (360-512 mm) grains make up 12% of the 2808 kg sample. For bank subsurface samples, the composite is 2983 kg and the 360-512 mm size class makes up 11% of the sample. Subsurface grainsize data for point bar heads are in Table C.1 and bank deposit grainsizes are listed in Table C.2. Other bulk samples, including those on the middle and tails of point bars and in Lake Mills reservoir are presented in Table C.3.

Table C.1: Bulk samples on point bar heads

	ELW02	ELW06	ELW01	ELW09	ELW03	ELW08	ELW07
Easting	455741	456544	457092	458027	458826	458315	458115
Northing	5319583	5323014	5324770	5326777	5329405	5331708	5332339
Size							
0.0625	0.62	1.11	0.52	0.46	0.41	0.86	0.75
0.0884	1.02	1.54	0.77	0.69	0.78	2.18	1.26
0.125	1.43	1.66	0.96	0.79	1.06	2.25	1.82
0.177	2.22	2.10	1.29	1.07	1.66	3.81	2.78
0.25	3.11	2.75	1.76	1.46	2.26	5.99	3.94
0.354	4.66	4.09	2.77	2.50	3.24	9.59	5.54
0.5	6.00	5.40	4.07	3.99	4.38	11.69	6.87
0.707	7.19	6.66	5.67	6.73	5.96	12.82	8.44
1	8.33	7.89	7.42	10.84	7.80	13.56	10.90
1.41	9.72	9.43	9.69	15.41	9.69	14.66	14.77
2	11.17	10.95	12.12	18.96	11.27	16.13	18.72
2.83	13.58	13.26	15.54	22.92	13.29	19.06	24.10
4	16.23	15.73	19.21	26.47	15.63	22.54	28.72
5.66	19.03	17.89	22.89	29.68	18.28	26.53	33.36
8	21.96	20.22	26.90	32.97	21.35	29.18	37.72
11.3	24.61	23.50	31.29	36.48	24.53	33.40	42.40
16	27.98	26.30	36.99	40.41	28.26	39.50	47.22
22.6	31.36	30.82	43.34	47.11	32.13	45.31	53.38
32	38.62	35.40	52.93	53.16	35.87	49.29	58.52
45.3	44.69	40.05	60.75	61.60	41.75	57.29	69.80
64	50.95	46.13	70.99	70.90	48.73	67.60	82.03
90.5	57.24	51.89	79.39	81.26	55.68	77.80	88.14
128	65.74	58.26	89.44	88.52	61.63	93.24	94.26
181	75.10	61.81	95.27	100.00	73.25	100.00	100.00
256	88.48	72.90	95.27	100.00	89.16	100.00	100.00
362	88.48	82.54	100.00	100.00	89.16	100.00	100.00
512	100.00	100.00	100.00	100.00	100.00	100.00	100.00
$\mathbf{D}_{16}$	3.88	4.18	2.95	1.50	4.20	1.94	1.58
$\mathbf{D}_{50}$	60.73	80.79	28.78	26.70	68.19	33.00	18.71
$\mathbf{D}_{84}$	227.95	372.70	106.10	103.14	228.80	104.03	71.57

Table C.2: Bulk samples on cutbank toes and collapse deposits

	ELW02	ELW06	ELW03	ELW01	ELW08	ELW07
Easting	455850	456520	458772	457092	458267	458198
Northing	5319375	5322916	5329334	5324770	5331886	5332397
Size						
0.0625	0.33	0.11	1.81	0.27	0.08	0.05
0.0884	0.72	0.25	3.14	0.55	0.41	0.12
0.125	0.86	0.44	4.36	0.79	0.69	0.19
0.177	1.22	0.82	5.95	1.18	0.92	0.37
0.25	1.71	1.27	7.12	1.68	1.40	0.63
0.354	2.71	2.10	8.32	2.69	1.95	1.07
0.5	3.98	3.08	9.44	4.03	2.68	1.46
0.707	6.05	4.29	10.89	6.16	4.12	1.85
1	9.51	5.77	12.35	9.07	6.50	2.31
1.41	14.25	7.58	13.56	12.55	9.40	2.89
2	18.26	9.21	14.40	15.35	11.81	3.40
2.83	22.97	11.52	15.46	18.65	14.96	4.04
4	26.76	13.91	16.68	21.44	18.56	4.78
5.66	30.06	16.40	17.94	24.58	23.12	5.46
8	32.57	19.09	20.54	28.04	25.62	6.32
11.3	35.86	21.55	23.12	31.58	28.94	7.57
16	38.68	24.20	25.89	36.00	32.65	9.40
22.6	41.97	27.13	30.28	40.74	36.96	11.59
32	46.98	28.27	36.33	44.13	43.42	15.16
45.3	54.10	31.86	43.26	49.73	52.61	24.93
64	61.69	36.29	51.56	58.37	62.07	36.54
90.5	70.45	42.60	64.65	68.47	71.84	50.22
128	81.88	47.59	80.63	78.92	85.00	60.65
181	93.88	57.09	90.66	88.84	100.00	69.65
256	100.00	72.79	95.67	91.95	100.00	91.10
362	100.00	83.20	100.00	100.00	100.00	100.00
512	100.00	100.00	100.00	100.00	100.00	100.00
$\mathbf{D_{16}}$	1.65	5.35	3.30	2.14	3.13	32.97
$\mathbf{D_{50}}$	37.06	139.76	59.96	45.75	41.02	90.01
$\mathbf{D_{84}}$	136.09	368.09	143.81	152.87	124.69	228.24

Table C.3: Bulk samples on other surfaces. The suffix PBH refers to the upper portion of the point bar. MI represents the middle of the point bar, and TL refers to the tail. TR refers to a sample from a terrace deposit in the former Lake Mills reservoir.

	ELW05TR	ELW04PBH	ELW04PBT	ELW07MI	ELW07TL
Easting	-	455132	455134	458181	458094
Northing	-	5316515	5316507	5332443	5332573
Size					
0.0625	0.11	0.18	0.16	0.28	0.44
0.0884	0.41	0.32	0.32	0.55	0.74
0.125	0.41	0.43	0.49	0.85	1.08
0.177	0.82	0.62	0.86	1.45	1.76
0.25	1.54	0.93	1.53	2.31	2.78
0.354	3.94	1.74	3.23	3.49	4.27
0.5	8.09	2.93	5.55	4.67	6.94
0.707	15.20	4.42	8.03	6.84	11.46
1	25.85	6.01	10.18	10.81	17.45
1.41	35.59	7.78	12.16	15.54	23.87
2	45.55	9.48	13.99	18.91	28.78
2.83	54.31	12.15	16.64	22.40	34.52
4	60.48	15.34	19.84	25.14	40.27
5.66	65.56	18.75	23.46	27.82	45.35
8	70.24	22.52	27.81	30.74	50.15
11.3	74.87	26.82	32.33	33.72	56.39
16	80.98	32.43	38.91	37.76	65.02
22.6	86.78	37.40	46.66	42.73	76.15
32	90.01	44.92	56.01	52.51	89.03
45.3	95.01	53.01	65.52	61.19	98.71
64	97.94	59.07	76.82	71.75	100.00
90.5	100.00	65.98	94.65	85.04	100.00
128	100.00	76.96	100.00	95.82	100.00
181	100.00	91.37	100.00	100.00	100.00
256	100.00	100.00	100.00	100.00	100.00
362	100.00	100.00	100.00	100.00	100.00
512	100.00	100.00	100.00	100.00	100.00
$\mathbf{D_{16}}$	0.73	4.28	2.60	1.48	0.92
$\mathbf{D_{50}}$	2.39	39.78	25.61	29.28	7.91
$\mathbf{D_{84}}$	19.17	151.61	73.59	88.08	27.95

C.3 Photosieving

To characterize longitudinal variability in grainsize, photos were taken of sediment on point bar heads and cutbank toe deposits using a Go-Pro camera with a fish-eye lens. A sampling square ranging between 2x2 and 3x3 meters was delineated on the ground (most samples were 2x2 m). The camera was held at the edge of the grid with a slight tilt at a height of 2 m. Wet areas and deposits with abundant woody debris and vegetation were avoided wherever possible.

Data on sediment size was extracted from the photos by Jane Walden at Seattle University using Digital Gravelometer software (http://www.sedimetrics.com). The software automatically corrects for camera tilt. We did not correct for the fisheye lens, but the samples were in the middle of the photo and we expect error from distortion to be small relative to total error. We followed software recommendations and truncated the grainsize distribution at approximately 32 mm.

Sediment size metrics extracted from the photos are presented in Table C.4 for point bar heads, Table C.5 for cutbanks, and Table C.6 for point bar and bank photos corresponding to bulk sample locations.

Table C.4: Photosieved grainsize data for point bar heads taken from photos

Sample ID	Coord* (m)	D_{16} (mm)	D_{50} (mm)	D_{84} (mm)
PH88	752.55	64.96	151.88	257.25
PH100	1245.41	61.76	142.37	301.47
PH90	1317.35	68.28	145.86	233.48
PH102	1349.04	46.76	109.91	518.13
PH92	1449.63	61.19	142.7	344.44
PH94	1798.32	63.66	122.89	262.99
PH104	2094.89	62.35	149.66	250.26
PH106	2332.02	63.73	131.96	312.46
PH107	2481.68	74.12	145.44	216.06
PH108	2944.37	69.1	156.53	399.9
PH97	3033.98	75.89	152.5	254.92
PH121	3202.84	58.58	140.51	299.25
PH109	3328.42	86.97	188.83	341.12
PH119	3560.37	81.33	170.37	269.2
PH117	4167.84	76.48	144.37	226.95
PH115	4292.19	86.09	197.59	292.23
PH114	4465.62	79.57	189.58	276.31

Table C.4: Photosieved grainsize data for point bar heads taken from photos

Sample ID	Coord* (m)	D_{16} (mm)	D_{50} (mm)	D_{84} (mm)
PH112	4626.86	69.23	153.23	246.81
PH111	4961.23	52.49	108.93	176.78
PH84	5274.56	74.99	174.56	319.65
PH86	5707.68	73.93	161.24	241.33
PH28	8338.11	51.35	87.86	158.21
PH27	8636.2	60.5	110.95	163.8
PH22	8846.52	57.23	106.8	179.96
PH26	8863.58	49.28	85.53	125.3
PH24	8924.24	50.35	77.91	165.54
PH21	8939.78	57.54	108.85	205.66
PH23	9102.24	61.28	123.83	183.5
PH20	9130.59	52.93	100.46	155.65
PH11	9600.59	54.83	110.33	210.76
PH13	10230.61	83.99	183.57	260.97
PH14	10401.3	43.31	83.72	178.39
PH15	10619.84	66.29	137.97	222.57
PH17	10807.6	66.48	143.51	262.43
PH19	11081.92	79.07	172.32	398.53
PH01	11423.9	70.25	148.08	262.53
PH03	11523.27	70.06	161.97	405.05
PH08	11795.76	99.46	192.07	348.29
PH07	12092.94	78.01	173.39	298.4
PH06	12219.13	49.78	83.97	164.87
PH83	12465.71	61.6	120.67	265.98
PH81	12743.08	96.1	247.0	394.51
PH77	13278.61	76.78	208.51	360.48
PH76	13841.58	98.14	233.32	349.23
PH75	14098.83	85.16	201.31	333.9
PH73	14322.25	58.21	168.28	293.02
PH71	14746.22	75.7	181.37	319.34
PH69	14936.11	78.83	156.31	361.44
PH68	15058.64	89.6	182.75	300.8
PH49	15443.61	61.94	181.6	284.1
PH50	15547.54	84.81	198.99	348.23
PH66	15906.29	78.57	182.93	284.95

Table C.4: Photosieved grainsize data for point bar heads taken from photos

Sample ID	Coord* (m)	D_{16} (mm)	D_{50} (mm)	D_{84} (mm)
PH52	16060.52	76.17	135.58	251.59
PH54	16442.74	70.04	181.5	525.43
PH55	16646.04	78.4	185.56	380.15
PH58	17112.08	123.14	270.47	432.57
PH60	17252.9	70.21	186.13	369.86
PH63	17910.96	89.44	219.02	275.97
PH45	18229.48	74.51	180.33	371.26
PH44	18389.19	72.5	176.92	336.85
PH30	18859.2	60.76	141.37	293.61
PH31	18974.41	75.58	207.35	338.78
PH39	18996.66	98.53	353.45	722.54
PH38	19032.93	77.22	166.71	305.91
PH33	19155.16	83.93	208.05	376.51
PH36	19255.13	97.31	191.25	274.59
PH34	19522.44	76.48	157.08	308.13
PH48	20424.95	83.16	197.06	499.98
PH46	20730.97	80.07	187.72	328.63
PH87	21515.89		248.13	
PH123	23774.4	86.86	192.04	432.67
PH122	24547.07	76.7	158.67	341.01

*Distance upstream of Strait of Juan de Fuca

Table C.5: Photosieved grainsize data for bank toes taken from photos

Sample ID	Coord* (m)	D_{16} (mm)	D_{50} (mm)	D_{84} (mm)
PHC87	548.64	49.55	108.67	192.28
PHC89	868.68	82.48	164.56	269.15
PHC99	1205.18	43.07	104.26	213.45
PHC101	1321.61	56.33	252.61	431.69
PHC91	1357.88	58.17	119.01	253.57
PHC96	1828.8	64.91	163.48	300.01
PHC103	1871.47	67.78	135.2	233.38
PHC105	2316.48	44.93	98.89	155.85

Table C.5: Photosieved grainsize data for bank toes taken from photos

Sample ID	Coord* (m)	D_{16} (mm)	D_{50} (mm)	D_{84} (mm)
PHC120	3276.9	62.03	115.17	185.05
PHC116	4311.7	45.27	99.25	194.57
PHC113	4511.34	65.77	141.57	262.34
PHC110	4824.98	52.87	136.53	258.68
PHC85	5340.71	102.54	199.59	461.17
PHC16	10789.92	70.24	164.39	238.34
PHC18	11097.77	83.07	182.63	332.52
PHC10	11864.34	69.09	158.99	314.05
PHC09	12130.13	71.18	145.72	280.99
PHC82	12696.14	65.18	136.31	246.67
PHC80	12911.02	64.17	139.61	258.18
PHC79	12989.97	60.01	125.67	223.97
PHC78	13315.19	82.28	179.67	335.37
PHC74	14173.2	65.47	178.73	279.04
PHC72	14707.21	44.04	87.19	157.38
PHC70	14853.21	56.83	133.03	241.9
PHC67	15193.67	59.94	161.34	355.46
PHC65	15524.07	71.47	181.16	385.27
PHC51	15731.64	62.68	190.0	319.93
PHC53	16308.93	93.7	182.13	348.83
PHC56	16729.56	64.7	150.31	352.46
PHC57	16881.04	81.63	196.68	466.07
PHC59	17244.97	53.22	161.49	295.26
PHC61	17511.98	56.5	113.49	237.43
PHC62	17853.66	54.23	113.24	218.98
PHC64	17976.8	69.53	233.11	389.78
PHC43	18221.25	72.25	182.49	322.71
PHC42	18539.46	65.56	133.25	223.72
PHC41	18552.57	95.6	210.22	392.49
PHC29	18850.66	64.42	145.0	232.74
PHC32	19110.96	68.99	168.13	285.11
PHC35	19404.18	60.28	131.37	243.79
PHC47	20594.12	84.32	250.53	450.77

*Distance upstream of Strait of Juan de Fuca

Table C.6: Photosieved grainsize data corresponding to bulk sample locations

Sample ID	D_{16} (mm)	D_{50} (mm)	D_{84} (mm)
ELW01PB	177.02	77.68	284.45
ELW09PB	69.08	36.57	114.87
ELW03PB	179.39	62.47	301.6
ELW06PB	173.54	80.5	282.58
ELW02PB	197.98	83.09	294.88
ELW08PB	80.25	39.82	122.5
ELW07MI(1/3)	137.95	48.45	184.21
ELW07MI(2/3)	138.93	57.44	185.19
ELW07MI(3/3)	127.07	61.38	238.07
ELW07TL	64.12	30.64	105.12
ELW04PBT	108.61	53.01	212.58
ELW04PBH	133.73	59.88	221.55
ELW05TR	105.62	53.76	247.51
ELW01CB	51.23	104.85	194.94
ELW03CB	82.5	187.53	401.48
ELW06CB	78.98	216.37	350.77
ELW02CB	65.19	119.83	215.38
ELW08CB	34.31	57.32	86.2

C.4 Survey data

To characterize the nature of sediment supply from the banks, we performed a semi-quantitative survey of cutbanks. We walked most alluvial and partly-alluvial portions of the channel, starting from just downstream of the canyon below Glines Canyon Dam and ending at the Strait of Juan de Fuca (Figure C.1). We noted bank stratigraphy at intervals of 10-20 m. For most locations, the height of each stratigraphic unit was estimated from a distance of several meters by eye, and, where necessary, aided by binoculars. Error in these measurements is likely up to about a meter. In select locations, measurements were made at the cutbank using surveying tape. Measurements began at the water surface and do not account for submerged bank toe deposits. We also noted presence of large wood along the bank. In addition, basic channel morphology was noted (pool, riffle, plane bed, etc).

The key used to describe morphologic units is presented in Table C.7 and the survey data is in Table C.8. Numbers represent elevation above the water surface in meters. For example, an entry with a CT value of 1 and a CE of 2 represents a location where a 1 meter exposure of cobble bank is visible above a 1 meter cobble toe deposit. Measurements made using the sur-

Table C.7: Survey data key

A	Former Lake Aldwell reservoir
AP	No bank exposure. Morphology determined by air photos/ground truthing.
B	Feature present on both banks
BD	Immobile boulders in channel
BK	Exposed bank
BR	Bedrock exposure
CB	Cobble bar
FCE	Fine cobble/gravel exposure
FCT	Fine cobble/gravel toe
CE	Cobble exposure
CT	Cobble toe
FB	Fine (fine gravel/sand) bar
GE	Gravel exposure
GT	Gravel toe
L	Left bank. *Secondary bank (same location as entry above it)
LWD	Large woody debris on bank
M	Middle Elwha
MO	Morphologic feature (riffle, pool, or plane bed)
OB	Overbank deposit
P	Pool
PA	Paleochannel
PB	Plane bed
PH	Photo ID
Pr	Present
RE	Reservoir deposits
R	Right bank. *Secondary bank (same location as entry above it)
RI	Riffle
RR	Rip-rap
RH	Reach
S	Stagnant water
SP	Spacing between observations (m)
tall	Deposit of reservoir fines; too tall to measure (at least 3 m)
TL	Till/outwash exposure

vey tape are presented in bold. The table is ordered from upstream to downstream. Locations that were sampled for photosieving (C.3) are noted. The coordinates for these points can be found in Tables C.4 and C.4.

Table C.8: Survey data

PH	RH	SP	BK	MO	RE	CT	CE	FCT	FCE	GT	GE	OB	CB	FB	LWD	RR	BD	TL	BR
PH46	M	20	L	RI	-	-	-	-	-	-	-	-	-	-	1	-	-	-	-
	M	20	L	RI	-	-	-	-	-	-	-	-	-	-	1	-	-	-	-
	M	20	L	RI	-	-	0.5	-	-	-	-	-	-	-	-	-	-	-	-
	M	20	L	RI	-	-	-	-	-	-	-	-	Pr	-	-	-	-	-	-
	M	20	L	RI	-	2	-	-	-	-	-	-	-	-	-	-	-	-	-
	M	20	L	RI	-	2	-	-	-	-	-	-	-	-	-	-	-	-	-
	M	20	L	RI	-	2	-	-	-	-	-	-	-	-	-	-	-	-	-
PHC47	M	20	L	RI	-	**1.65**	-	-	-	-	-	-	-	-	-	-	-	-	-
	M	20	L	RI	-	0.5	-	-	-	-	-	-	-	-	-	-	-	-	-
	M	20	L	P	-	0.25	-	-	-	-	-	-	-	-	-	-	-	-	-
	M	20	L	P	-	0.25	-	-	-	-	-	-	-	-	-	-	-	-	-
	M	20	L	P	-	0.1	-	-	-	-	-	-	-	-	-	-	-	-	-
	M	20	L	P	-	0.5	-	-	-	-	-	-	-	-	-	-	-	-	-
PH48	M	20	L	RI	-	-	-	-	-	-	-	-	-	-	1	-	Pr	-	-
PH34	M	20	L	RI	-	1.5	-	-	-	-	-	-	Pr	-	-	-	-	-	-
	M	20	L	RI	-	1	-	-	-	-	-	-	Pr	-	-	-	-	-	-
	M	20	L	RI	-	-	-	-	-	-	-	-	Pr	-	-	-	-	-	-
	M	20	L	RI	-	0.5	-	-	-	-	-	-	-	-	-	-	-	-	-
PH36	M	20	L	RI	-	2,1	-	-	-	-	-	1.2	-	-	-	-	-	-	-
	M	20	L	P	-	1	1.75	-	-	-	-	2	-	-	-	-	-	-	-
	M	20	L	P	-	1	1.75	-	-	-	-	2	-	-	-	-	-	-	-
PHC35	M	20	L	P	-	**1.78**	-	-	-	-	-	**2.08**	-	-	-	-	-	-	-
	M	20	L	P	-	1	1.45	-	-	-	-	1.5	-	-	1	-	-	-	-

Table C.8: Survey data

PH	RH	SP	BK	MO	RE	CT	CE	FCT	FCE	GT	GE	OB	CB	FB	LWD	RR	BD	TL	BR
	M	20	L	P	-	-	-	-	-	-	-	1.5	-	-	1	-	-	-	-
	M	20	L	P	-	1.2	1.45	-	-	-	-	1.5	-	-	-	-	-	-	-
	M	20	L	P	-	0.5	-	-	-	-	-	1	-	-	-	-	-	-	-
	M	20	L	P	-	-	-	-	-	-	-	1	-	-	1	-	-	-	-
	M	20	L	P	-	1	-	-	-	-	-	1.1	-	-	-	-	-	-	-
	M	20	R	RI	-	-	-	-	-	-	-	-	Pr	-	1	-	-	-	-
	M	20	R	RI	-	-	-	-	-	-	-	-	-	-	1	-	-	-	-
	M	20	R-PA	Dry	-	-	-	-	-	-	-	1.5	-	-	1	-	-	-	-
	M	20	R-PA	S	-	0.5	-	-	-	-	-	1	-	-	1	-	-	-	-
PH33	M	20	R	S	-	-	-	-	-	-	-	-	-	-	-	-	-	-	-
	M	20	R-PA	S	-	-	-	-	-	-	-	-	-	-	-	-	-	-	-
	M	20	R-PA	S	-	1.5	-	-	-	-	-	2.5	-	-	-	-	-	-	-
	M	20	R-PA	S	-	1	-	-	-	-	-	2	-	-	1	-	-	-	-
	M	20	R-PA	S	-	1	-	-	-	-	-	2	-	-	-	-	-	-	-
PHC32	M	20	R-PA	P	-	**1.2**	**1.95**	-	-	-	-	**2.45**	-	-	-	-	-	-	-
	M	20	L	P	-	0.75	-	-	-	-	-	-	-	-	-	-	-	-	-
	M	20	R-PA	P	-	-	-	-	-	-	-	-	-	-	1	-	-	-	-
	M	20	L	RI	-	1	1.5	-	-	-	-	-	-	-	-	-	-	-	-
	M	20	R-PA	P	-	-	-	-	-	-	-	1	-	-	-	-	-	-	-
	M	20	L	RI	-	1	1.3	-	-	-	-	-	-	-	-	-	-	-	-
	M	20	R-PA	P	-	0.75	-	-	-	-	-	1.5	-	-	-	-	-	-	-
	M	20	R-PA	RI	-	0.5	1	-	-	-	-	1.1	-	-	-	-	-	-	-
	M	20	L	RI	-	-	1.2,.75	-	-	-	-	1	-	-	-	-	-	-	-
PH31	M	20	R-PA	P	-	0.5	2.3	-	-	-	-	2.5	-	-	-	-	-	-	-

Table C.8: Survey data

PH	RH	SP	BK	MO	RE	CT	CE	FCT	FCE	GT	GE	OB	CB	FB	LWD	RR	BD	TL	BR
	M	20	L	P	-	1	-	-	-	-	-	1.5	-	-	-	-	-	-	-
	M	20	L	P	-	-	0.5	-	-	-	-	1	-	-	1	-	-	-	-
	M	20	L	P	-	-	0.75	-	-	-	-	1	-	-	-	-	-	-	-
PHC29	M	20	R-PA	P	-	**0.95**	**1.65**	-	-	-	-	**1.85**	-	-	-	-	-	-	-
	M	20	R-PA	P	-	-	0.3	-	-	-	-	-	-	-	-	-	-	-	-
	M	20	R-PA*	P	-	1.5	-	-	-	-	-	1.6	-	-	-	-	-	-	-
	M	20	L	RI	-	1	-	-	-	-	-	1.3	-	-	-	-	-	-	-
	M	20	R-PA*	RI	-	-	-	-	-	-	-	-	-	-	1	-	-	-	-
	M	20	L	RI	-	1	-	-	-	-	-	1.2	-	-	1	-	-	-	-
	M	20	R*	P	-	-	-	-	-	-	-	-	Pr	-	-	-	-	-	-
PH30	M	20	L	RI	-	1	-	-	-	-	-	1.2	-	-	1	-	-	-	-
	M	20	L	RI	-	-	0.5	-	-	-	-	0.6	1	-	-	-	-	-	-
	M	20	L	P	-	-	0.5	-	-	-	-	-	-	-	-	-	-	-	-
	M	20	L	P	-	-	-	-	-	-	-	-	0.5	-	1	-	-	-	-
	M	20	L	P	-	-	-	-	-	-	-	-	1	-	-	-	-	-	-
	M	20	R	RI	-	-	0.1	-	-	-	-	-	-	-	-	-	-	-	-
	M	20	R	RI	-	-	-	-	-	-	-	-	-	-	-	Pr	-	-	-
	M	20	R	RI	-	-	-	-	-	-	-	-	-	-	-	Pr	-	-	-
	M	20	R	RI	-	-	-	-	-	-	-	-	-	-	-	Pr	-	-	-
	M	20	R	RI	-	-	-	-	-	-	-	-	-	-	-	Pr	-	-	-
	M	20	R	P	-	-	-	-	-	-	-	-	-	-	-	Pr	-	-	-
	M	20	R	P	-	-	-	-	-	-	-	-	-	-	-	Pr	-	-	-

Table C.8: Survey data

PH	RH	SP	BK	MO	RE	CT	CE	FCT	FCE	GT	GE	OB	CB	FB	LWD	RR	BD	TL	BR
	M	20	R	P	-	-	-	-	-	-	-	-	-	-	-	Pr	-	-	-
	M	20	R	P	-	-	-	-	-	-	-	-	-	-	-	Pr	-	-	-
	M	20	R	P	-	-	-	-	-	-	-	-	-	-	-	Pr	-	-	-
	M	20	R	P	-	-	-	-	-	-	-	-	-	-	-	Pr	-	-	-
	M	20	R	P	-	0.3	-	-	-	-	-	-	-	-	-	-	-	-	-
	M	20	R	P	-	1	2	-	-	-	-	2.1	-	-	-	-	-	-	-
	M	20	R	P	-	-	-	-	-	-	-	-	-	-	1	-	-	-	-
	M	20	R	RI	-	1	-	-	-	-	-	-	-	-	1	-	-	-	-
PH44	M	20	R	RI	-	-	-	-	-	-	-	-	-	-	1	-	-	-	-
	M	20	L	RI	-	-	-	-	-	-	-	-	-	-	1	-	-	-	-
	M	20	L	RI	-	-	-	-	-	-	-	-	0.5	-	-	-	-	-	-
	M	20	R	P	-	-	0.5	-	-	-	-	0.6	-	-	-	-	-	-	-
	M	20	R	P	-	-	-	-	-	-	-	-	-	-	1	-	-	-	-
	M	20	R	P	-	-	1	-	-	-	-	-	-	-	1	-	-	-	-
	M	20	R	P	-	0.5	-	-	-	-	-	-	-	-	-	-	-	-	-
	M	20	R	P	-	-	-	-	-	-	-	-	0.75	-	-	-	-	-	-
	M	20	R	P	-	-	-	-	-	-	-	-	1	-	-	-	-	-	-
PH45	M	20	L	RI	-	0.3	-	-	-	-	-	-	-	-	-	-	-	-	-
	M	20	L	P	-	-	-	-	-	-	-	-	-	-	-	-	-	-	-
	M	20	L	S	-	-	-	-	-	-	-	0.3	-	-	-	-	-	-	-
	M	20	L	S	-	-	-	-	-	-	-	0.3	-	-	-	-	-	-	-
	M	20	L	S	-	-	-	-	-	-	-	-	-	-	-	-	-	-	-
	M	20	L	S	-	-	-	-	-	-	-	-	-	-	-	-	-	-	-
	M	20	L	S	-	-	-	-	-	-	-	-	-	-	-	-	-	-	-

Table C.8: Survey data

PH	RH	SP	BK	MO	RE	CT	CE	FCT	FCE	GT	GE	OB	CB	FB	LWD	RR	BD	TL	BR
PHC37	M	20	R	S	-	0.5	0.75	-	-	-	-	-	-	-	-	-	-	-	-
	M	20	L	S	-	-	-	-	-	-	-	-	-	-	-	-	-	-	-
PH38	M	20	L	S	-	-	-	-	-	-	-	-	-	-	-	-	-	-	-
	M	20	R	S	-	0.75	-	-	-	-	-	1	-	-	-	-	-	-	-
PH39	M	20	R	S	-	1.2	1.4	-	-	-	-	1.5	-	-	-	-	-	-	-
	M	20	R	S	-	1.4	-	-	-	-	-	1.5	-	-	-	-	-	-	-
	M	20	R	S	-	-	0.4	-	-	-	-	-	-	-	1	-	-	-	-
	M	20	R	S	-	1.4	-	-	-	-	-	-	-	-	-	-	-	-	-
	M	20	R	S	-	-	1	-	-	-	-	-	-	-	-	-	-	-	-
PHC40	M	20	R	S	-	-	1	-	-	-	-	-	-	-	-	-	-	-	-
	M	20	R	S	-	-	0.1	-	-	-	-	-	-	-	1	-	-	-	-
	M	20	R	S	-	-	-	-	-	-	-	-	-	-	1	-	-	-	-
	M	20	R	Dry	-	-	-	-	-	-	-	-	-	-	1	-	-	-	-
	M	20	R	Dry	-	-	-	-	-	-	-	-	-	-	-	-	-	-	-
	M	20	R	Dry	-	-	-	-	-	-	-	-	-	-	-	-	-	-	-
	M	20	R	Dry	-	-	-	-	-	-	-	-	-	-	-	-	-	-	-
PHC41	M	20	L	Dry	-	**0.9**	**1.35**	-	-	-	-	-	-	-	-	-	-	-	-
	M	20	L	S	-	-	1	-	-	-	-	-	-	-	-	-	-	-	-
	M	20	L	S	-	-	1.5	-	-	-	-	-	-	-	-	-	-	-	-
	M	20	R	S	-	-	-	-	-	-	-	-	-	-	1	-	-	-	-
	M	20	R	S	-	-	-	-	-	-	-	-	-	-	1	-	-	-	-
	M	20	R	S	-	-	0.5	-	-	-	-	-	-	-	-	-	-	-	-
	M	20	R	S	-	1	-	-	-	-	-	-	-	-	-	-	-	-	-
	M	20	R	S	-	0.75	-	-	-	-	-	-	-	-	-	-	-	-	-

Table C.8: Survey data

PH	RH	SP	BK	MO	RE	CT	CE	FCT	FCE	GT	GE	OB	CB	FB	LWD	RR	BD	TL	BR
	M	20	R	S	-	1	-	-	-	-	-	-	-	-	-	-	-	-	-
	M	20	R	S	-	-	1.5	-	-	-	-	-	-	-	1	-	-	-	-
PHC41	M	20	L	S	-	**1.55**	**2.1**	-	-	-	-	-	-	-	-	-	-	-	-
PHC42	M	20	R	S	-	2	**2.2**	-	-	-	-	-	-	-	-	-	-	-	-
	M	20	R	S	-	-	-	-	-	-	-	-	-	-	1	-	-	-	-
	M	20	R	S	-	-	-	-	-	-	-	-	-	-	1	-	-	-	-
	M	20	R	S	-	-	-	-	-	-	-	-	-	-	1	-	-	-	-
	M	20	R	S	-	-	-	-	-	-	-	-	-	-	-	-	-	-	-
	M	20	R	S	-	-	-	-	-	-	-	-	-	-	-	-	-	-	-
	M	20	L	S	-	0.5	-	-	-	-	-	-	-	-	-	-	-	-	-
	M	20	L	S	-	0.2	-	-	-	-	-	-	-	-	1	-	-	-	-
	M	20	L	S	-	1	-	-	-	-	-	-	-	-	-	-	-	-	-
	M	20	L	S	-	1.5	1.7	-	-	-	-	-	-	-	-	-	-	-	-
	M	20	L	S	-	0.5	-	-	-	-	-	-	-	-	-	-	-	-	-
	M	20	L	S	-	0.5	-	-	-	-	-	-	-	-	-	-	-	-	-
	M	20	L	S	-	-	-	-	-	-	-	-	-	-	1	-	-	-	-
PHC43	M	20	L	RI	-	**1.15**	-	-	-	-	-	-	-	-	**1.55**	-	-	-	-
	M	20	R	P	-	-	-	-	1.5	-	-	-	-	-	1	-	-	-	-
	M	20	R	P	-	-	-	-	1.5	0.5	-	-	-	-	-	-	-	-	-
	M	20	R	P	-	-	-	-	1.5	-	-	-	-	-	1	-	-	-	-
	M	20	R	P	-	-	0.5	-	-	-	-	-	-	-	-	-	-	-	-
	M	20	R	P	-	1	-	-	-	-	-	-	-	-	-	-	-	-	-
	M	20	R	P	-	1	1.3	-	-	-	-	-	-	-	-	-	-	-	-
	M	20	R	RI	-	1	1.5	-	-	-	-	-	-	-	-	-	-	-	-

Table C.8: Survey data

PH	RH	SP	BK	MO	RE	CT	CE	FCT	FCE	GT	GE	OB	CB	FB	LWD	RR	BD	TL	BR
	M	20	R	RI	-	1	-	-	-	-	-	-	-	-	-	-	-	-	-
	M	20	R	RI	-	1	-	-	-	-	-	-	-	-	1	-	-	-	-
	M	20	R	P	-	1.5	-	-	-	-	-	-	-	-	-	-	-	-	-
	M	20	R	P	-	1.5	-	-	-	-	-	-	-	-	-	-	-	-	-
	M	20	R	P	-	1.5	-	-	-	-	-	-	-	-	-	-	-	-	-
	M	20	R	P	-	1	-	-	-	-	-	-	-	-	-	-	-	-	-
	M	20	R	P	-	-	-	-	-	-	-	-	-	-	1	-	-	-	-
PHC64	M	20	R	P	-	**1.84**	-	-	-	-	-	-	-	-	-	-	-	-	-
	M	20	R	P	-	-	-	-	-	-	-	-	-	-	-	-	-	-	-
PH63	M	20	R	RI	-	3	-	-	-	-	-	-	-	-	-	-	-	-	-
	M	20	R	RI	-	2.5	-	-	-	-	-	-	-	-	-	-	-	-	-
	M	20	R	P	-	2	-	-	-	-	-	-	-	-	1	-	-	-	-
	M	20	R	P	-	1.5	2.5	-	-	-	-	-	-	-	-	-	-	-	-
PHC62	M	20	R	P	-	**1.25**	**2.15**	-	-	-	-	-	-	-	-	-	-	-	-
	M	20	R	P	-	0.3	0.7	-	-	-	-	-	-	-	-	-	-	-	-
	M	20	R	P	-	0.5	0.6	-	-	-	-	-	-	-	-	-	-	-	-
	M	20	R	RI	-	-	0.5	-	-	-	-	-	-	-	-	-	-	-	-
	M	20	R	RI	-	-	0.75	-	-	-	-	-	-	-	1	-	-	-	-
	M	20	R	P	-	-	0.5	-	-	-	-	-	-	-	1	-	-	-	-
	M	20	R	P	-	-	0.5	-	-	-	-	-	-	-	1	-	-	-	-
	M	20	R	P	-	-	-	-	1	-	-	-	-	-	-	-	-	-	-
	M	20	R	P	-	-	0.3	-	-	-	-	-	-	-	1	-	-	-	-
	M	20	R	P	-	0.5	0.7	-	-	-	-	1	-	-	-	-	-	-	-
	M	20	R	P	-	0.5	0.7	-	-	-	-	1	-	-	-	-	-	-	-

Table C.8: Survey data

PH	RH	SP	BK	MO	RE	CT	CE	FCT	FCE	GT	GE	OB	CB	FB	LWD	RR	BD	TL	BR
	M	20	R	P	-	-	0.5	-	-	-	-	-	-	-	-	-	-	-	-
	M	20	R	P	-	1	-	-	-	-	-	-	-	-	-	-	-	-	-
	M	20	R	P	-	-	0.5	-	-	-	-	-	-	-	1	-	-	-	-
	M	20	R	P	-	-	-	-	-	-	-	-	-	-	1	-	-	-	-
	M	20	L	RI	-	-	-	0.3	-	-	-	-	-	-	-	-	-	-	-
	M	20	L	RI	-	-	-	0.75,1.5	-	-	-	-	-	-	-	-	-	-	-
	M	20	L	RI	-	1,1.6	1.5	-	-	-	-	-	-	-	-	-	-	-	-
	M	20	L	P	-	1.5	-	-	-	-	-	-	-	-	-	-	-	-	-
	M	20	L	P	-	1.5	-	-	-	-	-	-	-	-	-	-	-	-	-
PHC61	M	20	L	P	-	**1.68**	**2.2**	-	-	-	-	-	-	-	-	-	-	-	-
	M	20	L	P	-	1	1.3	-	-	-	-	-	-	-	-	-	-	-	-
	M	20	L	P	-	-	-	2	-	-	-	-	-	-	-	-	-	-	-
	M	20	L	RI	-	-	-	-	-	-	-	-	-	-	1	-	-	-	-
	M	20	L	RI	-	-	0.3	-	-	-	-	-	1	-	-	-	-	-	-
	M	20	R	RI	-	-	-	-	-	-	-	-	1.5	-	-	-	-	-	-
	M	20	R	RI	-	-	-	-	-	-	-	-	-	-	1	-	-	-	-
	M	20	L	RI	-	-	0.5	-	-	-	-	-	-	-	-	-	-	-	-
	M	20	L	P	-	-	-	-	-	-	-	-	-	-	-	-	Pr	-	-
	M	20	L	P	-	-	-	-	-	-	-	-	-	-	-	-	Pr	-	-
	M	20	L	P	-	-	-	-	-	-	-	-	-	-	-	-	Pr	-	-
	M	20	L	P	-	-	-	-	-	-	-	-	-	-	-	-	Pr	-	-
PH60	M	20	L	RI	-	-	-	-	-	-	-	-	-	-	-	-	Pr	-	-
PHC59	M	20	R	P	-	-	**1.44**	-	-	-	-	**0.8**	-	-	-	-	-	-	-
	M	20	R	P	-	-	0.75	-	-	-	-	0.2	-	-	-	-	-	-	-

Table C.8: Survey data

PH	RH	SP	BK	MO	RE	CT	CE	FCT	FCE	GT	GE	OB	CB	FB	LWD	RR	BD	TL	BR
	M	20	R	P	-	-	0.3	-	-	-	-	0.4	-	-	-	-	-	-	-
	M	20	R	P	-	-	-	-	0.5	-	-	-	-	-	1	-	-	-	-
	M	20	R	P	-	-	0.5	-	-	-	-	2.5	-	-	-	-	-	-	-
	M	20	R	P	-	-	-	-	-	-	-	0.3	-	-	1	-	-	-	-
	M	20	L	RI	-	-	-	-	-	-	-	-	0.3	-	-	-	-	-	-
	M	20	L	RI	-	-	-	-	0.3	-	-	-	-	-	-	-	-	-	-
PH58	M	20	L	RI	-	-	-	-	-	-	-	-	0.75	-	-	-	-	-	-
	M	20	L	RI	-	-	-	-	-	-	-	-	1	-	-	-	-	-	-
	M	20	L	RI	-	-	-	-	-	-	-	-	1	-	-	-	-	-	-
	M	20	L	RI	-	-	-	-	-	-	-	-	1	-	-	-	-	-	-
	M	20	R	RI	-	-	-	-	-	-	-	-	-	-	1	-	-	-	-
	M	20	L*	RI	-	-	-	-	-	-	-	-	-	-	-	-	Pr	-	-
	M	20	R	RI	-	1	1.5	-	-	-	-	-	-	-	-	-	-	-	-
	M	20	L*	RI	-	0.75	-	-	-	-	-	-	-	-	-	-	-	-	-
	M	20	R	RI	-	1.5	-	-	-	-	-	-	-	-	-	-	-	-	-
	M	20	L*	RI	-	-	-	-	-	-	-	-	-	-	-	-	Pr	-	-
	M	20	R	RI	-	1.5	-	-	-	-	-	-	-	-	-	-	-	-	-
	M	20	L*	RI	-	-	-	-	-	-	-	-	-	-	-	-	Pr	-	-
	M	20	R	RI	-	1	-	-	-	-	-	-	-	-	-	-	-	-	-
	M	20	L*	RI	-	0.5	-	-	-	-	-	-	-	-	-	-	-	-	-
	M	20	R	RI	-	0.5	-	-	-	-	-	-	-	-	-	-	-	-	-
	M	20	L*	RI	-	-	-	-	-	-	-	-	-	-	-	-	Pr	-	-
PHC57	M	20	R	RI	-	**0.45**	**1.02**	-	-	-	-	-	-	-	-	-	-	-	-
	M	20	L*	RI	-	-	-	-	-	-	-	-	-	-	-	-	Pr	-	-

Table C.8: Survey data

PH	RH	SP	BK	MO	RE	CT	CE	FCT	FCE	GT	GE	OB	CB	FB	LWD	RR	BD	TL	BR
	M	20	R	RI	-	-	-	-	-	-	-	-	-	-	1	-	-	-	-
	M	20	L*	RI	-	-	-	-	-	-	-	-	-	-	-	-	Pr	-	-
	M	20	R	RI	-	0.75	-	-	-	-	-	-	-	-	-	-	-	-	-
	M	20	L*	RI	-	1	-	-	-	-	-	-	-	-	-	-	Pr	-	-
	M	20	R	RI	-	1.5	-	-	-	-	-	-	-	-	-	-	-	-	-
	M	20	L	RI	-	-	-	-	-	-	-	-	-	-	-	-	Pr	-	-
	M	20	L	P	-	-	2	-	-	-	-	2.1	-	-	-	-	-	-	-
	M	20	L	P	-	1.5	2	-	-	-	-	-	-	-	-	-	-	-	-
PHC56	M	20	L	P	-	**1.5**	-	-	**1.92**	-	-	-	-	-	-	-	-	-	-
	M	20	L	RI	-	0.5	-	-	-	-	-	-	-	-	-	-	-	-	-
	M	20	R	RI	-	-	-	-	-	-	-	-	-	-	-	-	-	-	-
PH55	M	20	R	RI	-	0.5	-	-	-	-	-	-	-	-	-	-	-	-	-
	M	20	R	RI	-	0.5	-	-	-	-	-	-	-	-	-	-	-	-	-
	M	20	L	P	-	-	-	-	-	-	-	-	-	-	-	-	-	-	-
	M	20	L	P	-	-	-	-	-	-	-	-	-	-	-	-	-	-	-
	M	20	L	P	-	-	-	-	-	-	-	-	-	-	-	-	-	-	-
	M	20	L	P	-	-	-	-	-	-	-	-	-	-	-	-	-	-	Pr
	M	20	L	P	-	-	-	-	-	-	-	-	-	-	-	-	-	-	Pr
	M	20	L	P	-	-	-	-	-	-	-	-	-	-	-	-	-	-	Pr
	M	20	L	P	-	-	-	-	-	-	-	-	-	-	-	-	-	-	Pr
	M	20	L	P	-	-	-	-	-	-	-	-	-	-	-	-	-	-	Pr
	M	20	L	P	-	-	-	-	-	-	-	-	-	-	-	-	-	-	Pr
PH54	M	20	R	RI	-	-	-	-	-	-	-	-	-	-	-	-	-	-	-
	M	20	R	RI	-	-	-	-	-	-	-	-	-	-	1	-	-	-	-

Table C.8: Survey data

PH	RH	SP	BK	MO	RE	CT	CE	FCT	FCE	GT	GE	OB	CB	FB	LWD	RR	BD	TL	BR
	M	20	R	RI	-	-	0.3	-	-	-	-	-	-	-	-	-	-	-	-
	M	20	L	RI	-	-	-	-	-	-	-	-	-	-	-	-	-	-	-
	M	20	L	P	-	0.3	-	-	-	-	-	-	-	-	-	-	-	-	-
	M	20	L	P	-	0.5	-	-	-	-	-	-	-	-	-	-	-	-	-
	M	20	L	P	-	-	-	-	-	-	-	-	-	-	1	-	-	-	-
PHC53	M	20	L	P	-	**1.64**	-	-	-	-	-	-	-	-	-	-	-	-	-
	M	20	L	P	-	0.75	-	-	-	-	-	-	-	-	-	-	-	-	-
	M	20	L	P	-	0.75	-	-	-	-	-	-	-	-	-	-	-	-	-
	M	20	R	RI	-	1.5	2.5	-	-	-	-	2.6	-	-	-	-	-	-	-
	M	20	R	RI	-	1.5	2.5	-	-	-	-	2.6	-	-	-	-	-	-	-
	M	20	R	RI	-	1.5	2.5	-	-	-	-	2.6	-	-	-	-	-	-	-
	M	20	R	RI	-	1.5	2.5	-	-	-	-	2.6	-	-	-	-	-	-	-
	M	20	R	RI	-	1.5	2.5	-	-	-	-	2.6	-	-	-	-	-	-	-
	M	20	R	RI	-	2	3	-	-	-	-	3.1	-	-	-	-	-	-	-
	M	20	R	P	-	2	3	-	-	-	-	3.1	-	-	-	-	-	-	-
	M	20	R	P	-	0.5	-	-	-	-	-	-	-	-	1	-	-	-	-
PH52	M	20	R	RI	-	1	-	-	-	-	-	-	-	-	1	-	-	-	-
	M	20	R	RI	-	1	2	-	-	-	-	2.1	-	-	-	-	-	-	-
	M	20	R	RI	-	1	2	-	-	-	-	2.1	-	-	-	-	-	-	-
	M	20	R	RI	-	1	-	-	-	-	-	-	-	-	1	-	-	-	-
	M	20	R	RI	-	1.5	1	-	-	-	-	2.1	-	-	-	-	-	-	-
	M	20	R	RI	-	-	1	-	-	-	-	-	-	-	1	-	-	-	-
	M	20	R	RI	-	-	0.5	-	-	-	-	-	-	-	-	-	-	-	-
	M	20	R	RI	-	-	-	-	-	-	-	-	0.75	-	-	-	-	-	-

Table C.8: Survey data

PH	RH	SP	BK	MO	RE	CT	CE	FCT	FCE	GT	GE	OB	CB	FB	LWD	RR	BD	TL	BR
	M	20	L	P	-	0.3	-	-	-	-	-	-	-	-	1	-	-	-	-
	M	20	L	P	-	1	-	-	-	-	-	-	-	-	1	-	-	-	-
	M	20	L	P	-	1.5	2	-	-	-	-	2.2	-	-	-	-	-	-	-
	M	20	L	P	-	1	2	-	-	-	-	2.5	-	-	-	-	-	-	-
	M	20	R	P	-	1.5	-	-	-	-	-	1.6	-	-	-	-	-	-	-
	M	20	R	P	-	2	3	-	-	-	-	3.1	-	-	-	-	-	-	-
	M	20	R	P	-	1	-	-	-	-	-	-	-	-	1	-	-	-	-
PHC51	M	20	R	P	-	**1.64**	-	-	-	-	-	**1.94**	-	-	-	-	-	-	-
	M	20	R	P	-	1	-	-	-	-	-	-	-	-	-	-	-	-	-
	M	20	R	RI	-	1.5	2	-	-	-	-	2.1	-	-	-	-	-	-	-
	M	20	R	RI	-	1	-	-	-	-	-	-	-	-	-	-	-	-	-
	M	20	R	RI	-	-	0.5	-	-	-	-	-	-	-	1	-	-	-	-
	M	20	R	RI	-	-	-	-	-	-	-	-	-	-	1	-	-	-	-
	M	20	R	RI	-	0.5	-	-	-	-	-	0.6	-	-	-	-	-	-	-
	M	20	R	RI	-	-	-	-	-	-	-	-	-	-	-	-	Pr	-	-
PH50	M	20	R	RI	-	1	-	-	-	-	-	-	-	-	-	Pr	-	-	-
	M	20	R	P	-	1	1.5	-	-	-	-	1.6	-	-	-	Pr	-	-	-
	M	20	R	P	-	1	-	-	-	-	-	1.1	-	-	-	-	-	-	-
	M	20	R	P	-	1	-	-	-	-	-	2.5	-	-	-	-	-	-	-
	M	20	R	P	-	1	-	-	-	-	-	-	-	-	-	-	-	-	-
PH49	M	20	R	RI	-	1	-	-	-	-	-	-	-	-	-	-	-	-	-
PHC65	M	20	R	RI	-	**1.64**	-	-	-	-	-	**2.24**	-	-	1	-	-	-	-
	M	AP	L	PB	-	0.5	-	-	-	-	-	-	-	-	-	-	-	-	-
	M	AP	L	PB	-	0.5	-	-	-	-	-	-	-	-	-	-	-	-	-

Table C.8: Survey data

PH	RH	SP	BK	MO	RE	CT	CE	FCT	FCE	GT	GE	OB	CB	FB	LWD	RR	BD	TL	BR
	M	AP	L	PB	-	0.5	-	-	-	-	-	-	-	-	-	-	-	-	-
	M	AP	L	PB	-	0.5	-	-	-	-	-	-	-	-	-	-	-	-	-
	M	AP	L	PB	-	0.5	-	-	-	-	-	-	-	-	-	-	-	-	-
	M	AP	L	PB	-	0.5	-	-	-	-	-	-	-	-	-	-	-	-	-
	M	AP	L	PB	-	0.5	-	-	-	-	-	-	-	-	-	-	-	-	-
	M	AP	L	PB	-	0.5	-	-	-	-	-	-	-	-	-	-	-	-	-
	M	AP	L	PB	-	0.5	-	-	-	-	-	-	-	-	-	-	-	-	-
	M	AP	L	PB	-	0.5	-	-	-	-	-	-	-	-	-	-	-	-	-
	M	20	L	PB	-	0.5	1.5	-	-	-	-	-	-	-	1	-	-	-	-
	M	20	L	PB	-	0.5	1.5	-	-	-	-	-	-	-	1	-	-	-	-
	M	20	L	PB	-	1	2	-	-	-	-	2.1	-	-	-	-	-	-	-
	M	20	L	PB	-	-	2	-	-	-	-	-	-	-	1	-	-	-	-
	M	20	L	PB	-	1	-	-	-	-	-	1.1	-	-	1	-	-	-	-
	M	20	L	PB	-	1.5	-	-	-	-	-	-	-	-	-	-	-	-	-
PHC67	M	20	L	PB	-	**1.2**	**1.66**	-	-	-	-	-	-	-	-	-	-	-	-
	M	20	L	PB	-	1	-	-	-	-	-	1.1	-	-	1	-	-	-	-
	M	20	L	PB	-	1.5	-	-	-	-	-	1.6	-	-	-	-	-	-	-
PH68	M	20	L	PB	-	0.5	-	-	-	-	-	0.6	-	-	1	-	-	-	-
	M	20	L	PB	-	1.5	0.5	-	-	-	-	-	-	-	-	-	-	-	-
	M	20	L	PB	-	0.5	-	-	-	-	-	-	-	-	1	-	-	-	-
	M	20	L	PB	-	0.5	-	-	-	-	-	-	-	-	1	-	-	-	-
	M	20	L	RI	-	0.5	1	-	-	-	-	-	-	-	1	-	-	-	-
PH69	M	20	L	RI	-	-	-	-	-	-	-	-	-	-	1	-	-	-	-
	M	20	L	P	-	1	-	-	-	-	-	-	-	-	1	-	-	-	-

Table C.8: Survey data

PH	RH	SP	BK	MO	RE	CT	CE	FCT	FCE	GT	GE	OB	CB	FB	LWD	RR	BD	TL	BR
	M	20	R	P	-	-	-	-	-	-	-	-	1.5	-	-	-	-	-	-
	M	20	R	P	-	-	-	-	-	-	-	-	0.15	-	-	-	-	-	-
PHC70	M	20	L	P	-	**1.54**	**2.2**	-	-	-	-	**2.3**	-	-	-	-	-	-	-
	M	20	R*	P	-	-	-	-	-	-	-	-	1.75	-	-	-	-	-	-
	M	20	L	P	-	1.5	-	-	-	-	-	-	-	-	-	-	-	-	-
	M	20	R*	P	-	-	-	-	-	-	-	-	1.75	-	-	-	-	-	-
	M	20	L	P	-	1.5	-	-	-	-	-	-	-	-	-	-	-	-	-
	M	20	R*	P	-	1	-	-	-	-	-	-	-	-	-	-	-	-	-
	M	20	L	P	-	-	-	-	-	-	-	-	-	-	1	-	-	-	-
	M	20	R*	RI	-	0.3	-	-	-	-	-	-	-	-	-	-	-	-	-
PH71	M	20	L	RI	-	0.5	-	-	-	-	-	-	-	-	-	-	-	-	-
	M	20	L	RI	-	1.5	-	-	-	-	-	1.6	-	-	-	-	-	-	-
	M	20	L	RI	-	0.5	-	-	-	-	-	2.5	-	-	-	-	-	-	-
	M	20	R*	RI	-	1.5	-	-	-	-	-	-	-	-	-	-	-	-	-
	M	20	L	RI	-	-	1	-	-	-	-	-	-	-	-	-	-	-	-
	M	20	R*	RI	-	0.5	-	-	1.5	-	-	-	-	-	-	-	-	-	-
	M	20	L	RI	-	1	-	-	-	-	-	-	-	-	-	-	-	-	-
	M	20	R	RI	-	1	-	-	-	-	-	-	-	-	-	-	-	-	-
	M	20	L	RI	-	1	-	-	-	-	-	-	-	-	1	-	-	-	-
	M	20	R	RI	-	1.5	-	-	-	-	-	-	-	-	-	-	-	-	-
	M	20	L	P	-	1.5	-	-	-	-	-	1.6	-	-	-	-	-	-	-
	M	20	R	P	-	-	0.5	-	-	-	-	0.6	-	-	-	-	-	-	-
	M	20	L	P	-	-	1	-	-	-	-	-	-	-	1	-	-	-	-
	M	20	R	P	-	-	-	-	-	-	-	-	-	-	1	-	-	-	-

Table C.8: Survey data

PH	RH	SP	BK	MO	RE	CT	CE	FCT	FCE	GT	GE	OB	CB	FB	LWD	RR	BD	TL	BR
	M	20	L	P	-	-	1.5	-	-	-	-	1.6	-	-	-	-	-	-	-
	M	20	L	P	-	1.5	-	-	-	-	-	-	-	-	-	-	-	-	-
PHC72	M	20	R	RI	-	**1.58**	2	-	-	-	-	-	-	-	-	-	-	-	-
	M	20	L	RI	-	2	-	-	-	-	-	-	-	-	-	-	-	-	-
	M	20	L	P	-	1.5	-	-	-	-	-	-	-	-	1	-	-	-	-
	M	20	R	P	-	1.5	-	-	-	-	-	-	-	-	-	-	-	-	-
	M	20	L	P	-	-	0.5	-	-	-	-	-	-	-	-	-	-	-	-
	M	20	L	P	-	-	0.5	-	-	-	-	-	-	-	1	-	-	-	-
	M	20	L	P	-	1.5	-	-	-	-	-	1.6	-	-	-	-	-	-	-
	M	20	R	P	-	1.5	-	-	-	-	-	-	-	-	-	-	-	-	-
	M	20	L	P	-	-	-	-	-	-	-	-	0.5	-	-	-	-	-	-
	M	20	L	P	-	-	0.5	-	-	-	-	-	-	-	-	-	-	-	-
	M	20	L	P	-	-	0.3	-	-	-	-	-	-	-	-	-	-	-	-
	M	20	L	P	-	-	-	-	-	-	-	-	-	-	-	-	-	-	-
	M	20	R	P	-	-	0.3	-	-	-	-	-	-	-	-	-	-	-	-
	M	20	R	P	-	-	0.3	-	-	-	-	-	-	-	-	-	-	-	-
PH73	M	20	R	RI	-	-	-	-	-	-	-	-	-	-	-	-	-	-	-
	M	20	R	RI	-	-	-	-	-	-	-	-	-	-	-	-	-	-	-
	M	20	R	P	-	-	-	-	-	-	-	-	-	-	-	-	-	-	-
	M	20	R	P	-	-	0.3	-	-	-	-	-	-	-	-	-	-	-	-
	M	20	R	P	-	-	0.3	-	-	-	-	-	-	-	-	-	-	-	-
	M	20	L	P	-	-	-	1.5	-	-	-	-	-	-	-	-	-	-	-
	M	20	L	P	-	1	-	-	-	-	-	-	-	-	-	-	-	-	-
PHC74	M	20	L	P	-	**1.76**	-	-	-	-	-	**1.77**	-	-	-	-	-	-	-

Table C.8: Survey data

PH	RH	SP	BK	MO	RE	CT	CE	FCT	FCE	GT	GE	OB	CB	FB	LWD	RR	BD	TL	BR
	M	20	L	RI	-	-	-	-	-	-	-	-	-	-	-	-	-	-	Pr
	M	20	L	RI	-	-	-	-	-	-	-	-	-	-	-	-	-	-	Pr
	M	20	L	RI	-	-	-	-	-	-	-	-	-	-	-	-	-	-	Pr
	M	20	L	RI	-	-	-	-	-	-	-	-	-	-	-	-	-	-	Pr
	M	20	L	RI	-	-	-	-	-	-	-	-	-	-	-	-	-	-	Pr
	M	20	L	RI	-	-	-	-	-	-	-	-	-	-	-	-	-	-	Pr
	M	20	L	RI	-	-	-	-	-	-	-	-	-	-	-	-	-	-	Pr
	M	20	L	RI	-	-	-	-	-	-	-	-	-	-	-	-	-	-	Pr
	M	20	L	RI	-	-	-	-	-	-	-	-	-	-	-	-	-	-	Pr
	M	20	L	RI	-	-	-	-	-	-	-	-	-	-	-	-	-	-	Pr
	M	20	L	RI	-	-	-	-	-	-	-	-	-	-	-	-	-	-	Pr
	M	20	L	RI	-	-	-	-	-	-	-	-	-	-	-	-	-	-	Pr
	M	20	L	RI	-	-	-	-	-	-	-	-	-	-	-	-	-	-	Pr
	M	20	L	RI	-	-	-	-	-	-	-	-	-	-	-	-	-	-	Pr
	M	20	L	RI	-	-	-	-	-	-	-	-	-	-	-	-	-	-	Pr
	M	20	R	P	-	-	-	-	-	-	-	-	-	-	-	-	-	-	Pr
	M	20	R	P	-	-	-	-	-	-	-	-	-	-	-	-	-	-	Pr
	M	20	R	P	-	-	-	-	-	-	-	-	-	-	-	-	-	-	Pr
	M	20	R	P	-	-	-	-	-	-	-	-	-	-	-	-	-	-	Pr
	M	20	R	P	-	-	-	-	-	-	-	-	-	-	-	-	-	-	Pr
	M	20	R	P	-	-	-	-	-	-	-	-	-	-	-	-	-	-	Pr
	M	20	R	P	-	-	-	-	-	-	-	-	-	-	-	-	-	-	Pr
	M	20	R	P	-	-	-	-	-	-	-	-	-	-	-	-	-	-	Pr
	M	20	R	P	-	-	-	-	-	-	-	-	-	-	-	-	-	-	Pr

Table C.8: Survey data

PH	RH	SP	BK	MO	RE	CT	CE	FCT	FCE	GT	GE	OB	CB	FB	LWD	RR	BD	TL	BR
	M	20	R	P	-	-	-	-	-	-	-	-	-	-	-	-	-	-	Pr
	M	20	R	P	-	-	-	-	-	-	-	-	-	-	-	-	-	-	Pr
	M	20	R	P	-	-	-	-	-	-	-	-	-	-	-	-	-	-	Pr
	M	20	R	P	-	-	-	-	-	-	-	-	-	-	-	-	-	-	Pr
	M	20	R	P	-	-	-	-	-	-	-	-	-	-	-	-	-	-	Pr
	M	20	R	P	-	-	-	-	-	-	-	-	-	-	-	-	-	-	Pr
	M	20	R	P	-	-	-	-	-	-	-	-	-	-	-	-	-	-	Pr
	M	20	R	P	-	-	-	-	-	-	-	-	-	-	-	-	-	-	Pr
	M	20	R	P	-	-	-	-	-	-	-	-	-	-	-	-	-	-	Pr
	M	20	R	RI	-	-	-	-	-	-	-	-	-	-	-	-	-	-	Pr
	M	20	R	RI	-	-	-	-	-	-	-	-	-	-	-	-	-	-	Pr
	M	20	R	RI	-	-	-	-	-	-	-	-	-	-	-	-	-	-	Pr
	M	20	R	RI	-	-	-	-	-	-	-	-	-	-	-	-	-	-	Pr
	M	20	R	RI	-	-	-	-	-	-	-	-	-	-	-	-	-	-	Pr
PHC78	M	20	L	RI	-	**1.34**	**1.86**	-	-	-	-	**2.2**	-	-	-	-	-	-	-
	M	20	L	RI	-	-	-	-	-	-	-	-	-	-	1	-	-	-	-
	M	20	L	RI	-	0.5	-	-	-	-	-	-	-	-	-	-	-	-	-
	M	20	L	RI	-	-	0.5	-	-	-	-	-	-	-	1	-	-	-	-
	M	20	L	RI	-	1	-	-	-	-	-	1.3	-	-	-	-	-	-	-
	M	20	L	RI	-	1.5	-	-	-	-	-	1.8	-	-	-	-	-	-	-
	M	20	L	RI	-	1.5	-	-	-	-	-	2.5	-	-	-	-	-	-	-
	M	20	L	RI	-	1.25	-	-	-	-	-	2	-	-	-	-	-	-	-
	M	20	L	RI	-	-	-	-	-	-	-	0.5	-	-	1	-	-	-	-
	M	20	L	RI	-	-	-	0.5	-	-	-	-	-	-	-	-	-	-	-

Table C.8: Survey data

PH	RH	SP	BK	MO	RE	CT	CE	FCT	FCE	GT	GE	OB	CB	FB	LWD	RR	BD	TL	BR
	M	20	L	RI	-	-	-	-	-	-	-	2.5	-	-	-	-	-	-	-
	M	20	L	RI	-	0.5	-	-	-	-	-	2	-	-	-	-	-	-	-
	M	20	L	P	-	0.5	-	-	-	-	-	-	-	-	1	-	-	-	-
	M	20	L	P	-	-	-	-	-	-	-	-	-	-	-	-	-	-	Pr
	M	20	L	P	-	-	-	-	-	-	-	-	-	-	-	-	-	6	Pr
	M	20	L	P	-	-	-	-	-	-	-	-	-	-	-	-	-	6	Pr
	M	20	L	P	-	-	-	-	-	-	-	-	-	-	-	-	-	6	Pr
	M	20	L	RI	-	-	-	-	-	-	-	-	-	-	-	-	-	-	Pr
	M	20	L	P	-	-	-	-	-	-	-	-	-	-	1	-	-	-	Pr
	M	20	L	P	-	-	-	-	-	-	-	-	-	-	-	-	-	-	Pr
	M	20	L	P	-	-	-	-	-	-	-	-	-	-	-	-	-	-	Pr
	M	20	R	P	-	2	-	-	-	-	-	2.3	-	-	-	-	-	-	-
PHC79	M	20	R	P	-	**1.86**	-	-	-	-	-	**2.32**	-	-	-	-	-	-	-
	M	20	L	P	-	-	-	-	-	-	-	-	-	-	-	-	-	-	Pr
	M	20	R	P	-	-	1.5	-	-	-	-	-	-	-	-	-	-	-	-
	M	20	L	P	-	0.75	-	-	-	-	-	-	-	-	-	-	-	-	-
	M	20	R	P	-	2	-	-	-	-	-	-	-	-	-	-	-	-	-
	M	20	L	P	-	1.5	-	-	-	-	-	-	-	-	-	-	-	-	-
	M	20	R	P	-	0.75	1.25	-	-	-	-	1.75	-	-	-	-	-	-	-
	M	20	L	P	-	1.5	-	-	-	-	-	1.7	-	-	-	-	-	-	-
	M	20	R	P	-	0.5	-	-	-	-	-	-	-	-	1	-	-	-	-
PHC80	M	20	L	P	-	2	-	-	-	-	-	-	-	-	-	-	-	-	-
	M	20	L	P	-	1.5	2	-	-	-	-	-	-	-	-	-	-	-	-
	M	20	L	RI	-	0.75	-	-	-	-	-	1.5	-	-	-	-	-	-	-

Table C.8: Survey data

PH	RH	SP	BK	MO	RE	CT	CE	FCT	FCE	GT	GE	OB	CB	FB	LWD	RR	BD	TL	BR
	M	20	L	RI	-	-	-	-	-	-	-	-	-	-	1	-	-	-	-
	M	20	L	RI	-	1	-	-	-	-	-	1.5	-	-	-	-	-	-	-
	M	20	L	RI	-	1.5	2	-	-	-	-	2.1	-	-	-	-	-	-	-
PH81	M	20	L	RI	-	2	3	-	-	-	-	-	-	-	-	-	-	-	-
	M	20	L	P	-	0.5	2	-	-	-	-	2.1	-	-	-	-	-	-	-
	M	20	L	P	-	1.5	-	-	2.25	-	-	2.35	-	-	-	-	-	-	-
	M	20	L	P	-	1	-	-	-	-	-	2	-	-	-	-	-	-	-
PHC82	M	20	L	P	-	**1.8**	**2.4**	-	-	-	-	-	-	-	-	-	-	-	-
	M	20	L	RI	-	0.5	1	-	-	-	-	1.1	-	-	-	-	-	-	-
	M	20	R	P	-	-	-	-	-	-	-	-	-	-	-	-	-	-	Pr
	M	20	R	P	-	-	-	-	-	-	-	-	-	-	-	-	-	-	Pr
	M	20	R	P	-	-	-	-	-	-	-	0.5	-	-	-	-	-	-	-
	M	20	R	P	-	-	-	-	-	-	-	-	1.5	-	-	-	-	-	-
	M	20	R	P	-	-	-	-	-	-	-	-	-	-	1	-	-	-	-
PH83	M	20	R	RI	-	-	-	1	-	-	-	1.3	-	-	-	-	-	-	-
	M	20	R	RI	-	2.5	-	-	-	-	-	-	-	-	-	-	-	-	-
	M	20	R	RI	-	2.5	-	-	-	-	-	-	-	-	-	-	-	-	-
	M	20	R	RI	-	-	-	-	-	-	-	-	-	-	1	-	-	-	-
	M	20	R	RI	-	-	-	0.75	-	-	-	-	-	-	-	-	-	-	-
	M	20	R	RI	-	-	-	-	-	-	-	3	-	-	-	-	-	-	-
	M	20	R	RI	-	-	-	-	-	-	-	3	-	-	-	-	-	-	-
	M	20	R	RI	-	-	-	-	-	-	-	-	-	-	-	-	-	-	Pr
	M	20	R	RI	-	-	-	-	-	-	-	-	-	-	-	-	-	-	Pr
	M	20	R	RI	-	-	-	-	-	-	-	-	-	-	-	-	-	-	Pr

Table C.8: Survey data

PH	RH	SP	BK	MO	RE	CT	CE	FCT	FCE	GT	GE	OB	CB	FB	LWD	RR	BD	TL	BR
PH06	A	10		P	-	-	-	-	-	-	-	-	-	-	-	-	-	-	-
	A	10		P	-	-	-	-	-	-	-	-	-	-	1	-	-	-	-
	A	10		P	-	-	-	-	-	-	-	-	-	-	1	-	-	-	-
	A	10		P	-	-	4	-	-	-	-	-	-	-	-	-	-	-	-
	A	10		P	-	-	4	-	-	-	-	-	-	-	-	-	-	-	-
	A	10		P	-	-	4	-	-	-	-	-	-	-	-	-	-	-	-
	A	10		P	-	-	4	-	-	-	-	-	-	-	-	-	-	-	-
PHC09	A	10		P	-	-	4	-	-	-	-	-	-	-	-	-	-	-	-
	A	10		P	-	-	4	-	-	-	-	-	-	-	-	-	-	-	-
	A	10		P	-	-	4	-	-	-	-	-	-	-	-	-	-	-	-
	A	10		P	-	-	4	-	-	-	-	-	-	-	1	-	-	-	-
	A	10		P	-	-	4	-	-	-	-	-	-	-	1	-	-	-	-
	A	10		P	-	-	4	-	-	-	-	-	-	-	1	-	-	-	-
	A	10		P	-	-	3.5	-	-	-	-	-	-	-	1	-	-	-	-
PH07	A	10		RI	-	2	3.5	-	-	-	-	-	-	-	-	-	-	-	-
	A	10		RI	-	1	-	-	-	-	-	-	-	-	1	-	-	-	-
	A	10		RI	-	-	-	-	-	-	-	-	-	-	1	-	-	-	-
	A	10		RI	-	-	-	-	-	-	-	-	-	-	1	-	-	-	-
	A	10		RI	-	-	-	-	-	-	-	-	-	-	1	-	-	-	-
	A	10		RI	-	0.5	-	-	-	-	-	-	-	-	1	-	-	-	-
	A	10		P	-	0.5	-	-	-	-	-	-	-	-	1	-	-	-	-
	A	10		P	-	0.5	-	-	-	-	-	-	-	-	1	-	-	-	-
	A	10		RI	-	1	-	-	-	-	3	-	-	-	1	-	-	-	-
	A	10		RI	-	-	-	-	-	-	3	-	-	-	1	-	-	-	-

Table C.8: Survey data

PH	RH	SP	BK	MO	RE	CT	CE	FCT	FCE	GT	GE	OB	CB	FB	LWD	RR	BD	TL	BR
	A	10		RI	-	-	-	-	-	-	3	-	-	-	1	-	-	-	-
	A	10		RI	-	-	-	-	-	-	3	-	-	-	1	-	-	-	-
	A	10		P	-	-	-	-	-	-	-	-	-	-	1	-	-	-	-
	A	10		P	-	-	-	-	-	-	2.7	-	-	-	-	-	-	-	-
	A	10		P	-	-	-	-	-	-	2.7	-	-	-	-	-	-	-	-
	A	10		P	-	1	-	-	-	-	2.5	-	-	-	-	-	-	-	-
	A	10		P	-	1	3	-	-	-	-	-	-	-	-	-	-	-	-
	A	10		RI	-	1	3	-	-	-	-	-	-	-	-	-	-	-	-
PHC10	A	10		RI	-	1	3	-	-	-	-	-	-	-	-	-	-	-	-
	A	10		RI	-	1	2.5	-	-	-	-	-	-	-	-	-	-	-	-
	A	10		RI	-	1	2.5	-	-	-	-	-	-	-	-	-	-	-	-
	A	10		RI	-	1	3	-	-	-	-	-	-	-	-	-	-	-	-
	A	10		RI	-	1	3	-	-	-	-	-	-	-	-	-	-	-	-
	A	10		RI	-	1	3	-	-	-	-	-	-	-	-	-	-	-	-
	A	10		RI	-	1	3	-	-	-	-	-	-	-	-	-	-	-	-
PH08	A	10		RI	-	1	3	-	-	-	-	-	-	-	-	-	-	-	-
	A	10		RI	-	-	-	-	-	-	-	-	-	-	-	-	-	-	-
PH05	A	10		P	-	-	-	-	-	-	-	-	1	-	1	-	-	-	-
	A	10		P	-	-	-	-	-	-	-	-	1	-	1	-	-	-	-
	A	10		P	-	-	-	-	-	-	-	-	1.5	-	1	-	-	-	-
	A	10		RI	-	-	-	-	-	-	-	-	1	-	1	-	-	-	-
	A	10		RI	-	-	-	-	-	-	-	-	1	-	-	-	-	-	-
	A	10		RI	-	-	-	-	-	-	-	-	1	-	-	-	-	-	-
	A	10		RI	-	-	-	-	-	-	-	-	PrB	-	-	-	-	-	-

Table C.8: Survey data

PH	RH	SP	BK	MO	RE	CT	CE	FCT	FCE	GT	GE	OB	CB	FB	LWD	RR	BD	TL	BR
	A	10		RI	-	-	-	-	-	-	-	-	PrB	-	-	-	-	-	-
	A	10		RI	-	-	-	-	-	-	-	-	PrB	-	-	-	-	-	-
	A	10		RI	-	-	-	-	-	-	-	-	PrB	-	-	-	-	-	-
	A	10		RI	-	-	-	-	-	-	-	-	PrB	-	-	-	-	-	-
PH04	A	10		RI	-	-	-	-	-	-	-	-	-	-	1	-	-	-	Pr
	A	10		P	-	-	-	-	-	-	-	-	-	-	1	-	-	-	Pr
	A	10		P	-	-	-	-	-	-	-	-	-	-	1	-	-	-	Pr
	A	10		P	-	-	-	-	-	-	-	-	-	-	1	-	-	-	Pr
	A	10		P	-	-	-	-	-	-	0.3	-	-	-	1	-	-	-	-
	A	10		RI	-	-	-	-	-	-	-	-	1.5	-	-	-	-	-	-
	A	10		RI	-	-	-	-	-	-	-	-	1.5	-	1	-	-	-	-
	A	10		P	-	-	-	-	-	-	-	-	1.5	-	-	-	-	-	-
	A	10		P	-	-	-	-	-	-	-	-	1.5	-	-	-	-	-	-
	A	10		P	-	-	-	-	-	-	-	-	1	-	-	-	-	-	-
	A	10		P	-	-	-	-	-	-	-	-	1	-	-	-	-	-	-
	A	10		P	-	-	-	-	-	-	-	-	PrB	-	-	-	-	-	-
	A	10		P	-	-	-	-	-	-	-	-	PrB	-	-	-	-	-	-
PH03	A	10		P	-	-	-	-	-	-	-	-	-	-	-	-	-	-	-
	A	10		RI	-	-	-	-	-	-	-	-	-	-	1	-	-	-	-
	A	10		RI	-	0.1	-	-	-	-	-	-	-	-	1	-	-	-	-
	A	10		RI	-	1.5	-	-	-	-	-	-	-	-	1	-	-	-	-
	A	10		RI	-	1	-	-	-	-	-	-	-	-	1	-	-	-	-
	A	10		RI	-	0.5	-	-	-	-	-	-	-	-	-	-	-	-	-
	A	10		RI	-	0.5	-	-	-	-	-	-	-	-	-	-	-	-	-

Table C.8: Survey data

PH	RH	SP	BK	MO	RE	CT	CE	FCT	FCE	GT	GE	OB	CB	FB	LWD	RR	BD	TL	BR
	A	10		RI	-	0.2	-	-	-	-	-	-	-	-	1	-	-	-	-
	A	10		RI	-	0.2	-	-	-	-	-	-	-	-	-	-	-	-	-
	A	10		RI	-	0.2	-	-	-	-	-	-	-	-	-	-	-	-	-
	A	10		RI	-	-	-	-	-	-	3	-	-	-	-	-	-	-	-
PH01	A	10		RI	-	-	-	-	-	1	-	-	-	-	-	-	-	-	-
	A	10		P	-	0.1	-	-	-	-	-	-	-	-	-	-	-	-	-
	A	10		P	-	4	-	-	-	-	-	-	-	-	-	-	-	-	-
	A	10		P	-	-	-	-	-	-	4	-	-	-	-	-	-	-	-
	A	10		P	-	-	-	-	-	-	5	-	-	-	-	-	-	-	-
	A	10		P	-	-	-	-	-	-	3	-	-	-	1	-	-	-	-
	A	10		P	-	-	-	-	-	-	5.4	-	-	-	1	-	-	-	-
	A	10		P	-	-	-	-	-	-	4.4	-	-	-	-	-	-	-	-
	A	10		P	-	0.6	-	-	-	-	-	-	-	-	1	-	-	-	-
	A	10		P	-	1	-	-	-	-	4.3	-	-	-	1	-	-	-	-
	A	10		P	-	0.5	-	-	-	-	4.2	-	-	-	-	-	-	-	-
	A	10		P	-	-	-	-	-	-	-	-	-	-	1	-	-	-	-
	A	10		P	tall	-	-	-	-	-	-	-	-	-	-	-	-	-	-
	A	10		P	tall	-	-	-	-	-	-	-	-	-	-	-	-	-	-
	A	10		P	tall	-	-	-	-	-	-	-	-	-	-	-	-	-	-
	A	10		P	tall	-	-	-	-	-	-	-	-	-	-	-	-	-	-
	A	10		P	tall	-	-	-	-	-	-	-	-	-	-	-	-	-	-
	A	10		P	tall	-	-	-	-	-	-	-	-	-	-	-	-	-	-
	A	10		P	tall	-	-	-	-	-	-	-	-	-	-	-	-	-	-
	A	10		P	tall	-	-	-	-	-	-	-	-	-	-	-	-	-	-

Table C.8: Survey data

PH	RH	SP	BK	MO	RE	CT	CE	FCT	FCE	GT	GE	OB	CB	FB	LWD	RR	BD	TL	BR
	A	10		P	tall	-	-	-	-	-	-	-	-	-	-	-	-	-	-
	A	10		P	tall	-	-	-	-	-	-	-	-	-	-	-	-	-	-
	A	10		P	tall	-	-	-	-	-	-	-	-	-	-	-	-	-	-
	A	10		P	tall	-	-	-	-	-	-	-	-	-	-	-	-	-	-
	A	10		P	tall	-	-	-	-	-	-	-	-	-	-	-	-	-	-
PH19	A	20		RI	tall	-	1	-	-	-	-	-	-	-	-	-	-	-	-
PHC18	A	20		RI	tall	-	1	-	-	-	-	-	-	-	-	-	-	-	-
	A	20		RI	tall	-	1	-	-	-	-	-	-	-	-	-	-	-	-
	A	20		RI	-	1.5	-	-	-	-	-	-	-	-	1	-	-	-	-
	A	20		RI	-	1.5	-	-	-	-	-	-	-	-	1	-	-	-	-
	A	20		RI	-	1.5	-	-	-	-	-	-	-	-	1	-	-	-	-
	A	20		RI	-	1.5	-	-	-	-	-	-	-	-	1	-	-	-	-
	A	20		RI	-	1.5	-	-	-	-	-	-	-	-	1	-	-	-	-
	A	20		RI	-	1.5	-	-	-	-	-	-	-	-	1	-	-	-	-
	A	20		RI	-	1.5	-	-	-	-	-	-	-	-	1	-	-	-	-
	A	20		RI	-	1.5	-	-	-	-	-	-	-	-	1	-	-	-	-
	A	20		RI	-	1.5	-	-	-	-	-	-	-	-	1	-	-	-	-
	A	20		RI	-	1.5	-	-	-	-	-	-	-	-	1	-	-	-	-
	A	20		P	-	-	-	-	-	-	-	-	0.75	-	-	-	-	-	-
	A	20		P	-	-	-	-	-	-	-	-	1	-	-	-	-	-	-
	A	20		P	-	-	-	-	-	-	-	-	-	-	-	-	-	-	Pr
	A	20		P	-	-	-	-	-	-	-	-	-	-	-	-	-	-	Pr
	A	20		P	-	-	-	-	-	-	-	-	-	-	-	-	-	-	Pr
PH17	A	20		RI	-	1.5	-	-	-	-	-	-	-	-	1	-	-	-	-

Table C.8: Survey data

PH	RH	SP	BK	MO	RE	CT	CE	FCT	FCE	GT	GE	OB	CB	FB	LWD	RR	BD	TL	BR
	A	20		RI	-	2.5	-	-	-	-	-	-	-	-	-	-	-	-	-
	A	20		RI	-	2.5	-	-	-	-	-	-	-	-	1	-	-	-	-
	A	20		RI	-	2.5	-	-	-	-	-	-	-	-	-	-	-	-	-
PHC16	A	20		RI	-	2	-	-	-	-	-	-	-	-	-	-	-	-	-
	A	20		RI	-	2	-	-	-	-	-	-	-	-	1	-	-	-	-
	A	20		RI	-	1.5	-	-	-	-	-	-	-	-	1	-	-	-	-
	A	20		RI	-	-	-	-	-	-	-	-	1	-	1	-	-	-	-
	A	20		RI	-	-	-	-	-	-	-	-	-	-	-	-	-	-	Pr
	A	20		RI	-	-	-	-	-	-	-	-	-	-	-	-	-	-	Pr
	A	20		RI	-	-	-	-	-	-	-	-	-	-	-	-	-	-	Pr
	A	20		RI	-	-	-	-	-	-	-	-	-	-	-	-	-	-	Pr
	A	20		RI	-	-	-	-	-	-	-	-	-	-	-	-	-	-	Pr
PH15	A	20		RI	-	-	-	-	-	-	-	-	-	-	-	-	-	-	Pr
	A	20		P	-	-	-	-	-	-	-	-	-	-	-	-	-	-	Pr
	A	20		P	-	-	-	-	-	-	-	-	-	-	-	-	-	-	Pr
	A	20		P	-	-	-	-	-	-	-	-	-	-	-	-	-	-	Pr
	A	20		P	-	-	-	-	-	-	-	-	-	-	-	-	-	-	Pr
	A	20		P	-	-	-	-	-	-	-	-	-	-	-	-	-	-	Pr
	A	20		P	-	-	-	-	-	-	-	-	-	-	-	-	-	-	Pr
	A	20		P	-	-	-	-	-	-	-	-	-	-	-	-	-	-	Pr
	A	20		P	-	-	-	-	-	-	-	-	-	-	-	-	-	-	-
	A	20		P	-	-	-	-	-	-	-	-	-	-	-	-	-	-	-
PH14	A	20		P	-	-	-	-	-	-	-	-	-	-	-	-	-	-	-
	A	20		P	-	-	-	-	-	-	-	-	-	-	-	-	-	-	-

Table C.8: Survey data

PH	RH	SP	BK	MO	RE	CT	CE	FCT	FCE	GT	GE	OB	CB	FB	LWD	RR	BD	TL	BR
	A	20		P	-	-	-	-	-	-	-	-	-	-	-	-	-	-	-
	A	20		P	-	-	-	-	-	-	-	-	-	-	-	-	-	-	-
	A	20		P	-	-	-	-	-	-	-	-	-	-	-	-	-	-	-
	A	20		P	-	-	-	-	-	-	-	-	-	-	-	-	-	-	-
	A	20		P	-	-	-	-	-	-	-	-	-	-	-	-	-	-	-
	A	20		P	-	-	-	-	-	-	-	-	0.8	-	-	-	-	-	-
PH13	A	20		RI	-	-	-	-	-	-	-	-	0.8	-	-	-	-	-	-
	A	20		P	-	-	-	-	-	-	-	-	0.8	-	-	-	-	-	-
	A	20		P	-	-	-	-	-	-	-	-	0.8	-	-	-	-	-	-
	A	20		P	-	-	-	-	-	-	-	-	0.8	-	-	-	-	-	-
	A	20		RI	-	-	-	-	-	-	-	-	0.8	-	-	-	-	-	-
	A	20		RI	-	-	-	-	-	-	-	-	0.8	-	-	-	-	-	-
PH12	A	20		RI	-	-	-	-	-	-	-	-	0.8	-	-	-	-	-	-
	A	20		P	-	-	-	-	-	-	-	-	-	-	-	-	-	-	Pr
	A	20		P	-	-	-	-	-	-	-	-	-	-	-	-	-	-	Pr
	A	20		P	-	-	-	-	-	-	-	-	-	-	-	-	-	-	Pr
	A	20		P	-	1	-	-	-	-	-	-	-	-	-	-	-	-	Pr
	A	20		P	-	1	-	-	-	-	-	-	-	-	-	-	-	-	-
	A	20		P	-	1.5	-	-	-	-	-	-	-	-	-	-	-	-	Pr
	A	20		RI	-	-	-	-	-	-	-	-	-	-	-	-	-	-	Pr
	A	20		RI	-	-	-	-	-	-	-	-	-	-	-	-	-	-	Pr
	A	20		RI	-	-	-	-	-	-	-	-	-	-	-	-	-	-	Pr
	A	20		P	-	-	-	-	-	-	-	-	-	-	-	-	-	-	Pr
	A	20		P	-	-	-	-	-	-	-	-	-	-	-	-	-	-	Pr

Table C.8: Survey data

PH	RH	SP	BK	MO	RE	CT	CE	FCT	FCE	GT	GE	OB	CB	FB	LWD	RR	BD	TL	BR
	A	20		P	-	-	-	-	-	-	-	-	-	-	-	-	-	-	Pr
	A	20		P	-	-	-	-	-	-	-	-	-	-	-	-	-	-	Pr
	A	20		P	-	-	-	-	-	-	-	-	-	-	-	-	-	-	Pr
	A	20		P	-	-	-	-	-	-	-	-	-	-	-	-	-	-	Pr
	A	20		P	-	-	-	-	-	-	-	-	-	-	-	-	-	-	Pr
	A	20		P	-	-	-	-	-	-	-	-	-	-	-	-	-	-	Pr
	A	20		RI	-	-	-	-	-	-	-	-	-	-	-	-	-	-	Pr
PH11	A	20		RI	-	-	-	-	-	-	-	-	-	-	-	-	-	-	Pr
PH20	A	20		RI	-	-	-	-	-	-	-	-	-	-	1	-	-	-	-
	A	20		P	-	-	-	-	-	-	-	-	-	-	1	-	-	-	-
	A	20		P	-	-	-	-	-	-	-	-	-	-	-	-	-	-	-
	A	20		P	-	-	-	-	-	-	-	-	-	-	-	-	-	-	-
	A	20		P	-	-	-	-	-	-	-	-	-	-	1	-	-	-	-
	A	20		P	-	-	-	-	-	-	-	-	-	-	1	-	-	-	-
	A	20		RI	-	-	-	-	-	-	-	-	-	-	-	-	-	-	-
	A	20		RI	-	-	-	-	-	-	-	-	-	-	-	-	-	-	Pr
PH21	A	20		RI	-	-	-	-	-	-	-	-	-	-	-	-	-	-	Pr
	A	20		P	-	-	-	-	-	-	-	-	-	-	-	-	-	-	Pr
	A	20		P	-	-	-	-	-	-	-	-	-	-	-	-	-	-	Pr
	A	20		RI	-	-	-	-	-	-	-	-	-	-	-	-	-	-	Pr
	A	20		RI	-	-	-	-	-	-	-	-	-	-	-	-	-	-	Pr
	A	20		RI	-	-	-	-	-	-	-	-	-	-	-	-	-	-	Pr
	A	20		P	-	-	-	-	-	-	-	-	-	-	-	-	-	-	Pr
	A	20		P	-	-	-	-	-	-	-	-	-	-	-	-	-	-	Pr

Table C.8: Survey data

PH	RH	SP	BK	MO	RE	CT	CE	FCT	FCE	GT	GE	OB	CB	FB	LWD	RR	BD	TL	BR
	A	20		P	-	-	-	-	-	-	-	-	-	-	-	-	-	-	Pr
	A	20		P	-	-	-	-	-	-	-	-	-	-	-	-	-	-	Pr
	A	20		P	-	-	-	-	-	-	-	-	-	-	-	-	-	-	Pr
PH22	A	20		RI	-	-	-	-	-	-	-	-	-	-	-	-	-	-	Pr
	A	20		P	-	-	-	-	-	-	-	-	-	-	-	-	-	-	-
PH23	A	20		RI	-	-	-	-	-	-	-	-	-	-	-	-	-	-	-
	A	20		RI	-	-	-	-	-	-	-	-	0.2	-	-	-	-	-	-
	A	20		RI	-	-	-	-	-	-	-	-	0.5	-	-	-	-	-	-
	A	20		RI	-	-	-	-	-	-	-	-	1	-	-	-	-	-	-
	A	20		RI	-	-	-	-	-	-	-	-	1	-	-	-	-	-	-
	A	20		RI	-	-	-	-	-	-	-	-	1.5	-	-	-	-	-	-
	A	20		RI	-	-	-	-	-	-	-	-	-	-	-	-	-	1	-
	A	20		P	-	-	-	-	-	-	-	-	-	-	-	-	-	1	-
PH24	A	20		RI	-	-	-	-	-	-	-	-	-	-	-	-	-	1	-
PHC25	A	20		RI	-	-	-	-	-	-	-	-	-	-	-	-	-	1	-
	A	20		P	-	-	-	-	-	-	-	-	0.5	-	-	-	-	-	-
PH26	A	20		RI	-	-	-	-	-	-	-	-	1	-	-	-	-	-	-
	A	20		RI	-	-	-	-	-	-	-	-	0.5	-	-	-	-	-	-
	A	20		P	-	-	-	-	-	-	-	-	-	-	-	-	-	-	Pr
	A	20		P	-	-	-	-	-	-	-	-	-	-	-	-	-	-	Pr
	A	20		P	-	-	-	-	-	-	-	-	-	-	-	-	-	-	Pr
	A	20		P	-	-	-	-	-	-	-	-	0.5	-	-	-	-	-	-
	A	20		P	-	-	-	-	-	-	-	-	0.5	-	-	-	-	-	-
	A	20		RI	-	-	-	-	-	-	-	-	-	-	-	-	-	-	Pr

Table C.8: Survey data

PH	RH	SP	BK	MO	RE	CT	CE	FCT	FCE	GT	GE	OB	CB	FB	LWD	RR	BD	TL	BR
	A	20		RI	-	-	-	-	-	-	-	-	-	-	-	-	-	-	Pr
PH27	A	20		RI	-	-	-	-	-	-	-	-	-	-	-	-	-	-	Pr
	A	20		P	-	-	-	-	-	-	-	-	-	-	-	-	-	-	Pr
	A	20		P	-	-	-	-	-	-	-	-	0.5	-	-	-	-	-	-
	A	20		P	-	-	-	-	-	-	-	-	0.5	-	-	-	-	-	-
	A	20		P	-	-	-	-	-	-	-	-	0.5	-	-	-	-	-	-
	A	20		P	-	-	-	-	-	-	-	-	0.5	-	-	-	-	-	-
	A	20		P	-	-	-	-	-	-	-	-	0.5	-	-	-	-	-	-
	A	20		P	-	-	-	-	-	-	-	-	1	-	-	-	-	-	-
	A	20		P	-	-	-	-	-	-	-	-	1	-	-	-	-	-	-
	A	20		P	-	-	-	-	-	-	-	-	1	-	-	-	-	-	-
	A	20		P	-	-	-	-	-	-	-	-	1	-	-	-	-	-	-
	A	20		P	-	-	-	-	-	-	-	-	1	-	-	-	-	-	-
PH28	A	20		RI	-	-	-	-	-	-	-	-	-	-	-	-	-	-	-
	A	20		RI	-	-	-	-	-	-	-	-	-	-	-	-	-	-	-
	A	20		P	-	-	-	-	-	-	-	-	-	-	-	-	-	-	-
	A	20		P	-	-	-	-	-	-	-	-	-	-	-	-	-	2	-
	A	20		P	-	-	-	-	-	-	-	-	-	-	-	-	-	2	-
	A	20		P	-	-	-	-	-	-	-	-	-	-	-	-	-	1	-
	A	20		P	-	-	-	-	-	-	-	-	-	-	-	-	-	1	-
	A	20		P	-	-	-	-	-	-	-	-	-	-	-	-	-	1	-
	A	20		P	-	-	-	-	-	-	-	-	-	-	-	-	-	2	-
	A	20		P	-	-	-	-	-	-	-	-	1.5	-	-	-	-	-	-
	A	20		P	-	-	-	-	-	-	-	-	1.5	-	-	-	-	-	-

Table C.8: Survey data

PH	RH	SP	BK	MO	RE	CT	CE	FCT	FCE	GT	GE	OB	CB	FB	LWD	RR	BD	TL	BR
	A	20		P	-	-	-	-	-	-	-	-	2	-	-	-	-	-	-
	L	20	L	RI	-	-	-	-	-	-	-	-	-	-	-	Pr	-	-	-
	L	20	L	S	-	-	-	-	-	-	-	-	-	-	-	Pr	-	-	-
	L	20	L	S	-	-	-	-	-	-	-	-	-	-	-	Pr	-	-	-
	L	20	L	S	-	-	-	-	-	-	-	-	-	-	-	Pr	-	-	-
	L	20	L	S	-	-	-	-	-	-	-	-	-	-	-	Pr	-	-	-
	L	20	L	S	-	-	-	-	-	-	-	-	-	-	-	Pr	-	-	-
	L	20	L	S	-	-	-	-	-	-	-	-	-	-	-	Pr	-	-	-
	L	20	L	S	-	-	-	-	-	-	-	-	-	-	-	Pr	-	-	-
PHC85	L	20	L	P	-	**1.87**	**3.1**	-	-	-	-	-	-	-	-	-	-	-	-
	L	20	R*	P	-	-	-	-	-	-	-	-	-	-	-	Pr	-	-	-
	L	20	L	P	-	1	1.5	-	-	-	-	1.6	-	-	-	-	-	-	-
	L	20	R*	P	-	-	-	-	-	-	-	-	-	-	-	Pr	-	-	-
	L	20	L	RI	-	1	-	-	-	-	-	1.3	-	-	-	-	-	-	-
	L	20	R*	RI	-	-	-	-	-	-	-	-	-	-	-	Pr	-	-	-
	L	20	L	RI	-	-	-	-	-	-	-	-	-	-	-	-	-	-	Pr
PH84	L	20	R*	RI	-	-	-	-	-	-	-	-	0.75	-	-	-	-	-	-
	L	20	L	P	-	-	-	-	-	-	-	-	-	-	-	-	-	-	-
	L	20	R*	P	-	-	-	-	-	-	-	-	1	-	-	-	-	-	-
	L	20	L	P	-	-	-	-	-	-	-	-	-	-	-	-	-	-	Pr
	L	20	R*	P	-	-	-	-	-	-	-	-	1	-	-	-	-	-	-
	L	20	L	P	-	-	-	-	-	-	-	-	-	-	-	-	-	-	Pr
	L	20	R*	P	-	-	-	-	-	-	-	-	1	-	-	-	-	-	-
	L	20	R	RI	-	-	-	-	-	-	-	-	-	-	-	Pr	-	-	-

Table C.8: Survey data

PH	RH	SP	BK	MO	RE	CT	CE	FCT	FCE	GT	GE	OB	CB	FB	LWD	RR	BD	TL	BR
	L	20	R	RI	-	-	-	-	-	-	-	-	-	-	-	Pr	-	-	-
	L	20	R	RI	-	-	-	-	-	-	-	-	-	-	-	Pr	-	-	-
	L	20	R	P	-	-	-	-	-	-	-	-	-	-	-	-	-	-	Pr
	L	20	R	P	-	-	-	-	-	-	-	-	-	-	-	-	-	-	Pr
	L	20	R	P	-	-	-	-	-	-	-	-	-	-	-	-	-	-	Pr
	L	20	R	P	-	-	-	-	-	-	-	-	-	-	-	-	-	-	Pr
	L	20	R	P	-	-	-	-	-	-	-	-	-	-	-	-	-	-	Pr
	L	20	R	P	-	-	-	-	-	-	-	-	-	-	-	-	-	-	Pr
	L	20	R	P	-	-	-	-	-	-	-	-	-	-	-	-	-	-	Pr
	L	20	R	P	-	-	-	-	-	-	-	-	-	-	-	-	-	-	Pr
	L	20	R	P	-	-	-	-	-	-	-	-	-	-	-	-	-	-	Pr
	L	20	R	P	-	-	-	-	-	-	-	-	-	-	-	-	-	-	Pr
	L	20	R	P	-	-	-	-	-	-	-	-	-	-	-	-	-	-	Pr
	L	20	R	RI	-	-	-	-	-	-	-	-	-	-	-	Pr	-	-	-
	L	20	R	RI	-	-	-	-	-	-	-	-	-	-	-	Pr	-	-	-
	L	20	R	RI	-	-	-	-	-	-	-	-	-	-	-	Pr	-	-	-
	L	20	R	RI	-	-	-	-	-	-	-	-	-	-	-	Pr	-	-	-
	L	20	R	RI	-	-	-	-	-	-	-	-	-	-	-	Pr	-	-	-
	L	20	R	RI	-	-	-	-	-	-	-	-	-	-	-	Pr	-	-	-
	L	20	R	RI	-	-	-	-	-	-	-	-	-	-	-	Pr	-	-	-
	L	20	R	RI	-	-	-	-	-	-	-	-	-	-	-	Pr	-	-	-
	L	20	R	RI	-	-	-	-	-	-	-	-	-	-	-	Pr	-	-	-
	L	20	R	RI	-	-	-	-	-	-	-	-	-	-	-	Pr	-	-	-
	L	20	R	RI	-	-	-	-	-	-	-	-	-	-	-	Pr	-	-	-

Table C.8: Survey data

PH	RH	SP	BK	MO	RE	CT	CE	FCT	FCE	GT	GE	OB	CB	FB	LWD	RR	BD	TL	BR
	L	20	R	RI	-	-	-	-	-	-	-	-	-	-	-	Pr	-	-	-
	L	20	R	RI	-	-	-	-	-	-	-	-	-	-	-	Pr	-	-	-
	L	20	R	RI	-	-	-	-	-	-	-	-	-	-	-	Pr	-	-	-
	L	20	L	P	-	-	-	-	-	-	-	-	-	-	-	-	-	-	Pr
	L	20	L	P	-	-	-	-	-	-	-	-	-	-	-	-	-	-	Pr
	L	20	L	P	-	-	-	-	-	-	-	-	-	-	-	-	-	-	Pr
	L	20	L	P	-	-	-	-	-	-	-	-	-	-	-	-	-	-	Pr
	L	20	L	P	-	-	-	-	-	-	-	-	-	-	-	-	-	-	Pr
	L	20	L	P	-	-	0.6	-	-	-	-	-	-	-	-	-	-	-	-
	L	20	L	P	-	-	1	-	-	-	-	-	-	-	-	-	-	-	-
	L	20	R	P	-	2	-	-	-	-	-	-	-	-	-	-	-	-	-
	L	20	R	P	-	2	-	-	-	-	-	-	-	-	-	-	-	-	-
	L	20	R	P	-	-	-	-	-	-	-	-	-	-	-	Pr	-	-	-
	L	20	R	P	-	-	-	-	-	-	-	-	-	-	-	Pr	-	-	-
	L	20	L	P	-	-	0.5	-	-	-	-	0.7	-	-	-	-	-	-	-
PH111	L	20	R	P	-	-	-	-	-	-	-	-	-	-	-	-	-	-	-
	L	20	R	P	-	-	-	-	-	-	-	-	-	-	-	-	-	-	-
	L	20	R	P	-	-	-	-	-	-	-	-	-	-	-	-	-	-	-
	L	20	L	P	-	-	0.5	-	-	-	-	-	-	-	-	-	-	-	-
	L	20	L	P	-	-	1.5	-	-	-	-	-	-	-	-	-	-	-	-
	L	20	L	P	-	-	2.5	-	-	-	-	-	-	-	-	-	-	-	-
	L	20	L	P	-	-	3	-	-	-	-	-	-	-	-	-	-	-	-
	L	20	L	RI	-	1.5	-	-	-	-	2	1.75	-	-	-	-	-	-	-
	L	20	L*	RI	-	1.5	-	-	-	-	-	-	-	-	1	-	-	-	-

Table C.8: Survey data

PH	RH	SP	BK	MO	RE	CT	CE	FCT	FCE	GT	GE	OB	CB	FB	LWD	RR	BD	TL	BR
PHC110	L	20	R	RI	-	**0.99**	**3.09**	-	-	-	-	-	-	-	-	-	-	-	-
	L	20	L*	RI	-	0.75	-	-	-	-	-	-	-	-	-	-	-	-	-
	L	20	R	RI	-	1.5	3	-	-	-	-	-	-	-	-	-	-	-	-
	L	20	L*	RI	-	-	-	-	-	-	-	-	-	-	-	-	-	1	-
	L	20	R	RI	-	2	-	-	-	-	-	-	-	-	-	-	-	-	-
	L	20	L*	RI	-	-	-	-	-	-	-	-	-	-	-	-	-	1	-
	L	20	R	RI	-	1.25	2	-	-	-	-	-	-	-	-	-	-	-	-
	L	20	L*	RI	-	-	-	-	-	-	-	-	-	-	-	-	-	1	-
	L	20	R	RI	-	0.5	1	-	-	-	-	1.1	-	-	-	-	-	-	-
	L	20	L*	RI	-	-	-	-	-	-	-	-	-	-	-	-	-	1	-
	L	20	R	RI	-	0.5	1	-	-	-	-	1.1	-	-	-	-	-	-	-
	L	20	L*	RI	-	-	-	-	-	-	-	-	-	-	-	-	-	1	-
	L	20	R	RI	-	0.5	-	-	-	-	-	0.7	-	-	1	-	-	-	-
PH112	L	20	L	RI	-	-	-	-	-	-	-	-	1	-	-	-	-	-	-
	L	20	L	P	-	-	-	-	-	-	-	-	1	-	-	-	-	-	-
	L	20	L	P	-	-	-	-	-	-	-	-	-	-	1	-	-	1	-
	L	20	L	P	-	-	-	-	-	-	-	-	-	-	-	-	-	1	-
	L	20	L	P	-	1.5	-	-	-	-	-	1.25	-	-	1	-	-	-	-
	L	20	L	P	-	1	-	-	-	-	-	2	-	-	-	-	-	-	-
	L	20	R	P	-	-	-	-	-	-	-	-	-	1	-	-	-	-	-
PHC113	L	20	L	RI	-	**1.78**	-	-	-	-	-	**1.98**	-	-	-	-	-	-	-
	L	20	R*	RI	-	-	-	-	-	-	-	-	-	1.5	-	-	-	-	-
PH114	L	20	L	RI	-	1.75	1.85	-	-	-	-	2	-	-	-	-	-	-	-
	L	20	R*	RI	-	-	-	-	-	-	-	-	-	1.5	-	-	-	-	-

Table C.8: Survey data

PH	RH	SP	BK	MO	RE	CT	CE	FCT	FCE	GT	GE	OB	CB	FB	LWD	RR	BD	TL	BR
	L	20	L	P	-	-	-	-	-	-	-	-	-	-	1	-	-	-	-
	L	20	R*	RI	-	-	-	-	-	-	-	-	-	-	1	-	-	-	-
	L	20	L	RI	-	-	-	1.25	-	-	-	-	-	-	-	-	-	-	-
	L	20	R*	RI	-	-	-	-	-	-	-	-	-	1	-	-	-	-	-
	L	20	R	RI	-	-	-	-	-	-	-	-	-	1.5	-	-	-	-	-
	L	20	R	RI	-	-	-	-	-	-	-	-	-	1	-	-	-	-	-
	L	20	R	RI	-	-	-	-	-	-	-	-	-	0.3	-	-	-	-	-
	L	20	R	RI	-	1.75	2	-	-	-	-	-	-	-	-	-	-	-	-
PH115/PHC116	L	20	R	RI	-	**2.24**	**2.81**	-	-	-	-	-	-	-	-	-	-	-	-
	L	20	R	P	-	1	2	-	-	-	-	-	-	-	-	-	-	-	-
	L	20	R	P	-	1	1.75	-	-	-	-	-	-	-	-	-	-	-	-
	L	20	R	P	-	1	1.5	-	-	-	-	1.6	-	-	-	-	-	-	-
	L	20	R	P	-	1	-	-	-	-	-	-	-	-	1	-	-	-	-
PH117	L	20	R	RI	-	-	-	-	-	-	-	-	-	-	-	-	-	-	-
	L	20	L	RI	-	-	-	-	-	-	-	-	-	-	-	-	-	-	-
	L	20	L	RI	-	-	-	-	-	-	-	-	-	-	1	-	-	-	-
	L	20	L	RI	-	-	-	-	-	-	-	-	-	-	1	-	-	-	-
	L	20	L	RI	-	-	-	-	-	-	-	-	1.5	-	-	-	-	-	-
	L	20	L	RI	-	0.75	1.5	-	-	-	-	-	-	-	1	-	-	-	-
	L	20	L	P	-	1	-	-	-	-	-	1.5	-	-	-	-	-	-	-
	L	20	L	P	-	-	-	1	-	-	-	1.5	-	-	-	-	-	-	-
	L	20	L	P	-	-	1.5	-	-	-	-	1.7	-	-	-	-	-	-	-
	L	20	L	P	-	2	3	-	-	-	-	-	-	-	-	-	-	-	-
	L	20	L	P	-	1.5	3	-	-	-	-	-	-	-	-	-	-	-	-

Table C.8: Survey data

PH	RH	SP	BK	MO	RE	CT	CE	FCT	FCE	GT	GE	OB	CB	FB	LWD	RR	BD	TL	BR
PHC118	L	20	L	RI	-	**1.4**	**3.2**	-	-	-	-	**4.2**	-	-	-	-	-	-	-
	L	20	L	P	-	-	-	-	-	-	-	-	-	-	1	-	-	-	-
	L	20	L	P	-	0.5	-	-	-	-	-	0.75	-	-	-	-	-	-	-
	L	20	L	P	-	-	-	-	-	-	-	-	-	-	-	-	-	-	-
	L	20	R	RI	-	-	-	-	-	-	-	0.7	0.5	-	-	-	-	-	-
	L	20	R	P	-	-	0.5	-	-	-	-	-	-	-	-	-	-	-	-
	L	20	R	P	-	-	-	-	-	-	-	-	-	-	-	-	-	-	-
	L	20	R	P	-	-	-	-	-	-	-	-	-	-	1	-	-	-	-
	L	20	R	P	-	-	-	-	-	-	-	-	0.5	-	-	-	-	-	-
	L	20	R	P	-	-	-	-	-	-	-	-	-	-	-	-	-	-	-
	L	20	R	RI	-	-	-	-	-	-	-	0.5	-	-	-	-	-	-	-
	L	20	R	RI	-	-	-	-	-	-	-	-	-	-	1	-	-	-	-
	L	20	R	RI	-	1	-	-	-	-	-	-	-	-	-	-	-	-	-
	L	20	R	RI	-	-	-	-	-	-	-	-	-	-	1	-	-	-	-
	L	20	R	RI	-	-	-	-	-	-	-	-	-	-	1	-	-	-	-
	L	20	R	RI	-	-	-	-	-	-	-	-	-	-	-	-	-	-	-
	L	20	R	RI	-	-	-	-	-	-	-	-	-	-	-	-	-	-	-
PH119	L	20	L	P	-	-	0.5	0.25	-	-	-	-	-	-	-	-	-	-	-
	L	20	L	P	-	-	-	-	-	-	-	-	-	-	1	-	-	-	-
	L	20	L	P	-	-	-	1	-	-	-	-	-	-	-	-	-	-	-
	L	20	L	P	-	-	-	-	-	-	-	-	-	-	1	-	-	-	-
	L	20	L	P	-	0.3	-	-	-	-	-	-	-	-	-	-	-	-	-
	L	20	L	P	-	0.3	0.75	-	-	-	-	-	-	-	-	-	-	-	-
	L	20	L	P	-	0.75	1.5	-	-	-	-	-	-	-	-	-	-	-	-

Table C.8: Survey data

PH	RH	SP	BK	MO	RE	CT	CE	FCT	FCE	GT	GE	OB	CB	FB	LWD	RR	BD	TL	BR
	L	20	L	RI	-	-	-	-	1.5	-	-	-	-	-	-	-	-	-	-
	L	20	L	RI	-	-	-	-	-	-	-	-	-	-	1	-	-	-	-
	L	20	L	RI	-	-	-	-	-	-	-	-	-	-	1	-	-	-	-
PH109	L	20	L	P	-	-	-	-	-	-	-	-	-	-	1	-	-	-	-
	L	20	L	P	-	-	-	-	-	-	-	-	1	-	-	-	-	-	-
	L	20	L	P	-	-	-	-	-	-	-	-	0.5	-	-	-	-	-	-
	L	20	L	P	-	-	-	-	-	-	-	-	-	0.5	-	-	-	-	-
	L	20	L	P	-	-	-	-	-	-	-	-	-	0.5	-	-	-	-	-
	L	20	L	P	-	-	0.3	-	-	-	-	-	-	-	-	-	-	-	-
	L	20	L	P	-	-	0.75	-	-	-	-	-	-	-	-	-	-	-	-
	L	20	R	RI	-	-	-	-	-	-	-	-	-	-	1	-	-	-	-
	L	20	R	P	-	-	-	-	0.5	-	-	-	-	-	-	-	-	-	-
	L	20	R	P	-	-	-	-	-	-	-	-	-	-	1	-	-	-	-
	L	20	R	RI	-	-	-	-	0.5	-	-	-	-	-	-	-	-	-	-
	L	20	R	RI	-	-	-	-	0.3	-	-	-	-	-	-	-	-	-	-
	L	20	R	RI	-	-	-	-	0.3	-	-	-	-	-	-	-	-	-	-
	L	20	R	P	-	-	-	-	-	-	-	-	-	-	1	-	-	-	-
	L	20	R	P	-	-	-	-	-	-	-	-	-	-	-	-	-	-	-
	L	20	R	P	-	-	-	-	-	-	-	-	-	-	-	-	-	-	-
	L	20	R	P	-	-	-	-	-	-	-	-	-	-	-	-	-	-	-
PH108	L	20	R	RI	-	-	-	-	-	-	-	-	-	-	1	-	-	-	-
	L	20	R	RI	-	-	-	-	-	-	-	-	-	-	1	-	-	-	-
	L	20	R	RI	-	-	-	0.5	-	-	-	-	-	-	-	-	-	-	-
	L	20	R	RI	-	-	-	-	-	-	-	-	-	-	-	-	-	-	-

Table C.8: Survey data

PH	RH	SP	BK	MO	RE	CT	CE	FCT	FCE	GT	GE	OB	CB	FB	LWD	RR	BD	TL	BR
	L	20	L	P	-	-	-	-	-	-	-	-	-	1	1	-	-	-	-
	L	20	L	P	-	-	-	-	-	-	-	-	-	0.75	-	-	-	-	-
	L	20	R	P	-	-	-	-	-	-	-	-	-	-	-	-	-	-	-
	L	20	R	P	-	-	-	-	-	-	-	1	-	-	-	-	-	-	-
	L	20	R	P	-	-	-	-	-	-	-	-	-	-	-	-	-	-	-
	L	20	R	P	-	-	-	-	-	-	-	-	-	-	-	-	-	-	-
	L	20	R	P	-	1.5	-	-	-	-	-	1.6	-	-	-	-	-	-	-
	L	20	R	P	-	-	0.5	-	-	-	-	-	-	-	-	-	-	-	-
	L	20	R	P	-	1.5	-	-	-	-	-	1.6	-	-	-	-	-	-	-
	L	20	R	P	-	1.5	-	-	-	-	-	1.6	-	-	-	-	-	-	-
	L	20	R	P	-	-	-	-	-	-	-	-	-	-	1	-	-	-	-
	L	20	R	P	-	2	-	-	-	-	-	-	-	-	-	-	-	-	-
	L	20	R	P	-	2	-	-	-	-	-	-	-	-	-	-	-	-	-
	L	20	R	P	-	-	-	-	-	-	-	1	-	-	-	-	-	-	-
	L	20	R	RI	-	-	-	-	-	-	-	0.5	-	-	-	-	-	-	-
	L	20	R	RI	-	-	-	-	-	-	-	-	-	-	1	-	-	-	-
	L	20	R	RI	-	-	-	-	-	-	-	0.5	-	-	-	-	-	-	-
	L	20	R	RI	-	-	-	-	-	-	-	0.5	-	-	-	-	-	-	-
PH107	L	20	R	RI	-	-	-	-	-	-	-	-	-	-	1	-	-	-	-
	L	20	R	RI	-	-	-	-	-	-	-	1	-	-	-	-	-	-	-
	L	20	R	P	-	-	-	-	-	-	-	-	-	-	1	-	-	-	-
	L	20	R	P	-	-	-	-	-	-	-	-	-	-	-	-	-	-	-
	L	20	R	P	-	-	-	-	-	-	-	-	-	-	1	-	-	-	-
	L	20	R	P	-	-	0.2	-	-	-	-	0.5	-	-	-	-	-	-	-

Table C.8: Survey data

PH	RH	SP	BK	MO	RE	CT	CE	FCT	FCE	GT	GE	OB	CB	FB	LWD	RR	BD	TL	BR
	L	20	R	P	-	-	1	-	-	-	-	2	-	-	-	-	-	-	-
PH106	L	20	R	RI	-	-	1.5	-	-	-	-	2	-	-	-	-	-	-	-
PHC105	L	20	R	RI	-	**1.02**	**1.67**	-	-	-	-	**2.22**	-	-	-	-	-	-	-
	L	20	R	RI	-	-	-	-	-	-	-	-	-	-	1	-	-	-	-
	L	20	R	RI	-	-	1.75	-	-	-	-	2	-	-	-	-	-	-	-
	L	20	R	RI	-	-	0.5	-	-	-	-	0.75	-	-	-	-	-	-	-
	L	20	L	RI	-	-	-	-	-	-	-	-	-	-	-	-	-	-	-
	L	20	L	P	-	-	-	-	-	-	-	-	-	-	1	-	-	-	-
	L	20	L	P	-	1	-	-	-	-	-	1.3	-	-	-	-	-	-	-
	L	20	L	P	-	-	-	-	-	-	-	-	-	-	1	-	-	-	-
	L	20	L	P	-	-	-	-	-	-	-	-	-	-	-	-	-	-	-
PH104	L	20	L	P	-	1	-	-	-	-	-	1.5	-	-	-	-	-	-	-
	L	20	L	RI	-	0.3	-	-	-	-	-	1	-	-	-	-	-	-	-
	L	20	L	RI	-	-	0.2	-	-	-	-	1	-	-	-	-	-	-	-
	L	20	L	P	-	1.5	-	-	-	-	-	-	-	-	-	-	-	-	-
	L	20	L	P	-	1.5	-	-	-	-	-	-	-	-	-	-	-	-	-
	L	20	L	P	-	0.2	-	-	-	-	-	1	-	-	-	-	-	-	-
	L	20	L	P	-	0.5	-	-	-	-	-	-	-	-	-	-	-	-	-
	L	20	L	P	-	-	-	-	-	-	-	-	-	-	-	-	-	-	-
	L	20	L	P	-	0.3	-	-	-	-	-	-	-	-	1	-	-	-	-
	L	20	L	RI	-	0.3	-	-	-	-	-	1	-	-	-	-	-	-	-
	L	20	L	RI	-	-	-	-	-	-	-	-	-	-	1	-	-	-	-
	L	20	L	P	-	-	0.5	-	-	-	-	-	-	-	-	-	-	-	-
PHC103	L	20	R	P	-	**1.46**	-	-	-	-	-	-	-	-	-	-	-	-	-

Table C.8: Survey data

PH	RH	SP	BK	MO	RE	CT	CE	FCT	FCE	GT	GE	OB	CB	FB	LWD	RR	BD	TL	BR
	L	20	L	P	-	-	-	-	-	-	-	1	-	-	-	-	-	-	-
	L	20	L	P	-	-	.5,2	-	-	-	-	1	-	-	-	-	-	-	-
	L	20	L	P	-	-	1	-	-	-	-	-	-	-	-	-	-	-	-
	L	20	L	P	-	-	1	-	-	-	-	-	-	-	-	-	-	-	-
	L	20	L	P	-	-	-	1	-	-	-	-	-	-	-	-	-	-	-
	L	20	L	P	-	-	1	-	-	-	-	-	-	-	-	-	-	-	-
	L	20	L	RI	-	-	0.5	-	-	-	-	-	-	-	-	-	-	-	-
	L	20	L	RI	-	-	-	-	-	-	-	-	-	-	1	-	-	-	-
	L	20	L	P	-	-	-	-	-	-	-	-	-	0.5	-	-	-	-	-
	L	20	L	P	-	-	-	-	-	-	-	1	-	-	-	-	-	-	-
	L	20	L	P	-	-	-	-	-	-	-	1	-	-	-	-	-	-	-
	L	20	L	P	-	-	-	-	-	-	-	1	-	-	1	-	-	-	-
	L	20	L	P	-	-	-	-	-	-	-	0.3	-	-	-	-	-	-	-
	L	20	L	P	-	-	-	-	-	-	-	-	-	-	-	-	-	-	-
	L	20	L	P	-	-	-	-	-	-	-	0.3	-	-	-	-	-	-	-
	L	20	L	P	-	-	-	-	-	-	-	-	-	-	-	-	-	-	-
	L	20	L	P	-	-	-	-	-	-	-	-	-	-	1	-	-	-	-
	L	20	L	P	-	-	-	-	-	-	-	1	-	-	1	-	-	-	-
	L	20	R	P	-	-	-	-	-	-	-	-	-	-	-	-	-	-	-
	L	20	R	P	-	-	-	-	-	-	-	1	-	-	-	-	-	-	-
	L	20	R	P	-	-	-	-	-	-	-	-	-	0.75	-	-	-	-	-
	L	20	R	P	-	-	-	-	-	-	0.3	1	-	-	-	-	-	-	-
PH102	L	20	R	P	-	-	-	-	-	-	-	-	-	-	-	-	-	-	-
	L	20	R	P	-	-	-	-	-	-	-	-	-	-	1	-	-	-	-

Table C.8: Survey data

PH	RH	SP	BK	MO	RE	CT	CE	FCT	FCE	GT	GE	OB	CB	FB	LWD	RR	BD	TL	BR
	L	20	R	P	-	-	-	-	-	-	-	-	-	-	1	-	-	-	-
	L	20	R	P	-	-	-	-	-	-	-	-	-	-	-	-	-	-	-
PHC101	L	20	L	RI	-	**0.66**	**1.24**	-	-	-	-	**1.68**	-	-	-	-	-	-	-
	L	20	L	P	-	-	-	-	-	-	-	-	-	-	-	-	-	-	-
	L	20	L	P	-	-	0.5	-	-	-	-	0.7	-	-	-	-	-	-	-
	L	20	L	P	-	-	-	-	-	-	-	-	-	-	1	-	-	-	-
PH100	L	20	R	RI	-	-	-	-	0.3	-	-	-	-	-	1	-	-	-	-
	L	20	R	RI	-	-	-	-	-	-	-	-	-	-	1	-	-	-	-
	L	20	R	RI	-	-	-	2.2	-	-	-	2.5	-	-	-	-	-	-	-
	L	20	L	RI	-	-	-	0.75	-	-	-	1	-	-	-	-	-	-	-
PHC99	L	20	L	RI	-	**0.82**	-	-	-	-	-	**0.86**	-	-	-	-	-	-	-
	L	20	L	P	-	0.3	-	-	-	-	-	1.5	-	-	1	-	-	-	-
	L	20	L	P	-	0.3	-	-	-	-	-	0.75	-	-	1	-	-	-	-
	L	20	L	P	-	0.3	-	-	-	-	-	0.75	-	-	-	-	-	-	-
	L	20	L	P	-	-	-	-	-	-	-	-	-	2	-	-	-	-	-
	L	20	L	P	-	-	-	-	-	-	-	-	-	1	-	-	-	-	-
	L	20	L	P	-	-	-	-	-	-	-	-	-	0.1	-	-	-	-	-
	L	20	L	P	-	-	-	-	-	-	-	-	-	0.5	-	-	-	-	-
	L	20	L	P	-	-	-	-	-	-	-	0.5	-	-	-	-	-	-	-
	L	20	L	P	-	-	-	-	-	-	-	-	-	-	1	-	-	-	-
	L	20	L	P	-	-	-	-	-	-	-	-	-	-	1	-	-	-	-
	L	20	R	P	-	-	-	-	-	-	-	-	-	-	1	-	-	-	-
	L	20	L	P	-	1.5	-	-	-	-	-	1.7	-	-	-	-	-	-	-
PHC120	L	20	L	RI	-	**1.29**	**1.72**	-	-	-	-	**2.33**	-	-	-	-	-	-	-

Table C.8: Survey data

PH	RH	SP	BK	MO	RE	CT	CE	FCT	FCE	GT	GE	OB	CB	FB	LWD	RR	BD	TL	BR
	L	20	L	RI	-	0.5	-	-	-	-	-	1.25	-	-	-	-	-	-	-
	L	20	L	RI	-	-	-	-	-	-	-	-	-	-	-	-	-	-	Pr
	L	20	L	P	-	-	-	-	-	-	-	-	-	-	-	-	-	-	Pr
	L	20	L	RI	-	-	-	-	-	-	-	-	-	-	-	-	-	-	Pr
PH121	L	20	L	RI	-	-	-	-	-	-	-	0.5	-	-	-	-	-	-	-
	L	20	R	RI	-	-	-	-	-	-	-	-	-	-	-	-	-	-	-
	L	20	R	RI	-	-	-	0.75	-	-	-	0.85	-	-	-	-	-	-	-
	L	20	R	RI	-	-	0.5	-	-	-	-	0.75	-	-	-	-	-	-	-
	L	20	R	P	-	-	-	-	-	-	-	1	-	-	1	-	-	-	-
	L	20	R	P	-	0.75	-	-	-	-	-	-	-	-	-	-	-	-	-
	L	20	R	P	-	-	-	0.5	-	-	-	-	-	-	-	-	-	-	-
	L	20	R	P	-	-	-	0.5	-	-	-	-	-	-	-	-	-	-	-
PHC98	L	20	R	RI	-	**1.06**	**1.98**	-	-	-	-	-	-	-	-	-	-	-	-
	L	20	R	RI	-	-	-	-	-	-	-	0.5	-	-	-	-	-	-	-
	L	20	R	RI	-	-	0.5	-	-	-	-	-	-	-	1	-	-	-	-
	L	20	R	RI	-	0.75	-	-	-	-	-	1	-	-	-	-	-	-	-
PH97	L	20	R	RI	-	-	-	-	-	-	-	-	-	-	-	-	-	-	-
	L	20	R	P	-	-	-	0.5	-	-	-	1.25	-	-	1	-	-	-	-
	L	20	R	RI	-	-	-	-	-	-	-	1	-	-	1	-	-	-	-
	L	20	R	RI	-	-	-	1	-	-	-	1.5	-	-	-	-	-	-	-
	L	20	R	RI	-	-	-	-	-	-	-	-	-	-	1	-	-	-	-
	L	20	R	RI	-	-	-	0.75	-	-	-	-	-	-	-	-	-	-	-
	L	20	R	RI	-	-	-	0.5	-	-	-	0.75	-	-	1	-	-	-	-
	L	20	R	RI	-	-	-	-	-	-	-	-	-	-	1	-	-	-	-

Table C.8: Survey data

PH	RH	SP	BK	MO	RE	CT	CE	FCT	FCE	GT	GE	OB	CB	FB	LWD	RR	BD	TL	BR
	L	20	L	P	-	-	-	-	-	-	-	-	-	1.5	-	-	-	-	-
	L	20	L	RI	-	-	-	-	-	-	-	-	-	0.5	-	-	-	-	-
	L	20	L	RI	-	-	-	1	-	-	-	2.5	-	-	-	-	-	-	-
	L	20	L	P	-	-	-	2	2.5	-	-	-	-	-	-	-	-	-	-
	L	20	L	RI	-	-	-	-	-	-	-	2.5	-	-	-	-	-	-	-
	L	20	L	RI	-	-	-	0.5	-	-	-	2.5	-	-	-	-	-	-	-
	L	20	L	RI	-	-	-	-	-	-	2.5	2.25	-	-	-	-	-	-	-
	L	20	L	RI	-	1.75	2	-	-	-	-	-	-	-	-	-	-	-	-
	L	20	L	RI	-	0.5	-	-	-	-	-	1.5	-	-	-	-	-	-	-
	L	20	L	RI	-	-	-	-	-	-	-	1.5	-	-	1	-	-	-	-
PHC96	L	20	L	RI	-	-	-	-	-	-	-	**1.5**	-	-	1	-	-	-	-
	L	20	L	RI	-	1.6	-	-	-	-	-	2.7	-	-	-	-	-	-	-
	L	20	L	P	-	1.75	2	-	-	-	-	3	-	-	-	-	-	-	-
	L	20	R	P	-	-	-	-	-	-	-	1	-	-	1	-	-	-	-
	L	20	L	P	-	-	-	-	-	-	-	-	-	-	1	-	-	-	-
	L	20	L	P	-	-	-	-	-	-	-	-	-	0.5	-	-	-	-	-
PH94	L	20	R	P	-	-	-	-	-	-	-	-	-	-	-	-	-	-	-
	L	20	R	RI	-	-	-	-	-	1	-	-	-	-	-	-	-	-	-
PHC93	L	20	R	P	-	**1.1**	**1.38**	-	-	-	-	-	-	-	-	-	-	-	-
	L	20	R	P	-	-	0.5	-	-	-	-	0.6	-	-	-	-	-	-	-
	L	20	R	P	-	-	0.5	-	-	-	-	-	-	-	-	-	-	-	-
	L	20	R	P	-	-	-	1	-	-	-	-	-	-	-	-	-	-	-
	L	20	R	P	-	-	-	1	-	-	-	-	-	-	-	-	-	-	-
PH92	L	20	R	RI	-	-	-	-	-	-	-	-	-	-	1	-	-	-	-

Table C.8: Survey data

PH	RH	SP	BK	MO	RE	CT	CE	FCT	FCE	GT	GE	OB	CB	FB	LWD	RR	BD	TL	BR
	L	20	L	RI	-	-	-	-	-	-	-	-	-	-	-	-	-	-	-
	L	20	L	RI	-	-	-	-	-	-	-	-	-	-	-	-	-	-	-
	L	20	L	RI	-	-	-	-	-	-	-	-	-	-	1	-	-	-	-
	L	20	R	RI	-	-	-	-	-	-	-	-	-	-	1	-	-	-	-
	L	20	R	RI	-	-	-	-	-	-	-	-	-	-	1	-	-	-	-
	L	20	R	RI	-	-	-	-	-	-	-	0.5	-	-	-	-	-	-	-
	L	20	R	RI	-	-	0.3	-	-	-	-	0.5	-	-	-	-	-	-	-
	L	20	R	RI	-	-	-	-	-	-	-	0.75	-	-	1	-	-	-	-
	L	20	R	RI	-	-	0.5	-	-	-	-	1	-	-	-	-	-	-	-
	L	20	R	RI	-	1.25	-	-	-	-	-	-	-	-	-	-	-	-	-
PHC91	L	20	R	RI	-	**1.2**	-	-	-	-	-	**1.46**	-	-	-	-	-	-	-
PH90	L	20	R	RI	-	-	1	-	-	-	-	-	-	-	-	-	-	-	-
	L	20	R	P	-	-	-	-	-	-	-	-	-	-	1	-	-	-	-
	L	20	R	P	-	-	1	-	-	-	-	-	-	-	-	-	-	-	-
	L	20	R	P	-	-	1	-	-	-	-	-	-	-	-	-	-	-	-
	L	20	R	P	-	-	-	-	-	-	-	-	-	-	-	-	-	-	-
	L	20	R	P	-	-	-	-	-	-	-	-	-	-	1	-	-	-	-
	L	20	R	P	-	-	-	-	-	-	-	-	-	-	1	-	-	-	-
	L	20	R	P	-	-	-	-	-	-	-	0.75	-	-	-	-	-	-	-
	L	20	L	RI	-	-	-	-	-	-	0.3	-	-	-	-	-	-	-	-
	L	20	L	RI	-	-	-	-	-	-	-	-	-	0.5	-	-	-	-	-
	L	20	L	RI	-	-	-	-	-	-	-	-	-	0.5	-	-	-	-	-
	L	20	L	P	-	-	-	-	-	-	-	-	-	-	-	-	-	1	-
	L	20	L	P	-	-	-	-	-	-	-	-	-	-	-	-	-	1	-

Table C.8: Survey data

PH	RH	SP	BK	MO	RE	CT	CE	FCT	FCE	GT	GE	OB	CB	FB	LWD	RR	BD	TL	BR
	L	20	L	P	-	-	-	-	-	-	-	-	-	-	-	-	-	1	-
	L	20	L	P	-	-	-	-	-	-	-	-	-	-	-	-	-	1	-
	L	20	L	P	-	-	-	-	-	-	-	-	-	-	-	-	-	1	-
	L	20	L	P	-	-	-	-	-	-	-	-	-	-	-	-	-	1	-
	L	20	L	P	-	-	-	-	-	-	-	-	-	-	-	-	-	1	-
	L	20	L	P	-	-	-	-	-	-	-	-	-	-	-	-	-	1	-
	L	20	L	P	-	-	-	-	-	-	-	-	-	-	-	-	-	1	-
	L	20	L	P	-	-	-	-	-	-	-	-	-	-	-	-	-	1	-
	L	20	L	P	-	-	-	-	-	-	-	-	-	-	-	-	-	1	-
	L	20	L	P	-	-	-	-	-	-	-	-	-	-	-	-	-	1	-
	L	20	L	P	-	-	-	-	-	-	-	-	-	-	-	-	-	1	-
	L	20	L	RI	-	-	-	-	-	-	-	-	-	-	-	-	-	1	-
	L	20	L	RI	-	-	-	-	-	-	-	-	-	-	-	-	-	1	-
	L	20	L	P	-	-	-	-	-	-	-	-	-	-	-	-	-	2	-
	L	20	L	P	-	-	-	-	-	-	-	-	-	-	-	-	-	3	-
PH88	L	20	L	RI	-	0.5	-	-	-	-	-	-	-	-	-	-	-	-	-
	L	20	L	RI	-	0.5	-	-	-	-	-	-	-	-	-	-	-	-	-
	L	20	L	P	-	-	-	-	-	-	-	-	-	-	1	-	-	-	-
	L	20	L	P	-	-	-	-	-	-	-	-	-	-	1	-	-	-	-
	L	20	L	P	-	-	-	-	-	-	-	-	1	-	-	-	-	-	-
	L	20	R	RI	-	-	-	-	-	-	0.75	-	-	-	1	-	-	-	-
	L	20	R	RI	-	-	-	0.5	-	-	-	1.25	-	-	-	-	-	-	-
	L	20	R	P	-	-	-	-	-	0.75	-	1	-	-	-	-	-	-	-
PHC87	L	20	R	P	-	-	**1.3**	-	-	-	-	**1.72**	-	-	-	-	-	-	-

Table C.8: Survey data

PH	RH	SP	BK	MO	RE	CT	CE	FCT	FCE	GT	GE	OB	CB	FB	LWD	RR	BD	TL	BR
	L	20	R	P	-	-	0.5	-	-	-	-	1	-	-	-	-	-	-	-
	L	20	R	P	-	-	0.75	-	-	-	-	1.5	-	-	-	-	-	-	-
	L	20	R	P	-	-	-	-	1.5	-	-	-	-	-	-	-	-	-	-
	L	20	R	P	-	0.5	-	-	-	-	-	-	-	-	-	-	-	-	-
	L	20	R	P	-	-	-	-	-	-	-	1.5	-	-	1	-	-	-	-
	L	20	R	P	-	0.5	-	-	-	-	-	1.5	-	-	-	-	-	-	-
	L	20	R	P	-	0.5	-	-	-	-	-	1.5	-	-	-	-	-	-	-
	L	20	R	P	-	0.5	-	-	-	-	-	1.5	-	-	-	-	-	-	-
	L	20	L	P	-	-	-	-	-	-	-	1	-	-	-	-	-	-	-
	L	20	L	P	-	-	-	-	-	-	-	-	2	-	-	-	-	-	-
	L	20	L	P	-	-	-	-	-	-	-	-	2	-	-	-	-	-	-
	L	20	L	P	-	-	-	-	-	-	-	-	1.5	-	-	-	-	-	-
	L	20	L	P	-	-	-	-	-	-	-	-	1.5	-	-	-	-	-	-
	L	20	L	P	-	-	-	-	-	-	-	-	1.5	-	-	-	-	-	-
	L	20	L	P	-	-	-	-	-	-	-	-	1.5	-	-	-	-	-	-
	L	20	L	P	-	-	-	-	-	-	-	-	1	-	-	-	-	-	-
	L	20	L	P	-	-	-	-	-	-	-	-	1	-	-	-	-	-	-
	L	20	L	P	-	-	-	-	-	-	-	-	1	-	-	-	-	-	-
	L	20	L	P	-	-	-	-	-	-	-	-	1	-	-	-	-	-	-
	L	20	L	P	-	-	-	-	-	-	-	-	1	-	-	-	-	-	-
	L	20	L	P	-	-	-	-	-	-	-	-	1	-	-	-	-	-	-
	L	20	L	P	-	-	-	-	-	-	-	-	0.5	-	-	-	-	-	-
	L	20	L	P	-	-	-	-	-	-	-	1	-	-	-	-	-	-	-

Appendix D

Air photo information

Available information on air photos used for the analysis in Chapter 3 are presented in Table D.1. These include photos for the Middle Elwha, which are also presented in Table 3.3 in Chapter 3, and for the Upper Elwha.

Table D.1: Air photos with available accompanying data

Photo date	Source	R/S	RE (m)	TE (m)	ME	UE
1939	NOAA Fisheries*	-	-	-	-	X
1968	NOAA Fisheries*	-	-	-	-	X
1976**	National Park Service***	-	7	12.2	X	-
1976	NOAA Fisheries*	-	-	-	-	X
1981	National Park Service***	-	15	18	X	-
1981	NOAA Fisheries*	-	-	-	-	X
1990-09-04	USGS DOQ	1:12500	2	10.2	-	X
1994-09-21	USGS DOQ	1:12000	3.9	10.7	X	-
2000	NOAA Fisheries*	-	-	-	-	X
2006-04-01	USDA NAIP	1 m	5	11.2	X	X
2009-10-08	USDA NAIP	1 m	5	11.2	X	X
2014-12-30	USGS/National Park Service	0.05 m	-	-	X	X
2015-04-16	USGS/National Park Service	0.05 m	-	-	X	-
2016-08-11	USGS/National Park Service	0.05 m	-	-	X	X

*Air photos digitized by NOAA Fisheries.
***Air photos digitized by author.
**Coverage of air photo does not extend to whole study area
R/S Resolution or scale
RE Registration error
TE Total error (registration + digitization)
MR Photo available for the Middle Elwha (between the dams)
UR Photo available for the Upper Elwha (upstream of Glines Canyon)